Numerical simulation of the interaction of atmospheric pressure plasma discharges with dielectric surfaces

François Pechereau

École Centrale Paris

THÈSE

présentée par

François Pechereau

pour l'obtention du

GRADE de DOCTEUR

Formation doctorale : Énergétique

Laboratoire d'accueil : Laboratoire d'Énergétique Moléculaire et Macroscopique, Combustion (EM2C) du CNRS et de l'ECP

Numerical simulation of the interaction of a plasma discharge at atmospheric pressure with dielectric surfaces

Soutenue le 19 décembre 2013

Rapporteurs :

M.	Paillol	Jean-Hugues	Professeur à l'Univ. de Pau, SIAME
M.	Pancheshnyi	Sergey	Principal Scientist, ABB Corporate Research

Jury :

Mme	Bourdon	Anne	Dir. de Recherche CNRS, EM2C
M.	Bonaventura	Zdeněk	Chercheur à l'Univ. Masaryk, Brno
M.	Guaitella	Olivier	Ing. de Recherche à Ecole Polytechnique, LPP
M.	Pouvesle	Jean-Michel	Dir. de Recherche CNRS, GREMI
M.	Tardiveau	Pierre	Maître de Conf. à l'Univ. PARIS-SUD, LPGP

École Centrale des Arts et Manufactures
Grand Établissement sous tutelle
du Ministère de l'Éducation Nationale
Grande Voie des Vignes
92295 Châtenay-Malabry Cedex
Tél : 33 (1) 41 13 10 00
Télex : 634 991 F EC PARIS

Laboratoire d'Énergétique Moléculaire et Macroscopique, Combustion (E.M2.C.)
UPR 288, CNRS et École Centrale Paris
Tél : 33 (1) 41 13 10 31
Fax : 33 (1) 47 02 80 35

2013ECAP0077

Remerciements

Je tiens tout d'abord à remercier ma directrice de thèse, Anne Bourdon. Je tiens à la remercier pour m'avoir accompagné pendant toute cette thèse. Elle a toujours fait preuve d'une grande écoute et de soutien. Je n'oublierai pas ses précieux conseils avant chaque prestation orale. Je la remercie sincèrement et travailler avec elle a été un vrai plaisir.
Je remercie chaleureusement Jean-Hugues Paillol et Sergey Pancheshnyi d'avoir accepté d'être rapporteurs de cette thèse. J'ai beaucoup apprécié leurs pertinentes remarques sur le manuscrit mais surtout leurs questions et remarques lors de la session de questions pendant la soutenance de thèse. Je tiens à remercier évidemment les membres de mon jury qui sont venus assister à ma soutenance de thèse: Pierre Tardiveau, Jean-Michel Pouvesle, Olivier Guaitella et spécialement à Zdenek Bonaventura qui a fait le voyage depuis Brno en République tchèque alors même qu'il était en béquilles!
Lors de ces trois années de thèse, j'ai eu grand plaisir à travailler avec les membres de l'équipe plasmas au laboratoire EM2C. En premier lieu avec Jaroslav Jansky qui m'a beaucoup appris et en particulier la façon de faire de belles images 2D avec Gnuplot! Ensuite avec Zdenek Bonaventura qui est toujours très enthousiastes pour realiser des simulations numériques complexes et est un virtuose des scripts de Gnuplot. Enfin avec Fabien Tholin avec qui j'ai eu de très grandes discussions sur les simulations de streamer et sur plein d'autres sujets!
Je tiens aussi à remercier les personnes du laboratoire EM2C dans lequel j'ai travaillé pendant ces trois ans. Je ne pensais pas rencontrer autant de gens si différents venant de tant d'horizons différents et de caractères si différents! Je voulais remercier Fara Kaddouri, François Doisneau, Florent Sainct, Mélanie Rochoux, Julien Jarrige, Max Duarte, Vincent Leroy, Diana Tudorache, Sorour Refahi, Adrien Lemal, Carolyn Jacobs, Mégane Mac Donald, Raphaël Baudoin, Jean-François Bourgoin, Laurent Tranchant et Marien Simeni Simeni et encore plein d'autres... Je remercie particulièrement mes collègues de bureau Clément Mirat et Aurélien Guy pour l'excellente ambiance de travail du bureau.

En dernier je tiens à remercier ma famille qui a été d'un énorme soutien et m'a beaucoup encouragé surtout dans les moments difficiles mais aussi pour le pot de thèse.

This work has been supported by a grant from the École Doctorale "Sciences pour l'Ingénieur (ED 287)" from École Centrale Paris. It has also been partly supported by the ALVEOPLAS (grant ANR-08-BLAN-0159-01) project.

Abstract

In this Ph.D. thesis, we have carried out 2D numerical simulations to study the influence of dielectric surfaces on the propagation dynamics of plasma discharges at atmospheric pressure.
First we have improved the computational efficiency of the discharge code used in this work in implementing parallelization techniques and more efficient numerical schemes. Then we have studied the dynamics of an air discharge at atmospheric pressure in a point-to-plane geometry with a dielectric layer on the cathode plane. For the surface discharge on the dielectric, we have shown that for a positive discharge, the discharge front is at a small distance from the dielectric surface, whereas the negative discharge front is on the dielectric. Then, we have studied the influence of a dielectric layer obstacle in the inter-electrode gap. We have shown that depending on the characteristics of the dielectric layer and the amplitude and polarity of the applied voltage, a second discharge may reignite or not below the dielectric in the second air gap. For a positive applied voltage at the point, the discharge reignition is mostly due to the potential redistribution in the inter-electrode gap after the positive streamer propagation in the first air gap and the reignited discharge is a positive ionization wave propagating from the dielectric towards the cathode. Conversely, for a negative voltage, the negative surface charges deposited on the upper surface of the dielectric layer have a significant contribution on the discharge reignition and the reignited discharge is a double headed discharge. The minimum applied voltage to have a discharge reignition is less in absolute value for a negative voltage than for a positive one.
The comparison of simulation results with experiments has shown that in a point-to-plane geometry with a sharp point and a high over-voltage, a single conical discharge structure is observed. A good agreement on the discharge diameter and propagation velocity has been obtained. With a dielectric obstacle in the gap, the simulated reignition dynamics is faster than in the experiments. To improve the agreement, we have studied the influence of several physico-chemical processes.
Finally, we have studied the dynamics of discharges in dielectric tubes at atmospheric pressure. For a $He - N_2$ mixture, we have put forward the importance of three body reactions. Last, the influence of the tube radius on the structure of discharges in $He - N_2$ and air is discussed.

Résumé

Dans cette thèse nous avons étudié l'influence de surfaces diélectriques sur la dynamique de propagation de décharges à pression atmosphérique. Tout d'abord, pour les simulations 2D réalisées dans ce travail, nous avons optimisé les performances du code de décharge en utilisant des schémas numériques performants et des techniques de parallélisation. Nous avons ensuite étudié la dynamique de propagation d'une décharge dans l'air à pression atmospherique dans une géométrie pointe-plan avec un plan diélectrique sur la cathode. Pour une décharge de surface positive, le front de la décharge se situe à une faible distance de la surface diélectrique alors que le front d'une décharge négative est sur la surface. Ensuite, nous avons étudié l'influence d'un obstacle plan diélectrique sur la dynamique de propagation d'une décharge. Nous avons montré que selon les caractéristiques du diélectrique, l'amplitude et la polarité de la tension appliquée, une seconde décharge peut s'initier ou pas dans l'air derrière le diélectrique. Pour une décharge positive initiée à la pointe, le processus de ré-allumage est dû à la redistribution du potentiel après la propagation de la première décharge et la seconde décharge est une onde d'ionisation positive. En revanche, pour une décharge négative à la pointe, les charges de surface négatives déposées sur la surface supérieure du plan diélectrique ont une influence sur le processus de ré-allumage et la seconde décharge est une décharge avec deux fronts positif et négatif. Le minimum de tension nécessaire au ré-allumage d'une décharge est plus faible en valeur absolue pour une polarité négative que positive. La comparaison des résultats avec les expériences a montré que dans une géométrie pointe-plan avec une pointe fine et une tension très élevée, une seule décharge de forme conique est observée. Un bon accord est obtenu sur le diamètre de la décharge et sa vitesse de propagation. Avec un obstacle plan diélectrique entre les éléctrodes, la dynamique de ré-allumage est plus rapide dans les simulations que dans les expériences. Pour améliorer la comparaison avec les expériences, nous avons étudié l'influence de plusieurs processus physico-chimiques. Pour finir, nous avons étudié la dynamique de décharges à pression atmosphérique dans des tubes diélectriques. Pour un mélange $He-N_2$, nous avons montré l'importance des réactions à trois corps. Enfin, nous avons mis en évidence l'influence du diamètre du tube sur la structure des décharges dans un mélange $He-N_2$ et dans l'air.

List of publications

Three articles have been written in the framework of this thesis:

- Pechereau, F., J. Jánský and A. Bourdon (2012), Simulation of the reignition of a discharge behind a dielectric layer in air at atmospheric pressure. *Plasma Sources Sci. Technol.*, 21 (5), 055011

- Pechereau, F., and A. Bourdon, Influence of polarity and voltage on the reignition of a discharge behind a dielectric layer in air at atmospheric pressure. *In preparation for Journal of Physics D: Applied Physics.*, (2013)

- Pechereau, F., P. Le Delliou, J. Jánský, P. Tardiveau, S. Pasquiers and A. Bourdon, Large conical discharge structure of an air discharge at atmospheric pressure in a point-to-plane geometry. *Submitted to IEEE Transactions on Plasma Science*, (November 2013)

Contents

Introduction

Framework and scope of this thesis

In plasma assisted catalysis for flue gas treatment or chemical synthesis, different types of catalyst supports are used. These supports are either random or organized two phase media such as pellets, monoliths or porous media (Kim 2004), (Becker et al. 2006). Then in the plasma reactors used, atmospheric pressure discharges interact with many obstacles and have to propagate in microcavities and pores of the considered materials, as shown for a monolith in Figure 1. While there have been extensive studies to evaluate the performances of the reactors (Mizuno et al. 1992), (Ogata et al. 1999), (Ibuka et al. 2001), (Kim 2004), (Hensel et al. 2009), little is known on the dynamics of atmospheric pressure discharges in complex two-phase media (Hensel et al. 2007), (Hensel and Tardiveau 2008), (Bhoj and Kushner 2008).

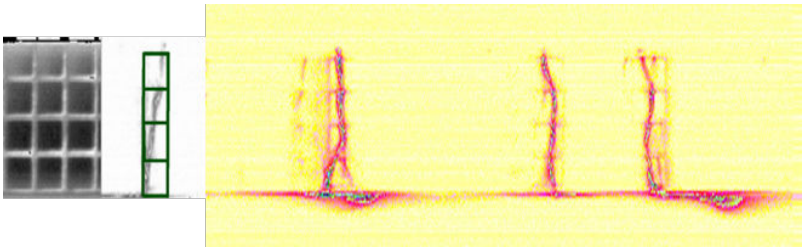

Figure 1: *Left : face view of a monolith of cordierite. Right : Light emission from plasma filaments created in a honeycomb monolith of cordierite, with 1* mm^2 *channel section. (Tardiveau et al. 2005)*

Most part of this PhD has been carried out within the framework of the ANR ALVEOPLAS (2009-2013) project involving four french research laboratories: LPGP (Univ. Paris Sud), EM2C, LSPM (Univ. Paris 13) and LMSME (Univ. Marne la vallée). The objective of this project was to better understand and characterize discharge propagation dynamics in

two-phase porous (random) and monolith (organized) systems. Four key questions have been identified at the beginning of this project:

- What would be the conditions that should be fulfilled to insure discharge propagation in materials such as monoliths, pellets, foams, micro-porous solids ?

- How discharges propagate in these materials ?

- At what extent can the discharge access the internal porosity of these solids ?

- How do the material physical characteristics (pore size distribution, dielectric properties, thermal properties) affect the discharge propagation mechanism ?

To address these complex questions, the strategy of the project was to proceed from the investigation of discharge propagation in small elementary structures or combination of structures found in such media, e.g., capillary, dead-end cavity, two-compartment cavity, etc, to more complex randomly distributed structures (porous, foam) or well organized macroscopic assembly of small structures (monolith).
In particular, within the ALVEOPLAS project the EM2C and LPGP laboratories have studied two simplified configurations chosen to represent the atmospheric pressure discharge propagation in small volumes and in the presence of obstacles as shown in a monolith in Figure 1:

- The propagation of a single streamer discharge in a capillary dielectric tube. The goal was to analyze the dynamics of an air discharge at atmospheric pressure as a function of the characteristics of the capillary tube (internal diameter and dielectric constant).

- The interaction of a discharge with a non-porous dielectric obstacle. The goal was to study the interaction between a streamer discharge in air at atmospheric pressure and a dielectric surface perpendicular to its propagation as in a monolith cell (Figure 1) and to identify the conditions in which a discharge may reignite below the dielectric obstacle.

For these two configurations, discharge simulations have been carried out at EM2C and compared with experimental results obtained at LPGP.

First, (Jánský et al. 2010; Jánský et al. 2011; Jánský and Bourdon 2011b) have studied the dynamics and structure of atmospheric pressure air discharges ignited by a point electrode and constrained to propagate in capillary tubes. In particular, (Jánský et al. 2011) have carried out a detailed comparison study between experiments and simulations for glass tubes with radii in the range $37.5 - 300$ μm. When comparing experimental results obtained at LPGP and simulation results, for small tube radius, the discharge front was found to be quite homogeneous inside the tube and to become tubular when the tube radius is increased. Experimentally, a maximum of the discharge propagation velocity in the tube is reached for a tube radius slightly less than 100 μm. For a tube radius of 100 μm, the discharge velocity was found to be three to four times higher than the velocity obtained without tube. (Jánský and Bourdon 2011b) have studied the dynamics of charging of the inner tube surface and have shown that the discharge is very efficient to charge the tube surface during its propagation.

One of the objectives of this PhD work was to study the second simplified configuration chosen in the ALVEOPLAS project: the interaction of an atmospheric pressure air discharge with a non-porous dielectric obstacle. It is interesting to note that these studies are also of interest for high voltage applications. Indeed, it is well known that inserting an insulating solid material between metallic electrodes results in an increase of the breakdown voltage of the inter-electrode gap (Naidu and Kamaraju 2004; Lebedev et al. 2005). Numerous experimental works have been carried out to improve the insulation performance of high voltage systems in varying for example the barrier position in the gap or the ratio of permittivities. However, it is important to note that so far, most models used in this field are based on the static behavior, taking into account the charges deposited on the dielectric surfaces and calculating the electric field in the gap (Abdel-Salam et al. 1998; Abdel-Salam et al. 2001a; Abdel-Salam et al. 2001b). Then usually, the dynamics of the discharge interaction with a dielectric layer acting as an axial geometrical constraint is not taken into account to evaluate the insulation performance of a given system.

Recently, spatially confining atmospheric pressure plasmas to dimensions of 1 mm or less has also appeared to be a promising approach to the generation of stable, glow discharges at atmospheric pressure for various applications and in particular for biomedical applications (Ehlbeck

et al. 2011; Lee et al. 2011). These last years, many studies have been devoted to plasma jets. Plasma jets are formed by pulsed atmospheric pressure discharges in rare gases (usually helium) ignited in thin dielectric tubes. High-speed photographs have demonstrated that a plasma jet is composed of discrete plasma bullets traveling with velocities in the range $10^6 - 10^8$ cm s^{-1} over up to several tenths of centimeters in ambient air (Teschke et al. 2005; Lu and Laroussi 2006; Sands et al. 2008; Lu et al. 2012). (Naidis 2010b; Naidis 2011b) showed that these bullets are in fact streamer discharges or ionization waves propagating in the easily ionized helium column and then constrained to propagate outside the dielectric tube in the region in which a sufficient concentration of helium is present. It is interesting to point out that recent studies on plasma jets have addressed also the question of discharge reignition. Indeed, experimental and numerical results show that after an ionization wave exit from a source tube, it impacts the outer surface of a spatially separate and electrode-less second tube and produces a new ionization wave inside the second tube (Xiong et al. 2013; Lu et al. 2009; Wu et al. 2011; Johnson et al. 2011). In (Xiong et al. 2013), this reignition process was called plasma transfer. In (Xiong et al. 2013), it was shown with 2D numerical simulations that whatever the polarity of the primary ionization wave ignited in the source tube, the secondary ionization wave ignited in the transfer tube is positive. It is interesting to note that a good qualitative agreement with experiments was obtained on the dynamics of the discharge reignition in the transfer tube in (Xiong et al. 2013) for both polarities of the primary discharge. So in this work, we will compare results for different polarities on the reignition dynamics of an air discharge at atmospheric pressure behind a dielectric obstacle with the results of (Xiong et al. 2013) obtained in Neon.

Finally, due to the wide range of medical applications (Laroussi et al. 2012), a lot of attention is focused on the characteristics of the plasma jet outside the tube (Sakiyama et al. 2010; Robert et al. 2012; Douat et al. 2012; Reuter et al. 2012; Naidis and Walsh 2013; Guaitella et al. 2013). Recently, different experimental groups (Algwari and O'Connell 2011; Mussard et al. 2013) have investigated more in detail the ignition and propagation of helium discharges in the tube and the discharge interaction with the tube surface. Then at the end of this PhD we have studied the interaction of a helium discharge with nitrogen impurities with the surface of a dielectric tube in a typical configuration used in plasma jets.

Outline of this thesis

At the EM2C laboratory, these last years, simulations of DBD discharges (in point-to-plane geometry (Célestin et al. 2008; Jánský et al. 2010) or in ring-ring geometry (Jánský et al. 2012)) have been carried out using a sequential code. The objective of the first part of this PhD thesis has been to improve the computational time and robustness of the discharge code:

- In Chapter 1, we present the fluid model used to simulate air discharges at atmospheric pressure. In this model, drift diffusion equations for charged species are coupled to Poisson's equation. Then the numerical methods used in the existing streamer discharge code are presented.

- In Chapter 2, we focus our numerical effort on the numerical method used to solve Poisson's equation. To improve the computational time, we present and test two parallel solvers. Then, we present and compare the performances of the implementation of a "semi-implicit" model compared to a full-explicit one.

- In Chapter 3, we present and compare different transport schemes for drift-diffusion equations.

- In Chapter 4, we present the parallel performances of a new MPI-OPENMP parallel discharge code using domain decomposition. Then, we summarize the different versions of the code used in the chapters of this thesis.

The second part of this thesis is focused on the interaction of discharges at atmospheric pressure with dielectric surfaces:

- In Chapter 5, we study the dynamics of an air discharge at atmospheric pressure in a point-to-plane geometry with a dielectric layer on the cathode plane. The objective is to study the propagation dynamics of positive and negative surface discharges on the dielectric surface and specifically the dynamics of surface charging, of the sheath formation and the structure of surface discharges.

- In Chapter 6, we study in a point-to-plane geometry the influence of a dielectric layer obstacle on the path of a propagating positive

discharge. The goal is to study the influence of the characteristics of the dielectric plane on the reignition process behind the dielectric obtacle.

- In Chapter 7, for the same point-to-plane geometry, we put emphasis on the influence of the amplitude and polarity of the applied voltage at the point electrode on the reignition dynamics behind the dielectric obtacle.

- In Chapter 8, we present a comparison of simulation results with experiments carried out at LPGP in a point-to-plane geometry with a sharp point and a high over-voltage. In this chapter, we compare results obtained without and with a dielectric plane obstacle.

- In chapter 9, we present first results on the dynamics of discharges in dielectric tubes at atmospheric pressure. We discuss the discharge dynamics with a detailed chemistry for a $He - N_2$ mixture. Then, we study the influence of the tube radius on the structure of discharges in $He - N_2$ and air.

Finally, we present a general conclusion on the outcomes of this work, and suggestions for future research.

Part I

Physical model, optimization and parallelization of the discharge code

Chapter 1

Physical model and status of the legacy discharge code

1.1 Introduction

The objective of this chapter is to present the physical model used for air discharges in this work and the numerical methods available in the discharge code of the EM2C laboratory at the beginning of this PhD work. Then, we present two typical geometries studied in this work and put forward the need to improve the numerical performances of the code. During the first year of this thesis in 2010, a new cluster called "igloo" was purchased by Ecole Centrale Paris. As all the simulations presented in this PhD thesis have been carried out on "igloo", we present here the characteristics of this multicore cluster architecture:

- Altix ICE 8400 LX of 68 nodes with two processors six-core Intel Xeon X5650 (2.66Ghz) per node, so 816 cores in total with 24Go of memory per node.

1.2 Physical model for air streamer discharge at atmospheric pressure

The most widely used model to study streamer dynamics in air at atmospheric pressure is based on continuity equations for electrons "e", positive "p" and negative ions "n":

$$\frac{\partial n_k}{\partial t} + \boldsymbol{\nabla} \cdot \boldsymbol{j}_k = S_k \ \ ; \ k = e, p, n \tag{1.1}$$

where n_k is the number density of species k, $\boldsymbol{j}_k$ is the flux of species k and S_k is the source term of species k due to chemical reactions and photo-ionization. We have used the classical drift-diffusion approximation, valid for highly collisional plasmas:

$$\boldsymbol{j}_k = \mu_k \; n_k \; \boldsymbol{E} - D_k \; \boldsymbol{\nabla} \; n_k \;\; ; \; k = e, p, n \; , \tag{1.2}$$

where D_k, μ_k are the diffusion coefficient and mobility of specie k respectively and $\boldsymbol{E}$ is the electric field.
The following equations describe the source terms for electrons S_e, positive ions S_p and negative ions S_n:

$$\begin{cases} S_e &= (\partial_t n_e)_{chem} &= (\alpha|W_e| - \eta|W_e| - \beta_{ep} n_p)\, n_e + S_{ph} \; , \\ S_n &= (\partial_t n_n)_{chem} &= -\beta_{np} n_p n_n + \eta|W_e| n_e \; , \\ S_p &= (\partial_t n_p)_{chem} &= -\left(\beta_{ep} n_e + \beta_{np} n_n\right) n_p + \alpha|W_e| n_e + S_{ph} \; , \end{cases} \tag{1.3}$$

where $|W_e| = |\mu_e \; E|$ is the absolute value of the electron drift velocity, α and η stand for the ionization and attachment coefficients respectively. β_{ep} is the recombination rate coefficient between positive ions and electrons and β_{np} is the recombination rate coefficient between positive and negative ions. In this work we use the local field approximation. Then, transport coefficients and source terms of the model are assumed to be explicit functions of the local reduced electric field E/N, where E the is the magnitude of the electric field and N is the air neutral density equal to $2.45{\times}10^{19}$ cm^{-3}. All reactions rates and transport coefficients are taken from (Morrow and Lowke 1997).
The S_{ph} term is the rate of electron-positive ion pair production due to the photo-ionization in the gas volume. For this term, we use the three group SP3 model (Bourdon et al. 2007) based on the work on (Zhelezniak et al. 1982). In this model, it is assumed that photons emitted in the range 98-102.5 nm by the radiative de-excitation of highly excited states of nitrogen N_2 are able to photo-ionize the molecular oxygen in air (Zhelezniak et al. 1982). In the SP3 photo-ionization model, to model the wavelength dependence of the photo-ionization source term, three effective wavelengths are considered. For each of the three effective wavelengths, 2 Poisson's like equations have to be solved with Larsen's boundary conditions (Liu et al. 2007) that require to iterate three times the solution of each of these Poisson's like equations. Further details may be found in (Célestin 2008) and (Bourdon et al. 2007).
Finally, the system of equations to study streamer dynamics in air at atmopsheric pressure is closed with Poisson's equation that takes into

account different dielectric permittivities (air or dielectric material):

$$\boldsymbol{\nabla} \cdot (-\varepsilon_0 \varepsilon_\mathrm{r} \boldsymbol{\nabla} \mathrm{V}) = q_\mathrm{e}(n_\mathrm{p} - n_\mathrm{n} - n_\mathrm{e}) \ , \tag{1.4}$$

where $\mathrm{q_e}$ is the absolute value of electron charge, ε_r is the relative permittivity, ε_0 is the permittivity of free space.

1.3 Numerical methods in the legacy discharge code (LDC)

In (Tholin and Bourdon 2011) and (Jánský et al. 2010), point to point and point to plane electrode geometries were simulated with the legacy discharge code (LDC) to study 2D axi-symmetric discharges. In (Célestin 2008) and (Jánský et al. 2010), dielectric surfaces were taken into account as a dielectric layer on the cathode plane or as a tube. In section 1.3.1, we present the numerical methods implemented in the LDC code to solve Poisson's equation (1.4). Then in section 1.3.2, we present the numerical methods to solve drift-diffusion equations (1.1) with (1.2).

1.3.1 Numerical resolution of Poisson's equation

For streamer simulations, the electric field is a key parameter since first, with the local field approximation, transport parameters and source terms have a non-linear dependence with it. Second, the electric field derived from the electric potential in Poisson's equation is directly related to charged species densities. Then, a small error in the calculation of the electric potential implies large variations on the electric field which may lead to considerable errors in the simulation results. Therefore, it is important to solve accurately Poisson's equation for the calculation of electric potential but also in the calculation of the photo-ionization source term. Indeed with the three group SP3 model (Bourdon et al. 2007), to calculate the photo-ionization source term, it is necessary to solve 18 Poisson's like equations (two Poisson's like equations for each of the three wavelengths and three iterations are performed for boundary conditions). It is important to note that in the simulations presented in this thesis, we calculate the photo-ionization source term every 5 time steps. We have checked that this has a negligible influence on the results but in turn saves a considerable computational time.
Three important points have to be considered for the numerical resolution of Poisson's equation:

- The discretization scheme: it gives the numerical accuracy of the resolution of Poisson's equation. The discretization we use is presented in Section 1.3.1.
- The boundary conditions: as it is an elliptic equation, the resolution of Poisson's equation requires the boundary conditions to be set. It is especially important in the case of Laplace's equation where the solution is entirely governed by the boundary conditions. We discuss this point in Section 1.3.1.
- The numerical method used: the resolution of Poisson's equation can be very time consuming. We will present here the direct solver MUMPS used in the LDC code.

Discretization of Poisson's equation without surface charges

First, we consider a medium with different permittivities but no surface charges. In this thesis, we study axi-symmetric discharges and thus cylindrical coordinates (x,r) are used with the x-axis as axis of the discharge. In cylindrical coordinates, equation (1.4) can be written as:

$$-\frac{\partial}{\partial x}\left(\epsilon\frac{\partial V}{\partial x}\right)-\frac{1}{r}\frac{\partial}{\partial r}\left(\epsilon r\frac{\partial V}{\partial r}\right)=\rho(x,r)\ , \tag{1.5}$$

where x and r are axial and radial coordinates, respectively, $\epsilon = \varepsilon_0\varepsilon_\mathrm{r}$ and $\rho = q_e(n_p - n_n - n_e)$. In this work, we consider that the computational domain is discretized on a rectilinear grid. The nodes of the grid are indexed with i and j in axial and radial directions respectively, such that $V_{i,j} = V(x_i, r_j)$. The edges of the cell indexed (i, j) are located by $x_{i\pm1/2}$ and $r_{j\pm1/2}$, in axial and radial direction, respectively.
Using a finite volume method, the second order discretization of Eq. (1.5) in cylindrical coordinates gives the classical five diagonal linear system. More details on the method to take into account dielectric surface in the discretization of Poisson's equation can be found in Appendix C:

$$V^E_{i,j}V_{i+1,j} + V^W_{i,j}V_{i-1,j} + V^S_{i,j}V_{i,j-1} + V^N_{i,j}V_{i,j+1} + V^C_{i,j}V_{i,j} = \pi\rho_{i,j}\Delta x_{i+1/2}\Delta r^2_{j-1/2}\ , \tag{1.6}$$

with:

$$\begin{cases} V_{i,j}^E &= -\pi \Delta r_{j-1/2}^2 \dfrac{\epsilon_{i+1,j}\epsilon_{i,j}}{\epsilon_{i+1,j}(x_{i+1/2}-x_i)+\epsilon_{i,j}(x_{i+1}-x_{i+1/2})} \ , \\ V_{i,j}^W &= V_{i-1,j}^E \ , \\ V_{i,j}^N &= -2\pi r_{j+1/2}\Delta x_{i-1/2} \dfrac{\epsilon_{i,j+1}\epsilon_{i,j}}{\epsilon_{i,j+1}(r_{j+1/2}-r_j)+\epsilon_{i,j}(r_{j+1}-r_{j+1/2})} \ , \\ V_{i,j}^S &= V_{i,j-1}^N \ , \\ V_{i,j}^{\mathrm{c}} &= -(V_{i,j}^W + V_{i,j}^E + V_{i,j}^S + V_{i,j}^N) \ , \end{cases} \tag{1.7}$$

where $\Delta x_{i+/2} = x_{i+1/2} - x_{i-1/2}$ and $\Delta r_{j-1/2}^2 = r_{j+1/2}^2 - r_{j-1/2}^2$. This symmetric discretization of Poisson's equation results in a symmetric positive definite matrix.

Discretization with surface charges

In the presence of a dielectric interface, we need to take into account the influence of the deposited surface charges due to the fluxes of charged species to the dielectric surface. Considering the numerical grid, as depicted in Figure 1.1, we assume that the dielectric surface is perpendicular to the axis of symmetry and the gas-dielectric interface lies on the interface between the nodes (i^*, j) and (i^*+1, j); i.e., on the edge cell $(i^*+1/2, j)$. In order to take into account surface charges deposited on the surface of the dielectric, we need to change the discretization of the

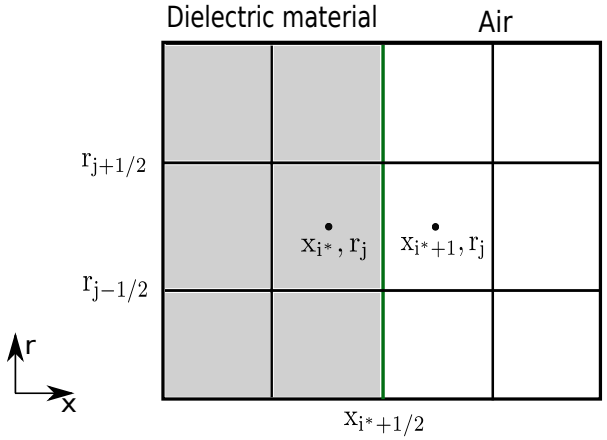

Figure 1.1: *Numerical grid in presence of a plane dielectric. The shaded domain represents the dielectric material region. The gas/dielectric interface lies at* $x_{i^*+1/2}$.

right hand side of equation 1.6. All the details can be found in Appendix C.
Finally to take into account the contribution of surface charges, the source term $\rho_{i,j}\pi\Delta x_{i+1/2}\Delta r^2_{j-1/2}$ of equation (1.6) has to be replaced with $\rho^{'}_{i,j}$ only at the point $(i = i^*, j)$ and $(i = i^* + 1, j)$, such that:

$$\begin{cases} \rho^{'}_{i^*+1,j} &= \rho^{'}_{i^*+1,j} + \dfrac{\epsilon_{i+1,j}\sigma_j(x_{i+1/2} - x_{i+1})(\pi\Delta r^2_{j-1/2})}{\epsilon_{i,j}(x_{i+1} - x_{i+1/2}) + \epsilon_{i+1,j}(x_{i+1/2} - x_i)} \ , \\ \rho^{'}_{i^*,j} &= \rho^{'}_{i^*,j} + \dfrac{\epsilon_{i,j}\sigma_j(x_{i+1} - x_{i+1/2})(\pi\Delta r^2_{j-1/2})}{\epsilon_{i,j}(x_{i+1} - x_{i+1/2}) + \epsilon_{i+1,j}(x_{i+1/2} - x_i)} \ . \end{cases} \tag{1.8}$$

Boundary conditions of Poisson's equation

Different sets of boundary conditions are used for Poisson's equation, depending on the problem studied.
Two different types of boundary conditions can be used at the domain boundaries. First, the homogeneous Neumann boundary condition ($\nabla V \cdot \mathbf{n} = 0$, $\mathbf{n}$ being the normal vector of the surface boundary) and second, the Dirichlet boundary condition.
In this work, we have mostly studied point to plane axi symmetric geometries with a discharge propagating on the discharge axis. In this case, in the radial direction for both the symmetry axis ($r = 0$) and the border of the computational domain ($r =$R$_{lim}$), Neumann boundary conditions are used. To neglect the influence of charges inside the computational domain on the boundary at $r =$R$_{lim}$, it is necessary to consider a sufficiently large value of R$_{lim}$. Then, for the simulations presented in this work, we have carried out preliminary tests to carefully determine the value of R$_{lim}$.
At the grounded plane and at the point electrode, Dirichlet boundary conditions are applied. At the border of the computational domain at $x =$X$_{lim}$ and above the point electrode, Neumann boundary conditions is used. At the metallic point electrode-air interfaces, the ghost fluid method is used (Célestin et al. 2009) that allows to accurately describe the complex geometry of the point electrode in the calculation of the electric potential.

Numerical methods to solve Poisson's equation

Usually for streamer simulations, the discretized form of Poisson's equation (C.11) inside the computational domain is solved using the sym-

metrical successive over-relaxation (SOR) method (Morrow and Lowke 1997), (Ducasse et al. 2007) and (Liu and Pasko 2006). This method has been widely used as it is simple to implement and robust. However, the SOR method is well-known to converge rather slowly. As in (Célestin 2008), first we have used the iterative NAG solver (`http://www.nag.co.uk`) which is much faster than the SOR method. However, due to the huge memory capabilities of modern multi-core cluster architecture, direct solvers can also be used to solve the discretized form of the Poisson's equation. Without going into details, we present the general principle of a direct solver. If we rewrite equation (C.11):

$$\mathbf{Ax} = \mathbf{b} \ . \tag{1.9}$$

Where $\mathbf{A}$ is the positive definite matrix resulting from the discretization of Poisson's equation. Here the vector $\mathbf{x}$ is the potential solution and $\mathbf{b}$ is a vector in which the right hand side of Poisson's equation is stored. To solve equation (1.9), the direct solver performs three steps:

- **Analysis**: The matrix is preprocessed to improve its structural properties. During the analysis, a symbolic factorization is performed. Let $\mathbf{A}_{pre}$ denotes the preprocessed matrix.

- **Factorization**: A direct factorization is carried out $\mathbf{A}_{pre} = \mathbf{LDL}^T$. There are various methods to perform the factorization depending on the direct solver. In MUMPS (Amestoy et al. 2001), the method is called "multifrontal approach". In the direct solver PaStiX (PaStiX 2012), the method is called " left-right looking" approach. After the factorization, the factor matrices are kept in memory and they will be used in the solution phase.

- **Solution**: The solution of $\mathbf{LDL}^T \ \mathbf{x}_{pre} = \mathbf{b}_{pre}$ (where $\mathbf{x}_{pre}$ and $\mathbf{b}_{pre}$ are respectively the transformed solution $\mathbf{x}$ and the right-hand side $\mathbf{b}$ associated to the preprocessed matrix $\mathbf{A}_{pre}$) is obtained through a forward elimination step:

  $$\mathbf{LDy} = \mathbf{b}_{pre} \ , \tag{1.10}$$

  followed by a backward elimination step:

  $$\mathbf{LT}\mathbf{x}_{pre} = \mathbf{y} \ . \tag{1.11}$$

A forward elimination and a backward substitution are then performed to obtain $\mathbf{x}_{pre}$. The solution $\mathbf{x}_{pre}$ is finally post processed to obtain the

solution $\mathbf{x}$ of the original system $\mathbf{Ax} = \mathbf{b}$.
The choice to implement a direct solver in the LDC code was motivated by the following reasons:

- For relatively small domains (i.e. less than 3×10^6 points) direct solvers are faster than iterative solvers.
- A direct solver always gives the correct solution contrary to an approximate solution calculated with an iterative solver.
- The factorization is computed only once and kept in memory (if the coefficients of the matrix coming from the discretization of Poisson's equation are kept constant).
- At each time-step, we only need to compute the solution.

Therefore, in the discharge code, the iterative NAG solver was replaced by new and more efficient direct solvers like SuperLU (Tholin and Bourdon 2011) and MUMPS (Jánský et al. 2010) and (Pechereau et al. 2012). In the LDC code, we used the sequential version of the direct solver MUMPS. It is important to note that, in the LDC code, the coefficients of the matrix $\mathbf{A}$ do not change in time as they depend only on geometry and permittivities so the first two steps can be done only once at the beginning of the simulation. Then, during the simulation we only need to perform the solution step.

1.3.2 Numerical resolution of drift-diffusion-reaction equations

Many problems have to be overcome to solve drift-diffusion equations (1.1) with (1.2) applied to streamer simulations. It is important to note that most of these problems are connected to the existence inside the ionizing wave of a very fast variation in space of charged species densities.
Then, to solve the drift-diffusion equations applied to streamer simulations, a suitable numerical method has to comply with two requirements: a sufficient accuracy for exact description of the solution gradients and density positivity.
In this section, first, we present finite volume methods used to discretize the drift-diffusion equations and then we present the improved Scharfetter-Gummel (ISG) scheme used to solve the drift-diffusion equation in the LDC code.

Finite volume methods

Finite volume methods are based on the integral formulation of the partial differential equations to be solved. By construction, these methods guarantee the conservation of the transported physical quantity (Ferziger and Peric 2002). For streamer simulations, this property is essential because it is particularly important to conserve the charge during the whole streamer simulation. In finite volume (or control volume) methods, the domain is subdivided into a finite number of small control volumes by a grid. In this work we use only structured grids. For this type of grid one can work either with the nodes centered in control volumes or with the faces centered between nodes (Ferziger and Peric 2002). Both approaches have their own advantages, and in the present work we have used node-centered grids, as they are used more frequently in the literature (Ferziger and Peric 2002).

Temporal splitting approach

In the literature, there are different methods to solve a drift-diffusion-reaction equation (Hundsdorfer and Verwer 2003) as:

$$\frac{\partial n}{\partial t} + \boldsymbol{\nabla} \cdot \boldsymbol{j} = S \ . \tag{1.12}$$

In the LDC code, we split the solution of (1.12) into:

$$\frac{\partial n}{\partial t} = S \ , \tag{1.13}$$

$$\frac{\partial n}{\partial t} = - \boldsymbol{\nabla} \cdot \boldsymbol{j} \ . \tag{1.14}$$

By doing so, we solve an ordinary differential equation with a chemistry source term (equation (1.13)) and then we solve the drift-diffusion equation (equation (1.14)). To solve equation (1.14), we first integrate it over the volume element $\Omega_{i,j}$ of the cell (i, j):

$$\frac{\partial \bar{n}_{i,j}}{\partial t} + \frac{1}{\Omega_{i,j}} \int_{\Omega_{i,j}} \boldsymbol{\nabla} \cdot \boldsymbol{j} \mathrm{d}\Omega = \ 0 \ , \tag{1.15}$$

where we define $\bar{n}_{i,j}$ as the average of $n(x, r, t)$ over $\Omega_{i,j}$:

$$\bar{n}_{i,j} = \ \frac{1}{\Omega_{i,j}} \int_{\Omega_{i,j}} n(x, r, t) \mathrm{d}\Omega \ . \tag{1.16}$$

Using the Gauss-Ostrogradsky theorem one obtains:

$$\frac{\partial \bar{n}_{i,j}}{\partial t} + \frac{1}{\Omega_{i,j}} \int_{\partial\Omega_{i,j}} \boldsymbol{j} \cdot \boldsymbol{n} \mathrm{d}\Sigma = 0 \ , \tag{1.17}$$

where $\mathrm{d}\Sigma$ measures the infinitesimal surface of the cell boundaries and $\boldsymbol{n}$ is the outward unit normal vector. Decomposing the surface integral on the edges of the cell, one obtains:

$$\frac{\partial \bar{n}_{i,j}}{\partial t} + \frac{1}{\Omega_{i,j}} \left(F^x_{i+1/2} + F^x_{i-1/2} + F^r_{j+1/2} + F^r_{j-1/2} \right) = 0 \ , \tag{1.18}$$

where $\mathrm{F^x_{i\pm1/2}}$ and $\mathrm{F^r_{j\pm1/2}}$ are convective and diffusion fluxes. The main problem in solving equation (1.18) concerns the determination of fluxes at the interfaces of the control volume. Indeed, these fluxes only strictly depend on the (unknown) values of the densities at the interfaces and not on the (known) mean value of the density $n_{i,j}$ inside the control volume. Thus, the difficulty is to express the different fluxes as approximate functions of $n_{i,j}$. After temporal integration, equation (1.18) becomes:

$$\bar{n}^{k+1}_{i,j} = \bar{n}^{k}_{i,j} - \frac{\Delta \mathrm{t}}{\Omega_{i,j}} \left(F^x_{i+1/2} + F^x_{i-1/2} + F^r_{j+1/2} + F^r_{j-1/2} \right) \ . \tag{1.19}$$

In cylindrical coordinates, the volumes $\Omega_{i,j}$ and the surfaces $\Sigma_{i+1/2,j}$ and $\Sigma_{i,j+1/2}$ are given by:

$$\begin{aligned} \Sigma_{i+1/2,j} &= \pi \left(r^2_{i,j+1/2} - r^2_{i,j-1/2} \right) \ , \\ \Sigma_{i,j+1/2} &= 2\pi r_{i,j+1/2} \left(x_{i+1/2,j} - x_{i-1/2,j} \right) \ , \\ \Omega_{i,j} &= \pi \left(r^2_{i,j+1/2} - r^2_{i,j-1/2} \right) \left(x_{i+1/2,j} - x_{i-1/2,j} \right) \ . \end{aligned} \tag{1.20}$$

It is interesting to note that diffusion fluxes are calculated simultaneously with drift fluxes in the improved Scharfetter-Gummel (ISG) scheme. For other schemes, diffusion and drift fluxes are calculated separately.

Improved Scharfetter-Gummel (ISG) scheme for drift-diffusion fluxes

The original Scharfetter-Gummel method was introduced in 1969 to obtain self-consistent numerical solutions for equations describing carrier transport, carrier generation, and space-charge balance in semiconductor devices (Scharfetter and Gummel 1969) This method is essentially a discretization scheme for variables in convection-dominated problems that employs an exponential fitting technique. One main advantage of

this scheme is that it calculates drift and diffusion fluxes at the same time. The Scharfetter-Gummel method has the very important property of monotonicity, but it has been shown that this method is accurate only if the potential drop between to adjacent nodes is much less than the electron temperature (Kulikovsky 1995a). For problems in gas discharges, it is necessary to use fine grids to satisfy this condition, and therefore the computational cost becomes very expensive. In 1995, (Kulikovsky 1995a) proposed a modified version of the original explicit Scharfetter-Gummel method that improves the accuracy of the original scheme significantly without requiring the use of a fine grid. Kulikovsky's basic idea is to put a pair of virtual nodes, one on each side of the cell interface where the flux has to be calculated (Figure 1.2).

The distance between these virtual nodes is chosen to be small enough

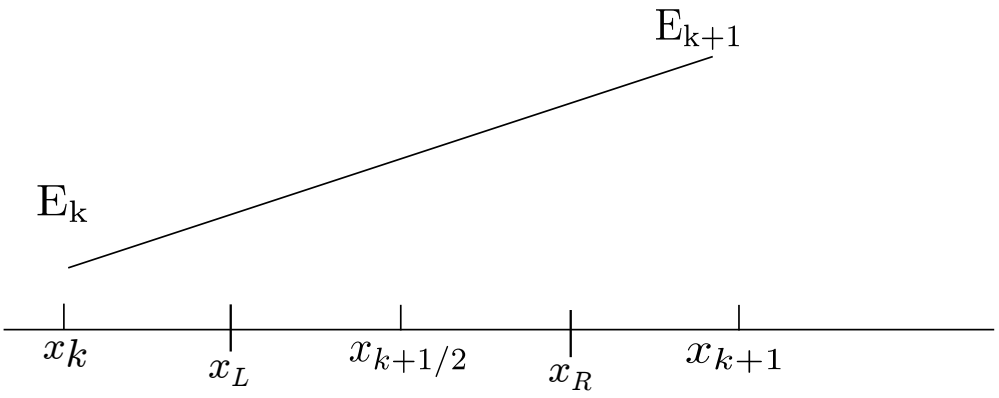

Figure 1.2: *Position of virtual nodes x_L and x_R. This Figure was reproduced from (Kulikovsky 1995a)*

to satisfy the condition for which the Scharfetter-Gummel method is accurate. Densities at virtual nodes are obtained using an interpolation of the density between two grid nodes. Then, based on the densities at the virtual nodes, the flux at the cell edge can be calculated accurately using the Scharfetter-Gummel scheme. It is interesting to note that in the original Scharfetter-Gummel method the electric field is assumed to be constant between the virtual nodes. Kulikovsky has proposed a more accurate approximation of the flux, in which the field is assumed to vary linearly between the virtual nodes. In (Kulikovsky 1995a), it was shown that accounting for the linear field profile has a minor influence on the results obtained on a simplified test-case. In the improved Scharfetter-Gummel (ISG) scheme, the determination of the location of the virtual nodes is essential, and Kulikovsky has proposed a criterion with a constant factor which has to be selected ϵ_{ISG}. When ϵ_{ISG} changes from 0

to 1, the scheme transforms from a very accurate but dispersive one to a less accurate, diffusive but monotonic Scharfetter-Gummel algorithm. The actual value of this parameter should be chosen experimentally, and Kulikovsky suggests that a value of in the range $[0.01, 0.04]$ gives good results in most cases. For the interpolation of the densities at the virtual nodes, (Kulikovsky 1995a) has proposed two interpolation schemes: exponential and local cubic spline piecewise interpolation. After having checked both interpolations, and we have chosen to use the local cubic spline interpolation in this work. We present here the scheme formulation given in (Kulikovsky 1995a).
Given the parameters at the two nodes k and k+1 of the basic mesh, we calculate the distance between the virtual nodes h_v using:

$$h_v = \sqrt{\epsilon_{\mathrm{ISG}} D_{k+1/2} h_k \ / \ |W_{k+1} - W_k|} \ , \tag{1.21}$$

where $h_k = x_{k+1} - x_k$, $W_k = (W_{k+1/2} - W_{k-1/2})/2$ and $D_{k+1/2}$ is the diffusion coefficient and , $W_{k+1/2} = -\mu E$ the drift velocity defined at $_{k+1/2}$. If $h_v \geq h_k$, $F^x_{i+1/2}$ is calculated by the original Scharfettel-Gummel scheme:

$$F^x_{i+1/2} = \frac{D_{k+1/2}}{h_k I_0} \left(n_k - \ e^{\alpha} n_{k+1}\right) \ , \tag{1.22}$$

where:

$$\begin{aligned} I_0 &= \frac{e^{\alpha} - 1}{\alpha} \ , \\ \alpha &= \frac{\mu h_k E_{k+1/2}}{D_{k+1/2}} \ . \end{aligned} \tag{1.23}$$

If $h_v < h_k$, then we define the positions of the virtual nodes x_L and x_R and the corresponding velocities:

$$\begin{aligned} x_{L,R} &= \frac{x_k + x_{k+1}}{2} \mp \frac{h_v}{2} \ , \\ W_{L,R} &= W_{k+1/2} \mp \frac{1}{2} \Delta W_v \ \text{ where,} \\ \Delta W_v &= \frac{h_v}{h_k} \left(W_{k+1} - (W_k\right) \ . \end{aligned} \tag{1.24}$$

Then we define densities n_L and n_R at the virtual nodes using the local cubic spline interpolation.

The more accurate approximation is obtained in taking into account that the electric field is linear between the virtual nodes. In this case $F^x_{i+1/2}$ is given by:

$$F^x_{i+1/2} = \begin{cases} \frac{D_{k+1/2}}{h_v I_1} & [n_L - e^{\alpha_v}(1+\alpha_v\beta_v)\, n_R] \ , \\ \frac{D_{k+1/2}}{h_v I_1'} & \left[e^{-\alpha_v'}\left(1+\alpha_v'\beta_v' \ ,\right)^{-1} n_L - n_R\right] \ , \end{cases} \tag{1.25}$$

where :

$$\begin{aligned} \alpha_v &= \frac{h_v W_L}{D_{k+1/2}}; \quad \beta_v = \frac{W_R - W_L}{2W_L} \ , \\ I_1 &= -\frac{\alpha_v^2 + 2\alpha_v\beta_v}{\alpha_v^3} + \frac{e^{\alpha_v}}{\alpha_v^3} \ ,(\alpha_v^3\beta_v + \alpha_v^2 + 2\alpha_v\beta_v - 2\alpha_v^2\beta_v) \ , \end{aligned} \tag{1.26}$$

and:

$$\begin{aligned} \alpha_v' &= \frac{h_v W_R}{D_{k+1/2}}; \quad \beta_v' = \frac{W_R - W_L}{2W_R} \ , \\ I_1' &= \frac{\alpha_v'^2 + 2\alpha_v'\beta_v'}{\alpha_v'^3} - \frac{e^{-\alpha_v'}}{\alpha_v'^3}(\alpha_v'^3\beta_v' + \alpha_v'^2 + 2\alpha_v'\beta_v' + 2\alpha_v'^2\beta_v') \ . \end{aligned} \tag{1.27}$$

It is important to note that the improved Scharfetter-Gummel (ISG) scheme was developed in 1D. We have adapted it to 2D by splitting the numerical problem into two 1D problems in the x and r directions, respectively. To improve the accuracy of the splitting method, we alternate the order between the x and r axes in two successive time steps. The improved Scharfetter-Gummel scheme has been successfully applied to several 2D streamer simulations by Kulikovsky [(Kulikovsky 1995a), (Kulikovsky 1995b), (Kulikovsky 1997)] and also other authors [(Liu and Pasko 2004), (Liu and Pasko 2006), (Jánský et al. 2010), (Jánský et al. 2011) and (Tholin and Bourdon 2011)].

Boundary conditions

In this work, we have taken into account simplified boundary conditions for continuity equations at the surfaces of metallic electrodes. On the grounded electrode (mostly a plane in this work) Neumann boundary conditions are applied for all charged particle fluxes. At the high voltage electrode (mostly a point in this work), positive, negative ions and electrons fluxes ($\mathbf{J^a_p}$, $\mathbf{J^a_n}$ and $\mathbf{J^a_e}$ respectively) are given by:

$$\mathbf{J^a_p} = n_p \ \min(0, \ \mu_p \ \mathbf{E}\cdot\mathbf{n_a}).\mathbf{n_a} \ ,$$

$$\mathbf{J_n^a} = n_n \min(0,\ -\mu_n \mathbf{E}\cdot\mathbf{n_a}).\mathbf{n_a} \ ,$$

$$\mathbf{J_e^a} = -n_e\mu_e\mathbf{E},\ \text{if } \mathbf{E}\cdot\mathbf{n_a} > 0 \text{ or } \nabla.\mathbf{J_e^a} = 0 \text{ if } \mathbf{E}\cdot\mathbf{n_a} < 0 \ ,$$

where $\mathbf{E}$ is the electric field and $\mathbf{n_a}$ is the unit outward normal vector at the anode surface. At each gas-dielectric interface, surface charges are obtained by time integrating fluxes of positive, negative ions and electrons at the dielectric surface ($\mathbf{J_p^d}$, $\mathbf{J_n^d}$ and $\mathbf{J_e^d}$ respectively) which are given by:

$$\mathbf{J_p^d} = n_p \min(0,\ \mu_p \mathbf{E}\cdot\mathbf{n_d}).\mathbf{n_d} \ ,$$

$$\mathbf{J_n^d} = n_n \min(0,\ -\mu_n \mathbf{E}\cdot\mathbf{n_d}).\mathbf{n_d} \ ,$$

$$\mathbf{J_e^d} = n_e \min(0,\ -\mu_e \mathbf{E}\cdot\mathbf{n_d}).\mathbf{n_d} \ - \gamma\ \mathbf{J_p^d} \ ,$$

where $\mathbf{n_d}$ is the unit outward normal vector at a dielectric surface and γ is the secondary emission coefficient of electrons by impact of positive ions. In this study, we have assumed that $\gamma = 0.1$. This high value is a way to take into account roughly other secondary emission processes as secondary emission of electrons by photoemission or by impact of excited species.
For the open boundaries of the computational domain the following boundary conditions are used:

$$\mathbf{J_p^b} = n_p \min(0,\ \mu_p \mathbf{E}\cdot\mathbf{n_b}).\mathbf{n_b} \ ,$$

$$\mathbf{J_n^b} = n_n \min(0,\ -\mu_n \mathbf{E}\cdot\mathbf{n_b}).\mathbf{n_b} \ ,$$

$$\mathbf{J_e^b} = n_e \min(0,\ -\mu_e \mathbf{E}\cdot\mathbf{n_b}).\mathbf{n_b} \ ,$$

where $\mathbf{n_b}$ is the unit normal vector at the boundaries of the computational domain directed towards it.

1.3.3 Time integration

In the explicit LDC code, we have used a simple first-order Euler time integration for drift-diffusion fluxes in equation (1.18) and the photoionization source term and a fourth-order Runge-Kutta method (Ferziger and Peric 2002) for the time integration of the chemistry source terms in equation (1.13). For the temporal splitting, a 1^{st} order operator splitting method was used: $U^{t+\Delta t} = CD^{\Delta t}\ R^{\Delta t}\ U^t$, where U^t and $U_1^{t+\Delta t}$ are the solution at t and $t+\Delta t$ respectively. $CD^{\Delta t}$ and $R^{\Delta t}$ stands for the convection-diffusion and the chemistry operator respectively applied on the duration Δt.

Time step

For the calculation of the time step in the fully explicit simulations, as in (Vitello et al. 1994), we have to follow the fastest dynamics given either by drift, diffusion or chemistry. In order to have a stable and accurate simulation we evaluate different characteristic time steps:
The drift dynamics time step Δt_c:

$$\Delta t_c \;=\; \min\left[\frac{\Delta x_i}{v_{x_{(i,j)}}}\;,\;\frac{\Delta r_j}{v_{r_{(i,j)}}}\right]\;, \tag{1.28}$$

the diffusion dynamics Δt_d time step:

$$\Delta t_d \;=\; \min\left[\frac{(\Delta x_i)^2}{D_{x_{(i,j)}}}\;,\;\frac{(\Delta r_j)^2}{D_{r_{(i,j)}}}\right]\;, \tag{1.29}$$

the chemistry dynamics Δt_I time step:

$$\Delta t_I \;=\; \min\left[\frac{n_{k_{(i,j)}}}{S_{k_{(i,j)}}}\right]\;. \tag{1.30}$$

Considering the inter-electrode gap from a dielectric point of view, if the local electric field changes, the polarization of the material takes some time to relax towards an equilibrium. The dielectric relaxation time step corresponds to the time required for the charged species to align themselves according to the direction of the local electric field and so Δt_{Diel} is defined:

$$\Delta t_{Diel} \;=\; \min\left[\frac{\varepsilon_0}{q_e \mu_{e_{(i,j)}} n_{e_{(i,j)}}}\right]\;. \tag{1.31}$$

The general time step Δt is then determined according to:

$$\begin{aligned} &\Delta t \;=\; \min\;(A_c\Delta t_c,\; A_d\Delta t_d,\; A_I\Delta t_I,\; A_{diel}\Delta t_{Diel})\;;\\ &A_c = 0.5,\; A_d = 0.5,\; A_I = 0.25 \text{ and } A_{diel} = 0.5\;. \end{aligned} \tag{1.32}$$

1.4 Studied geometries

In this PhD report, we mainly study two different point to plane electrode geometries with a dielectric plane obstacle placed perpendicular to

the axis of symmetry.
The sharper is the point and the larger is the inter-electrode gap, the higher is the number of mesh points to carry out simulations. It is interesting to note that the presence of a dielectric plane does not require any specific increase of the number of mesh points in the axial direction. However, due to the radial spreading of the discharge on the dielectric surface, a sufficiently large computational domain has to be considered.
In order to present and discuss the improvements of the discharge code, in the following sections and chapters 2 to 4, we will consider two test-cases without dielectric plane obstacle.

1.4.1 Test-case 1 (TC-1): 5 mm gap with a point to plane geometry with a stump point electrode

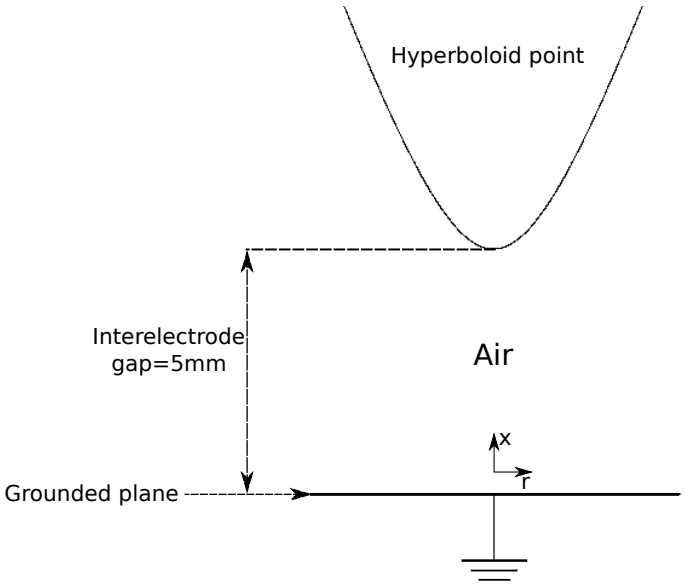

Figure 1.3: *Discharge set-up for the TC-1.*

The simulated geometry of TC-1 is shown on Figure 1.3 and is a point to plane electrode geometry with a stump hyperboloid point electrode of 647 μm of radius of curvature. A constant positive voltage of $U_a = 13$ kV is applied at the point electrode and the inter-electrode gap is of 0.5 cm. We consider an initial density of charged species of $n_{e,p} = 10^4$ cm^{-3}. The computational domain is 1 cm $\times$ 17 cm with a Cartesian grid. For $0 \leq x \leq 0.5$ cm, an axial mesh size of 5 μm is used and then for

$0.5 \leq x \leq 1$ cm, the mesh size increases according to a geometric progression. Radially, for $0 \leq r \leq 0.3$ cm, a mesh size of 5 μm is used and for $0.3 \leq r \leq 17$ cm the mesh size increases also according to a geometric progression. This level of refinement required a grid size of $n_x \times n_r = 1287 \times 1000$ so 1.287×10^6 points.
This simulation was done with the LDC code using the physical model described in section 1.2 and the numerical methods presented in section 1.3. It is important to note the Laplacian electric field at the anode tip is equal to 120 kV.cm^{-1} at the beginning of the simulation.

Figure 1.4 shows the discharge dynamics at t=0.8, 3.6 and 6.0 ns. At

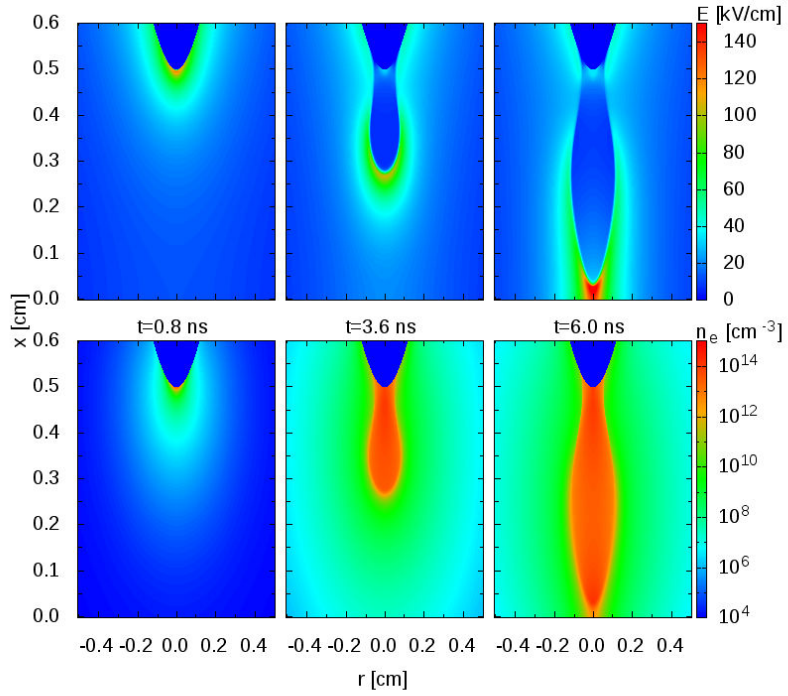

Figure 1.4: *Dynamics of the ignition and propagation of the streamer discharge ignited at the point electrode for TC-1. Cross-sectional views of the absolute value of the electric field and the electron density at t=0.8, 3.6, 6.0 ns*

t=0.8 ns, the ignition of a positive streamer discharge is observed at the point anode. As the positive discharge propagates towards the cathode plane, it reaches the middle of the inter-electrode gap at t=3.6 ns where the radius of the discharge is equal to 0.2 cm. At t=3.6 ns, the magnitude of electric field in the head of the discharge is 110 kV.cm^{-1} and the

electron density in the conductive channel is $n_e = 3 \times 10^{13}$ cm^{-3} and increases to $n_e = 1 \times 10^{14}$ cm^{-3} close to the anode point. It is interesting to note that behind the head of the discharge, in the conductive channel and close to the anode point, the magnitude of the electric field goes to quite low values ~ 7 kV.cm^{-1}. The discharge finally impacts the cathode plane at t_c=6.0 ns.

The general time step throughout the simulation is almost constant and equal to $\Delta t = 5.10^{-12}$ s. It is important to note here that all the different time steps (equations (1.28) to (1.31)) are equivalent during the propagation. This means that all physical processes are of the same time scale. Then to reduce the computational time required for this simulation (t=4 hours) on the "igloo" cluster with the LDC code, the only way is to introduce parallel protocols into the sequential discharge code.

MUMPS solver in LDC code

In the LDC code, as mentioned section 1.3.1, we use the sequential implementation of the direct solver MUMPS (Amestoy et al. 2001) to solve Poisson's equation (Jánský et al. 2010), (Jánský and Bourdon 2011b) and (Pechereau et al. 2012).

Memory used Mo	Factorization (MUMPS) (s)	Solution (MUMPS) (s)	One time-step (s)
664	64.12	1.27	5.76

Table 1.1: *Memory used by MUMPS solver, computational time for the factorization with MUMPS solver, the solution of Poisson's equation with MUMPS solver and the total time for one time-step (solving Poisson's equation and the drift-diffusion-reaction equation for each charged species without photo-ionization) for a grid size of* $n_x \times n_r = 1287 \times 1000$ *in TC-1.*

In Table 1.1, for TC-1, we present the memory required by MUMPS solver and the computational time for the factorization with the MUMPS solver, the solution of Poisson's equation with MUMPS solver and the total time for one time-step (taking into account the solution for Poisson's equation and the solution of the drift-diffusion equations without taking into account the photo-ionization contribution). In section 1.3.1, we have explained that the first step to compute a solution with a direct solver is

to analyze and then in a second step, to do a factorization of the matrix **A** resulting from the discretization of Poisson's equation. It is obvious that the memory used by MUMPS to store the factorized matrices is quite high (664 Mo for 1.287×10^6 points) which means that as the domain size or the number of points increases, the memory requirement will increase linearly with the number of points.
We also stated in section 1.3.1, that in the LDC code, the coefficients of the matrix **A** do not change during the simulation. So we can manage in this case the 64.12 s required for the factorization of **A** at the beginning of the simulation. To compute the solution of the Poisson's equation, 1.27 s are required which represent 22% of the time required for one time-step (5.76 s) where Poisson and the drift-diffusion-reaction equation for each charged species are solved (without photo-ionization). In the LDC code, when we take into account the calculation of the photo-ionization source term, the memory requirement to store in memory 7 factorizations (1 for Poisson and 6 for the photo-ionization source term (2 per wavelength)) is 4.6 Go and the total time for one time-step increases from 5.76 to 28.6 s (7 factorizations but 19 calculations of the solution of Poisson's like equations).
The memory requirement for TC-1 is low ($\sim$ 5 Go) and is below the maximum memory available per node (24 Go on the "igloo" cluster).

1.4.2 Test-case 2 (TC-2): 10 mm gap with a point to plane geometry with a sharp point electrode

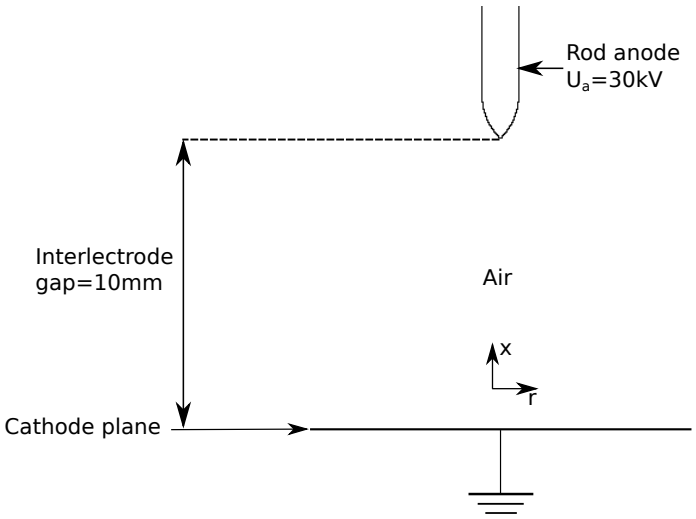

Figure 1.5: *Discharge set-up for TC-2.*

The simulated geometry of TC-2 is shown on Figure 1.5 and is close to the geometry used in experiments at LPGP. It is a point to plane geometry with a sharp rod anode of 50 μm of radius of curvature. A constant positive voltage of $U_a = 30$ kV is applied at the point electrode and the inter-electrode gap is of 1 cm. We consider an initial density of charged species of $n_{e,p} = 10^4$ cm^{-3}. The computational domain is 2 cm $\times$ 2 cm with a Cartesian grid. A "fine" mesh is used: For $0 \leq x \leq 1$ cm, an axial mesh size of 10 μm is used and is refined to 1 μm close to the anode tip. Then for $1 \leq x \leq 2$ cm, the mesh size is increased from 1 μm to 30 μm. Radially, for $0 \leq x \leq 0.5$ cm a mesh size of 5 μm is used and is refined to 1 μm close to the axis of symmetry and for $0.5 \leq x \leq 2$ cm, the radial mesh size is increased from 5 μm to 30 μm. This level of refinement required a grid size of $n_x \times n_r = 3353 \times 1725$ or 5.8×10^6 points.

It is interesting to note that a high applied voltage of $U_a = 30$ kV at the sharp point electrode in TC-2, has required to significantly reduce the mesh size close to the point from 5 μm to 1 μm in order to accurately compute the electric field close to the sharp point electrode. Compared to TC-1, this leads to a substantial increase of the number points from 1.5 to 5.8 $\times 10^6$ points.

The dynamics of ignition and propagation of the streamer discharge are shown on Figure 1.6.

At the point electrode, the laplacian electric field is equal to 2.2 MV.cm^{-1}.

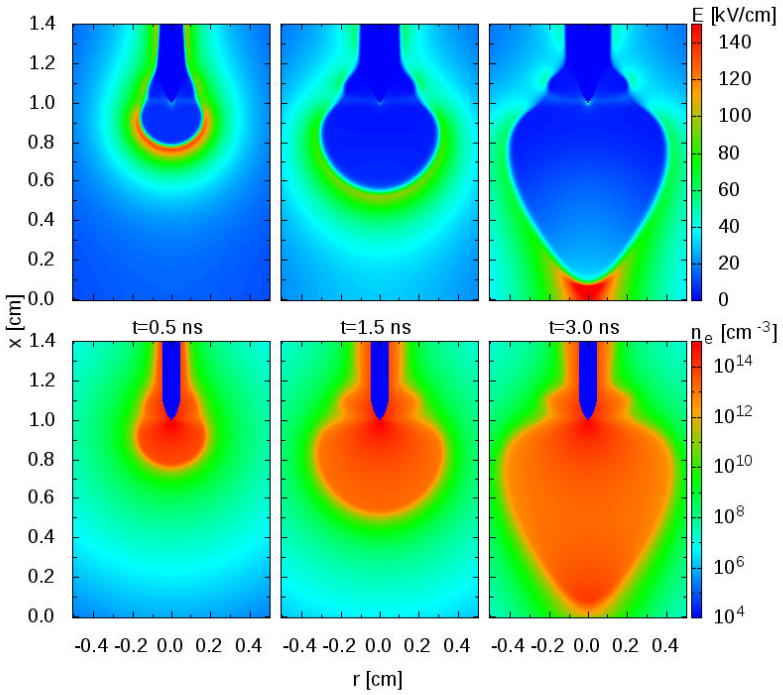

Figure 1.6: *Dynamics of the ignition and propagation of the streamer discharge ignited at the point electrode for TC-2. Cross-sectional views of the absolute value of the electric field and the electron density at t=0.5, 1.5, 3.0 ns*

Compared to the positive streamer discharge in TC-1, in TC-2, the size of the ignited discharge at the point anode, on Figure 1.6, has a larger radius of 0.8 cm. This radius is necessary to shield the laplacian electric field and have an electric field in the head of the discharge equal to $\sim$ 100 kV.cm^{-1} at t=1.5 ns. This is an usual value of the magnitude of the electric field in the head of a streamer discharge in air at atmospheric pressure. For t>1.5 ns, the discharge propagates and impacts the cathode at t_c=3.0 ns.

In TC-2, at the ignition of the discharge, the chemistry time step is the smallest one ($\Delta t_I = 9.10^{-14}$ s) due to the huge Laplacian electric field at the point electrode. As the density of charged species increases to $n_e = 10^{15}$ cm^{-3}, the dielectric relaxation time step decreases to

$\Delta t_{Diel} = 3 \times 10^{-14}$ s and this low value of the dielectric relaxation time step is the minimum one for the rest of the propagation dynamics until the discharge impacts the cathode at t_c=3.0 ns.
It is important to note that it was not possible to carry out this simulation with the LDC code at the beginning of the thesis. Indeed, this simulation with the LDC code would require at least a month of calculations on the "igloo" cluster. Aside from the computational time, the memory requirement for this simulation would be of the order of 30 Go, well beyond the memory capacity of a regular node on the "igloo" cluster (24 Go). To obtain the results presented in Figure 1.6, we have used the latest version of the discharge code developed in this thesis:

- Full parallel MPI-OPENMP discharge code with domain decomposition (chapter 4)
- Fast hybrid parallel MPI-OPENMP iterative solver SMG (HYPRE library) for Poisson's equation and photo-ionization source term (section 2.3)
- Explicit UNO3 scheme (3^{rd} order in time and space) coupled with the MACHO operator for the spatial splitting to solve the convection equation (section 3.2.1)
- Explicit 2^{nd} order in time and space for the diffusion equation (section 3.3.2)
- Explicit 4^{th} order Runge-kutta scheme for the chemistry source term (section 1.3.3)
- 1^{st} order operator splitting method:
  $U^{t+\Delta t} = C^{\Delta t}\, D^{\Delta t}\, R^{\Delta t}\, U^t$,
  where U^t and $U_1^{t+\Delta t}$ are the solution at t and $t+\Delta t$ respectively. $C^{\Delta t}$,$D^{\Delta t}$ and $R^{\Delta t}$ stands for the convection, diffusion and the chemistry operator respectively applied on the duration Δt.
- Semi-implicit scheme (to remove the dielectric relaxation time-step constraint in equation (1.31)) (section 2.4)

With the latest version of the discharge code, the calculations for TC-2 took 3 hours using 72 cores on the "igloo" cluster with a memory requirement of less than 1 Go per core.

1.5 Proposed strategy to improve the numerical accuracy and computational performances of the discharge code

In the following chapters, we present the different numerical developments carried out during this PhD to improve the numerical accuracy and computational performances of the discharge code:

- In chapter 2, we focus on the solver used for the calculations of Poisson's equation. We present two parallel solvers and compare their performances with the sequential direct solver MUMPS implemented in the LDC code for test-cases TC-1 and TC-2.
- In chapter 3, we discuss the ability of any transport scheme to handle density gradients of several orders of magnitude in the head of a streamer discharge. In order to increase the robustness and accuracy of the discharge code, we present different transport schemes and discuss their respective properties.
- In chapter 4, we present a new hybrid MPI-OPENMP discharge code using domain decomposition and present its parallel performance.

Chapter 2

Optimization and parallelization of the discharge code: Poisson's equation

2.1 Introduction

One important and computationally expensive equation to solve in streamer discharge simulations at atmosheric pressure is Poisson's equation. In the last few years, efficient numerical libraries provide access to numerous methods to solve differential equations like PETSc (Balay et al. 2013), COMSOL (COMSOL 2009) and HYPRE (HYPRE 2007). In fact one has to carefully choose the appropriate method according to the type of problem, desired speed and accuracy. In a streamer discharge code, Poisson's equation is solved at each time-step. As the typical time scale of a streamer discharge propagation in centimeter gaps is about a few tens of nanoseconds with time-step usually of the order of 10^{-14} - 10^{-12} s, the number of time-steps is usually higher than 10^5. Then it is crucial to choose a numerical method to solve Poisson's equation that is fast and accurate. Depending on the size of the simulated domain and the computer on which the simulations are done, one should carefully test the performances of either direct or iterative solvers to choose the solver that provides the best speed, memory requirement and accuracy properties. An other parameter to take into account is the level of parallelism available on the computer where the calculations are done and the parallel capabilities of the chosen solver. On the "igloo" cluster, we have the possibility to run either sequential, parallel memory shared OPENMP, parallel distributed memory MPI and hybrid MPI-OPENMP codes. It is then interesting to investigate the parallel capabilities of direct and

iterative solvers on the "igloo" cluster and choose the appropriate solver depending on the numerical requirements.
In section 2.2, for the test-case TC-1 (presented in section 1.4.1), we will compare the characteristics of the direct solver MUMPS used to compute the solution for the Poisson's equation from the legacy code with an other direct solver called PaStiX. Then we will compare the computational efficiency between the legacy code and an OPENMP version of the code with the PaStiX solver. In section 2.3, we will present an iterative solver SMG in the HYPRE library and its parallel performances on the simulated domain of TC-2. In section 2.4, a "semi-implicit scheme" will be presented that allows to choose time-steps one order of magnitude higher than with a fully explicit code with a rather simple change in the discretization of Poisson's equation.

2.2 Comparison MUMPS/PaStiX (OPENMP)

On the "igloo" cluster, we have the possibility to improve the computational efficiency of the code by implementing parallel protocols.
First, it is important to note that the implementation of MPI protocols requires deep changes in the code structure. Then, as a first step to gradually implement parallelism in the discharge code, we chose to implement OPENMP protocols in our sequential code as it only requires to add few lines in the code. As the computation of Poisson's equation is the most expensive part in a streamer discharge code, we needed to use a direct solver with OPENMP capabilities.
The direct solver MUMPS has MPI capabilities only. Therefore, another effective parallel direct solver PaStiX (PaStiX 2012) was implemented in the code. The PaStiX solver has the following interesting characteristics:

- The solver is a hybrid MPI-OPENMP direct solver
- We can choose either the OPENMP version only, MPI only or the MPI-OPENMP version.
- It is easy to compile, to implement and to use
- The library is regularly updated and widely used in the scientific community

In this work, we only used the OPENMP capabilities of the solver. This is a first key step in the parallelization of the discharge code. It is important to note here that 70 % of the LDC code was written in FORTRAN 77 with implicit variables declared throughout the code. As a first step for the development of the code, the LDC code was profiled and key parts

of the code were optimized for a better stability for the implementation of OPENMP protocols.

Code with:	MUMPS	PaStiX			
Nb thread	1	1	2	4	6
Factorization (s)	64.12	24.87	21.55	19.91	19.48
Solution (s)	1.27	0.64	0.38	0.25	0.22
One time-step (s)	5.76	2.71	1.76	1.51	1.36

Table 2.1: *Comparison between the LDC code with MUMPS and the parallel code with PaStiX of the computational time for the factorization, the solution of Poisson's equation and the total time for one time-step (solving Poisson equation and the drift-diffusion-reaction equation for each charged species without photo-ionization) for a grid size of* $n_x \times n_r = 1287 \times 1000$ *for TC-1.*

On Table 2.1, for the TC-1, we compare the computational time for the LDC code with MUMPS and for the parallel OPENMP discharge code with PaStiX. First it is interesting to compare the solution time to solve Poisson's equation with the sequential code (1 thread) with MUMPS and PaStiX.
We note that this solution time is divided by 1.98 with PaStiX compared with MUMPS. This difference is due to the different methods used in MUMPS and PaStiX in the analysis and the factorization steps described in section 1.3.1. We also note here that due to the code optimization, the total time for one time-step for the PaStiX code is 2.71 s which is 2.12 times less than the total time for one time-step with the MUMPS code.
Then Table 2.1 shows the results for 2 to 6 threads for PaStiX. Considering only the solution time of Poisson's equation, the speed up increases from 1.7 (2 threads) to 2.9 (6 threads) compared with the sequential PaStiX code. Of course if we compare with the MUMPS code then the speed up goes from 3.34 (2 threads) to 5.77 (6 threads). If we now compare the time for one time-step with the PaStiX code, the speed up increases from 1.53 (2 threads) to 2 (6 threads). Again if we compare with the MUMPS version then the speed up goes from 3.27 (2 threads) to 4.23 (6 threads).
One important information left out of Table 2.1 is the memory requirement. The PaStiX solver, in the TC-1, requires 886 Mo, more than MUMPS (664 Mo), to compute the solution of one Poisson's equation.
In conclusion, this parallel (OPENMP) version of the discharge code with the PaStiX solver allowed us to have a speed up of ~ 4 compared with the legacy discharge code with MUMPS solver. We also have a speed up

of 5.77 in the computation of the solution of Poisson's equation which is a considerable amount of time saved when calculating the photo-ionization source term (with 18 Poisson's like equations to solve). The only drawback of this code is the increase of the memory required by the PaStiX solver. We note here that to simulate the complete dynamics of the simulation TC-1, we only required $\sim$ 43 minutes with the OPENMP parallel code with PaStiX compared to the 4 hours with the LDC code with MUMPS on the "igloo" cluster.
For the results presented in chapters 5 and 6, with the same point-to-plane geometry as TC-1 and with a dielectric plane obstacle, the size of the simulated domain ($n_x \times n_r = 1535 \times 1000$ or $1.5{\times}10^6$ points) is comparable with the one in the TC-1. In chapters 5 and 6, the average computational time with the fully explicit LDC code is on average 10 days. With the parallel OPENMP version of the discharge code with the PaStiX direct solver, the computational time was decreased significantly to 2 days.
The test-case TC-2, presented in section 1.4.2 was run on the "igloo" cluster with the parallel OPENMP PaStiX code with 6 threads. In the simulation of TC-2, it took 2.47 s to compute the solution of one Poisson's equation with the PaStiX solver with 6 threads and 4 Go of memory usage. Because of the very low value of time-step used and even with the OPENMP parallel code, it took at least a week of calculations. Aside from the high computational cost, the memory requirement for the TC-2 with the parallel OPENMP discharge code with the PaStiX solver, was more than 30 Go of memory. On the "igloo" cluster it exists one node with 72 Go of memory available but it is very difficult to have access to it. In the TC-2, the memory requirement with a direct solver is too high for such a large simulated domain. It means that for the simulation of the TC-2, it is now interesting to implement an iterative solver that requires much less memory and starts to be computationally competitive with such large simulated domain compared to direct solvers.

2.3 The MPI-OPENMP iterative solver SMG in the HYPRE library

2.3.1 The iterative solver SMG in the HYPRE library

We have chosen to test and implement iterative solvers available in the HYPRE (HYPRE 2007) library because it fulfilled the following require-

ments:

- Easy to use the hybrid (MPI-OPENMP) parallelization properties of the library.
- Easy to compile, to implement and to use.
- Simple to test different kinds of iterative solvers provided with the library.
- Regular updating of the library.
- This library is already widely used in the scientific community.

The most suitable interface provided in the HYPRE library package is the "STRUCT" interface for our application. With the "STRUCT" (structured) interface, we found after testing all the compatible iterative solvers available in the HYPRE library, that the SMG solver, without preconditioner, was the most robust and fastest solver available. We note here that for the calculation of the electric potential for the TC-2, the solver SMG converged for a minimum tolerance set at $\mathrm{Tol}_{\mathrm{min}} = 10^{-15}$. We also point out that depending on the simulated geometry this minimum tolerance can vary and so after any change in the simulated geometry, it is necessary to recheck this minimum value.

In Figure 2.1, we present the number of inner iterations and % of error between the electric potential solution on the axis of symmetry for a given tolerance Tol between 10^{-14} and 10^{-5} with the electric potential solution calculated with the minimum tolerance $\mathrm{Tol}_{\mathrm{min}} = 10^{-15}$ set in the SMG solver without preconditioner.

As the tolerance increases, the number of inner iterations in the SMG solver decreases but at the same time the % of error increases. From $\mathrm{Tol} = 10^{-14}$ to 10^{-5}, the number of iterations in the SMG solver decreases from 19 to 1 iterations while at the same time the error increases from 3.38×10^{-8} to 2.90 %. Considering the % of error and the number of iterations for the TC-2, we have used a tolerance of $\mathrm{Tol} = 10^{-8}$ for the SMG solver which corresponds to a small number of iterations (iter = 4) and a very reasonable level of error (0.12 %). It is now important to balance here the % error acceptable with the computational cost. On Figure 2.2, we show the time to compute the potential solution with the sequential version of the SMG solver and % of error. As the tolerance set for the SMG solver increases from 10^{-14} and 10^{-5}, the time to compute the solution decreases. If we choose a tolerance of $\mathrm{Tol} = 10^{-8}$ then the time required to calculate the solution is 5.68 s. We must point out that the memory requirement is very low and well under 1 Go of memory usage.

It is obvious that 5.68 s to compute a solution is quite time consuming. With the OPENMP parallel discharge code using the direct solver PaStiX, it took 2.47 s to compute a solution for Poisson's equation with

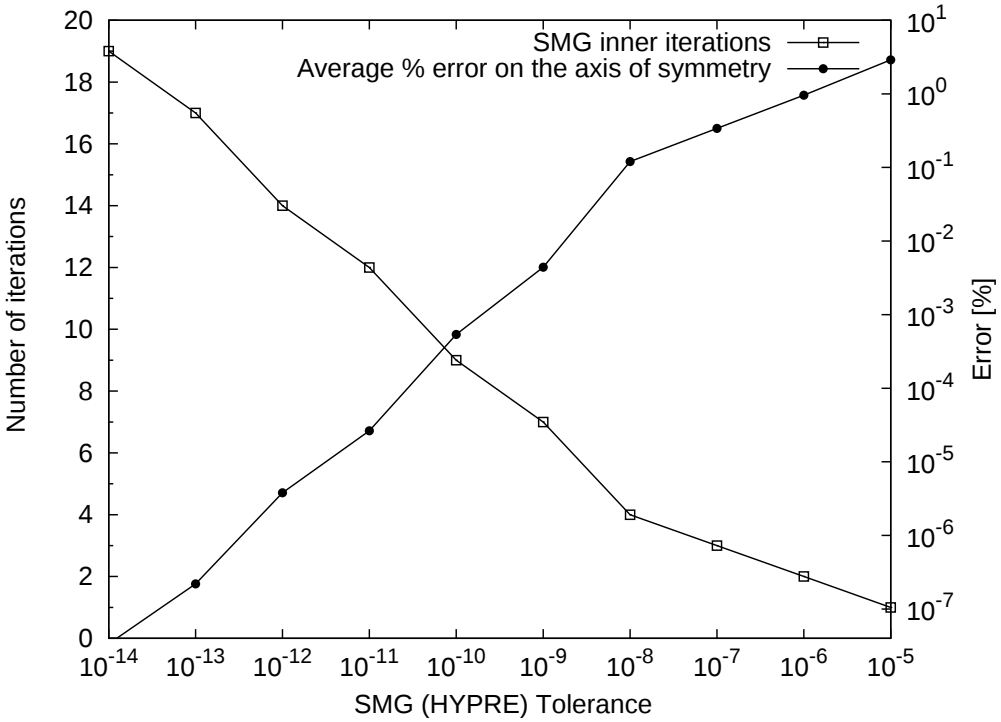

Figure 2.1: *Number of inner iterations and % of error between the reference potential solution on the axis of symmetry for a given tolerance set in the SMG solver without preconditioner for the TC-2 where* $\mathrm{n_x} \times \mathrm{n_r} = 3353 \times 1725$

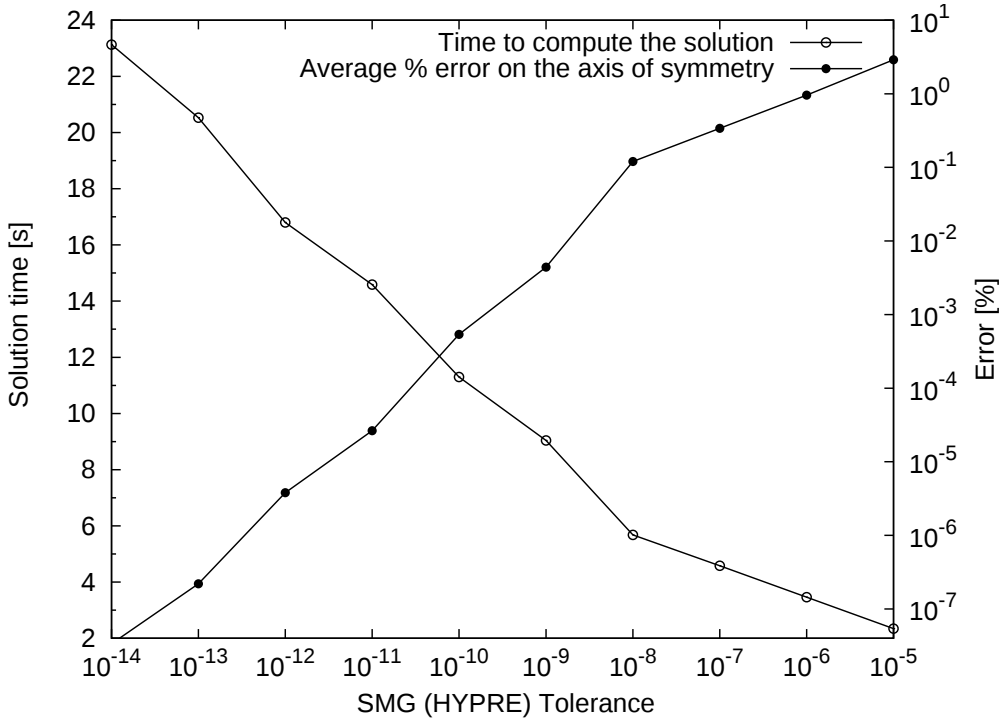

Figure 2.2: *Computational time to compute the solution with the sequential version of the SMG solver and % of error between the reference potential solution on the axis of symmetry for a given tolerance set in the SMG solver without preconditioner for the TC-2 where* $\mathrm{n_x} \times \mathrm{n_r} = 3353 \times 1725$

6 threads. Then, in the next sections we present the performances of the MPI and MPI-OPENMP versions of the SMG solver.

2.3.2 Performances of the HYPRE solver: MPI only

In this section we present the MPI parallel performances of the SMG solver. In the MPI only version of the SMG solver, the user has to divide the simulated domain and create sub-domains according to the number of cores required (with on each core a MPI process). The parallel capabilities of the SMG solver in the HYPRE library are quite easy to use. The only requirement is to provide the coefficients of the matrix coming from the discretization of the Poisson's equation to the "STRUCT" interface.

On Figure 2.3, we show the time to compute Poisson's equation with the

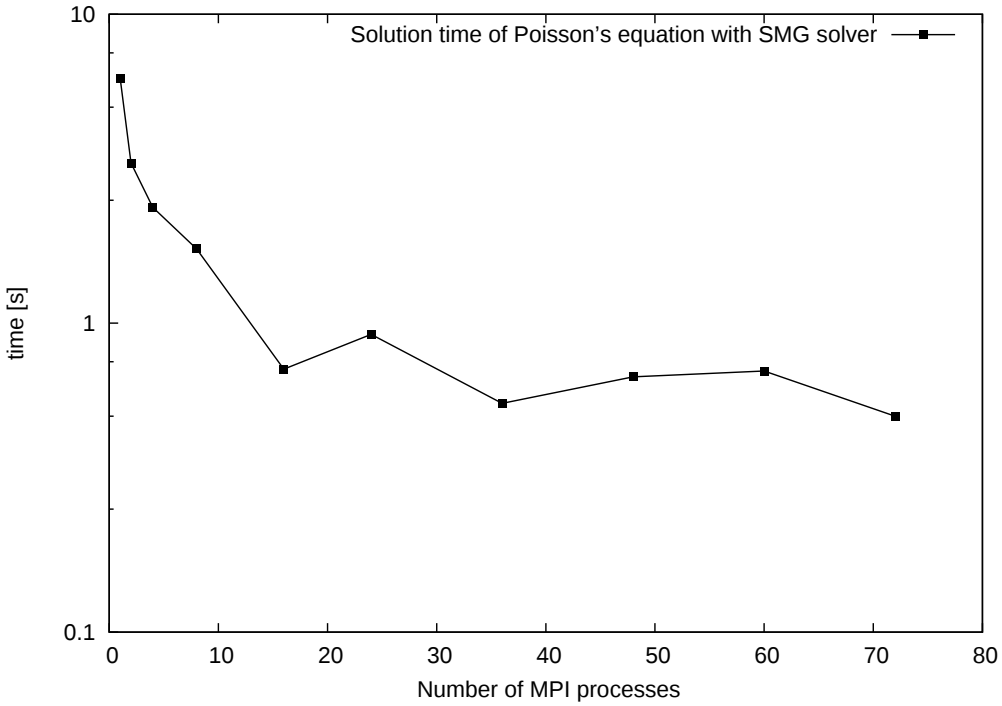

Figure 2.3: *Computational time to compute Poisson's equation with the SMG solver depending on the number of MPI processes for the TC-2 where* $n_x \times n_r = 3353 \times 1725$

SMG solver depending on the number of MPI processes for the TC-2. As we increase the number of MPI processes, we see a decrease of the time required to solve Poisson's equation. It is interesting to note that with just 4 MPI processes, the time to compute a solution is almost the same as the time with the parallel OPENMP version of the code with PaStiX

and 6 threads. As we increase the number of MPI processes from 1 to 72 (or 1 MPI process per core on each of the 6 nodes reserved on the "igloo" cluster), we see a general decrease in the solution time from 5.68 s to 0.5 s.

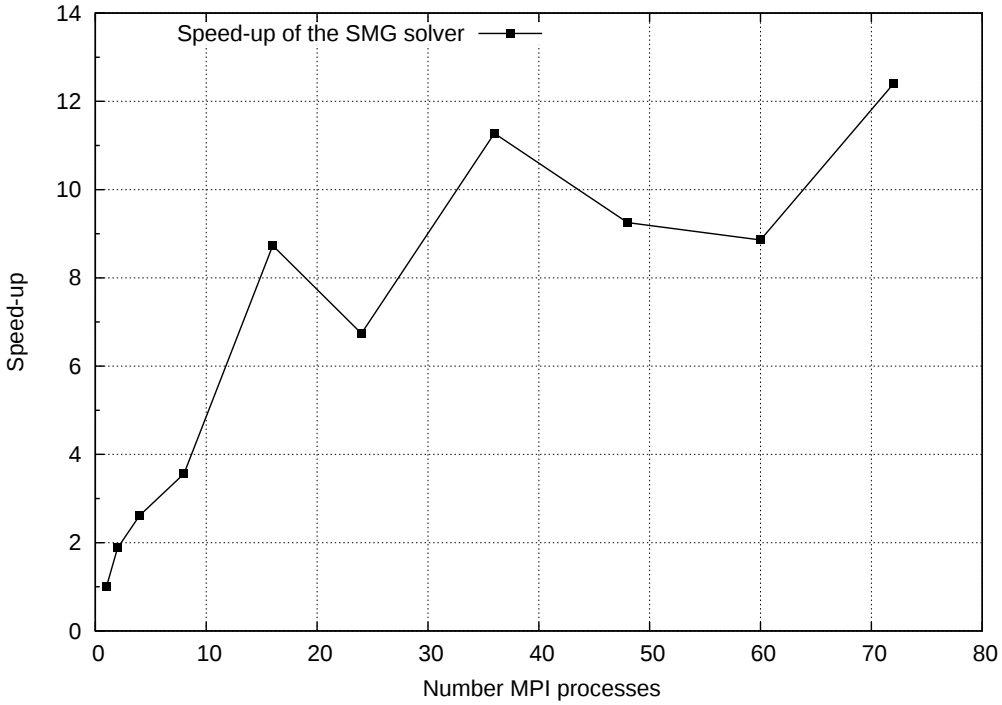

Figure 2.4: *Speed-up for Poisson's equation with the SMG solver depending on the number of MPI processes for the TC-2 where* $n_x \times n_r = 3353 \times 1725$

On Figure 2.4, we present the speed-up for Poisson's equation with the SMG solver depending on the number of MPI processes for the TC-2. As the number of MPI processes increases, we see a general increase of the speed-up. For 72 MPI processes, the speed-up is equal to 12.4.

2.3.3 Performances of the HYPRE solver: MPI-OPENMP

In the HYPRE library there is also the possibility to use the hybrid MPI-OPENMP implementation. If one would use 2 MPI processes and 2 OPENMP threads per MPI process, one would reserve 4 cores on 1 node and assign 2 MPI processes on two cores and in turn launch 2 OPENMP threads per MPI process on each of the 4 cores reserved.

MPI × OPENMP	Poisson (s)	MPI × OPENMP	Poisson (s)
12x1	2.88	72x1	0.5
6x2	1.57	36x2	0.53
4x3	1.49	24x3	0.4
3x4	1.7	18x4	0.53

Table 2.2: *Comparison of the time for computing Poisson's equation for a given combination of MPI processes × OPENMP threads = 12 and 72 cores with the SMG solver for the TC-2 where* $n_x \times n_r = 3353 \times 1725$.

In Table 2.2, we present a comparison of the time for computing Poisson's equation for a given combination of MPI processes × OPENMP threads = 12 and 72 cores with the SMG solver for the TC-2. In the first column in Table 2.2, we compare the performances of the SMG solver on 12 cores. We have tested different combinations of MPI processes × OPENMP threads from 12 MPI processes to 3 MPI processes and 4 OPENMP threads per MPI process. We show here that for 12 cores the combination of 4 MPI processes×3 OPENMP threads solves Poisson's equation in 1.49 s whereas with 12 MPI processes it takes 2.88 s.
In the previous section, we found that with 72 MPI processes, the computational time is the fastest with the SMG solver on the TC-2. In Table 2.2, we show that the combination: 24 MPI processes ×3 OPENMP threads solve Poisson's equation in 0.4 s compared to 0.5 s with 72 MPI processes. This means that on the TC-2 with the same number of cores available, we can decrease further the computational time by adopting an hybrid MPI-OPENMP strategy.
Using the parallel capabilities of the SMG solver we significantly decreased the solution time of Poisson's equation from 2.47 s with the direct solver PaStiX to 0.4 s with the iterative SMG solver (Table 2.2) in the TC-2 (section 1.4.2).
As a conclusion, we have implemented an efficient iterative hybrid MPI-OPENMP solver SMG. With the implementation of this solver we have solved the problem of memory requirement and decreased significantly the time to compute the solution of Poisson's equation. However, in section 1.4.2, we also mentioned that in the fully explicit model, the dielectric relaxation time-step imposes a quite low value for the chosen time-step during most of the simulation. In the next section, we will present a simple "semi-implicit" scheme that allows to choose a time-step one order of magnitude higher than with the fully explicit code for the TC-2.

2.4 Semi-implicit scheme for Poisson's equation

2.4.1 "Semi-implicit" scheme

As mentioned in section 2.2, the calculations of the TC-2 with a fully explicit code take at least one week. Indeed due to the high density of electrons $n_e = 1 \times 10^{15}$ cm^{-3}, the dielectric relaxation time-step is the smallest characteristic time-step and then the general time-step is limited to only $\Delta t = \Delta t_{Diel} = 3 \times 10^{-14}$ s.
In order to circumvent this constraining time-step limitation by the dielectric relaxation time-step problem, different authors (Ventzek et al. 1993), (Hagelaar and Kroesen 2000), (Lin et al. 2012) and (Villa et al. 2013) have implemented a "semi-implicit" scheme that changes the discretization of Poisson's equation.

2.4.2 "Semi-implicit" scheme

The idea of the "semi-implicit" scheme is to use throughout the code the electric field at $t + \Delta t$:

$$-(\boldsymbol{\nabla} V^{t}) = \boldsymbol{E^{t}} \qquad \rightarrow \quad -(\boldsymbol{\nabla} V^{t+\Delta t}) = \boldsymbol{E^{t+\Delta t}} \ . \tag{2.1}$$

As in (Ventzek et al. 1993) and (Hagelaar and Kroesen 2000), the net charge density is predicted at a future time. Based on Poisson's equation:

$$\varepsilon_0 \boldsymbol{\nabla} \cdot (\varepsilon_r \boldsymbol{\nabla} V(t + \Delta t)) = -\left[\rho^t + \Delta t \frac{\partial \rho}{\partial t}\right] \ . \tag{2.2}$$

Chemistry source terms do not create any space charge and so based on the drift-diffusion equation:

$$\frac{\partial \rho}{\partial t} = \boldsymbol{\nabla} \cdot \left[\sum_i |q_e| \left(\mu_i^t \ n_i^t \ \boldsymbol{E^{t+\Delta t}} - D_i \ \boldsymbol{\nabla} \ n_i^t\right)\right] \ . \tag{2.3}$$

At that point we simplify equation (2.3) in which we neglect the diffusion part as was proposed in (Lin et al. 2012) and (Villa et al. 2013) and so equation (2.3) becomes:

$$\frac{\partial \rho}{\partial t} = \boldsymbol{\nabla} \cdot \left[\sum_i |q_e| \left(\mu_i^t \ n_i^t \ \boldsymbol{E^{t+\Delta t}}\right)\right] \ . \tag{2.4}$$

And then we combine equations (2.4) in equation (2.2):

$$\varepsilon_0 \boldsymbol{\nabla}\cdot(\varepsilon_{\mathrm{r}}\boldsymbol{\nabla}\mathrm{V}(t+\Delta t)) = -\left[\rho^t + \Delta t \boldsymbol{\nabla}\cdot\left[\sum_i |\mathrm{q_e}|\left(\mu_i^t\ n_i^t\ \boldsymbol{E^{t+\Delta t}}\right)\right]\right]\ . \quad (2.5)$$

After some rewriting, one obtains:

$$\boldsymbol{\nabla}\cdot(\varepsilon^{'}\boldsymbol{\nabla}\mathrm{V}(t+\Delta t)) = -\rho^t\ , \quad (2.6)$$

with:

$$\varepsilon^{'} = \varepsilon_0\varepsilon_{\mathrm{r}} + \sum_i \Delta t|\mathrm{q_e}|\left(\mu_i^t\ n_i^t\right)\ , \quad (2.7)$$

or:

$$\varepsilon^{'} = \varepsilon_0\varepsilon_{\mathrm{r}} + \Delta t\sigma_{conduc}\ . \quad (2.8)$$

By implicitly solving the electric field that way, we actually change the conductivity of the air gap to compensate any change in the net charge density due to drift (Ventzek et al. 1993) and (Villa et al. 2013). The only drawback of that scheme is that, in the discretization of Poisson's equation, the resulting matrix will change at each time-step. Using a direct solver like MUMPS (Amestoy et al. 2001) would require to do the factorization at each time-step. Then for this "semi-implicit" scheme we have used the efficient parallel iterative solver SMG in the HYPRE library (HYPRE 2007).

2.4.3 Comparison of the semi-implicit and the full explicit model

In this section, we compare the computational efficiency between two codes for the TC-2. The first code is fully explicit: Poisson's and the drift-diffusion equations are solved explicitly and all the physical time-steps have to be taken into account (equations (1.28) - (1.31)).
In the "semi-implicit" code, the drift-diffusion equations are also solved explicitly but we solve Poisson's equation using the "semi-implicit" method presented in section 2.4. In this code we take into account the characteristic time-steps (equations (1.28) - (1.30)) except the dielectric relaxation time-step Δt_{Diel}. To implement this "semi-implicit" scheme we used the efficient parallel iterative solver SMG in the HYPRE library (section 2.3).
On Figure 2.5, we present the simulation time-step for the fully explicit

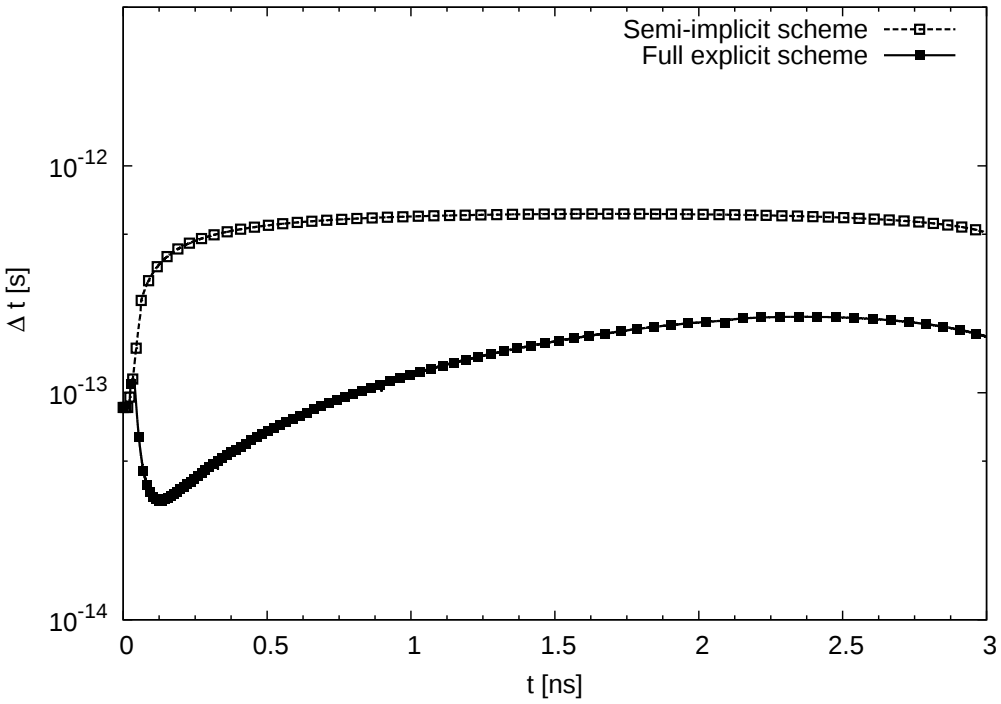

Figure 2.5: *Comparison of time-step between a full explicit simulation and a simulation with the "semi-implicit scheme" on the TC-2.*

code and for the "semi-implicit" code. In the beginning of the simulation, as in section 1.4.2, the chosen time-step is the chemistry time-step Δt_I in both simulations.

We recall here that, at the beginning of the simulation a constant voltage of $U_a = 30$ kV is applied at the point electrode anode. Due to the high voltage at the point electrode that induces an electric field of 2.2 MV.cm^{-1}, and the quite low initial density for charged species ($n_{e,p} = 10^4$ cm^{-3}), the creation of charged species is the fastest physical process at the beginning. As the electron density reaches a sufficiently high value ($n_e \simeq 10^{14}$ cm^{-1}) at $t = 2.9 \times 10^{-10}$ s, in the fully explicit simulation, the minimum time-step is the dielectric relaxation one Δt_{Diel}. In the simulation with the "semi-implicit" scheme, at that time of the simulation, the chosen time-step is the convection one Δt_c. For $t > 2.9 \times 10^{-10}$ s, the difference of chosen time-steps between the two codes starts to increase and in the simulation with the "semi-implicit" scheme the chosen time-step is one order of magnitude higher than the simulation with the fully explicit model.

On Figure 2.6, we compare the axial profiles of the magnitude of the electric field on the discharge axis for the fully explicit code and the

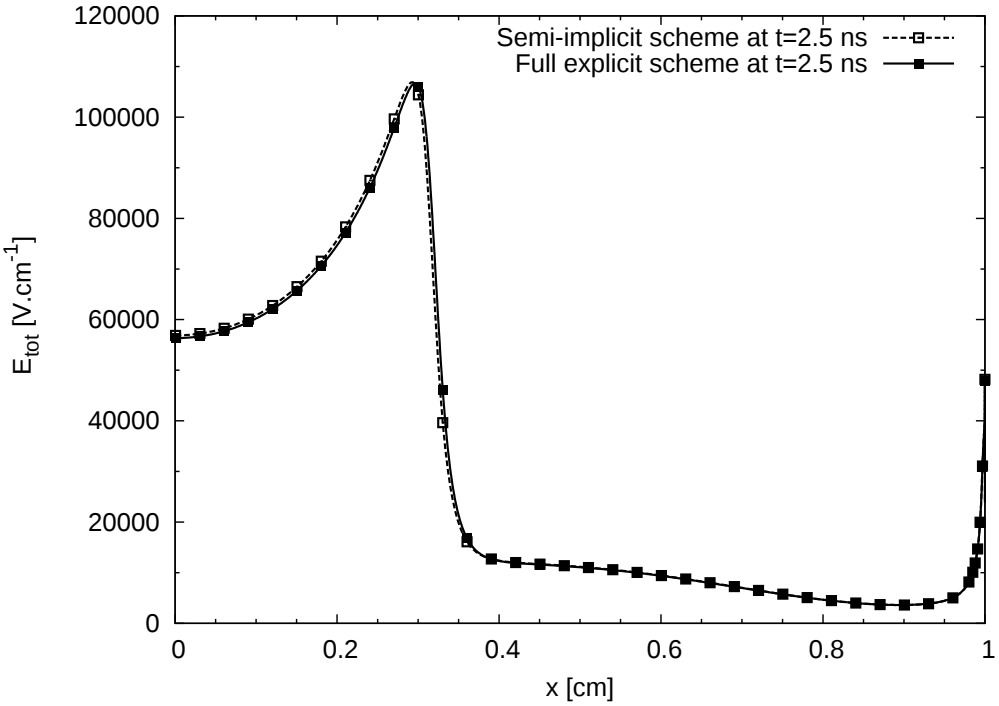

Figure 2.6: *Comparison of axial profiles of the magnitude of the electric field on the discharge axis of a fully explicit simulation with a simulation with a "semi-implicit" scheme at t=2.5 ns on the TC-2.*

"semi-implicit" code at t=2.5 ns. We see that in both simulations, the peak of electric field representing the location of the head of the streamer discharge is located at the same location on the discharge axis. But if we make a zoom on the head of the discharge where x $\in$ [0.2 cm : 0.4 cm], we see on Figure 2.7, with the "semi-implicit" scheme the location of this peak is slightly closer (1.3 %) to the cathode plane (located at x = 0cm) than the peak electric field in the full explicit simulation.

In conclusion, we see that implementing this "semi-implicit" scheme allows to carry out simulations with time-steps 10 times higher than in simulations with a fully explicit model that resulted in a minor difference of 1.3 % on the location of the discharge front during its propagation.

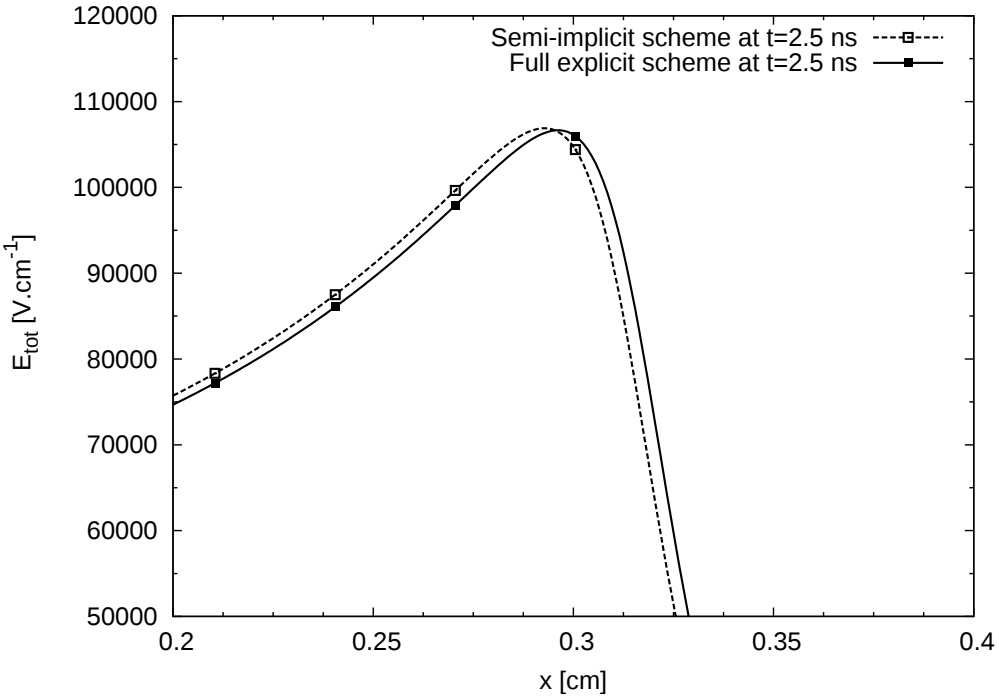

Figure 2.7: *Comparison of axial profiles of the magnitude of the electric field on the discharge axis of a full explicit simulation with a simulation with a "semi-implicit" scheme at t=2.5 ns zoomed on* $x \in [0.2\text{ cm} : 0.4\text{ cm}]$.

2.5 Conclusion

In this chapter, we have improved the computational efficiency of the discharge code by changing the sequential direct solver MUMPS with the parallel OPENMP direct solver PaStiX. We also have implemented OPENMP protocols in the rest of the discharge code. We have shown that using this new parallel OPENMP discharge code with the PaStiX solver, we were able to speed-up the calculations in the test-case TC-1 by a factor of 5.7.

In the test-case TC-2, with the fully explicit parallel OPENMP with the PaStiX solver, we have pointed out that the limiting time-step was the dielectric relaxation one Δt_{Diel} and that the amount of memory required was too high for the simulation to run on a regular node on the "igloo" cluster. We have solved the memory problem by changing the direct solver PaStiX with an iterative solver SMG in the HYPRE library. We have shown that the parallel version of the SMG solver was quite fast and required less than a 1 Go of memory. Coupled with the fast iterative solver SMG, we have also shown that a simple "semi-implicit" scheme al-

lows, in a streamer discharge code, to remove the constraint of the limiting dielectric relaxation time-step Δt_{Diel}. With the resulting "semi-implicit" code, we were able to simulate the TC-2, with a time-step which is one order of magnitude higher than the one used in the fully explicit code.

Chapter 3

Optimization and parallelization of the discharge code: Drift-diffusion equations

3.1 Introduction

Many difficulties appear when one tries to solve a drift-diffusion equation. In the particular case of the simulation of streamer discharges, we have to solve highly non-linear drift-diffusion equations coupled with stiff ordinary differential equations for the chemistry source terms (equation (1.13)). We also need to take into account the multiscale nature of streamer discharges. In the head of a streamer discharge, a transport scheme needs to handle density gradients of several orders of magnitude. And so the chosen numerical method needs to be sufficiently accurate but also robust to exactly describe these density gradients and ensure the positivity of charged species densities.
In this chapter, in section 3.2, we will present and compare two 1D convection schemes the UNO3 and the ULTIMATE QUICKEST schemes. Then in section 3.3, we will compare the results obtained on the test-case TC-2 with the ISG scheme used in the LDC code and the UNO3 scheme. Finally the choice between these two schemes for streamer simulations will be discussed.

3.2 1D convection schemes

3.2.1 Construction of UNO schemes

Numerically solving an advection equation is notoriously difficult. As of yet, no "perfect scheme" has been found to solve this equation accurately in its discrete form. In (Leonard 1991), it is stated that even the one-dimensional scalar advection at constant velocity is a simple problem but surprisingly difficult to solve. One of the main obstacle in the development of advection schemes are numerical oscillations associated with high-order schemes like the (Lax and Wendroff 1960) scheme. One of the differences between convection schemes of different order is their inherent numerical diffusion. The first-order upstream (UPWIND) scheme is widely known to be too diffusive and using higher order schemes tends to reduce the numerical diffusion. However in (Leonard 1991), it is stated that the reduction of the numerical diffusion becomes negligible as soon as the order of the scheme is higher than the third order. Increasing the order of the schemes to orders higher than the third order one is useless if the physical diffusion is considered in the same model (Li 2008). So it should be enough to choose an advection scheme of one order higher than the real diffusion. As in this work, we use a second order scheme for diffusion (section 3.3.2), we will use at maximum a third order scheme for drift. It is also pointed out in (Li 2008) that a higher accuracy should be also obtained by better resolution. We will briefly present here the idea behind the UNO3 scheme that is extensively described in (Li 2008).

The most important feature of a convection scheme is its ability to be oscillation free. To illustrate this, we consider the simple situation depicted on Figure 3.1 where at the point "j" the average density is equal to 0 and at the point "j+1" the average density is equal to 1. It will be shown here how the different schemes behave in this situation where the flow is assumed to be non-divergent. In this 1D case, the velocity is constant and assumed positive.

It is important here to follow the same cell notation initially given by (Leonard 1991) and also used in (Li 2008). At a given cell face, "j+1/2" with a velocity $u_{j+1/2}$ here positive, a *central* (C) cell is defined as the donor cell j when $u_{j+1/2} \geq 0$. The *downstream* cell (D) is the cell that receives the flux (cell $j+1$ when $u_{j+1/2} \geq 0$). So the cell located at $j-1$ next to the *central* cell at the opposite side is the *upstream* cell (U) when $u_{j+1/2} \geq 0$. In the same way if $u_{j+1/2} \leq 0$, the *upstream* cell is located at $j+2$, the *central* cell is located at $j+1$ and the *downstream* cell is located at j. All subsequent formulations will be given in this upstream-

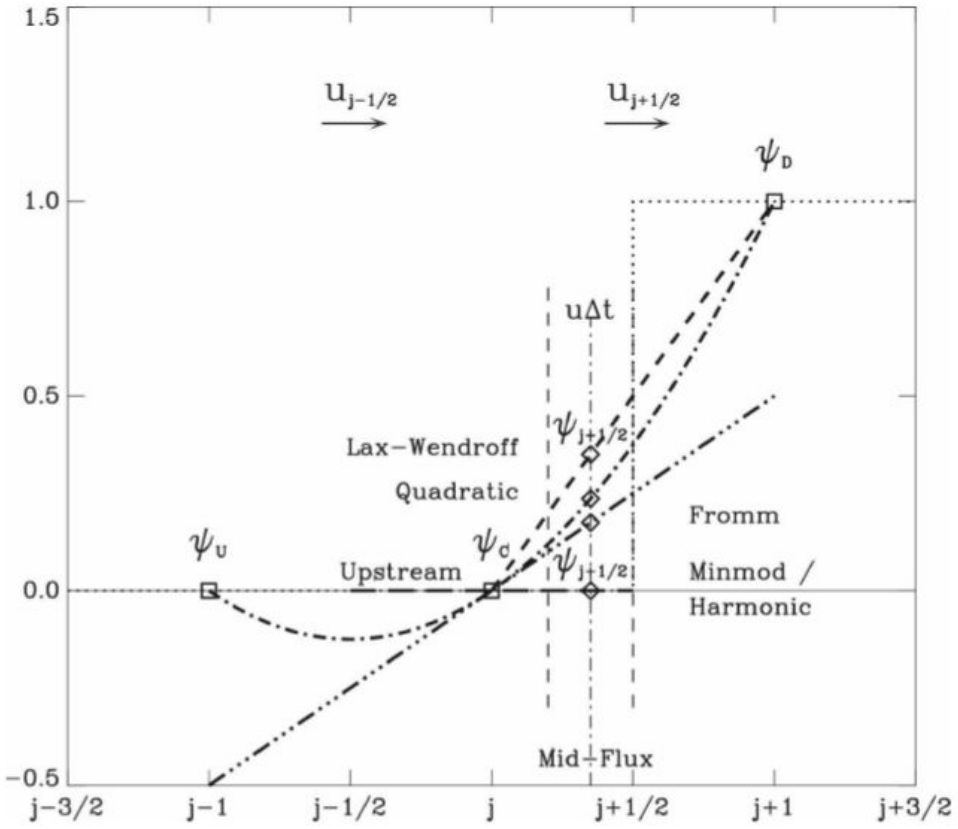

Figure 3.1: *Comparison of six classical advection schemes for interpolation of the MF (mid flux) value of a step function. This Figure was taken from (Li 2008)*

central-downstream (UCD) notation. To account for irregular grids, the finite difference will be based on the cell center coordinate and a gradient notation G_{AB} is defined between any two cells **A** and **B** as:

$$G_{AB} \equiv \frac{(\psi_A - \psi_B)}{(x_A - x_B)} . \tag{3.1}$$

That is symmetrical in the ordering of the two cells, that is $G_{AB} = G_{BA}$. Any convection scheme will use some form of interpolation to calculate an interpolated density at each cell face called *mid-flux* (MF) point, which is $|u|\Delta t/2$ upstream from the cell face or $(\Delta x - |u|\Delta t)/2$ downstream from the donor cell center (Li 2008).

$$\psi^{MF}_{j+1/2} = \psi^n_C + 0.5\mathrm{sgn}(u_{j+1/2})\,(\Delta x - |u|\Delta t)\,G_C , \tag{3.2}$$

where ψ^n_C is the central (or donor) cell value at time level n relative to the $j + 1/2$ face velocity $u_{j+1/2}$, $\mathrm{sgn}(u)$ is the sign function and G_C the

selected gradient for the central cell. Of course the interpolated value will be equal to the central cell value when the Current number (or CFL number) approaches unity no matter what central gradient is used in equation (3.2). The updated cell j value will be given in the conservative flux form as:

$$\psi_j^{n+1} \;=\; \psi_j^n + \left(u_{j-1/2}\psi_{j-1/2}^{MF} - u_{j+1/2}\psi_{j+1/2}^{MF}\right)\Delta t/\Delta x_j \;. \tag{3.3}$$

Let us now review some of the schemes shown on Figure 3.1 and see how these schemes induce a nonzero flux or not:

$$\begin{cases} \text{UPWIND scheme :} \\ G_C \;=\; 0 \;\Rightarrow\; F_{j+1/2} \;=\; 0 \;. \end{cases} \tag{3.4}$$

$$\begin{cases} \text{Lax} - \text{Wendroff scheme (Lax and Wendroff 1960):} \\ G_C \;=\; G_{DC} \;\Rightarrow\; F_{j+1/2} \;\neq\; 0 \;. \end{cases} \tag{3.5}$$

$$\begin{cases} \text{Fromm scheme (Fromm 1968):} \\ G_C \;=\; G_{DU} \;\Rightarrow\; F_{j+1/2} \;\neq\; 0 \;. \end{cases} \tag{3.6}$$

$$\begin{cases} \text{Roe scheme (Roe 1985):} \\ G_C \;= \min\left(|G_{DC}|, |G_{CU}|\right) \text{ when } G_{DC}G_{CU} > \; 0 \;, \\ \text{otherwise } G_C \;=\; 0 \;\Rightarrow\; F_{j+1/2} \;=\; 0 \;. \end{cases} \tag{3.7}$$

$$\begin{cases} \text{Takacs scheme (Takacs 1985):} \\ G_C \;=\; G_{DC} - \frac{\left(\Delta x_D + |u_{j+1/2}|\Delta t\right)}{1.5\ sgn(u_{j+1/2})}\left(\frac{G_{DC}-G_{CU}}{x_D - x_U}\right) \;\Rightarrow\; F_{j+1/2} \;\neq\; 0 \;. \end{cases} \tag{3.8}$$

In all the schemes listed here, only the Roe scheme will produce a zero flux in the situation on Figure 3.1. In this scheme, the min-mod scheme is used only in the monotone region defined by $G_{DC}G_{CU} > \; 0$. Outside the monotone region, the gradient is simply set to zero (UPWIND scheme). In (Li 2008), the author extended the min-mod scheme outside the monotone region if the sign of the local side gradient G_{DC} is used which gives the following second order in time and space scheme UNO2:

$$\text{UNO2 :}\;\; G_C \;=\; \text{sgn}(G_{DC})\,\min\left(|G_{DC}|, |G_{CU}|\right) \;. \tag{3.9}$$

And if we put equation (3.9) in equation (3.2):

$$\psi^{MF}_{j+1/2} \;=\; \psi^n_C + 0.5\,(\psi^n_D - \psi^n_C)\,(\Delta x \;-\; |u|\Delta t)\;\min\left(|G_{DC}|, |G_{CU}|\right)\;. \quad (3.10)$$

The scheme presented in equation (3.10) is as Li put it in (Li 2008) the simplest second-order non oscillatory scheme. The third order scheme UNO3 is:

$$\text{UNO3:}\;\; G_C \;=\; \begin{cases} G_{DC} - \frac{\left(\Delta x_D + |u_{j+1/2}|\Delta t\right)}{1.5\;\; sgn(u_{j+1/2})}\left(\frac{G_{DC}-G_{CU}}{x_D - x_U}\right), \\ \;\text{for}\; |G_{DC} - G_{CU}| \;<\; 1.2|G_{DU}|\;; \\ 2\;\text{sgn}(G_{DC})\; min\left(|G_{DC}|, |G_{CU}|\right), \\ \;\text{for}\; G_{DC}G_{CU} > \;0\;; \\ \text{sgn}(G_{DC})\;\min\left(|G_{DC}|, |G_{CU}|\right),\;\text{otherwise.} \end{cases} \quad (3.11)$$

In this scheme, the Takacs scheme is used in the limited monotone zone defined on an irregular grid by $|G_{DC} - G_{CU}| \;<\; 1.2|G_{DU}|$ and outside this limited region but still in the monotone region, the UNO2 scheme multiplied by 2 is used. Outside the monotone region, the UNO3 scheme retains second order accuracy by using the UNO2 scheme.
The UNO3 scheme is third order accurate, non-oscillatory (preserved positivity of the density solution), written for uniform as well as for non-uniform mesh and by the construction of the scheme, extremely easy to implement in codes.

3.2.2 ULTIMATE QUICKEST scheme

In this section, we present the 3rd order QUICKEST scheme (Leonard 1991) coupled with the so-called ULTIMATE flux limiter which results in a non oscillatory scheme called the ULTIMATE QUICKEST. We briefly present the general characteristics of the scheme with the same notations as in (Du 2000). More details can be found in (Du 2000). This scheme was used in streamer discharge simulations in (Bessières et al. 2007).
We rewrite here equation (3.3) as in (Du 2000):

$$\psi^{n+1}_j \;=\; \psi^n_j - \left(c_{j+1/2}\psi^{MF}_{j+1/2} - c_{j-1/2}\psi^{MF}_{j-1/2}\right),\; \text{with}\; c_{j\pm1/2} \;=\; u_{j\pm1/2}\Delta t/\Delta x_j\;. \quad (3.12)$$

With the QUICKEST scheme, $\psi^{MF}_{j+1/2}$ can be written as:

$$\psi^{MF}_{j+1/2} = \psi^{2}_{j+1/2} - \frac{(1-c^2_{j+1/2})}{6} \left[\frac{1+\mathrm{sgn}(c_{j+1/2})}{2}\left(\psi^n_{j+1} - 2\psi^n_j + \psi^n_{j-1}\right) + \frac{1-\mathrm{sgn}(c_{j+1/2})}{2}\left(\psi^n_{j+2} - 2\psi^n_{j+1} + \psi^n_j\right)\right], \tag{3.13}$$

where:

$$\psi^2_{j+1/2} = \frac{1}{2}\left[\left(\psi^n_{j+1} + \psi^n_j\right) - c_{j+1/2}\left(\psi^n_{j+1} - \psi^n_j\right)\right]. \tag{3.14}$$

Then we use the one dimensional universal limiters shown in Table 3.1:

$_{j+1/2}$ face velocity $u_{j+1/2}$	Local monotonicity	j+1/2 limiters for $\psi^{MF}_{j+1/2}$	
		upper limiter ψ_{upper}	lower limiter ψ_{lower}
$u_{j+1/2} > 0$	$\psi^n_u \le \psi^n_c \le \psi^n_d$	ψ_{lim}	ψ^n_c
$u_{j+1/2} > 0$	$\psi^n_d \le \psi^n_c \le \psi^n_u$	ψ^n_c	ψ_{lim}
$u_{j+1/2} < 0$	$\psi^n_u \le \psi^n_c \le \psi^n_d$	ψ^n_c	ψ_{lim}
$u_{j+1/2} < 0$	$\psi^n_d \le \psi^n_c \le \psi^n_u$	ψ_{lim}	ψ^n_c

Table 3.1: *One-dimensional universal limiters*

where ψ_{lim} is defined as:

$$\psi_{lim} = \min\left[\psi^n_d, \frac{\min\left(c_{j-1/2}\psi^n_u,\ c_{j-1/2}\psi^n_c\right) + \psi^n_c - \psi^n_u}{c_{j+1/2}}\right].$$

Where the subscripts U, C and D are the same subscripts as described in section 3.2.1 and $\psi^{MF}_{j+1/2}$ is chosen as follows:

$$\psi^{MF}_{j+1/2} = \max\left(\psi_{lower}, \min\left(\psi_{upper}, \psi^{MF}_{j+1/2}\right)\right). \tag{3.15}$$

In conclusion we have a third order accurate scheme that is non oscillatory but as shown in Table 3.1 a lot of conditions have to be checked by the ULTIMATE limiter. These numerous tests reduce the computational efficiency of the scheme.

3.2.3 1D constant velocity convection test case

We now consider the classical test case of the advection of an initial profile composed of a Gaussian wave, a square wave, a triangular wave and an ellipse with periodic boundaries. This is a difficult test case because it includes discontinuities as well as smooth portions of curves and extrema. The initial condition $u_0(x)$ is defined on the interval x $\in [-1:1]$ as (taken from (Daru and Tenaud 2004)):

$$\begin{cases} u_0(x) = \exp(-\log(2)(x+0.7)^2/0.0009)\ ; & \text{if } -0.8 \geq x \geq -0.6 \\ u_0(x) = 1\ ; & \text{if } -0.4 \geq x \geq -0.2 \\ u_0(x) = 1 - |10(x-0.1)|\ ; & \text{if } 0 \geq x \geq 0.2 \\ u_0(x) = (1 - 100(x-0.5)^2)^{1/2}\ ; & \text{if } 0.4 \geq x \geq 0.6 \\ u_0(x) = 0\ ; & \text{otherwise .} \end{cases} \tag{3.16}$$

We will test here three convection schemes: the UPWIND scheme, the ULTIMATE QUICKEST scheme used in (Bessières et al. 2007) and the UNO3 scheme (Li 2008).

Figure 3.2 (a),(b) and (c) presents for 200, 800 and 1600 points respectively the results obtained with the different schemes after 10 periods. Figure 3.2 shows clearly how diffusive the UPWIND scheme is. After 10 periods, even on the finest mesh of 1600 points, the numerical diffusion of this scheme has completely erased the initial profile. It is however clear that third order schemes, the ULTIMATE QUICKEST and UNO3 schemes are able to better reproduce the initial profile over 10 periods. We also see that on the 200 points mesh, the ULTIMATE QUICKEST scheme is more accurate than the UNO3 scheme. As the mesh is refined, we see that the UNO3 scheme tends to be as good as the ULTIMATE QUICKEST scheme. Figure 3.3 shows the same results as Figure 3.2 but for 100 periods. We note that after 100 periods, the differences between the schemes is even more pronounced. It is shown here that the numerical diffusion of the UNO3 scheme is a bit higher than the ULTIMATE QUICKEST scheme.

In Table 3.2, the average % of error compared to the initial profile and the CPU time (in s) are presented for the UPWIND scheme, the ULTIMATE QUICKEST scheme and the UNO3 scheme for three different meshes for 10 and 100 periods. It is clear here that the ULTIMATE QUICKEST scheme, regardless of the resolution of the mesh, is the most accurate

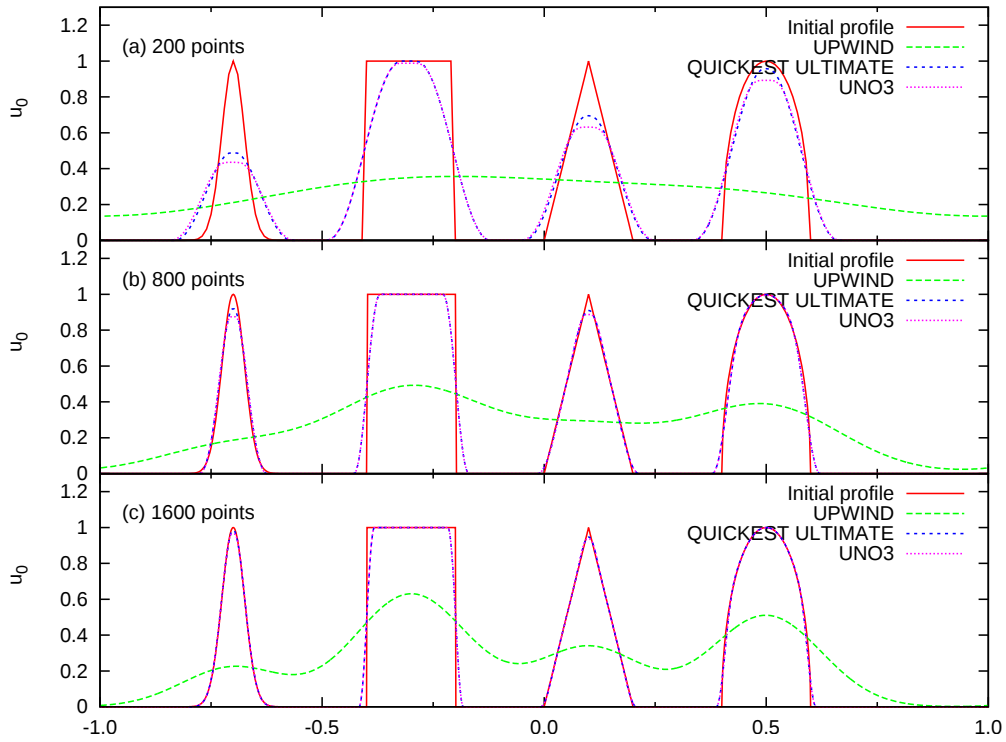

Figure 3.2: *Comparison of the UPWIND scheme, ULTIMATE QUICKEST scheme and UNO3 scheme on a mesh of: (a) 200, (b) 800 and (c) 1600 points. The Courant number = 0.5 and results are given after 10 periods.*

Numerical scheme	Number of points	After 10 periods		After 100 periods	
		Error (%)	CPU time (s)	Error (%)	CPU time (s)
UPWIND	1600	23.6	0.5	32.33	5.03
	800	28.2	0.13	33.4	1.27
	200	32.1	$1.2\ 10^{-2}$	34.5	$8.4\ 10^{-2}$
QUICKEST	1600	0.88	3.5	1.96	35.01
	800	1.8	0.9	3.8	9.0
	200	7.8	$6.0\ 10^{-2}$	17.2	0.64
UNO3	1600	0.91	2.0	2.03	20.41
	800	1.9	0.5	4.0	5.1
	200	8.5	$3.2\ 10^{-2}$	19.6	0.34

Table 3.2: *comparison of errors and computation times for the different schemes for a Courant number = 0.5. (Calculations were done on a UBUNTU Version 12.04 64 bits with Intel Core i7-2630QM CPU*

scheme. But accuracy is not the only criterion to consider to choose a scheme. That is why we show in this table also the computational cost

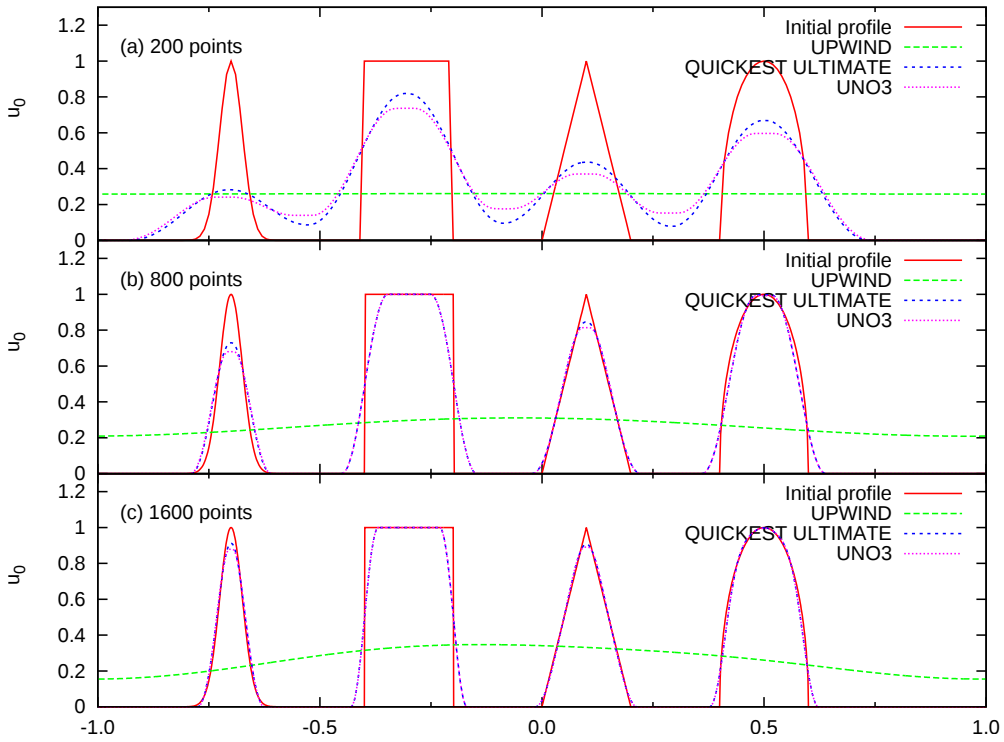

Figure 3.3: *Comparison of the UPWIND scheme, ULTIMATE QUICKEST scheme and UNO3 scheme on a mesh of: (a) 200, (b) 800 and (c) 1600 points. The Courant number = 0.5 and results are given after 100 periods.*

of each scheme. The UPWIND scheme is the less expensive but the average % of error is too high on any mesh. The ULTIMATE QUICKEST scheme is the most accurate but it has also the highest computational cost due to the use of limiter that induces a lot of conditional checks (section 3.2.2) (Li 2008). The UNO3 scheme is less accurate than the ULTIMATE QUICKEST scheme (UNO3: 19.6 % and ULTIMATE QUICKEST: 17.2 % on the coarser mesh after 100 periods) but the difference seems quite small.

On the other hand, we also need to check the positivity of the solution. Of course the UPWIND scheme always gives positive density solution. We have observed that the ULTIMATE QUICKEST scheme may give very small negative values in the computed density whereas the UNO3 scheme always gives positive density values.

To conclude on this simple test case, we have demonstrated here the advantages to choose the UNO3 scheme. It is third order accurate, its computational cost is reasonable compared to the ULTIMATE QUICKEST scheme. Furthermore, the UNO3 scheme is very easy to implement

and by construction always gives positive density values.

3.3 2D convection-diffusion schemes

3.3.1 2D implementation of the UNO3 scheme

As stated in (Li 2008), the extension of the 1D scheme to 2D scheme is straightforward by applying the 1D scheme simultaneously to each of the two dimensions before updating the next time level values. But this method may lead to reduced stability conditions, $|\mu_x| + |\mu_r| < 1.0$ where $\mu_x = v_x \Delta t/\Delta x$ and $\mu_r = v_r \Delta t/\Delta r$ are the courant number for the x direction and r direction respectively. On the other hand, if a time splitting approach is applied and the 1D scheme is applied one dimension after the other, the stability condition is relaxed to $\max(|\mu_x|\ ,\ |\mu_r|) < 1.0$. But it results in the so-called time splitting error. To avoid the time splitting error, in (Leonard et al. 1996) the authors constructed a multidimensional advective-conservative hybrid operator (MACHO) to extend a 1D advection scheme to 2D with preserved constancy. As formulated in (Li 2008), the operator is similar to the time-splitting approach except that the *mid-flux* (MF) value for the second dimension ψ^{*MF} is calculated with a temporary advective-form update of the first dimensional ψ^* using the cell center velocity:

$$\psi^*_{i,j} \ = \ \psi^n_{i,j} + \left(\psi^{MF}_{i-1/2,j} - \psi^{MF}_{i+1/2,j}\right)\left(u_{i-1/2,j} + u_{i+1/2,j}\right)\Delta t/2\Delta x_i \ . \quad (3.17)$$

In order for the MF values for both dimensions to be interpolated from the same constant field, this temporary update in equation (3.17) is used. The final update of the cell (i,j) value is given by:

$$\begin{aligned} \psi^{n+1}_{i,j} \ = \ & \psi^n_{i,j} + \left(u_{i-1/2,j}\psi^{MF}_{i-1/2,j} - u_{i+1/2,j}\psi^{MF}_{i+1/2,j}\right)\Delta t/\Delta x_i \\ & + \ \left(v_{i,j-1/2}\psi^{MF}_{i,j-1/2} - v_{i,j+1/2}\psi^{MF}_{i,j+1/2}\right)\Delta t/\Delta y_j \ . \end{aligned} \quad (3.18)$$

We must point out that by construction the UNO3 scheme can be applied on either uniform or non uniform mesh.

3.3.2 2D Diffusion fluxes

In the improved Scharfetter-Gummel (ISG) scheme used in the LDC-code, diffusion and drift fluxes are calculated simultaneously. However,

diffusion fluxes are usually calculated separately from drift fluxes and equation (1.19) is thus splitted into two equations: one with drift fluxes (calculated with the UPWIND or UNO3 scheme) and a second one with diffusion fluxes. In this case, we have used a classical second-order central-difference scheme, representing the diffusion fluxes in the form:

$$\begin{aligned} F^D_{i+1/2,j}(k) &= D^k_{i+1/2,j}\frac{\bar{n}^k_{i,j}-\bar{n}^k_{i+1,j}}{x_{i+1,j}-x_{i,j}}\Sigma_{i+1/2,j}\ , \\ F^D_{i,j+1/2}(k) &= D^k_{i,j+1/2}\frac{\bar{n}^k_{i,j}-\bar{n}^k_{i,j+1}}{r_{i,j+1}-r_{i,j}}\Sigma_{i,j+1/2}\ . \end{aligned} \tag{3.19}$$

3.3.3 Comparison of transport schemes on the TC-2

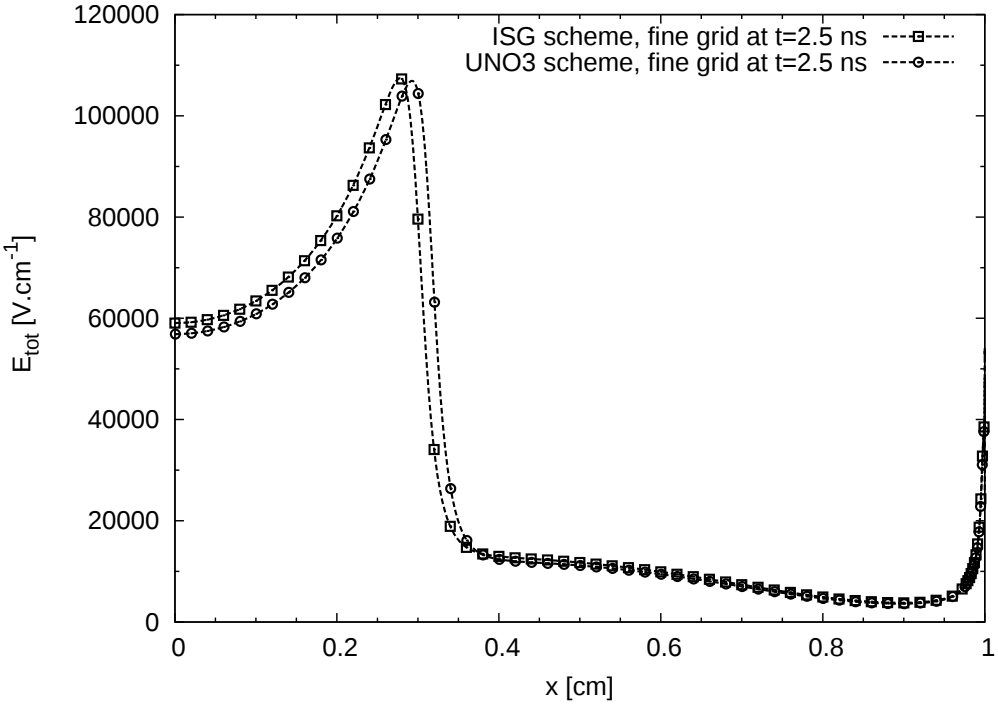

Figure 3.4: *Axial profiles of the magnitude of the electric field on the fine mesh with the ISG scheme and the UNO3 scheme at t=2.5 ns on the TC-2.*

In this section we compare the 2D implementation of the ISG and UNO3 schemes on the TC-2. In the simulation of the TC-2 presented in section 1.4.2, we have shown results of the propagation of a streamer on a "fine" mesh (1 μm of mesh size close to the point electrode) required for a sufficient resolution of the discharge dynamics.

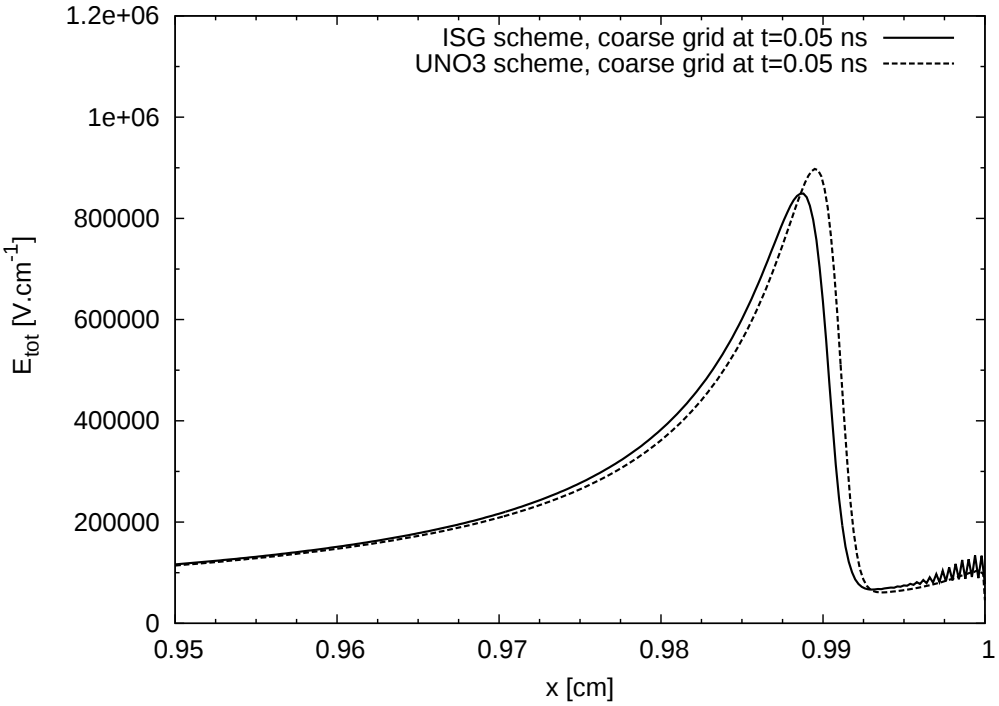

Figure 3.5: *Axial profiles of the magnitude of electric field on a coarse mesh with the ISG scheme and the UNO3 scheme at t=0.05 ns in the TC-2.*

On Figure 3.4, we present the axial profiles of the magnitude of the electric field on the "fine" mesh with the ISG scheme and UNO3 scheme at t=2.5 ns.
Figure 3.4 shows that the axial location of the peak of electric field in the streamer head is almost the same in both simulations. If we compare the general dynamics of the streamer discharge between both simulations, there is almost no difference, with for example, the time required for the streamer discharge to cross the inter-electrode gap and impact the cathode plane at t_c=3.0 ns in both simulations.
For the computational efficiency and time of calculation, it is interesting to have a transport scheme that can provide the same accuracy with a reduced number of points. So we define a "coarse" mesh as follows: from $0 \leq x \leq 1$ cm, an axial mesh size of 20 μm is used and is refined to 2 μm close to the anode tip. Radially, a mesh size of 5 μm is used and is refined to 1 μm close to the axis of symmetry. This level of refinement required a grid size of $n_x \times n_r = 1659 \times 1725$. On Figure 3.5, we present the axial profiles of the magnitude of electric field with the ISG scheme and the UNO3 scheme at t=0.05 ns for the TC-2 simulation on the "coarse" mesh. This Figure indicates that even on the "coarse" mesh, the peak

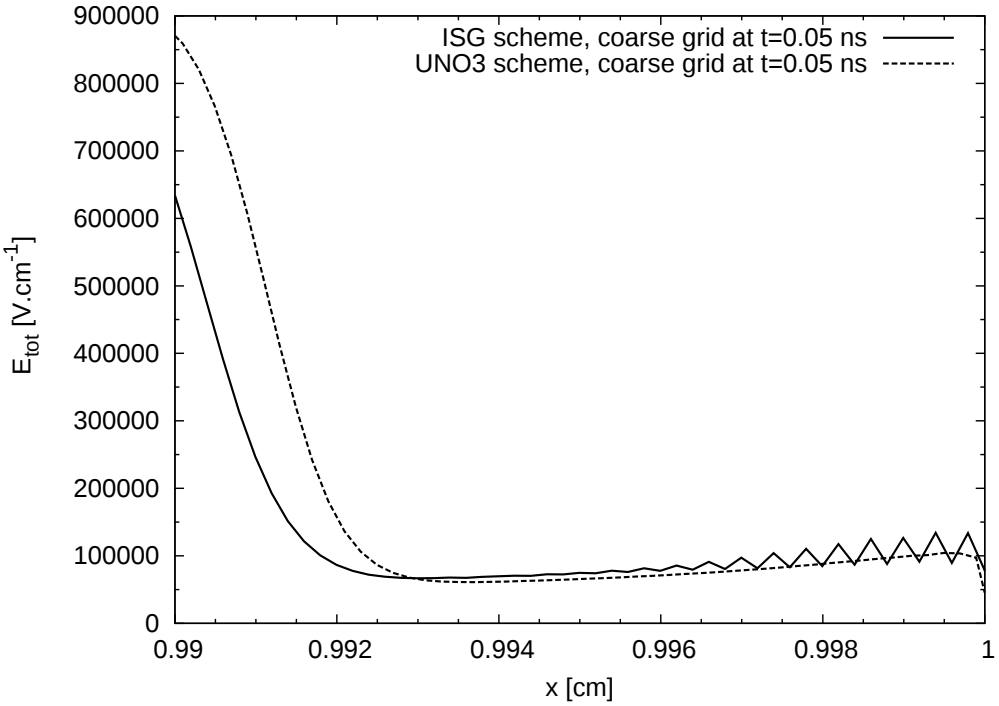

Figure 3.6: *Axial profiles of the magnitude of field on a coarse mesh with the ISG and the UNO3 scheme at t=0.05 ns zoomed on* $x \in [0.99 \text{ cm} : 1 \text{ cm}]$.

magnitude of electric field with the ISG scheme and the UNO3 scheme are almost at the same axial location. On Figure 3.5, we see that close to the point electrode at x = 1 cm, some oscillations are present with the ISG scheme. It is interesting to note that no oscillations are observed when the UNO3 scheme is used during the whole discharge simulation.
On Figure 3.6, we zoomed on $x \in [0.99 \text{ cm} : 1 \text{ cm}]$ to take a closer view on these oscillations. These oscillations are mainly due to the difficulties of the cubic spline interpolation scheme used in the ISG scheme on the coarser mesh. This leads to less accurate flux calculations in equation (1.25) and oscillations in the net charge calculation in the right hand side of Poisson's equation (1.4). This in turn will induce some oscillations in the calculation of the electric field.
On Figure 3.7, we compare the axial profiles of the magnitude of the electric field on a "coarse" and "fine" mesh with the ISG and the UNO3 scheme at t=2.5 ns zoomed on $x \in [0.25 \text{ cm} : 0.35 \text{ cm}]$ where the peaks of electric field are axially located. At t=2.5 ns the values of peaks of electric field are very close. On the other hand we demonstrate here that in the simulation with the UNO3 scheme the profiles coming from either the "coarse" or the "fine" mesh are almost identical. These results show

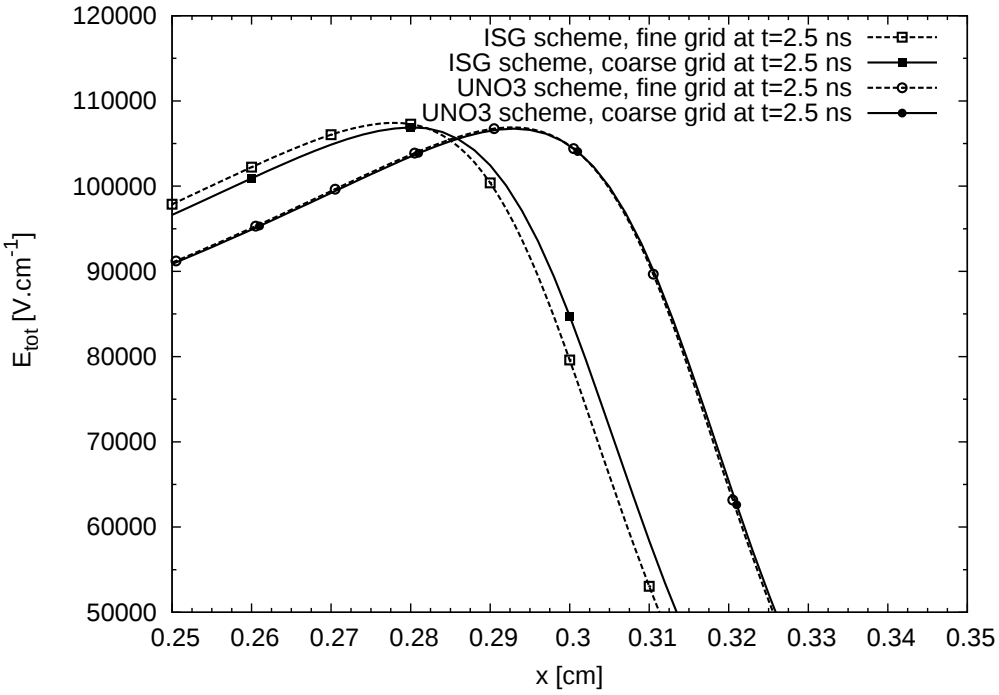

Figure 3.7: *Axial profiles of the magnitude of electric field on a coarse and fine mesh with the ISG and the UNO3 scheme at t=2.5 ns zoomed on* $x \in [0.25\text{ cm} : 0.35\text{ cm}]$.

that the UNO3 scheme is able to reproduce the same profile with less points or with a lower resolution. On the other hand, in the case of simulations with the ISG scheme, the peaks of the electric field are not axially at the same location and their magnitude are not exactly the same. On a "coarser" mesh, the loss of resolution induces a lower electric field and slightly slows down the discharge propagation compared to the simulation with ISG on the "fine" mesh.

3.4 Conclusion

In this chapter, we have demonstrated on a 1D constant velocity convection test case, that the third order UNO3 scheme is as accurate as the third order ULTIMATE QUICKEST convection scheme with a lower computational cost. We have also demonstrated that the UNO3 scheme is non oscillatory and always gives positive density values. By construction, the UNO3 scheme can be used on uniform and non uniform meshes.
To solve the drift-diffusion equations in our discharge model, we have splitted the resolution with the UNO3 scheme for the convection part with

a classical second order accurate scheme for the diffusion part. Then, we tested the performances of the UNO3 scheme on the 2D test-case TC-2 and compared the robustness of the UNO3 scheme with the ISG scheme. We have shown that the use of the UNO3 scheme increases the general robustness and accuracy of the streamer discharge code and so the UNO3 scheme can be successfully used in 2D streamer discharge modelling.

Chapter 4

Domain decomposition and numerical strategy of the new discharge code

4.1 Introduction

In this chapter we present a new hybrid MPI-OPENMP discharge code that integrates the iterative solver SMG presented in Chapter 2 (section 2.3) and the convection scheme UNO3 presented in Chapter 3 (section 3.2.1). In section 4.2 we present the domain decomposition strategy for the complete MPI-OPENMP implementation. Then we carry out a performance analysis of the MPI only implementation as well as a performance analysis of the MPI OPENMP implementation of the code. In section 4.3, to summarize, we present the different versions of the discharge code and their respective use in the different chapters of this thesis.

4.2 Domain decomposition and hybrid parallelization (MPI-OPENMP)

In this section we present a new version of the code fully parallelized developed on the "igloo" cluster. As mentioned in section 2.2, an OPENMP implementation has only a limited capability to speed up the calculation as the number of possible shared memory threads on a node on "igloo" is limited to 12. So for the small computational domain as for the TC-1, this implementation was sufficient. But for larger simulation domain as for TC-2, it was necessary to use more invasive changes in the code structure to extend the parallel capabilities of the code.

Implementing OPENMP protocols in a sequential code did not require to change the structure of the code. But for an MPI-OPENMP implementation with domain decomposition, it was necessary to change the structure of the code and then the code was completely rewritten.
There are different strategies to use domain decomposition where on each MPI process a sub domain of the general grid is assigned:

- Choose the number of MPI processes and adjust the mesh in order to have an equivalent balancing workload on each sub domain.
- Create the mesh first and then according to the number of MPI processes requested, create each sub domain (balance of workload not assured).

In this work, we have chosen the second strategy that allows to define the grid and then the MPI implementation creates the sub domain for each MPI process. Of course we do not have a optimal load balance on each MPI processes with this strategy. Doing so was also motivated by the resources available. On the "igloo" cluster, from a run to an other, we may not have access to all the resources required for an optimal simulation run. With the second strategy, we are not dependent on the resources available and the simulated domain does not need to be changed which guarantees that we simulate exactly the same geometry regardless of the resources available.
We must point out here, that writing a full MPI-OPENMP code for streamer discharges was done thanks to the remarkable simplicity to handle the domain decomposition for the Poisson's equation with the HYPRE library. Before showing the performances of the code we give details on the code used in the following sections to simulate the TC-2:

- Poisson's equation and photo-ionization source term (SMG solver with Tol $= 10^{-8}$) with or without the "semi-implicit" scheme (section 2.4)
- Explicit UNO3 scheme (3^{rd} order in time and space) coupled with the MACHO operator for the spatial splitting to solve the convection equation (section 3.2.1)
- Explicit 2^{nd} order in time and space for the diffusion equation (section 3.3.2)
- Explicit 4^{th} order Runge-kutta scheme for the chemistry source term (section 1.3.3)
- 1^{st} order operator splitting method:
  $U^{t+\Delta t} = C^{\Delta t}\, D^{\Delta t}\, R^{\Delta t}\, U^t$,
  where U^t and $U_1^{t+\Delta t}$ are the solution at t and $t+\Delta t$ respectively. $C^{\Delta t}$,$D^{\Delta t}$ and $R^{\Delta t}$ stands for the convection, diffusion and the chemistry operator respectively applied on the duration Δt.

In this chapter, we present the performances of the code without the photo-ionization source term calculation.

4.2.1 Performances of the code with MPI only

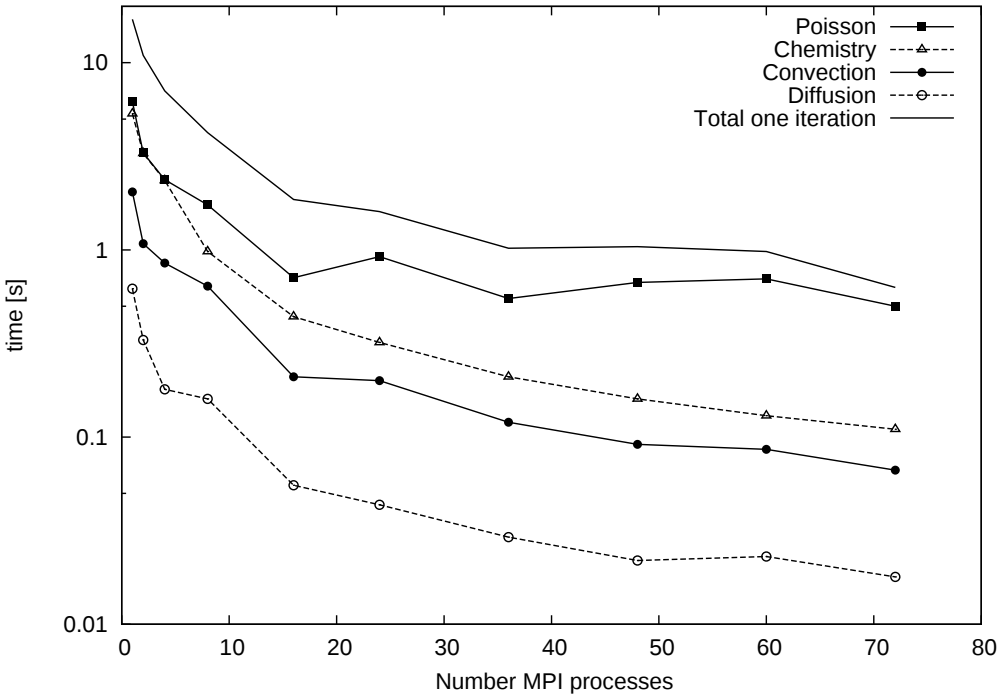

Figure 4.1: *Computational time to compute Poisson, diffusion, convection and chemistry equations and the time for a complete time-step depending on the number of MPI processes for the TC-2 where* $\mathrm{n_x} \times \mathrm{n_r} = 3353 \times 1725$

In Figure 4.1, we present the computational time to compute Poisson, diffusion, drift and chemistry equations and the time for a complete time-step depending on the number of MPI processes for the TC-2.
Figure 4.1, shows that no matter the number of MPI processes used, the calculation of Poisson's equation is the most expensive equation to solve, followed in order by the chemistry, convection and diffusion equations. If only one MPI process is used, it takes 17.05 s for one time-step. On the other hand if 72 MPI processes are used, it will only take 0.63 s for one time-step. On Figure 4.2, we present the speed-up for Poisson, diffusion, convection and chemistry equations and the speed-up for a complete time-step depending on the number of MPI processes for the TC-2. We can see that the general speed-up is increasing. For 72 MPI processors,

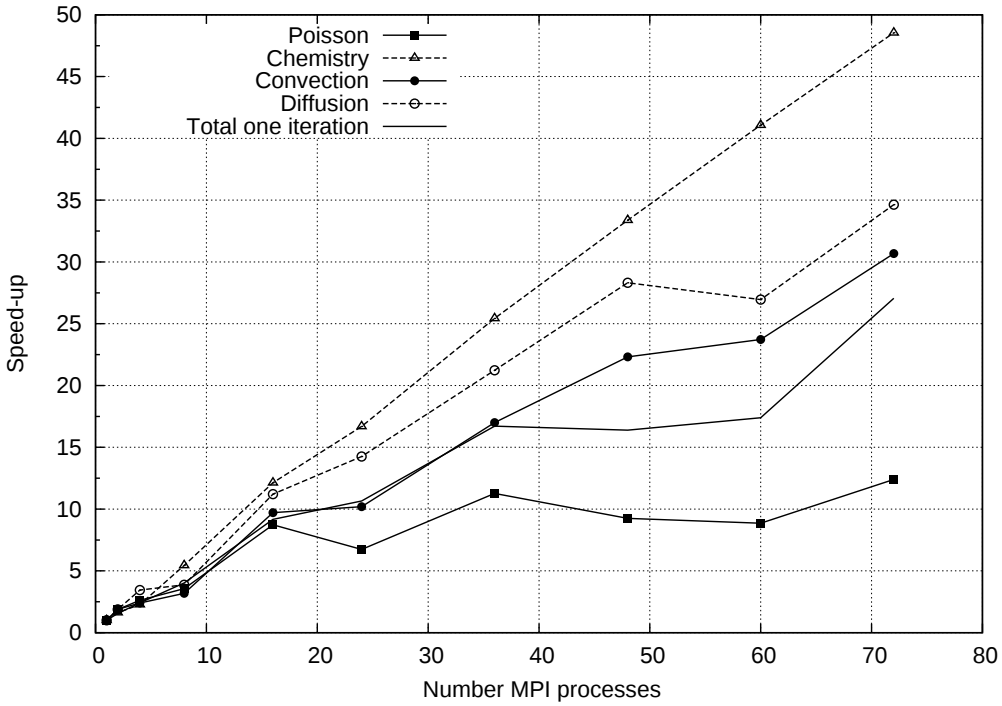

Figure 4.2: *Speed-up for Poisson, diffusion, convection and chemistry equations and the speed-up for a complete time-step depending on the number of MPI processes for the TC-2*

the most scalable part is the speed-up of chemistry (48.5) due to the fact that the calculation is simply local to each cell which is not the case for the rest of the code. The speed-up of diffusion part (34.6) is the second most scalable part of the calculation followed by the the speed-up of convection part (30.7) of the code. The calculation of the Poisson's equation is the less scalable part with a speed-up of 12.4.
On Figure 4.1, we see that most of the computational time is spent in the calculation of Poisson's equation. So it is understandable that the general speed-up of the code is strongly influenced by the calculation of Poisson's equation. Nevertheless, for the simulation TC-2 with $n_x \times n_r = 3353 \times 1725 = 5.78 \times 10^6$ points and 72 MPI processes, it only takes 0.63 s to do one time-step.

4.2.2 Performances of the code with MPI-OPENMP

In the HYPRE library (HYPRE 2007), there is also a version with MPI-OPENMP capabilities. It was then possible to write a hybrid (MPI-

OPENMP) code. We have implemented the classical approach of Fine-grain (FG) for the OPENMP part of the code where we only share the workload between threads in parallel loops with the "DO" directive. An even more intrusive approach called Fine-grain (CG) exists but it introduces more complexity and requires a high amount of deep changes in the code structure (comparable to changing a sequential code to a MPI only version).
The main difficulty to do hybrid parallelization is how the programmer handles the MPI calls in a shared parallel region of the code. There exists three levels of multi-threading support for that:

- MPI THREAD SINGLE:
  OpenMP can not be used
- MPI THREAD FUNNELED:
  MPI calls have to be made outside OPENMP shared parallel region or in OPENMP region but inclosed in $MASTER$ region (only the master thread is allowed to make a MPI call)
- MPI THREAD MULTIPLE:
  No restrictions

Even though the MPI implementation on the "igloo" cluster allows MPI THREAD MULTIPLE support, we found after trials and error that only in inclosed $MASTER$ region we could safely make MPI calls.

MPI x OPENMP	Poisson (s)	Diffusion (s)	Convection (s)	Chemistry (s)	Total (s)
12x1	2.88	0.3	1.41	1.07	5.85
6x2	1.57	0.29	0.57	2.1	5.47
4x3	1.49	0.17	0.43	1.12	4.25
3x4	1.7	0.21	0.51	1.83	5.56

Table 4.1: *Comparison of the time for computing Poisson, diffusion, convection and chemistry equation and the total time for one time-step for a given combination of MPI processes × OPENMP threads = 12 cores for a grid size of* $n_x \times n_r = 3353 \times 1725$ *in TC-2.*

In Table 4.1, for 12 cores available (one node on "igloo") we compare the performance of the code between 12 MPI processes and a combination of MPI processes and OPENMP threads. We show here that better performances are obtained when we increase the number of OPENMP threads per MPI process. The best combination in this case is obtained when using 4 MPI processes combined with 3 OPENMP threads per MPI pro-

cess. We point out also that increasing the number of OPENMP threads per MPI process to values higher than 3 decreases the performance of the code in general. This is due mainly to the Fine Grain implementation.

MPI x OPENMP	Poisson (s)	Diffusion (s)	Convection (s)	Chemistry (s)	Total (s)
72x1	0.5	$1.79\ 10^{-2}$	$6.65\ 10^{-2}$	0.11	0.63
36x2	0.53	$2.68\ 10^{-2}$	0.19	0.17	1.05
24x3	0.4	$3.18\ 10^{-2}$	$7.61\ 10^{-2}$	0.20	0.86
18x4	0.53	$4.67\ 10^{-2}$	0.14	0.38	1.28

Table 4.2: *Comparison of the time for computing Poisson, diffusion, convection and chemistry equation and the total time for one time-step for a given combination of MPI processes x OPENMP threads = 72 cores for a grid size of* $n_x \times n_r = 3353 \times 1725$ *in TC-2.*

In Table 4.2, we see that combining MPI processes and OPENMP threads decreases the efficiency of the code in the case where 72 cores are used. In this case, the MPI only version is faster than any combination of MPI-OPENMP with the same number of cores.

4.3 Conclusion of the numerical strategy for the simulations presented in this thesis

During this thesis the streamer discharge code was gradually parallelized to improve its performance. For example, with the MPI-OPENMP discharge code, we are able to simulate the TC-2 with a grid size of $n_x \times n_r = 3353 \times 1725$ in less than 3 hours compared with the week of calculations required with the parallel OPENMP discharge code with PaStiX.
During this thesis, we have validated the different versions of the code, in particular in comparison to the reference case of the propagation of a positive streamer discharge in air at atmospheric pressure in a point-to-plane geometry (Kulikovsky 1998). In Appendix D, we present the validation of the MPI-OPENMP discharge code. As we have developed several versions of the streamer discharge code during this thesis, we summarize here the different versions of the code used in the following chapters:

- Chapter 5 and 6: For the simulation of a **positive** air discharge in a point to plane geometry with a dielectric obstacle on its path, we

used the sequential legacy code:

- Full explicit code
- MUMPS solver for Poisson's equation and photo-ionization source term
- Explicit Improved Scharfettel-Gummel (ISG) scheme for the convection-diffusion equation
- 4^{th} order Runge-kutta scheme for the chemistry source term
- 1^{st} order operator splitting method: $U^{t+\Delta t} = CD^{\Delta t}\ R^{\Delta t}\ U^t$, where U^t and $U_1^{t+\Delta t}$ are the solution at t and $t+\Delta t$ respectively. $CD^{\Delta t}$ and $R^{\Delta t}$ stands for the convection-diffusion and the chemistry operator respectively applied on the duration Δt.
- Average computational time : 10 days.

Chapter 5 and 7: For the simulation of a **negative** air discharge in a point to plane geometry with a dielectric obstacle on its path, we used the parallel OPENMP code:

- Full explicit code
- PaStiX solver for Poisson's equation and photo-ionization source term
- Explicit Improved Scharfettel-Gummel (ISG) scheme for the convection-diffusion equation
- Explicit 4^{th} order Runge-kutta scheme for the chemistry source term
- 1^{st} order operator splitting method: $U^{t+\Delta t} = CD^{\Delta t}\ R^{\Delta t}\ U^t$, where U^t and $U_1^{t+\Delta t}$ are the solution at t and $t+\Delta t$ respectively. $CD^{\Delta t}$ and $R^{\Delta t}$ stands for the convection-diffusion and the chemistry operator respectively applied on the duration Δt.
- Average computational time : 2 days with 6 OPENMP threads.

Chapter 8: For the comparisons of experimental results with simulations of a positive air discharge in a point to plane geometry with a dielectric obstacle on its path, we used the hybrid parallel (MPI-OPENMP) code:

- Semi-implicit scheme (to remove the dielectric relaxation time-step constraint in equation (1.31))
- HYPRE (SMG solver) library for Poisson's equation and photo-ionization source term
- Explicit UNO3 scheme (3^{rd} order in time and space) coupled

with the MACHO operator for the spatial splitting to solve the convection equation
  - Explicit 2^{nd} order in time and space for the diffusion equation
  - Explicit 4^{th} order Runge-kutta scheme for the chemistry source term
  - 1^{st} order operator splitting method:
    $U^{t+\Delta t} = C^{\Delta t}\, D^{\Delta t}\, R^{\Delta t}\, U^t$,
    where U^t and $U_1^{t+\Delta t}$ are the solution at t and $t+\Delta t$ respectively. $C^{\Delta t}$,$D^{\Delta t}$ and $R^{\Delta t}$ stands for the convection, diffusion and the chemistry operator respectively applied on the duration Δt.
  - Average computational time : 12 hours with 72 MPI processes.

  In chapter 9, we also investigated the dynamics of helium discharges at atmospheric pressure in dielectric tubes. The detailed physical model for helium will be described in this chapter.
- In air, all physical processes studied (convection, diffusion and chemistry) are almost on the same timescale that is why explicit schemes were used in air discharge simulation.
- In helium, the different physical processes have different timescales.
  - In the chemistry model used for helium, fast reactions impose quite low chemistry time-step in the order of $\Delta t_d = 10^{-16}$s. For streamer dynamics that needs to be studied on 50 ns timescale, the 4^{th} order Runge-Kutta scheme is not relevant anymore and the implicit 5^{th} order RADAU5 solver (Hairer and Wanner 1996) was used for the calculation of the chemistry source term.
  - The electron diffusion in helium is much higher than in air compared to the electron mobility, so it requires a finer mesh size for better resolution. But in equation (1.29), the diffusion time-step is proportional to the square of the mesh size and so the diffusion time step is in the order of $\Delta t_d = 10^{-15}$s. For long timescale study, we changed the explicit 2^{nd} order scheme for the diffusion equation to the explicit 4^{th} order ROCK4 (Abdulle 2001) solver with dynamic inner time-step.
  - 1^{st} order operator splitting method:
    $U^{t+\Delta t} = C^{\Delta t}\, D^{\Delta t}\, R^{\Delta t}\, U^t$,
    where U^t and $U_1^{t+\Delta t}$ are the solution at t and $t+\Delta t$ respectively. $C^{\Delta t}$,$D^{\Delta t}$ and $R^{\Delta t}$ stands for the convection, diffusion and the chemistry operator respectively applied on the duration Δt.
  - Semi-implicit scheme (to remove the dielectric relaxation time-step constraint (1.31))
  - HYPRE (SMG solver) library for Poisson's equation and photo-

ionization source term
- Explicit UNO3 scheme (3^{rd} order in time and space) coupled with the MACHO operator for the spatial splitting to solve the convection equation
- Average computational time : one day with 4 MPI processes and 12 OPENMP threads.

Part II

Influence of dielectric surfaces on the propagation dynamics of a discharge at atmospheric pressure

Chapter 5

Study of positive and negative air discharges at atmospheric pressure in a point-to-plane geometry with a dielectric on the cathode

5.1 Introduction

Before studying in chapters 6, 7 and 8 the influence of placing a dielectric plane obstacle in the path of a propagating discharge, as a first step in this chapter, we study the dynamics of an air discharge at atmospheric pressure in a point-to-plane geometry with a dielectric on the cathode plane. As a reference, this configuration will be referred to as cathode dielectric barrier discharge (CDBD) configuration.
In Section 5.2 we present the studied set-up and the model. In Section 5.3, we study the dynamics of impact of a positive streamer discharge on the dielectric surface. Then we study the influence of the relative permittivity and thickness of the dielectric layer on the dynamics of charge deposition on the dielectric surface. In Section 5.4, we study the dynamics of impact of a negative streamer discharge on the dielectric surface and we compare surface discharge dynamics and characteristics for positive and negative discharges.

5.2 Studied CDBD configuration and model formulation

The CDBD discharge set-up is shown in Figure 5.1. The anode is an hyperboloid point, and its shape is given by:

$$\left(\frac{x}{a}\right)^2 - \left(\frac{r}{b}\right)^2 = 1, \tag{5.1}$$

where $a = 0.5$ cm and $b = 0.18$ cm which corresponds to a radius of curvature of $R_c = b^2/a$ =648 μm. The anode tip is located at 5 mm from a grounded metallic cathode plane ($x = 0$ cm). In this chapter, we consider that a constant voltage of $U_a = \pm 13$ kV is applied at the beginning of the discharge simulation. We study the influence of the thickness Δ of the dielectric layer and of its permittivity ε_r on the discharge dynamics. It is important to note that the same anode shape, gap, dielectric characteristics and applied voltage will be used for reignition studies in chapters 6-7 to compare with CDBD results. In this chapter, we have varied Δ in the range $176 - 1000$ μm and ε_r in the range $1 - 2$. For $\Delta = 176\mu$m, the dielectric layer will be referred as thin and for Δ=1 mm as thick.

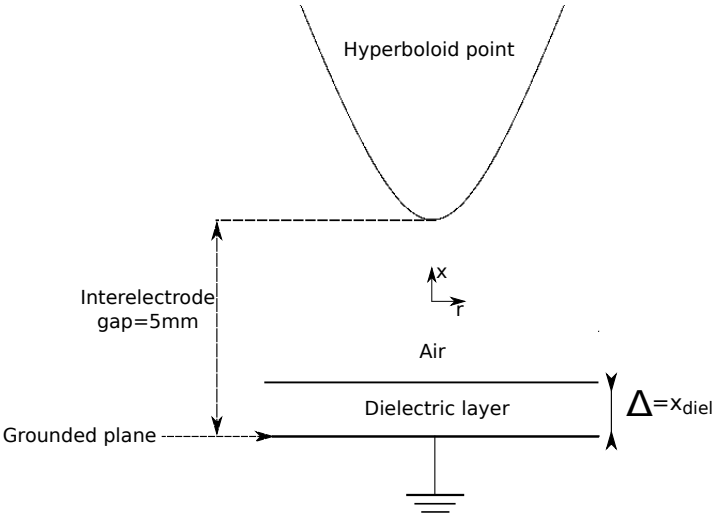

Figure 5.1: *Side view schematics of the discharge set-up. The thickness of the dielectric layer is* Δ*. The axial position of the upper surface of the dielectric layer is* x_{diel}=Δ*.*

As mentioned in chapter 4, the simulations presented in this chapter have been carried out with the LDC code. We have used the improved

Scharfettel-Gummel scheme with $\epsilon_{\mathrm{ISG}} = 0.1$. In (Jánský et al. 2010) it has been checked that this value has a very small influence on the results but allows to remove small oscillations on some cases when compared to simulations with lower values of ϵ_{ISG}. At each gas-dielectric interface, surface charges are obtained by time integrating charged particle fluxes to the different dielectric surfaces and we have also considered secondary emission of electrons by ion bombardment (with a secondary emission coefficient of $\gamma = 0.1$). That relatively high value is a way to take into account roughly other secondary emission processes as photoemission and secondary emission of electrons by impact of metastable molecules. Finally, we have assumed as initial condition, a low uniform density of 10^4 cm^{-3} electrons and positive ions in the air gap above the dielectric layer. All other details of the model are presented in chapter 1.
The computational domain is 1 cm × 17 cm with a Cartesian grid. In the axial direction, close to dielectric/air interfaces, a mesh size of 1 μm is used and then the mesh size is increased following a geometric progression up to 5 μm and is kept constant in the gas gap and close to the electrodes. In the radial direction, a mesh size of 5 μm is used from the axis of symmetry up to $r = 0.3$ cm and then the mesh follows a geometric progression until $r = 17$ cm. As an example, for the results presented on Figure 5.2, with a 176 μm thick dielectric layer on the cathode surface, the grid is $n_x \times n_r = 1535 \times 1000$.

5.3 Simulation of a positive discharge in a point-to-plane geometry with the dielectric layer on the cathode plane

First we consider a thin dielectric layer with a thickness of $\Delta = 176\,\mu$m. Figure 5.2 shows the distributions of the electron density and absolute value of the electric field at t= 4.5, 6 and 9.8 ns for a dielectric with $\varepsilon_{\mathrm{r}} = 2$ and Table 5.1 gives some characteristics of the discharge dynamics. With an initial applied voltage of $\mathrm{U}_a = +13\,$kV, a positive streamer discharge is ignited at $\tau_{\mathrm{ignition}} = 0.8$ ns close to the point and propagates axially in the gap as shown at $t = 4.5$ ns in Figure 5.2. As the streamer front crosses the middle of the air gap, the peak electric field on the axis is 104 kV cm^{-1} and the electron density is $2.8{\times}10^{13}$ cm^{-3}, which are typical values for streamer discharges in air at atmospheric pressure. As already noted in (Célestin et al. 2008; Babaeva and Kushner 2011), we have checked that secondary processes at the dielectric surface have

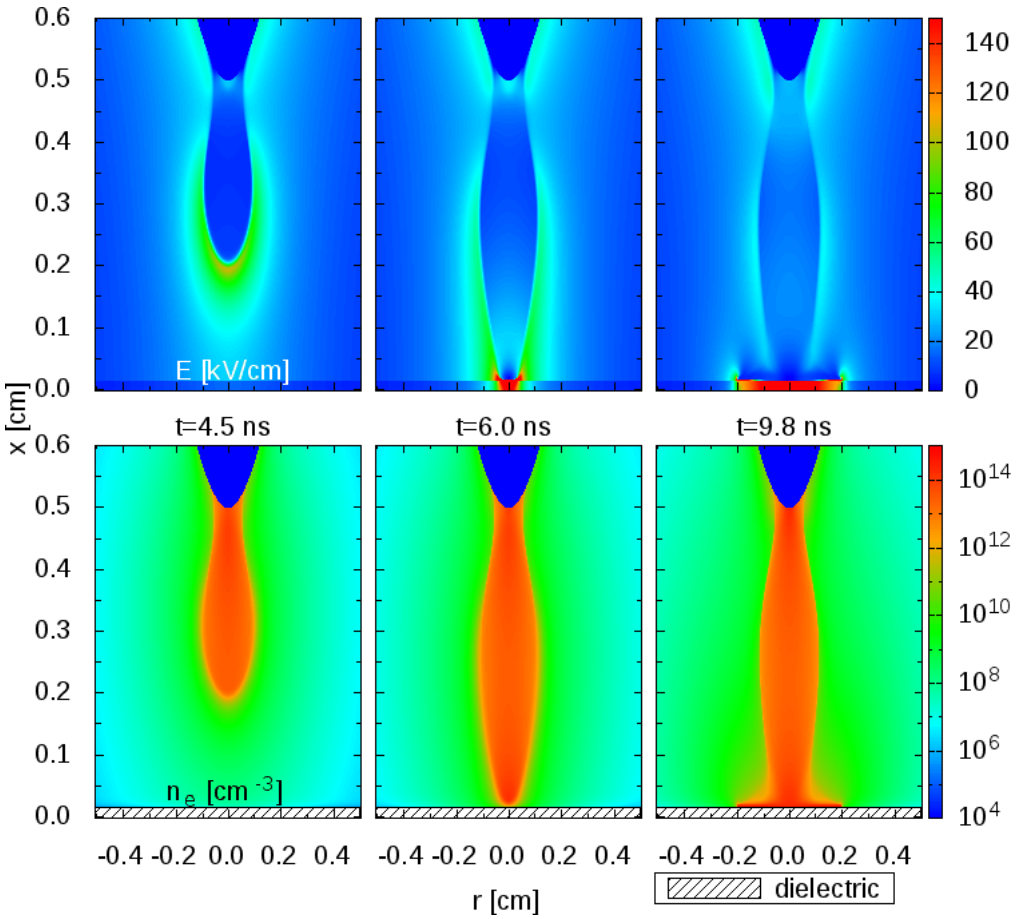

Figure 5.2: *Dynamics of the discharge in the positive CDBD configuration for* $U_a = +13\,\mathrm{kV}$. *The thickness of the dielectric is* $\Delta = 176\,\mu\mathrm{m}$ *and its permittivity is* $\varepsilon_\mathrm{r} = 2$. *Cross-sectional views of the absolute value of the electric field and electron density at* $t = 4.5$, 6 *and* 9.8 *ns. Peak values of the scales of electric field and electron density are of 150 kV* cm^{-1} *and* 10^{15} cm^{-3}, *respectively. Peak values of electric field after the discharge impact on the dielectric are higher and given in the text.*

a negligible influence on the discharge dynamics during its propagation in the gas gap until the discharge is close to the dielectric surface. At t= 5.9 ns, the positive streamer discharge impacts the dielectric. In the following, this time will be referred to as the time of impact τ_{impact} (Table 5.1). We observe here that the electric field in the head of the discharge is directed towards the cathode and so electrons mainly drift towards the head of the streamer discharge and positive ions drift towards the surface of the dielectric. As the electric field in the trailing conductive channel of the streamer is much less than in the streamer head, when the streamer strikes the dielectric surface, most of the applied potential is transferred to the resulting sheath at the dielectric surface, which increases the electric field in the dielectric. Figures 5.3 to 5.5 (top Figures) show the absolute value of the electric field and its local direction at t=5.9 (τ_{impact}), 6.1 and 9.8 ns. For t=τ_{impact} +0.2 ns = 6.1 ns, the peak electric field in the sheath on the discharge axis is of 350 kV cm^{-1} for a sheath thickness of 29 μm and the electric field in the dielectric has a peak value of 175 kV cm^{-1}. After the impact, the streamer discharge spreads along the dielectric surface in agreement with previous works (Célestin et al. 2008; Babaeva and Kushner 2011; Papageorghiou et al. 2009). As we use an axisymmetric approach, the computed surface discharge on the dielectric has a disk shape with a non homogeneous structure: a high radial electric field in its front (peak value of the radial electric field of 184 kV cm^{-1} at t= 9.8 ns) to enable the surface discharge propagation on the dielectric and, a low radial electric field in its channel as shown on Figures 5.3 to 5.5. This high value of the radial electric field is due to the fact after the impact of the discharge on the dielectric surface, the only source of electrons able to drift towards the streamer head are the ones located close to the radial edge of the space charge close to the dielectric surface. Then, as the radial electric field increase, it becomes the front of the discharge that allows the radial propagation of the streamer discharge (from t=6.1 ns to t=9.8 ns on Figures 5.4 to 5.5 (top Figures)). In the surface streamer front at t=9.8 ns, the peak of the radial electric field is located at 36.5 μm in height above the dielectric layer in agreement with (Solov'ev et al. 2008). As shown on Figures 5.4 to 5.5, behind the surface streamer head, the electric field is directed perpendicular to the dielectric surface as already observed in (Babaeva and Kushner 2011). Figure 5.2 and Figures 5.4 to 5.5 show that during the surface discharge propagation, the electric field in the dielectric increases. For t=9.8 ns, the peak value of the electric field in the dielectric layer is of 200 kV cm^{-1}. For the condition of Figure 5.2, t=9.8 ns corresponds to τ_{impact} + 3.9 ns (Table 5.1). In the following, to study surface discharge characteristics for different dielectrics, we will

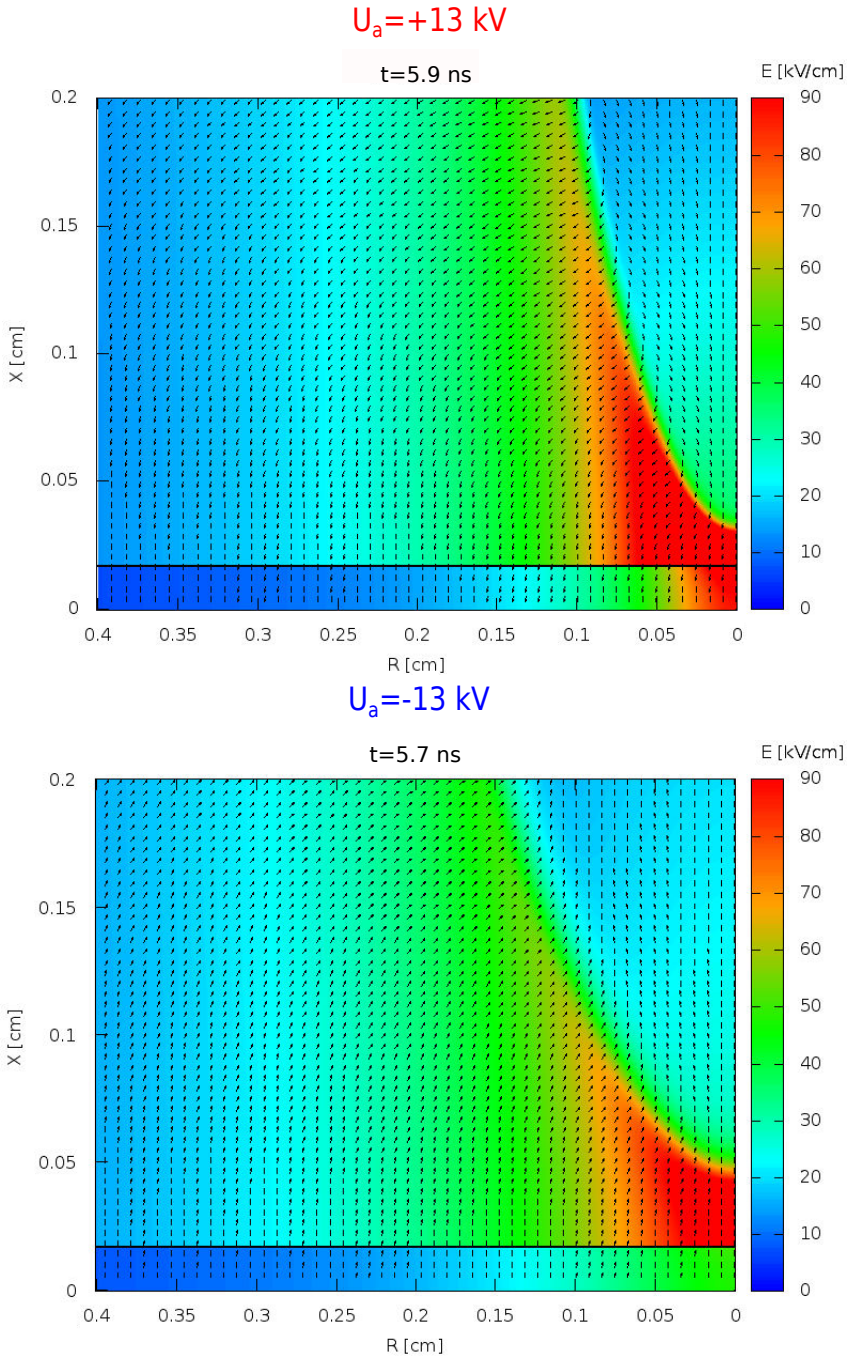

Figure 5.3: *Dynamics of the discharge interaction with the dielectric in the CDBD configuration for* $U_a = +13\,\mathrm{kV}$ *(top Figure) at t=5.9 ns and* $U_a = -13\,\mathrm{kV}$ *(bottom Figure) with* $\Delta = 176\,\mu\mathrm{m}$ *and* $\varepsilon_\mathrm{r} = 2$ *at t=5.7 ns. Cross-sectional views of the absolute value of the electric field is presented and the arrows represent the local direction of the electric field. Peak values of electric field after the discharge impact on the dielectric are higher than 90 kV* cm^{-1} *and given in the text.*

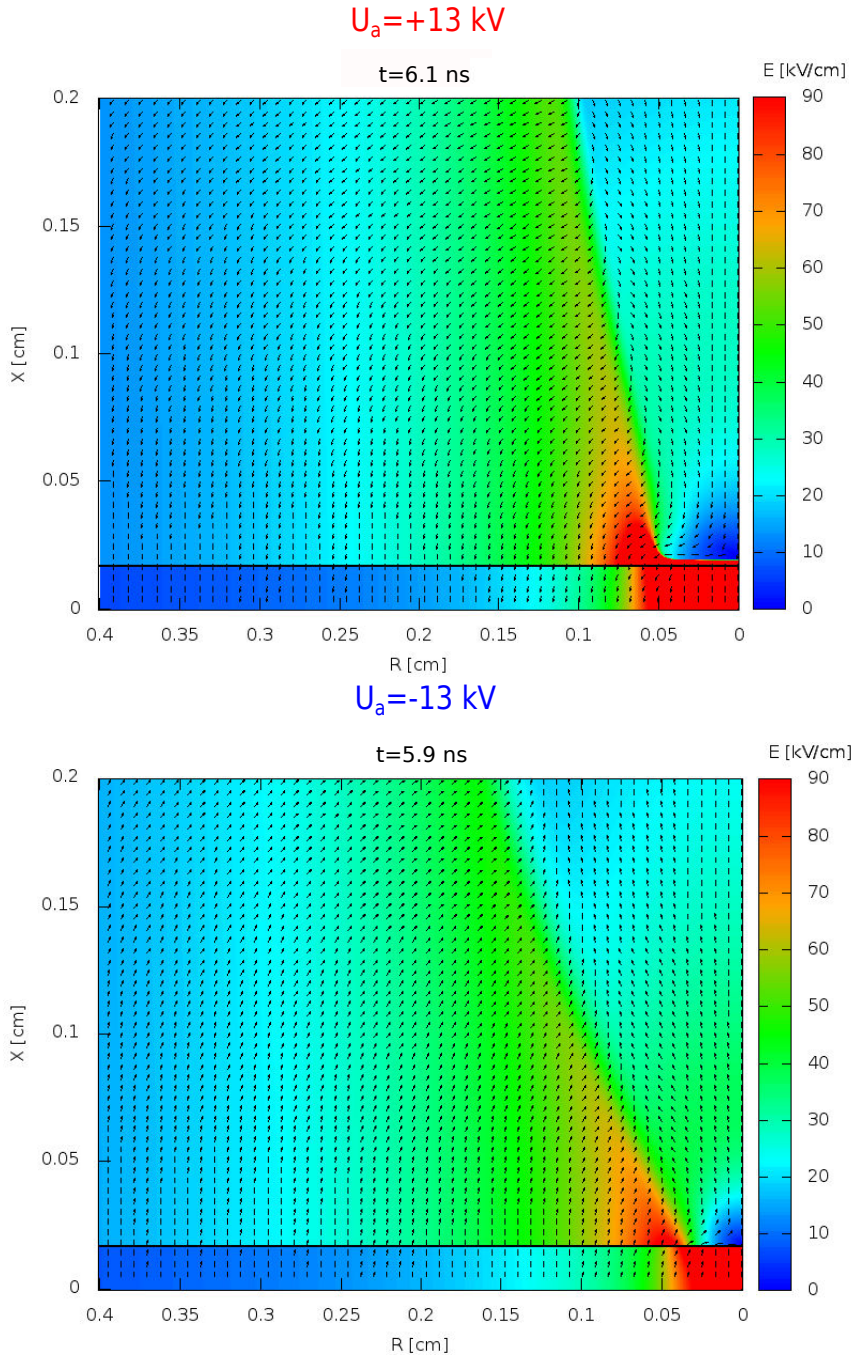

Figure 5.4: *Dynamics of the discharge interaction with the dielectric in the CDBD configuration for* $U_a = +13\,\mathrm{kV}$ *(top Figure) at t=6.1 ns and* $U_a = -13\,\mathrm{kV}$ *(bottom Figure) with* $\Delta = 176\,\mu\mathrm{m}$ *and* $\varepsilon_\mathrm{r} = 2$ *at t=5.9 ns. Cross-sectional views of the absolute value of the electric field is presented and the arrows represent the local direction of the electric field. Peak values of electric field after the discharge impact on the dielectric are higher than 90 kV cm*$^{-1}$ *and given in the text.*

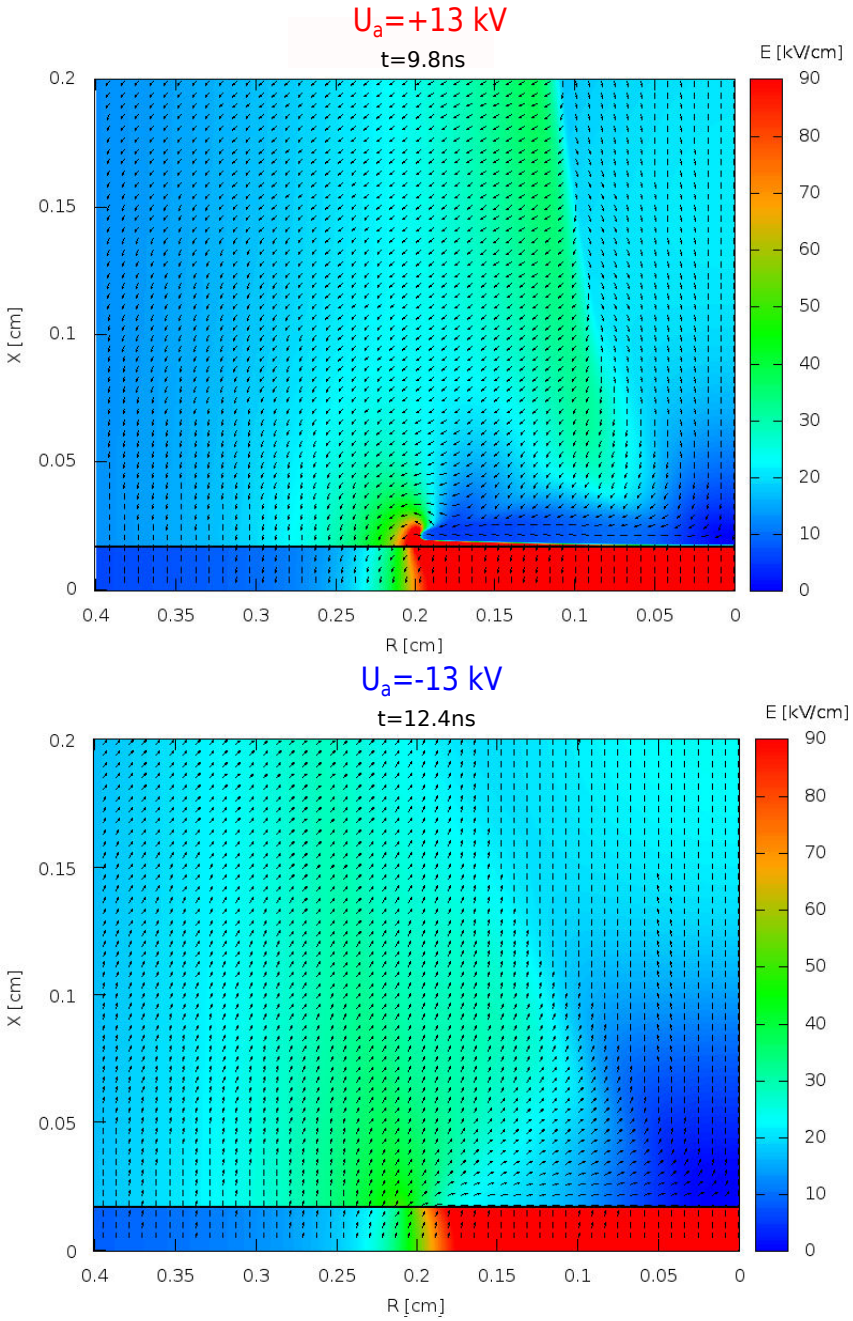

Figure 5.5: *Dynamics of the discharge interaction with the dielectric in the CDBD configuration for* $U_a = +13\,\mathrm{kV}$ *(top Figure) at t=9.8 ns and* $U_a = -13\,\mathrm{kV}$ *(bottom Figure) with* $\Delta = 176\,\mu\mathrm{m}$ *and* $\varepsilon_\mathrm{r} = 2$ *at t=12.4 ns. Cross-sectional views of the absolute value of the electric field is presented and the arrows represent the local direction of the electric field. Peak values of electric field after the discharge impact on the dielectric are higher than 90 kV* cm^{-1} *and given in the text.*

compare results after the same delay after impact on the dielectric, at the time $\tau_s = \tau_{\text{impact}} + 3.9$ ns. As the positive surface streamer propagates, it charges the dielectric surface with positive charges. Figure 5.6(a) shows the time evolutions of the radial profiles of surface charges up to t=16 ns for the condition of Figure 5.2. The vertical arrows show the radial position of the surface streamer front R_{front} (corresponding to the peak of the radial electric field) at t= 9.8 and 16 ns. At t=9.8 ns, we have R_{front} =0.2 cm and at t=16 ns, R_{front} =0.31 cm. We note that the positive surface charge increases behind the surface streamer front and as proposed by (Akishev et al. 2011), the local dynamics of surface charging behind the surface streamer front can be considered as the charging of a local resistor-capacitor circuit element. As the surface discharge spreads along the dielectric, Figure 5.6(a) shows that the positive surface charge increases and expands radially on the dielectric surface. For the condition of Figure 5.6(a), we note that the maximum of the surface charge is close to the discharge axis and decreases as r increases. Close to the discharge axis, after the streamer impact on the dielectric, Figure 5.6(a) shows that the surface charge increases rapidly up to about 12 ns and then increases much slower. In particular, at t= 9.8 ns, Figure 5.6(a) shows the radial profile of surface charges on the dielectric surface for the same time as the distributions of electron density and electric field in Figure 5.2. It is interesting to note that the radial profile of surface charges at t=9.8 ns corresponds to a total amount of positive surface charges of 0.74 nC (Table 5.1).

In this work, we have calculated the velocity of the surface discharge spreading on the dielectric based on the radial movement of the location of the maximum radial electric field in the surface discharge front. We have computed this velocity for $r \geq 0.1$ cm, when the surface discharge has a stable propagation on the surface but for $r \leq 0.3$ cm to calculate the velocity in the fine mesh area. Figure 5.7 shows the velocity of the surface discharge as a function of the radial position r for the condition of Figure 5.2. We note that the velocity is about $5{\times}10^7$ cm s^{-1} at $r = 0.11$ cm and decreases as the discharge expands radially down to $1.6{\times}10^7$ cm s^{-1} at $r = 0.3$ cm. Similar values of surface streamer velocity on a dielectric were found in a point-to-plane dielectric geometry in (Célestin et al. 2008) and in plane-plane dielectric barrier discharges (Babaeva and Kushner 2011), (Papageorghiou et al. 2009). The decrease of the surface discharge velocity as it propagates on the dielectric surface has been also obtained in (Papageorghiou et al. 2009). To study the influence of the permittivity of the dielectric on the discharge dynamics, we have carried out simulations in the limit case with $\varepsilon_{\text{r}} = 1$. Table 5.1 shows that the ignition time is the

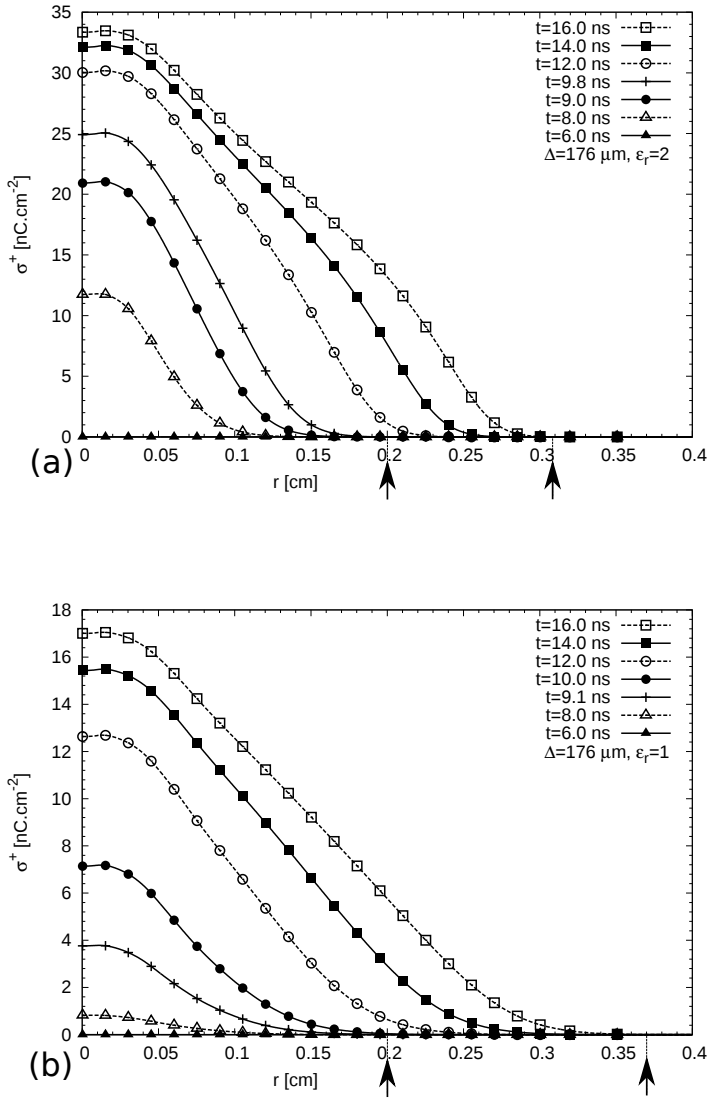

Figure 5.6: *Time evolutions of radial profiles of the positive surface charge on the dielectric for the positive CDBD configuration for* $U_a = +13\,\mathrm{kV}$. *The dielectric thickness is* $\Delta = 176\,\mu\mathrm{m}$ *with* $\varepsilon_\mathrm{r} = 2$ *(a) and* $\varepsilon_\mathrm{r} = 1$ *(b). The arrows indicate the position of the surface streamer front at* $t = 9.8$ *ns (a) and* $t = 9.1$ *ns (b) and for both cases at* $t = 16$ *ns.*

same as for $\varepsilon_r = 2$ and that the time of impact on the dielectric surface is slightly increased as ε_r decreases. Indeed, for a fixed geometry, the increase of ε_r, increases the capacitance of the dielectric on the cathode which is proportional to ε_r. For a sphere-plane geometry, an analytical expression of the capacitance of the interelectrode gap is given in (Durand 1966). Considering a dielectric layer on the plane for a sphere-cathode plane gap of 5 mm, we have checked that the capacitance of the whole interelectrode gap also increases as the permittivity ε_r of the dielectric layer increases. As a consequence, the Laplacian electric field in the air gap increases as ε_r increases which results in a slightly faster propagation of the discharge in the air gap. Figure 5.6(b) shows the time evolutions of the radial profiles of surface charges on the dielectric surface with $\varepsilon_r = 1$. We note that the increase of surface charges close to the discharge axis is slower than for $\varepsilon_r = 2$. Consequently the total amount of positive surface charges at $t = \tau_s$ (Table 5.1) increases as ε_r increases. For $\varepsilon_r = 2$, at $t = 9.8$ ns the surface discharge front is located at $R_{\text{front}} = 0.2$ cm (Figure 5.2). For $\varepsilon_r = 1$, we have checked that the surface discharge front is at the same radial position at $t = 9.1$ ns. For $t = 16$ ns, for $\varepsilon_r = 2$, $R_{\text{front}} = 0.31$ cm and for $\varepsilon_r = 1$, $R_{\text{front}} = 0.37$ cm. Figures 5.6 (a) and (b) show the radial surface charges for these times for both values of ε_r. We note that the increase of the surface charge behind the surface discharge front is smaller for $\varepsilon_r = 1$ than for $\varepsilon_r = 2$. This seems to indicate a faster local charging of the dielectric surface by the surface discharge as ε_r increases. For a fixed geometry, we have checked that the increase of ε_r results in the increase of the electric field in the sheath over the dielectric surface after the streamer impact, in agreement with (Babaeva and Kushner 2011). As a consequence, as ε_r increases, the charge deposited on the dielectric surface has to be higher to shield the higher electric field in the sheath.
Figure 5.7 compares the velocity of the surface discharge for $\varepsilon_r = 1$ and $\varepsilon_r = 2$. We note that this velocity increases as ε_r decreases, as already observed for air discharges propagating in thin dielectric tubes at atmospheric pressure (Jánský et al. 2010; Jánský et al. 2011). Figures 5.6 and 5.7 show that the faster local charging of the dielectric surface as ε_r increases, corresponds to a slower propagation of the surface discharge on the dielectric.

To further study the influence of ε_r, we have carried out simulations with $\varepsilon_r = 1$ and 2 for a thick dielectric layer with a thickness of $\Delta = 1$ mm. As for the thin case, Table 5.1 shows that for a thick dielectric, the impact time decreases as ε_r increases and that the total surface charge deposited

ε_r	1	2	2	1	2
$\Delta(\mu m)$	176	176	352	1000	1000
ε_r/Δ (m^{-1})	5680	11360	5682	1000	2000
$\tau_{ignition}$ (ns)	0.8	0.8	0.7	0.8	0.7
τ_{impact} (ns)	6.1	5.9	5.7	5.7	4.7
τ_s=τ_{impact}+3.9 (ns)	10	9.8	9.6	9.6	8.6
R_{front} (cm) at $t = \tau_s$	0.23	0.20	0.22	0.27	0.26
Q_t^+ (nC) at $t = \tau_s$	0.19	0.74	0.29	4.5×10^{-3}	4.8×10^{-2}

Table 5.1: *For the positive CDBD configuration with $U_a = +13\,kV$: Influence of the dielectric thickness (Δ) and permittivity (ε_r) on $\tau_{ignition}$, the ignition time of the discharge, τ_{impact}, the time of impact of the discharge on the dielectric, $\tau_s = \tau_{impact} + 3.9$ ns, R_{front} the radial position of the surface streamer front at τ_s and Q_t^+, the total surface charge on the dielectric surface at τ_s.*

on the surface at $t = \tau_s$ increases as ε_r increases. Furthermore, Figure 5.7 shows that the velocity of the surface discharge increases as ε_r decreases. Then, Table 5.1 and Figure 5.7 allow also to compare discharge characteristics for a given ε_r and different values of Δ. As expected, an increase of Δ for a given ε_r, decreases the time of the discharge impact on the dielectric. Indeed, for a given interelectrode gap, as Δ increases, the size of the air gap decreases and then the discharge has to propagate on a smaller distance before impacting the dielectric surface. It is interesting to note that, as Δ increases, the capacitance of the dielectric layer on the cathode decreases as it is inversely proportional to Δ. Conversely, as the interelectrode gap is fixed, the capacitance of the air gap and the capacitance of the whole interelectrode gap increase as Δ increases and then, the time of impact of the discharge on the dielectric plane decreases. Table 5.1 shows that the total amount of surface charges deposited on the surface at $t = \tau_s$ decreases as Δ increases for a given ε_r, and then as the capacitance of the dielectric layer on the cathode decreases. Then, to study more precisely the influence of the capacitance of the dielectric layer on the discharge dynamics, we have calculated the ratio ε_r/Δ for the different cases studied in Table 5.1. Furthermore, we have added results for a dielectric layer of $\varepsilon_r = 2$ and $\Delta = 352$ μm which has the same value of the ratio ε_r/Δ as the case $\varepsilon_r = 1$ and $\Delta = 176$ μm. It is interesting to note on Figure 5.7 that the velocity of the surface discharge is equal for these two cases, agreeing with the theory developed in (Akishev et al. 2013a) where the surface streamer velocity is proportional to the ratio ε_r/Δ. Furthermore, for all cases studied in this section, Figure 5.7 shows that the velocity of the surface discharge depends on the value of the capacitance of the

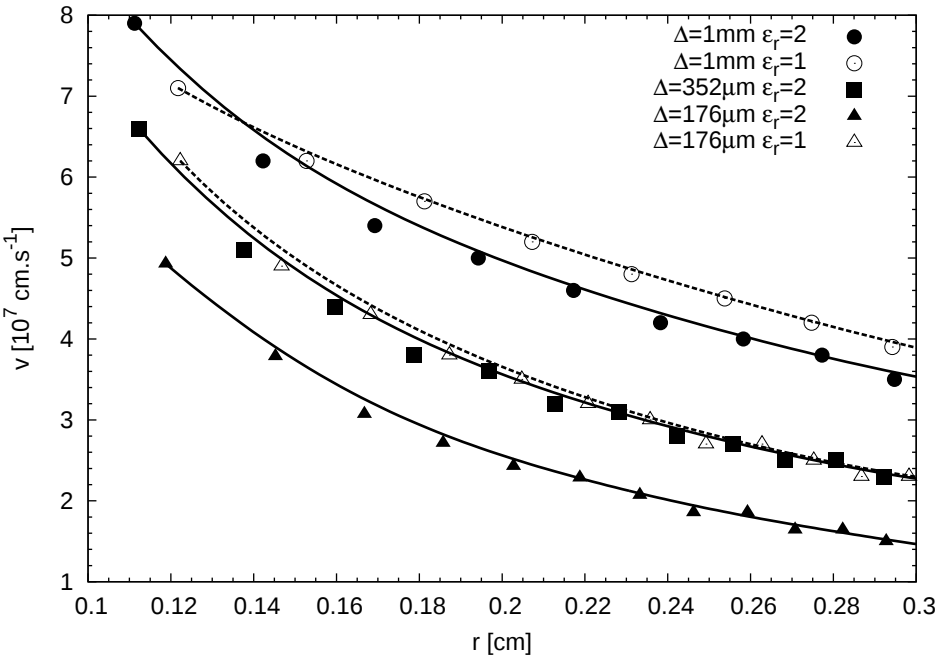

Figure 5.7: *For the positive CDBD configuration with $U_a = +13\,\mathrm{kV}$: Influence of the thickness (Δ) and permittivity (ε_r) of the dielectric layer on the velocity of the surface streamer front.*

dielectric layer on the cathode and decreases as its capacitance increases. Conversely, Table 5.1 shows that the amount of charges deposited by the surface discharge on the dielectric at $t = \tau_s$ is not directly related to the value of the capacitance of the dielectric layer. Indeed, if we compare the two cases with the same value of the ratio $\varepsilon_\mathrm{r}/\Delta$, we note that the amount of surface charges is higher for the case $\varepsilon_\mathrm{r} = 2$ and $\Delta = 352$ μm than for the case $\varepsilon_\mathrm{r} = 1$ and $\Delta = 176$ μm. These results seem to indicate that for the same value of the capacitance of the dielectric layer, the surface charging is higher for a higher value of the permittivity of the dielectric in contact with the discharge. For a plane-plane DBD in nitrogen at atmospheric pressure, (Golubovskii et al. 2006) also varied the thickness and permittivity of dielectrics on electrodes to compare cases with the same capacitance. Their study was dedicated to the conditions of discharge homogeneity and then is different from ours. However, it is interesting to note that they showed that the discharge homogeneity depends on the permittivity of the dielectric in contact with the discharge, for the same value of the capacitance of the dielectrics on the electrodes.

Finally, for all cases studied in this section, Table 5.1 shows that when the capacitance of the dielectric is increased either in increasing ε_r for a

given Δ, or for a given ε_r in decreasing Δ, the amount of surface charges increases. This more significant surface charging slows down the surface streamer propagation.
In conclusion, we have shown that after the impact of a positive discharge with the dielectric layer on the cathode plane, the positive discharge starts to spread on the dielectric surface and charge the surface of the dielectric with positive surface charges. We have also shown that by increasing the capacitance of the dielectric layer (either by increasing its relative permittivity or decreasing its thickness), more charges are deposited and the radial velocity of the surface discharge is decreased.

5.4 Study of the influence of the polarity of the applied voltage on the discharge dynamics and structure

To compare with the results obtained in the previous section for a positive polarity, in this section, we present discharge simulations in a CDBD configuration for a negative constant applied voltage of $U_a = -13\,kV$ at the point electrode.
Figure 5.8 shows the distributions of the electron density and absolute value of the electric field at t= 4.5, 5.7 and 9.6 ns for a thin dielectric layer with $\varepsilon_r = 2$ and Table 5.2 gives some characteristics of the discharge dynamics. With an initial applied voltage of $U_a = -13\,kV$, a negative streamer discharge is ignited at $\tau_{ignition} = 0.5$ ns close to the point and propagates axially in the gap as shown at $t = 4.5$ ns in Figure 5.8.
First it is interesting to compare the influence of the polarity of the applied voltage on the ignition and propagation of the discharge before it impacts the dielectric surface. In Table 5.2 for a thin dielectric layer with $\varepsilon_r = 2$, we first note that the discharge is ignited faster (0.5 ns) for a negative applied voltage than for a positive one (0.8 ns). For a negative applied voltage, as shown in Figure 5.8, when the discharge front crosses the middle of the gap, the electric field in the negative streamer head is equal to 80 kV cm^{-1}. For the same condition but for a positive applied voltage, Figure 5.2 shows that the electric field in the head of the positive streamer head is higher and equal to 104 kV cm^{-1}. It is well known that positive and negative streamers have different characteristics (Raizer 1991). Indeed, a negative streamer discharge propagates in the same direction as the drift velocity of electrons, whereas a positive streamer propagates in the opposite direction. As a consequence, a

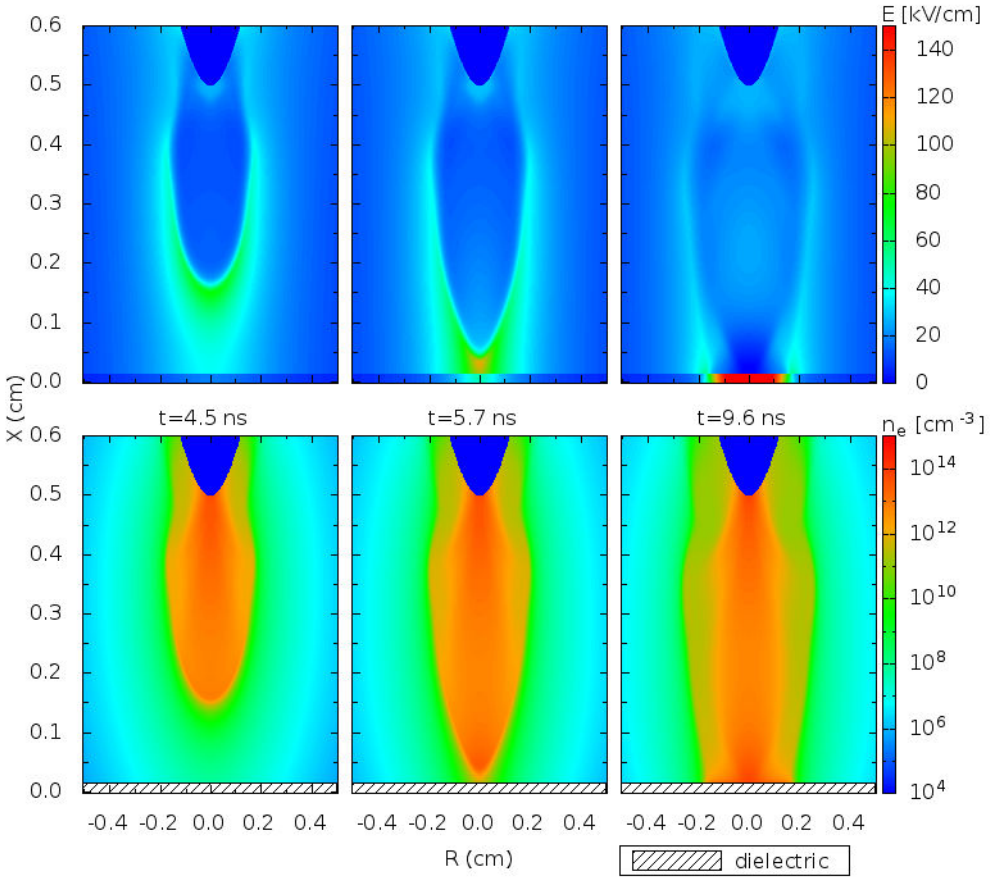

Figure 5.8: *Dynamics of the discharge in the CDBD configuration for an applied voltage of* $U_a = -13\,\mathrm{kV}$. *The thickness of the dielectric is* $\Delta = 176\,\mu\mathrm{m}$ *and its permittivity is* $\varepsilon_r = 2$. *Cross-sectional views of the absolute value of the electric field and electron density at* $t = 4.5$, 5.7 *and* 9.6 *ns. Peak values of the scales of electric field and electron density are of 150 kV* cm^{-1} *and* 10^{15} cm^{-3}, *respectively.*

higher electric field is required in a positive streamer head, in comparison to a negative one, to sustain the streamer discharge propagation. For the small 5 mm gap considered in this work, Table 5.2 shows that the duration of the discharge ignition and propagation before the impact is about the same with for the negative case τ_{impact}=5.7 ns and for the positive case τ_{impact}=5.9 ns.

U_a	13 kV	-13 kV	13 kV	-13 kV
ε_r	1	1	1	1
$\Delta(\mu m)$	176	176	1000	1000
τ_{ignition} (ns)	0.8	0.5	0.8	0.5
τ_{impact} (ns))	6.1	5.9	5.7	5.2
τ_s=τ_{impact}+3.9 (ns)	10	9.8	9.6	9.1
R_{front} (cm) at $t = \tau_s$	0.23	0.19	0.27	0.23
Q_t (nC) at $t = \tau_s$	+0.19	-1.69	$+4.5\times10^{-3}$	-1.18
U_a	13 kV	-13 kV	13 kV	-13 kV
ε_r	2	2	2	2
$\Delta(\mu m)$	176	176	1000	1000
τ_{ignition} (ns)	0.8	0.5	0.7	0.4
τ_{impact} (ns))	5.9	5.7	4.7	4.1
τ_s=τ_{impact}+3.9 (ns)	9.8	9.6	8.6	8.0
R_{front} (cm) at $t = \tau_s$	0.20	0.16	0.26	0.22
Q_t (nC) at $t = \tau_s$	+0.74	-1.93	$+4.8\times10^{-2}$	-1.75

Table 5.2: *For the CDBD configuration: Influence of the dielectric thickness (Δ), permittivity (ε_r) and polarity of the applied voltage (U_a) on τ_{ignition}, the ignition time of the discharge, τ_{impact}, the time of impact of the discharge on the dielectric, $\tau_s = \tau_{\text{impact}} + 3.9$ ns, R_{front} the radial position of the surface streamer front at τ_s and Q_t, the total surface charge on the dielectric surface at τ_s.*

On Figure 5.8 at τ_{impact}=5.7 ns, the negative streamer discharge impacts the dielectric surface and the discharge axial propagation is stopped. Figures 5.3 to 5.5 (bottom Figures) show the interaction of the negative discharge with the dielectric surface at t=5.7 (τ_{impact}), 5.9 and 12.4 ns. In the negative case, the electrons are the ones that mainly impact the dielectric surface thus depositing negative surface charges. We have observed on the axis of symmetry, that at t=τ_{impact}+0.1 ns, the negative surface charge on the dielectric surface is high enough to reverse the electric field close to the dielectric surface. Therefore, we have studied the influence of allowing or not electrons deposited on the dielectric surface

to be released into the gas phase depending on the drift velocity calculated at the air/dielectric interface. We found that in the negative CDBD configuration, with both boundary conditions, the sheath is formed very rapidly and at t=τ_{impact} + 0.2 = 5.9 ns the electric field on the axis of symmetry is very low (E< 1kV cm^{-1}) close to the dielectric surface. Then, at t=5.9 ns, the radial electric field at the radial edge of the space charge increases in amplitude which enables the start of the radial propagation of a surface discharge on the dielectric. Figures 5.4 to 5.5 (bottom Figures) show that in the negative case, the location of the maximum value of the radial electric in the radial front of the discharge is at the surface of the dielectric, in agreement with (Gibalov and Pietsch 2000; Solov'ev et al. 2008). Indeed, as soon as the radial front of the negative discharge moves radially, the sheath is formed quickly just behind the front due to the rapid and significant deposition of negative charges on the dielectric surface. That charging can be considered as the charging of a local resistor-capacitor circuit element (Akishev et al. 2013b). If we compare the structures of positive and negative surface discharges during their stable propagation on the dielectric surface (i.e. at t=9.8 ns and t=12.4 ns, on Figure 5.5, we note that in the negative case, the maximum absolute value of the radial electric field at the dielectric surface is equal to -33 kV cm^{-1} whereas in the positive case, the maximum absolute value of the radial electric field is equal to 184 kV cm^{-1} and it is located at 36.5 μm in height above the dielectric layer.

As the negative surface discharge propagates, it charges the dielectric surface with negative charges. Figure 5.9(a) shows the time evolutions of the radial profiles of the absolute values of surface charges up to t = 16 ns for the condition of Figure 5.8. The vertical arrows show the radial position of the negative surface discharge front R_{front} (corresponding to the peak of the radial electric field) at t= 9.6 and 16 ns. We note that the absolute value of the surface charge density increases in time along the dielectric surface. It is interesting to point out that the absolute value of the surface charge density increases faster to higher values for a negative CDBD than for a positive one. For $\Delta = 176\,\mu$m and $\varepsilon_{\text{r}} = 2$, at t=$\tau_{\text{impact}}$+0.1 ns=6 ns on Figure 5.6(a), the maximum value of the positive surface charge density is equal to +2.70 10^{-3} nC cm^{-2} in the positive case whereas in the negative case on Figure 5.9 (a), at t=τ_{impact}+0.3 ns=6 ns the maximum value of the negative surface charge density is equal to -23 nC cm^{-2}. In Table 5.2, at τ_s=τ_{impact}+3.9 ns, for $\Delta = 176\,\mu$m and $\varepsilon_{\text{r}} = 2$, the total amount of charges deposited on the dielectric surface is higher (in absolute value) for the negative case Q_t=-1.93 nC than for the positive one where Q_t=+0.74 nC.

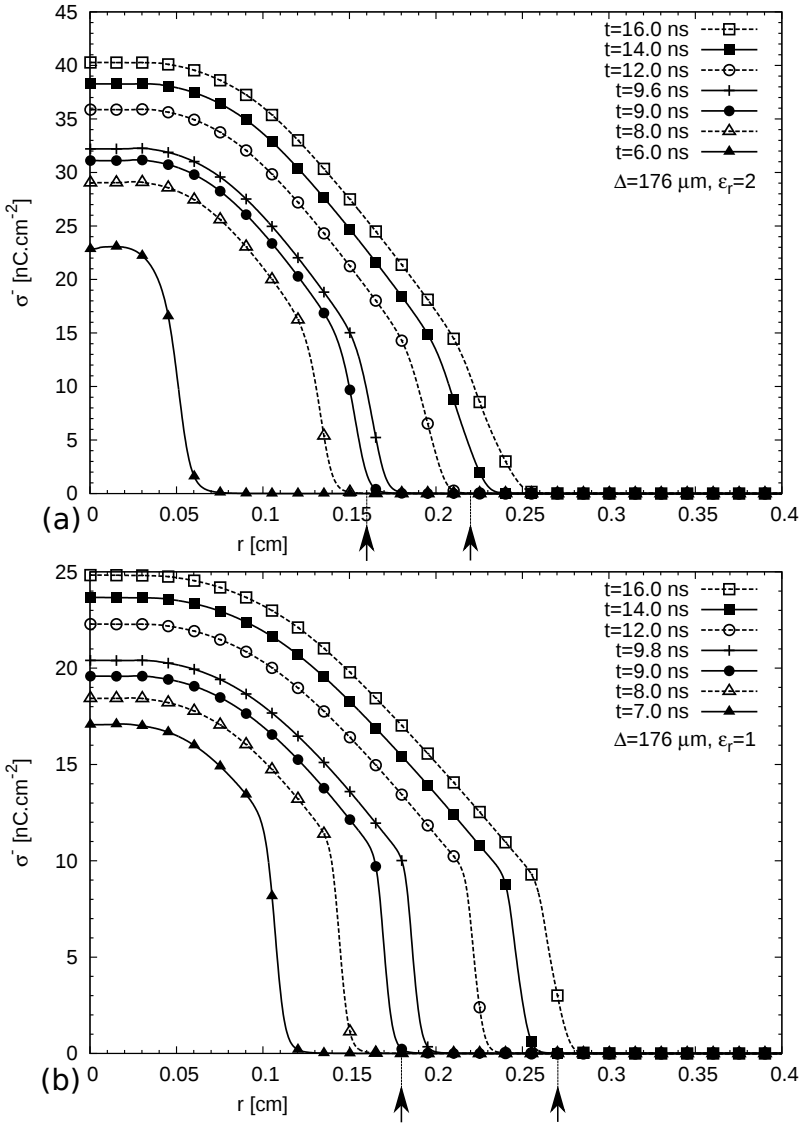

Figure 5.9: *Time evolutions of radial profiles of the absolute value of the surface charge on the dielectric for the negative CDBD configuration for* $U_a = -13\,\mathrm{kV}$. *The dielectric thickness is* $\Delta = 176\,\mu\mathrm{m}$ *with* $\varepsilon_\mathrm{r} = 2$ *(a) and* $\varepsilon_\mathrm{r} = 1$ *(b). The arrows indicate the position of the negative surface discharge front at* $t = 9.6$ *ns (a) and* $t = 9.8$ *ns (b) and for both cases at* $t = 16$ *ns.*

When comparing the radial location of the surface discharge front for positive and negative applied voltages, Table 5.2 shows that for ε_r=2 and $\Delta = 176\,\mu$m, the more charging negative discharge front is located at $R_{\text{front}} = 0.16$ cm at t=τ_s whereas in the less charging positive case, the positive surface discharge front is located at $R_{\text{front}} = 0.20$ cm. So, in agreement with (Gibalov and Pietsch 2000), and as already observed in Section 5.3 for a positive surface discharge, we note that the higher is the amount of charges deposited on the dielectric surface, the slower is the radial velocity of the surface discharge.
On Figure 5.9 (a) and (b), we observe for a negative surface discharge that the amount of surface charges (in absolute value) increases when the relative permittivity ε_r increases from 1 to 2. As expected, Figure 5.9 (a) and (b) shows that at τ_s, R_{front} decreases from 0.19 cm to 0.16 cm (Table 5.2) as ε_r increases from 1 to 2. Figure 5.10 shows the influence of ε_r and

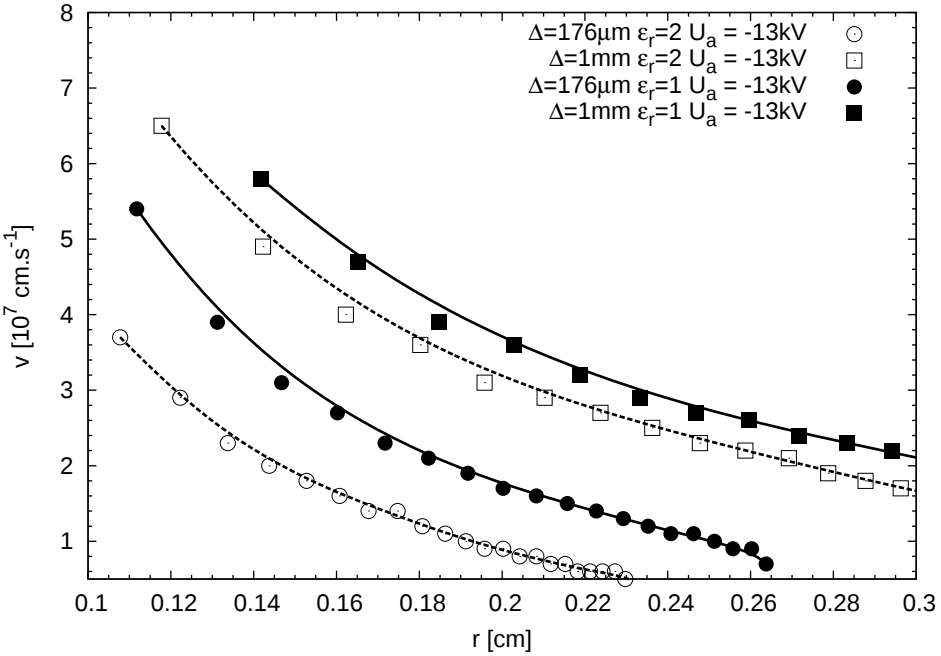

Figure 5.10: *For the negative CDBD configuration with $U_a = -13$ kV: Influence of ε_r and Δ on the velocity of the negative surface streamer front.*

Δ on the velocity of the surface streamer front for U_a=-13 kV. We observe that for a fixed value of Δ, when ε_r increases from 1 to 2, as expected, the radial velocity decreases. Figure 5.10 also shows that when the thickness of the dielectric Δ decreases from 1 mm to 176 μm for a constant ε_r, the radial velocity of the surface discharge decreases. That decrease can be related to the increase of the total amount of surface charges (in absolute

value) from -1.18 nC to -1.69 nC at τ_s for ε_r=1 (and from -1.75 nC to -1.93 nC for ε_r=2).

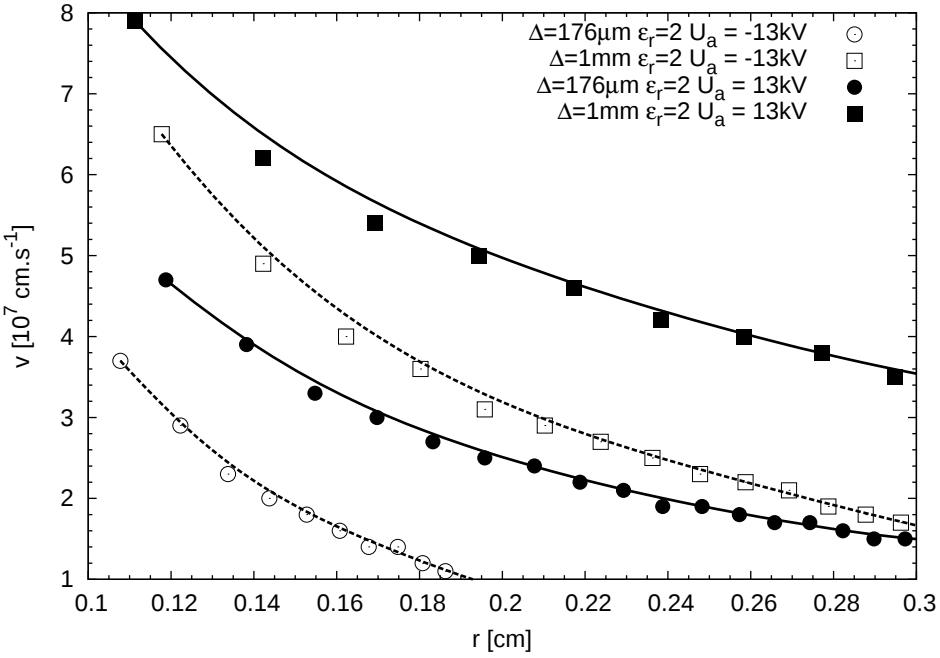

Figure 5.11: *For the CDBD configuration: Influence of the polarity of the applied voltage U_a on the velocity of the surface streamer front for ε_r=2 and $\Delta = 176\,\mu$m − 1 mm.*

Figure 5.11 shows the influence of the polarity of the applied voltage U_a on the radial velocity of the surface discharge for ε_r=2 and for a thickness of $\Delta = 176\,\mu$m - 1 mm. As expected, Figure 5.11 shows that for $r \leq 0.3$ cm, for a given thickness of the dielectric layer, the radial velocity in the case of a negative surface discharge is less than in the case of a positive surface discharge.

In Table 5.2, we have shown that at τ_s=τ_{impact}+3.9 ns (i.e. for t $\leq$ 8 to 10 ns), more negative charges are deposited for a negative surface discharge than for a positive one. Then, we have also studied the differences between the dynamics of surface charging for discharges of both polarities for t> 10 ns. Table 5.3 shows the amount of surface charges at τ_s and t=15 ns and the rate at which the absolute value of the total amount of charges increases from t=τ_s to t=15 ns. We observe that the increase of surface charges is more significant for the case of a positive surface discharge compared to a negative one. At t = τ_s, more charges (in absolute

U_a	13 kV	-13 kV	13 kV	-13 kV
ε_r	1	1	1	1
$\Delta(\mu m)$	176	176	1000	1000
τ_s=τ_{impact}+3.9 (ns)	10	9.8	9.6	9.1
Q_t (nC) at $t = \tau_s$	+0.19	-1.69	$+4.5\times10^{-3}$	-1.18
Q_t (nC) at t=15 ns	+1.41	-3.42	$+7.14\times10^{-2}$	-2.61
Rate of increase	7.42	2.0	15.9	2.2
U_a	13 kV	-13 kV	13 kV	-13 kV
ε_r	2	2	2	2
$\Delta(\mu m)$	176	176	1000	1000
τ_s=τ_{impact}+3.9 (ns)	9.8	9.6	8.6	8.0
Q_t (nC) at $t = \tau_s$	+0.74	-1.93	$+4.8\times10^{-2}$	-1.75
Q_t (nC) at t=15 ns	+2.96	-3.95	+0.84	-4.13
Rate of increase	4.0	2.1	17.5	2.4

Table 5.3: *For the CDBD configuration: Influence of the dielectric thickness (Δ), permittivity (ε_r) and polarity of the applied voltage (U_a) on Q_t, the total surface charge on the dielectric surface at τ_s and at t=15 ns and on the rate of increase of total charge between Q_t at t=15 ns and $t = \tau_s$.*

value) are deposited in the case of a negative surface discharge compared to a positive one. But from τ_s to t=15 ns, we observe that the absolute value of the amount of charges increases at a different rate for negative and positive surface discharges. It is interesting to note that for Δ=1 mm and ε_r=2, the amount of total charges accumulated on the dielectric surface increases by a factor of 17.5 for the positive case (from $+4.8\times10^{-2}$ nC to +0.84 nC) whereas for the negative case the amount of total charges in absolute value increases only by a factor of 2.4 (from -1.75 nC to -4.13 nC). Results show that, the lowest is the amount of surface charges in absolute value at τ_s (which corresponds to most positive cases), the highest is the rate of increase from τ_s to t=15 ns. However, if the amount of surface charges in absolute value is already high ($|Q_t|$>1 nC) at τ_s (which corresponds to most negative cases), the rate of increase is low. Then, for the conditions studied in this work, for $t > 15$ ns, the absolute value of the amount of surface charges deposited by either a positive or a negative surface discharge in a CDBD configuration will be of the same order, in agreement with (Gibalov and Pietsch 2000; Solov'ev et al. 2008).

5.5 Conclusion

The main results obtained in this chapter on the dynamics of an air discharge at atmospheric pressure in the cathode dielectric barrier discharge (CDBD) configuration with a point-to-plane geometry and a dielectric layer on the cathode can be summarized as follows:

- For a positive applied voltage at the point electrode, a positive discharge ignites and propagates in the gap. After the impact of the discharge on the dielectric surface, a positive surface discharge starts spreading along the upper dielectric surface and charging it with positive surface charges. We have shown that the velocity of the surface discharge on the dielectric surface depends on the capacitance of the dielectric layer on the cathode plane and decreases as this capacitance increases. Conversely, the amount of surface charges deposited by the surface discharge on the dielectric surface is not directly related to the value of the capacitance of the dielectric layer. However, the amount of surface charges deposited increases and the surface streamer propagation slows down as the capacitance of the dielectric layer increases either in increasing the permittivity of the dielectric for a given layer thickness, or for a given permittivity in decreasing the layer thickness.
- For a negative applied voltage at the point electrode, a negative streamer discharge ignites at the point and propagates in the gap. After the impact on the dielectric, a negative surface discharge starts spreading on the dielectric surface and charging it with negative surface charges. We have shown that the structure of a negative surface discharge is different from the one of a positive surface discharge. Indeed, for a negative surface discharge, the discharge head is on the dielectric surface and the sheath is formed directly behind the front whereas in the positive discharge case, the radial front is located at a small distance from the dielectric surface and the formation of the sheath is much slower. In the studied CDBD configuration, we have shown that for $t \leq 8$ to 10 ns, the radial velocity of the negative surface discharge is less than the one of a positive surface discharge due to a higher amount (in absolute value) of surface charges deposited. When the permittivity of the dielectric layer increases for a given layer thickness (or for a given permittivity when the layer thickness decreases), the amount of surface charges (in absolute value) increases. It is interesting to point out that the difference between the dynamics of charging of positive and negative surface discharges decreases in time and in the studied CDBD configura-

tion, for $t > 15$ ns, the amount of charges deposited by a positive surface discharge tends to be of the same order (in absolute value) as the one deposited by a negative surface discharge.

Chapter 6

Study of the dynamics of reignition of a positive air discharge at atmospheric pressure behind a dielectric plane obstacle

6.1 Introduction

In this chapter, we study the dynamics of propagation of an air discharge at atmospheric pressure in a point-to-plane configuration with a dielectric layer obstacle placed in the path of the propagating discharge. The objective of this study is to find conditions in which a second discharge may reignite behind the dielectric obstacle. We have used the same geometry of electrodes as in chapter 5 to compare the interaction of the discharge with the dielectric layer when the dielectric is on the cathode or in the gap. It is important to note that in parallel to the presented numerical studies, an experimental study was carried out at the LPGP laboratory in Orsay (France). The simulation of the experimental geometry and the detailed comparison with experiment will be discussed in chapter 8.
The studied point-to-plane geometry and the discharge model are described in section 6.2. In Section 6.3 the interaction of the streamer discharge ignited at the point electrode with a dielectric layer placed in the path of the discharge between electrodes is studied. Then, in Section 6.4, the influence of two closely spaced dielectric layers on the discharge dynamics and reignition is discussed.

6.2 Studied configuration and model

The discharge set-up is shown in Figure 6.1. The electrode geometry and the mesh are the same as in chapter 5. In this chapter, we consider that a constant voltage of U_a=+13 kV is applied at the beginning of the discharge simulation. As in the experiments, an electrically floating dielectric layer, parallel to the plane cathode, is positioned between the electrodes. In Section 6.3, we study the influence of the thickness Δ of the dielectric layer, its permittivity ε_r, its axial position x_{diel} in the gap and its opacity to radiation on the discharge dynamics. In this work, we have varied Δ in the range $176 - 1000$ μm, x_{diel} in the range 0.15 cm − 0.35 cm and ε_r in the range $1 - 5$. Finally in Section 6.4, the reignition dynamics behind two dielectric layers will be presented.

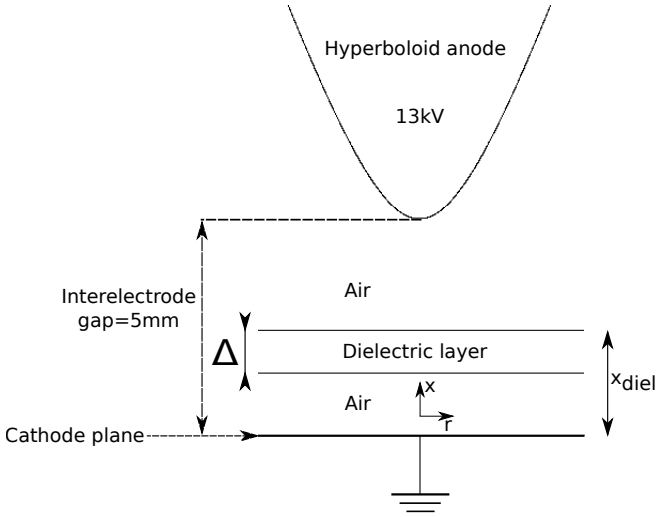

Figure 6.1: *Side view schematics of the discharge set-up. The thickness of the dielectric layer is* Δ*. The axial position of the upper surface of the dielectric layer is* x_{diel}*.*

For the simulations presented in this chapter, as mentioned in Chapter 4, we have used the LDC code. All the details of the model are given in chapter 1.
In section 6.3, the dielectric layer is first considered to be opaque to radiation. Then, the photoionization source term is calculated separately in the two air domains above and below the dielectric layer and boundary conditions for the photoionization source term are used at each dielectric-air interface. To study the influence of the opacity of the dielectric layer on the discharge reignition, we have then considered that the dielectric layer

is transparent to the discharge emission leading to the air photoionization. For this condition, the dielectric layer will be referred to as transparent. In this case, the photoionization source term for air is calculated in the whole computational domain between metallic electrodes.
Finally, for all the simulation results presented in this chapter, we have assumed as initial condition, a low uniform density of 10^4 cm^{-3} of electrons and positive ions in air below and above the dielectric layer.

6.3 Study of the reignition of a positive discharge behind a dielectric plane obstacle

6.3.1 Rreignition dynamics behind a thin and opaque dielectric layer located close to the grounded electrode

In this section, we present simulations of the discharge dynamics for a thin ($\Delta = 176\,\mu$m) and opaque dielectric layer with $\varepsilon_r = 2$ located close to the cathode at $x_{\text{diel}} = 0.15$ cm. First, Figure 6.2 shows the evolution of the initial Laplacian potential on the symmetry axis. As expected the Laplacian potential decreases rapidly in the first air gap (i.e. from the point to the edge of the dielectric) and then decreases linearly in the dielectric and in the second air gap between the dielectric and the cathode.

In comparison to the positive CDBD configuration studied in Section 5.3 with the same dielectric layer, approaching the dielectric close to the anode, decreases the size of the first air gap, which increases slightly the Laplacian electric field close to the point. In the second air gap, the Laplacian electric field is nearly uniform on the discharge axis and has a magnitude of 13.4 kV cm^{-1} which is below the breakdown field in air and then is too low to ignite a discharge in the second air gap. Figure 6.3 shows the distributions of the electron density and the absolute value of the electric field at $t = 4.9, 6.3$ and 7 ns. As expected, Figure 6.3 shows that a streamer discharge is ignited at the point anode and propagates axially in the first air gap towards the dielectric. As the streamer front crosses the middle of the first air gap, the peak electric field on the discharge axis has a magnitude of 114 kV cm^{-1} and the electron density is 4.1×10^{13} cm^{-3}. This first streamer impacts the dielectric at $t = 4.9$ ns. As the first discharge approaches the dielectric surface, the electric field close to the discharge axis in the dielectric and in the air gap below the layer increases. Then avalanches originating from seed electrons, appear in the second air gap, close to the discharge axis. At the time of impact,

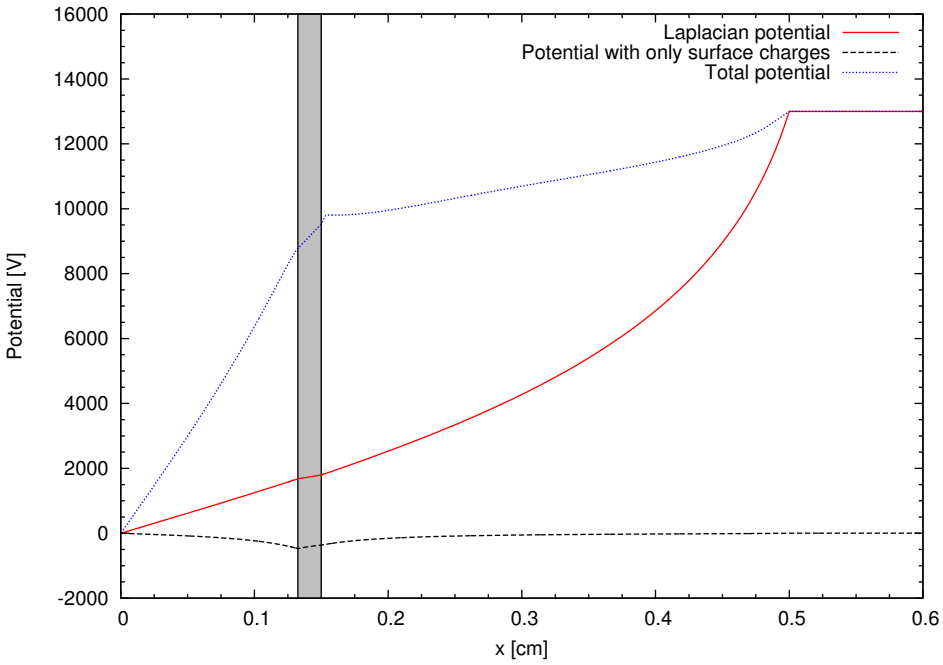

Figure 6.2: *Potential on the symmetry axis for the point-to-plane geometry with a thin and opaque dielectric layer located at* $x_{\text{diel}} = 0.15$ *cm. The applied voltage is* U_a*=+13 kV. The thickness of the dielectric is* $\Delta = 176\,\mu$m *and its permittivity is* $\varepsilon_r = 2$*. Laplacian potential at* $t = 0$ *ns, total potential at* $t = \tau_{\text{reigni}} = 6.3$ *ns and potential calculated in taking into account only surface charges deposited on both faces of the dielectric layer at* $t = \tau_{\text{reigni}}$*.*

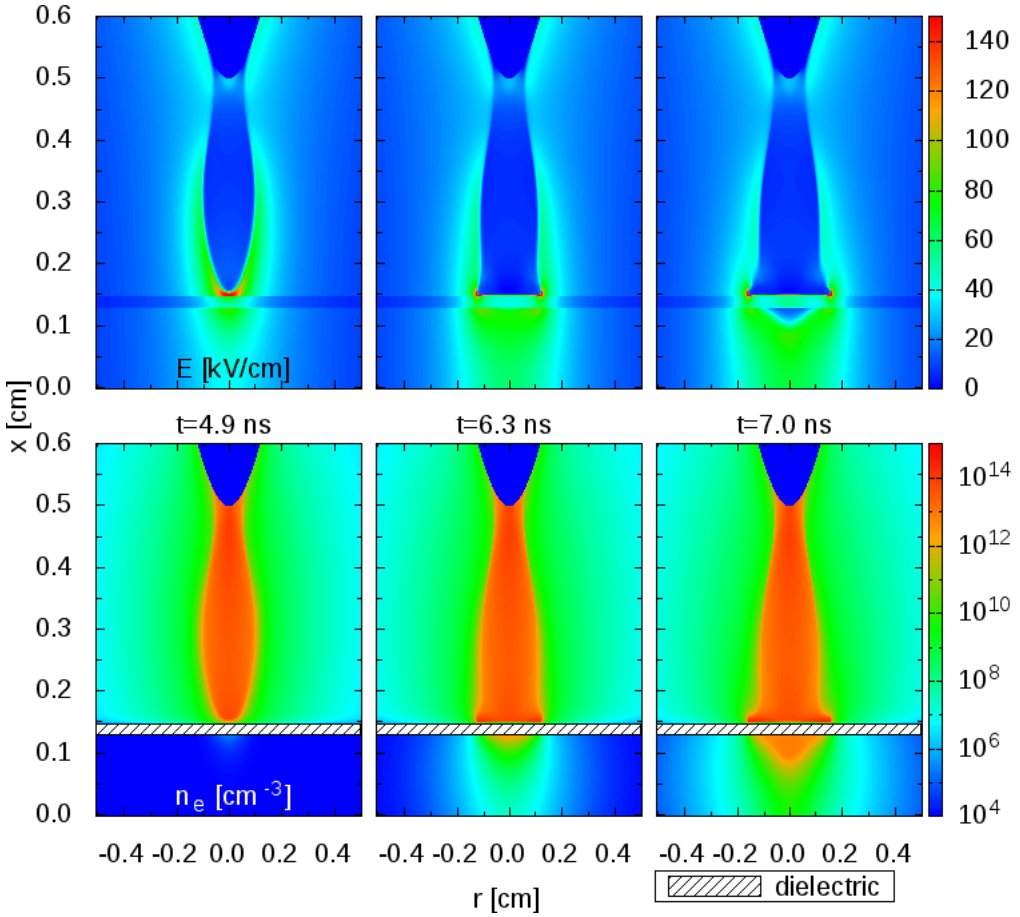

Figure 6.3: *Dynamics of the discharge in the point-to-plane geometry with a thin and opaque dielectric layer located at* $x_{\mathrm{diel}} = 0.15$ *cm. The thickness of the dielectric is* $\Delta = 176\,\mu$m *and its permittivity is* $\varepsilon_{\mathrm{r}} = 2$*. The applied voltage is* $\mathrm{U_a}$*=+13 kV. Cross-sectional views of the absolute value of the electric field and electron density at* $t = 4.9$*, 6.3 and 7.0 ns. Peak values of the scales of electric field and electron density are of 150 kV cm*$^{-1}$ *and* 10^{15} *cm*$^{-3}$*, respectively. Peak values of electric field after the discharge impact on the dielectric are higher and given in the text.*

the peak electron density on the discharge axis in the second air gap just below the dielectric surface is of 3.0×10^5 cm^{-3} and the magnitude of the peak electric field is 90 kV cm^{-1}. After impact, the first discharge starts to spread on the upper dielectric surface as observed in Section 5.3 for the positive CDBD configuration. At $t = 6.3$ ns, that is to say 1.4 ns after the first discharge impact, the electron density on the discharge axis below the dielectric has increased up to 3.0×10^{12} cm^{-3} with a magnitude of the peak electric field of 78 kV cm^{-1} and we observe in Figure 6.3 the start of the axial propagation of a second discharge from the bottom dielectric surface towards the cathode. This time is referred to as the reignition time τ_{reigni} in the following. When the discharge front crosses the middle of the second air gap, the magnitude of the peak electric field and the electron density on the axis are of 85 kV cm^{-1} and 1.2×10^{13} cm^{-3}, respectively (Table 6.1). Behind the discharge front, Figure 6.3 shows that the electric field is significantly reduced in the ionized discharge channel and we can consider that the second discharge ignited below the dielectric layer and propagating axially towards the cathode plane is a positive streamer discharge. In Figure 6.3 at $t = 7$ ns, the second discharge has a cone shape with a larger radius close to the bottom surface of the dielectric. Indeed, due to the surface discharge on the upper dielectric surface and the positive space charge in its discharge front, an increase of the norm of the electric field is induced below the dielectric layer. As the surface discharge spreads along the upper dielectric surface, the positive space charge in its front moves radially and so does the increase of electric field below the dielectric. Then, as the second discharge propagates axially towards the cathode, its radius close to the bottom surface of the dielectric becomes larger than the radius of its front in the gap and the second discharge has a cone shape. The second streamer discharge arrives at the cathode at $t = 7.5$ ns and in the following, the time of arrival of the discharge at the cathode is referred to as the connection time τ_{connect} (Table 6.1). As a reference, we have presented in chapter 1 Section 1.4.1 (test-case 1) simulations results for the same interelectrode gap without any dielectric layer. In this case a positive streamer propagates from the point anode to the cathode plane in $\tau_{\text{connect}} = 6$ ns. As expected, placing an obstacle on the streamer path slows down the propagation of the discharge in the whole interelectrode gap. For the condition of Figure 6.3, Figure 6.4(a) shows the time evolutions of the radial profiles of surface charges on both faces of the dielectric layer. For $t \geq \tau_{\text{impact}} = 4.9$ ns, we note that the first discharge spreads along the upper dielectric surface and charges it very weakly with positive surface charges. As observed for the positive CDBD configuration, the positive surface charge expands radially as the

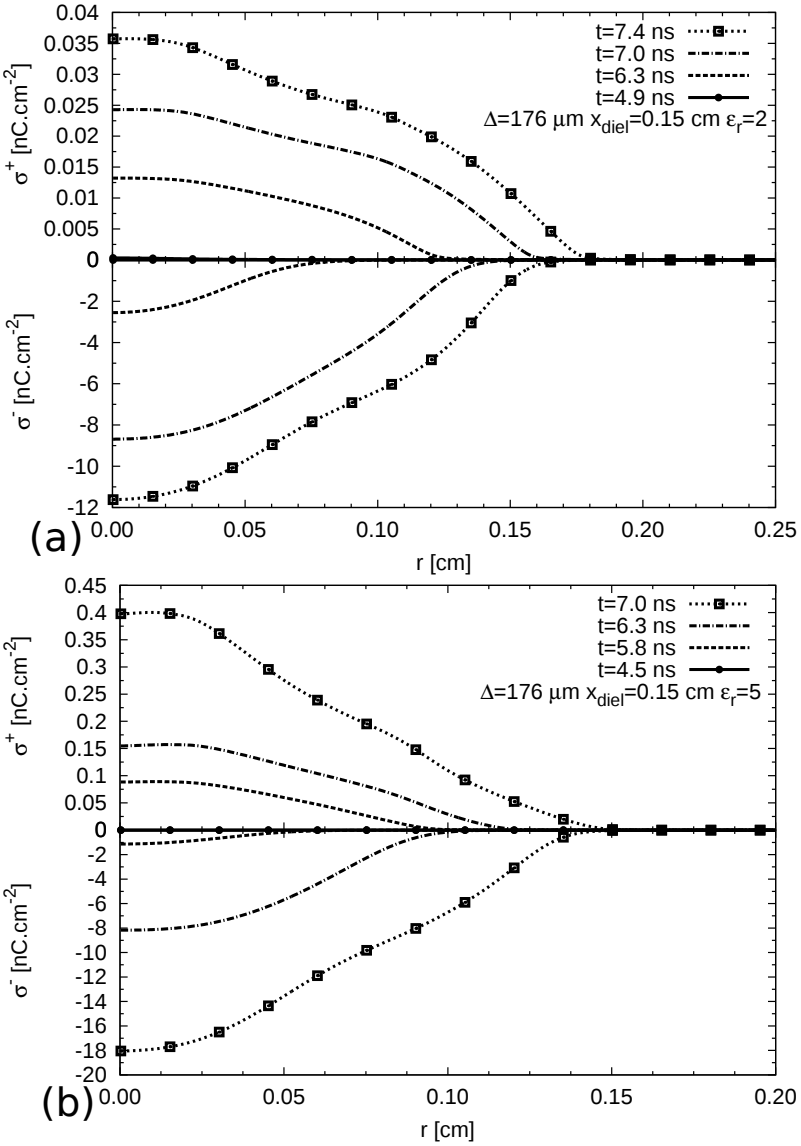

Figure 6.4: *Time evolutions of the radial profiles of the surface charges on both faces of the dielectric layer for the point-to-plane geometry with a thin and opaque dielectric layer located at* $x_{\mathrm{diel}} = 0.15$ *cm from the cathode. The thickness of the dielectric is* $\Delta = 176\,\mu$m *and its permittivity is* $\varepsilon_{\mathrm{r}} = 2$ *(a) and* $\varepsilon_{\mathrm{r}} = 5$ *(b). The applied voltage is* $\mathrm{U_a}$*=+13 kV.*

surface streamer propagates on the upper dielectric surface. Conversely, Figure 6.4(a) shows that the negative surface charge on the bottom dielectric surface increases (in absolute value) rapidly after τ_{impact}. Indeed, as the first discharge approaches and impacts the dielectric, the electric field below the dielectric close to the axis increases and then avalanches originating from seed electrons, appear in the second air gap, close to the discharge axis. As electrons are much more mobile than ions, electrons drift towards the point anode and are stopped by the dielectric obstacle and then charge its bottom surface negatively. It is interesting to note that positive and negative charge depositions on opposite poles of a dielectric particle have been also observed in (Babaeva et al. 2006) during the dynamics of an atmospheric pressure air streamer intersecting with a particle. Figure 6.4(a) shows that positive and negative surface charges increase (in absolute value) and expand radially as time increases, due to the surface streamer propagation on the upper dielectric surface.
Electrostatically, depositing a disk of positive surface charges on the upper dielectric surface increases the absolute value of the axial electric field in the air gap below the dielectric on the symmetry axis and then may enhance discharge reignition. Conversely, depositing a disk of negative charges on the bottom dielectric surface increases the absolute value of the axial electric field on the symmetry axis close to the upper dielectric surface and decreases its absolute value in the second air gap which may prevent reignition. Figure 6.2 compares the Laplacian potential calculated on the discharge axis with the potential calculated in taking into account only surface charges deposited at $\tau_{\text{reigni}} = 6.3$ ns, and the total potential calculated at t=τ_{reigni}. We note that the small amount of deposited surface charges on both faces of the dielectric layer at the reignition time induces a small peak of negative potential of -473 V at the surface of the dielectric on the cathode side and then decreases slightly the electric field in the second air gap. However, in comparison to the value of the total potential (8780 V) at the same axial position, we note that the decrease of potential due to surface charges is almost negligible and then one can assume that surface charges deposited on both faces of the dielectric layer have a negligible influence on the reignition of the discharge in the second air gap. Figure 6.2 shows that after the first streamer impact on the dielectric surface, due to the space charges in the streamer channel, the voltage drop in the first air gap is significantly decreased in comparison to the initial Laplacian voltage drop. Then at the time of reignition, Figure 6.2 shows that the most significant voltage drop in the whole interelectrode gap is applied on the second small air gap, with close to the bottom surface of the dielectric a peak electric field of 78 kV cm^{-1}.

As at $t = \tau_{\text{reigni}} = 6.3$ ns, that is to say 1.4 ns after the first streamer impact on the upper dielectric surface, the electron density on the discharge axis below the dielectric has increased up to 3.0×10^{12} cm^{-3}, we observe in Figure 6.3 the start of the axial propagation of a second discharge. It is interesting to note that the reignition of the discharge below the dielectric in this case, is due to the potential redistribution after the first streamer propagation in the first air gap and not due to surface charge deposition on the two faces of the dielectric layer. In this work, we have stopped simulations at $t = 8$ ns, shortly after the connection of the discharge at the cathode.

6.3.2 Influence of the permittivity of an opaque dielectric layer on the discharge dynamics and reignition

In this section, we study the influence of the permittivity of the dielectric layer on the discharge dynamics and reignition and we have carried out simulations for $\varepsilon_{\text{r}} = 1, 2$ and 5 for the same thickness of the dielectric ($\Delta = 176\mu$m) and the same $x_{\text{diel}} = 0.15$ cm as in section 6.3.1. Table 6.1 shows that the impact, reignition and connection times increase slightly as ε_{r} decreases. In the positive CDBD configuration, for a fixed geometry, the increase of ε_{r} increases the capacitance of the dielectric layer and the capacitance of the whole interelectrode gap. This is also the case when the dielectric layer is located at some distance ($x_{\text{diel}} > \Delta$) from the cathode plane. As a consequence, the Laplacian electric field in the first air gap increases as ε_{r} increases which results in a slightly faster propagation of the discharge in the first air gap and then an earlier impact on the dielectric. After the impact, the first discharge starts spreading along the upper dielectric surface and charging it. For $t \geq \tau_{\text{impact}}$ =4.5 ns, Figure 6.4(b) shows the radial profiles of surface charges on both faces of the dielectric layer for $\varepsilon_{\text{r}} = 5$. As for $\varepsilon_{\text{r}} = 2$ in Figure 6.4(a), we note that for $t \geq \tau_{\text{impact}}$, the amount of charges deposited on both faces increases (in absolute value) and that the absolute value of amount of negative surface charges on the bottom surface is larger than the one of positive surface charges on the upper dielectric surface. As for the positive CDBD configuration, Figure 6.4(a) and (b) show that, as ε_{r} increases, the amount of positive surface charges close to the axis on the upper dielectric surface increases faster to higher values. This is also the case for the absolute value of amount of negative charges close to the axis below the dielectric surface, but the influence of the value of ε_{r} is more significant on the amount of positive charges than on negative ones. It is interesting to note that the

amount of negative surface charges close to the discharge axis increases (in absolute value) during the second discharge propagation and we have observed that this increase becomes steeper as the second discharge moves closer to the cathode plane. At the connection time $\tau_{\text{connect}} = 7$ ns for $\varepsilon_r = 5$, the increase of the absolute value of negative surface charge up to 18 nC cm^{-2} close to the discharge axis, increases the magnitude of the electric field in the first air gap close to the upper dielectric surface, and as a consequence, Figure 6.4(b) shows a steep increase of the positive surface charge close to the axis on the upper dielectric surface.
It is interesting to note that for all values of ε_r studied in this section, we have checked that at the time of reignition, the amount of positive and negative surface charges deposited on both faces of the dielectric layer is too low to explain the reignition below the dielectric. Then, in all studied cases, the reignition in the second air gap is due to the potential redistribution in the interelectrode gap after the first streamer impact on the upper dielectric surface as observed for $\varepsilon_r = 2$ in section 6.3.1. Table 6.1 shows that the peak electric field and the electron density in the discharge front when it crosses the middle of the second air gap, decrease as ε_r decreases. For $\varepsilon_r = 2$ and 5, in the middle of the second air gap, the peak electric field in the discharge front is in the range $88 - 101$ kV cm^{-1} and the electron density is in the range $1.2 - 2.2 \times 10^{13}$ cm^{-3}, and then these discharges are positive streamers. Conversely, for $\varepsilon_r = 1$, the reignited discharge is a weaker ionization front propagating axially with, in the middle of the second air gap, a peak electric field of 75 kV cm^{-1} and an electron density of 7.4×10^{12} cm^{-3}.

To further study the influence of ε_r on the discharge dynamics, we have carried out simulations for a different position of the dielectric layer ($x_{\text{diel}} = 0.24$ cm), closer to the point electrode. Table 6.1 shows that, as observed for $x_{\text{diel}} = 0.15$ cm, for $x_{\text{diel}} = 0.24$ cm the times of impact, reignition and connection increase as ε_r decreases with for the case $\varepsilon_r = 1$, no observed reignition within the 14.7 ns of the simulated discharge.
Figure 6.5(a) compares the velocity of the surface discharge on the upper dielectric surface for the different values of ε_r for $x_{\text{diel}} = 0.24$ cm. We note that the velocity increases as ε_r decreases as observed for the positive CDBD configuration. Figure 6.5(b) shows the radial profiles of positive and negative surface charges when for both values of ε_r the surface discharge front on the upper dielectric surface is located at $R_{\text{front}} = 0.2$ cm which corresponds to $t = 7.1$ ns for $\varepsilon_r = 5$ and 6.9 ns for $\varepsilon_r = 2$. As for the positive CDBD configuration, we note that the slope of dielectric

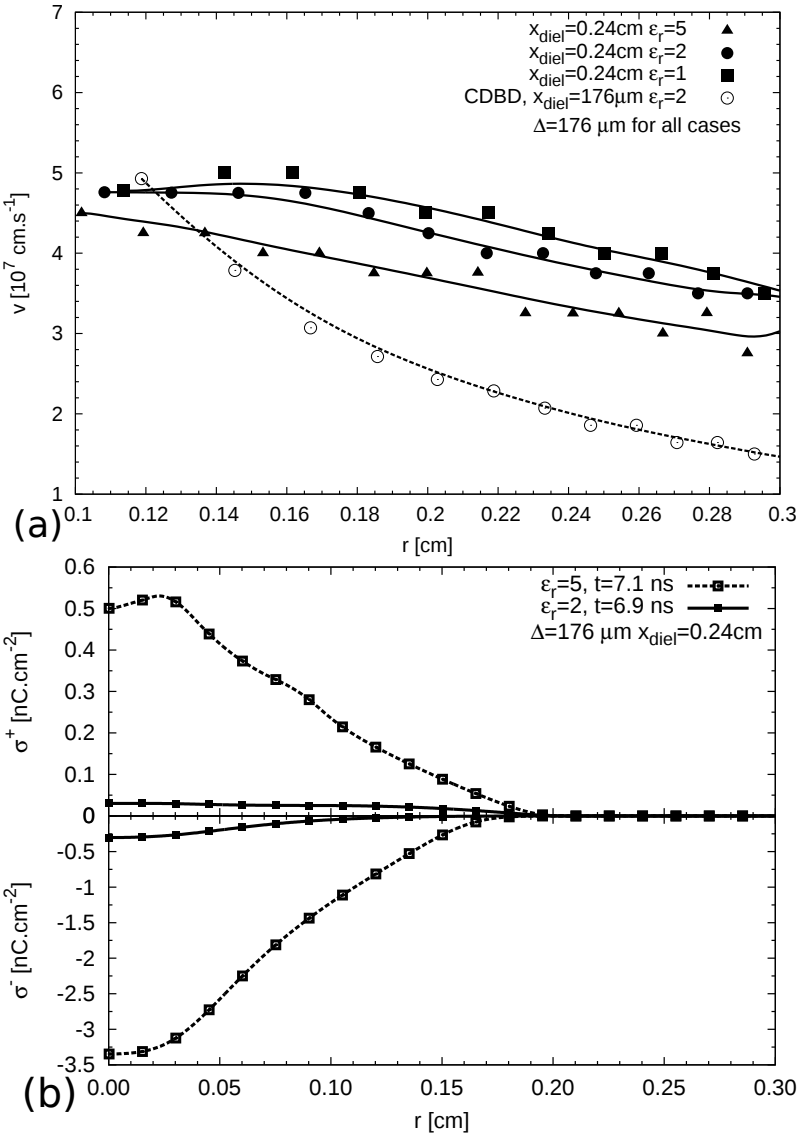

Figure 6.5: *(a) Radial velocity of the surface discharge front on the upper dielectric surface as a function of the radius for a thin dielectric layer ($\Delta = 176\,\mu m$) located at $x_{\rm diel} = 0.24$ cm with $\varepsilon_{\rm r} = 1, 2$ and 5 and comparison with a CDBD configuration ($x_{\rm diel} = 176$ μm) for $\varepsilon_{\rm r} = 2$. (b) Radial profiles of surface charges on both dielectric surfaces for the same radial position ($R_{\rm front} = 0.2$ cm) of the surface discharge front for a thin dielectric layer with $\varepsilon_{\rm r} = 2$ and 5 located at $x_{\rm diel} = 0.24$ cm. The applied voltage is* $\rm U_a$*=+13 kV.*

ε_r	1	1	2	2
$\Delta(\mu m)$	176	176	176	176
x_{diel} (mm)	1.5	2.4	1.5	2.4
τ_{impact} (ns)	5.1	3.8	4.9	3.5
τ_{reigni} (ns)	7.3	-	6.3	9
$\delta\tau_{reigni}$ (ns)	2	-	1.4	5.5
$\tau_{connect}$ (ns)	8.8	-	7.5	20
E^{sg}_{max}(kV cm^{-1})	75	-	88	48
$n^{sg}_{e,max}$ (cm^{-3})	7.4×10^{12}	-	1.2×10^{13}	2×10^{12}

ε_r	5	5	5	5^t
$\Delta(\mu m)$	176	176	176	176^t
x_{diel} (mm)	1.5	2.4	3.5	3.5^t
τ_{impact} (ns)	4.5	3.3	2	2
τ_{reigni} (ns)	5.8	6	-	2.5
$\delta\tau_{reigni}$ (ns)	1.3	2.7	-	0.5
$\tau_{connect}$ (ns)	7.0	12.8	-	7.1
E^{sg}_{max}(kV cm^{-1})	101	75.4	-	111
$n^{sg}_{e,max}$ (cm^{-3})	2.2×10^{13}	8.7×10^{12}	-	3.6×10^{13}

Table 6.1: *Influence of the permittivity (ε_r) and axial position (x_{diel}) of a thin ($\Delta = 176$ μm) dielectric layer on the time of impact τ_{impact}, the reignition time τ_{reigni}, the reignition delay $\delta\tau_{reigni} = \tau_{reigni} - \tau_{impact}$, the time of discharge connection to the cathode $\tau_{connect}$, the peak electric field E^{sg}_{max} and electron density $n^{sg}_{e,max}$ in the discharge front when it crosses the middle of the second air gap. All cases are for an opaque dielectric layer, except the last column, where the subscript t is for a transparent dielectric layer as defined in section 1.2. The symbol "-" is used for cases with no reignition during the simulated time. The applied voltage is* U_a*=+13 kV.*

surface charging behind the surface discharge front is steeper for $\varepsilon_r = 5$ than for $\varepsilon_r = 2$. Table 6.2 compares the position of the surface streamer front on the upper dielectric surface, and total positive and negative surface charges after the same time delay after impact (namely at $t = \tau_s$ defined in section 5.3). We note that the amount of deposited positive and negative surface charges increases (in absolute value) as ε_r increases. Comparing the amount of positive surface charges at t=τ_s in Table 6.2 for a dielectric layer at $x_{diel} = 0.24$ cm and in Table 5.1 for the positive CDBD, we note that this amount is much higher for the CDBD configuration.

On Figure 6.5(a), we compare the velocity of the surface discharge for these two cases and we note that the more significant positive charging of

ε_r	1	2	5
$\Delta(\mu m)$	176	176	176
x_{diel} (mm)	2.4	2.4	2.4
τ_s=τ_{impact}+3.9 (ns)	7.7	7.4	7.2
R_{front} (cm) at t=τ_s	0.23	0.22	0.20
Q_t^+ (nC) at t=τ_s	1.4×10^{-3}	3.2×10^{-3}	$2.\times10^{-2}$
Q_t^- (nC) at t=τ_s	1.8×10^{-4}	8.6×10^{-3}	0.10

Table 6.2: *Influence of the permittivity (ε_r) on the total surface charges at $\tau_s = \tau_{impact} + 3.9$ (ns) for a thin ($\Delta = 176$ μm) dielectric layer located at $x_{diel} = 0.24$ cm. The applied voltage is U_a=+13 kV.*

the dielectric surface for the CDBD configuration corresponds to a slower propagation of the surface streamer on the upper dielectric surface, in agreement with the results of section 5.3.

6.3.3 Influence of the position of the thin and opaque dielectric layer on the discharge dynamics and reignition

In this section, we study the influence of the position of the dielectric layer x_{diel} on the discharge dynamics. Figure 6.6 shows the distributions of the electron density and absolute values of the electric field for $x_{diel} = 0.15, 0.24$ and 0.35 cm for a thin dielectric layer with $\varepsilon_r = 5$. We compare the results at the same time of $t = 7$ ns, which is $\tau_{connect}$ for the case $x_{diel} = 0.15$ cm. As expected, Figure 6.6 and Table 6.1 show that the time of impact of the streamer ignited at the point is the smallest for the dielectric which is the closest to the point ($x_{diel} = 0.35$ cm) and then the first discharge starts spreading on the upper dielectric surface earlier for this x_{diel} than for the others. Below the dielectric layer, we note that the discharge dynamics depends strongly on the location of the dielectric layer. Indeed, when the dielectric layer is the closest to the cathode ($x_{diel} = 0.15$ cm), as discussed in Section 6.3.2, we observe 1.3 ns after the impact, the ignition of a second streamer discharge below the dielectric and its fast propagation towards the cathode with a connection time of 7 ns. As the dielectric layer is placed closer to the point as for $x_{diel} = 0.24$ cm, the reignition delay increases up to 2.7 ns and we observe the reignition of a weak positive streamer below the dielectric (axial values of the peak electric field and electron density in the discharge front as it crosses the middle of the second air gap are of 75.4 kV cm^{-1} and 10^{13} cm^{-3}, respectively) which impacts the cathode at 12.8 ns. Finally,

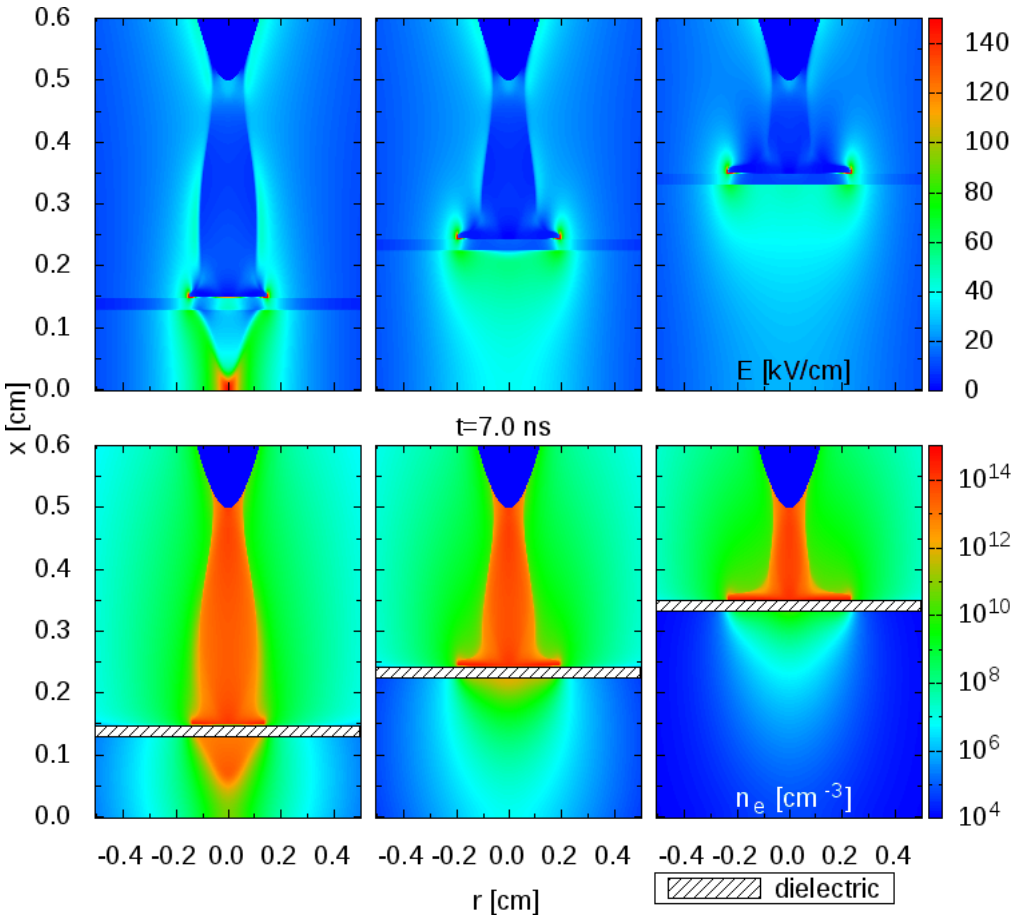

Figure 6.6: *Influence of the position (x_{diel}) of the thin and opaque dielectric layer on the discharge propagation. The applied voltage is* $\mathrm{U_a}$*=+13 kV. Cross-sectional views of the absolute value of the electric field and electron density at* $t = 7.0$ *ns. The thickness of the dielectric is* $\Delta = 176\,\mu$m *and its permittivity is* $\varepsilon_{\mathrm{r}} = 5$*. Peak values of the scales of electric field and electron density are of 150 kV cm*$^{-1}$ *and* 10^{15} *cm*$^{-3}$*, respectively. Peak values of electric field after the discharge impact on the dielectric are higher and given in the text.*

for the case with a dielectric layer located at $x_{\text{diel}} = 0.35$ cm, we have not observed any discharge reignition below the dielectric during the 16 ns simulated in this work. Then these results show, that in a point-to-plane geometry with a dielectric obstacle, to have the discharge propagation in the whole interelectrode gap, it is more efficient to place the obstacle closer to the plane cathode than to the point anode.
It is interesting to note that placing a dielectric layer with fixed values of thickness and permittivity at different axial positions changes the size and then the capacitances of the air gaps below and above the dielectric. Conversely, it has no influence on the capacitance of the dielectric. For a plane-plane geometry, the axial position of a dielectric layer between electrodes has also no influence on the capacitance of the whole interelectrode gap. Using the analytical expression of the capacitance for a sphere-plane geometry (Durand 1966) with a 5 mm gap and considering a thin dielectric layer between electrodes, we have checked that the capacitance of the whole interelectrode gap increases of only about 10% as the dielectric layer is moved from $x_{\text{diel}} = 0.15$ to 0.35 cm, closer to the point electrode. Then, this variation of the capacitance of the whole interelectrode gap is too small to explain the significant differences observed on the discharge dynamics for the different positions of the dielectric layer.

ε_{r}	5	5	5	5^t
$\Delta(\mu\text{m})$	176	176	176	176^t
x_{diel} (mm)	1.5	2.4	3.5	3.5^t
Q_t^+ (nC)	8.7×10^{-3}	1.79×10^{-2}	3.77×10^{-2}	0.11
Q_t^- (nC)	0.44	8.67×10^{-2}	3.42×10^{-3}	0.8

Table 6.3: *Influence of the position (x_{diel}) of the thin dielectric layer with $\varepsilon_{\text{r}} = 5$ on total surface charges at $t = 7.0$ ns. All cases are for an opaque dielectric layer, except the last column, where the subscript t is for a transparent dielectric layer as defined in section 1.2. The applied voltage is U_a=+13 kV.*

For the applied voltage of U_a=+13 kV studied in this work, a streamer discharge is rapidly ignited at the point electrode and propagates towards the upper dielectric surface whatever the position of the dielectric layer. After the impact, on the axis, the voltage drop is very low from the point electrode to the upper dielectric surface and then most of the voltage drop is applied to the second air gap. If the dielectric layer is closer to the anode, the axial propagation of the first discharge is stopped more rapidly and then as the size of the second air gap is larger, its capacitance is lower and the electric field in the second air gap is smaller, which is

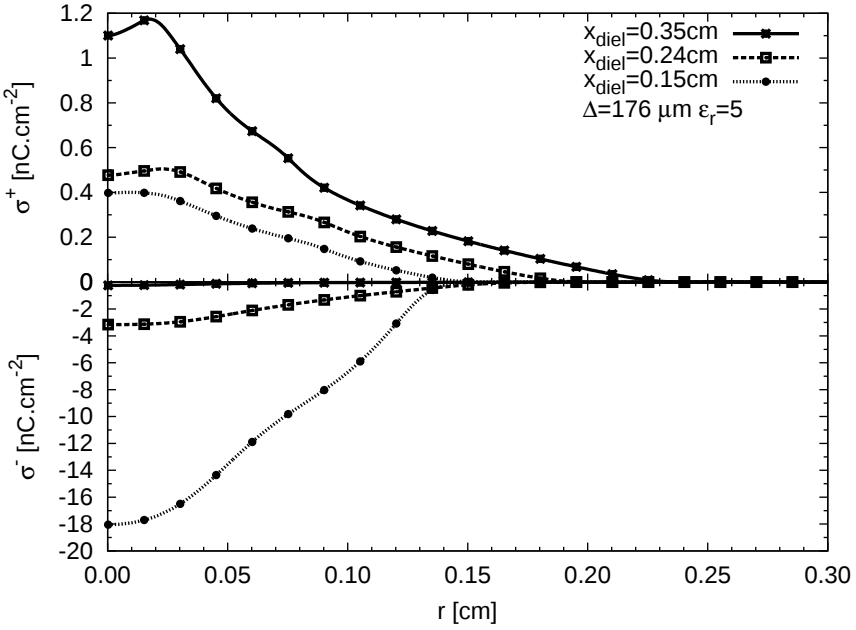

Figure 6.7: *Influence of the position (x_{diel}) of the thin and opaque dielectric layer on the surface charge distributions on both faces of the dielectric layer at $t = 7.0$ ns. The thickness of the dielectric is $\Delta = 176\,\mu$m and its permittivity is $\varepsilon_{\mathrm{r}} = 5$. The applied voltage is $\mathrm{U_a}$=+13 kV.*

less favorable for reignition. Furthermore, when the dielectric layer is closer to the anode, if a second discharge reignites below the layer (as for $x_{\mathrm{diel}} = 0.24$ cm in comparison to $x_{\mathrm{diel}} = 0.15$ cm), we note that this second discharge is an ionization wave with lower values of peak electric field and electron density. Then, when the layer is closer to the anode, the first impact on the dielectric occurs earlier but it is more difficult for the second discharge to reignite and, as a consequence, the reignited discharge arrives later at the cathode plane. Figure 6.7 shows the radial profiles of surface charges on both faces of the dielectric at $t = 7.0$ for the different x_{diel} and values of total surface charges are given in Table 6.3. We observe that in all cases, the amount of positive surface charges on the upper dielectric surface is low. As expected, the highest amount of positive surface charges is obtained when the dielectric layer is the closest to the anode point. Indeed, as the impact on the upper dielectric surface occurs earlier when the dielectric layer is closer to the point, the surface discharge for $x_{\mathrm{diel}} = 0.35$ cm has the largest radial spreading on the upper dielectric surface and then the highest amount of positive surface charges at $t = 7.0$ ns. Conversely, the highest amount of negative surface charges (in absolute value) on the bottom surface of the dielectric is obtained for

the dielectric layer which is the closest to the cathode plane. Indeed, at $t = 7.0$ ns, for $x_{\text{diel}} = 0.15$ cm, the second discharge is almost connected to the cathode whereas for the two other positions of the dielectric layer, the dynamics of the discharge below the dielectric layer is much slower. For a fixed applied voltage of $U_a = +13$ kV, we have put forward that it is easier to obtain a discharge reignition in the second air gap with an obstacle which is closer to the plane cathode than to the point anode. If a discharge reignites in the second air gap, we consider that we have a discharge propagation in the whole point-to-plane interelectrode gap, that is to say we obtain the breakdown of the interelectrode gap. Then results obtained in this work show that the breakdown voltage of the whole interelectrode gap increases if the obstacle is closer to the plane cathode than to the point anode. These results are in good agreement with experiments for high voltage applications reviewed in (Lebedev et al. 2005).

6.3.4 Influence of the thickness of the opaque dielectric layer on the discharge dynamics and reignition

In this section, we study the influence of the thickness Δ of the dielectric layer on the discharge dynamics and reignition. Figure 6.8 shows the distributions of the electron density and absolute values of the electric field for $\Delta = 176\,\mu$m and 1 mm, with $\varepsilon_r = 5$ and $x_{\text{diel}} = 0.24$ cm. We compare the results at the same times of 9 and 10.5 ns, which correspond to τ_{reigni} and τ_{connect} for $\Delta = 1$ mm. Table 6.4 gives the values of the impact, reignition and connection times for the thick dielectric layer located at $x_{\text{diel}} = 0.24$ cm for $\varepsilon_r = 5$ and also for $\varepsilon_r = 1$ and 2. In comparing results in Tables 6.1 and 6.4 for $x_{\text{diel}} = 0.24$ cm, we note that the time of impact decreases as Δ increases for $\varepsilon_r = 2$ and 5, and remains constant for $\varepsilon_r = 1$. For a given point-to-plane geometry, the presence of a thicker dielectric layer with $\varepsilon_r > 1$ in the air gap, increases the capacitance of the whole interelectrode gap. As a consequence, the Laplacian electric field in the first air gap increases which results in a slightly faster propagation of the discharge and then an earlier impact on the dielectric. Then, for $\varepsilon_r = 5$, Figure 6.8 shows that at $t = 9$ ns the first streamer discharge is more spreaded on the upper dielectric surface in the thick case than in the thin case. Conversely, Tables 6.1 and 6.4 show that for $\varepsilon_r = 2$ and 5, as Δ increases, the reignition delay increases (for $\varepsilon_r = 5$, from 2.7 ns for $\Delta = 176$ μm to 6.4 ns for 1 mm). For $\varepsilon_r = 1$, with a thick dielectric, no reignition has been observed within the 15.7 ns of the simulated discharge.

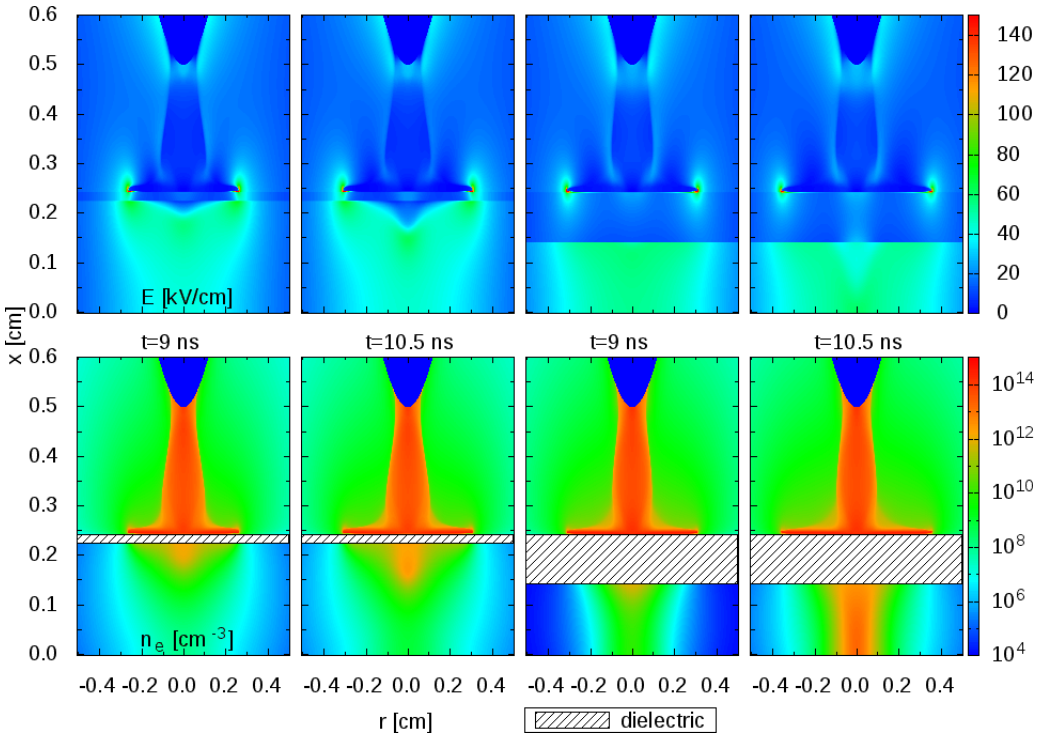

Figure 6.8: *Discharge dynamics for two thicknesses of the dielectric layer* $\Delta = 176\,\mu$m *and* 1 mm *with* $x_{\mathrm{diel}} = 0.24$ *cm. The applied voltage is* $\mathrm{U_a}$=*+13 kV and the permittivity of the dielectric layer is* $\varepsilon_{\mathrm{r}} = 5$. *Cross-sectional views of the absolute value of the electric field and electron density at* $t = 9$ *and 10.5 ns. Peak values of the scales of electric field and electron density are of 150 kV* cm^{-1} *and* 10^{15} cm^{-3}, *respectively. Peak values of electric field after the discharge impact on the dielectric are higher and given in the text.*

In the simulations, we have observed for $\varepsilon_r = 2$ and 5, that the reignited discharge below the dielectric is more diffuse and weaker for the thick dielectric layer than for the thin one. For example, for $\varepsilon_r = 5$, in the middle of the second air gap on the axis, the peak electric field and the electron density are of 61 kV cm^{-1} and 4.6×10^{12} cm^{-3} in the discharge front for the thick dielectric layer, and 75 kV cm^{-1} and 10^{13} cm^{-3} for the thin case, respectively. However, as the size of the second air gap decreases as Δ increases, Table 6.4 shows that for $\varepsilon_r = 2$ and 5, the connection to the cathode is observed earlier in the thick dielectric case than in the thin one. Indeed, as Δ increases, the capacitance of the whole interelectrode gap increases and we note that the connection time of the discharge decreases. For $\varepsilon_r = 5$ in Figure 6.8, the propagation of the weak ionization front in the second air gap is very fast for the thick dielectric, with an average velocity of 9×10^7 cm s^{-1}, about 3 times faster than for the thin case. Figure 6.9 shows the radial profiles of surface charges on both faces of the dielectric at $t = 9$ and 10.5 ns and Table 6.5 gives at $t = 9$ ns the total amount of surface charges. At $t = 9$ ns, as the surface discharge is more spreaded on the upper dielectric surface for the thick dielectric, we note that the positive surface charge is also higher and more expanded radially than for the thin dielectric. Conversely, on the bottom dielectric surface, the amount of negative surface charges (in absolute value) is smaller for the thick dielectric than for the thin one as at $t = 9$ ns, the second discharge for the thin dielectric is already reignited which is not the case for the thick dielectric. Between 9 and 10.5 ns, we note that the evolution of the radial profiles of positive surface charges is small for both values of Δ, but is more significant for negative surface charges. Indeed, between 9 and 10.5 ns, the amount of negative surface charges increases (in absolute value) particularly close to the axis due to the propagation of the second discharge below the dielectric.

In all cases studied in this work, when the dielectric layer is thin, we have observed that the amount of positive surface charges deposited on the dielectric before reignition is too low to explain the discharge reignition below the dielectric. For the thick case of Figure 6.8, Figure 6.9 shows that the amount of positive surface charges on the upper dielectric surface after the impact is more significant. We have calculated that, at the reignition time (9 ns in this case), surface charges on both dielectric faces enhance the magnitude of the electric field below the dielectric of 12.5 kV cm^{-1} which is less than the magnitude of the total electric field (48.2 kV cm^{-1}). Therefore, even in the thick case, surface charges have

ε_r	1	2	5
$\Delta(\mu m)$	1000	1000	1000
x_{diel} (mm)	2.4	2.4	2.4
τ_{impact} (ns)	3.8	3.0	2.5
τ_{reigni} (ns)	-	14	9
$\delta\tau_{reigni}$ (ns)	-	11	6.4
$\tau_{connect}$ (ns)	-	15.9	10.5
E^{sg}_{max}(kV cm^{-1})	-	47	61
$n^{sg}_{e,max}$ (cm^{-3})	-	2.7 $\times 10^{12}$	4.6 $\times 10^{12}$

Table 6.4: *For a thickness of the dielectric layer of $\Delta = 1$ mm, influence of permittivity (ε_r) for an opaque dielectric layer located at $x_{diel} = 0.24$ cm on the time of impact τ_{impact}, the reignition time τ_{reigni}, the reignition delay $\delta\tau_{reigni} = \tau_{reigni} - \tau_{impact}$, the time of discharge connection to the cathode $\tau_{connect}$, the peak electric field E^{sg}_{max} and electron density $n^{sg}_{e,max}$ in the discharge front in the middle of the second air gap. The symbol "-" is used for the case $\varepsilon_r = 1$ as no reignition is observed during the simulated time. The applied voltage is* U_a*=+13 kV.*

ε_r	5	5
$\Delta(\mu m)$	176	1000
x_{diel} (mm)	2.4	2.4
Q^+_t (nC)	5.3$\times 10^{-2}$	0.64
Q^-_t (nC)	0.30	1.4$\times 10^{-2}$

Table 6.5: *Total surface charges at $t = 9$ ns for the condition of Figure 6.9.*

only a small influence on the reignition of the discharge below the dielectric and reignition is mostly due to the potential redistribution after the streamer propagation in the first air gap. It is interesting to note in Figure 6.9 that for a given time, for a thin dielectric the radial expansions of positive and negative surface charges of both faces of the dielectric are rather close. This is also clearly observed in Figures 6.4, 6.5 and 6.7. As mentioned in previous sections, for a thin dielectric, the radial expansion of negative surface charges follows the radial spreading of the surface discharge on the upper dielectric surface. Conversely, for a thick dielectric, Figure 6.9 shows that at a given time the radial expansion of negative surface charges is less than the radial expansion of positive surface charges. As a consequence, for a thick dielectric, the second discharge has a more cylindrical structure in comparison to the cone shape observed for a thin dielectric.

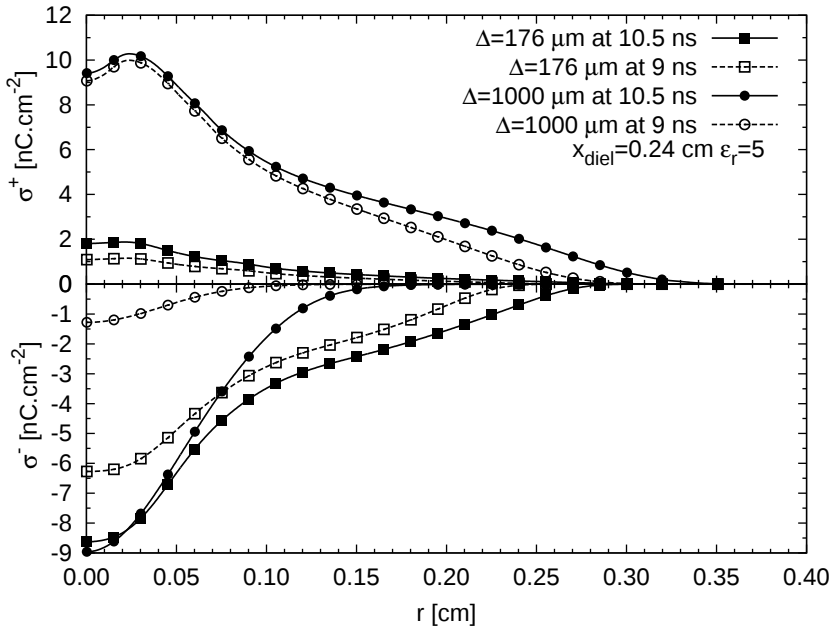

Figure 6.9: *Radial profiles of surface charges on both faces of the dielectric layer for the same conditions as Figure 6.8.*

6.3.5 Study of the reignition of a discharge behind a thin and transparent dielectric layer

In this section, we assume that the dielectric layer is transparent to the part of the discharge radiation responsible for the air photoionization. We present results for the case where the thin dielectric layer with $\varepsilon_r = 5$ is located at $x_{diel} = 0.35$ cm, for which no reignition was observed when the dielectric is opaque (Figure 6.6 and Table 6.1). Figure 6.10 shows the distributions of the electron density and the absolute value of the electric field at $t = 2$, 2.5 and 6.0 ns. The last column of Table 6.1 gives the impact, reignition and connection times. As expected, the time of impact is the same (2 ns) for the transparent and opaque dielectric layers. Figure 6.10 shows that at $t = 2$ ns the electron density below the dielectric has significantly increased (peak value of 1.02×10^{10} cm^{-3}) due to the photoionization source term in the second air gap during the first discharge propagation. Therefore at $t = \tau_{reigni} = 2.5$ ns in Figure 6.10, the electron density reaches on the discharge axis close to the bottom surface of the dielectric layer a peak value of 1.05×10^{13} cm^{-3} with a peak electric field of 84 kV cm^{-1} and we observe the start of the axial propagation of a second discharge from the bottom dielectric surface towards the cathode. This second discharge is a positive streamer with, on the

axis, a peak electric field of 109 kV cm^{-1} and an electron density of 3.4 $\times 10^{13}$ cm^{-3} in the discharge front as it crosses the middle of the second air gap. As already observed in Section 6.3.1, the second streamer ignited below the dielectric has a cone shape which is more clearly seen in Figure 6.10 as the size of the second air gap is larger. This discharge propagates rapidly in the second air gap and impacts at $t = 7.1$ ns the cathode plane. If we compare with other conditions studied in this work with a thin opaque layer with $\varepsilon_r = 5$, we note that this is the shortest connection time. It is interesting to note however, that it is 1.1 ns longer than the connection time without any dielectric layer in the interelectrode gap. Figure 6.11 shows the surface charge distributions on both faces of the dielectric layer at $t = 2.5$, 6 and 7.0 ns for the same condition as Figure 6.10. At $t = \tau_{reigni} = 2.5$ ns, the reignition time, as already observed for thin opaque layers, the amount of positive surface charges is very small and then has no influence on the second discharge reignition. As expected, due to the photoionization source term in the second air gap during the first streamer propagation, the deposition of negative surface charges starts earlier for a transparent dielectric than for an opaque one and this may prevent reignition. However, at $t = \tau_{reigni} = 2.5$ ns, the amount of deposited negative surface charges is rather small and the electric field and the charged species density in the second air gap volume are high enough to reignite a second discharge. We note that the amount of negative surface charges increases (in absolute value) rapidly as the second discharge propagates in the second air gap. As a consequence, the magnitude of the electric field above the dielectric layer increases which enhances the positive surface charge deposition on the upper dielectric surface. The amount of positive surface charges on the upper dielectric surface reaches at $t = 7$ ns a value of 11 nC cm^{-2}, much higher than the amount of positive charges obtained at $t = 7$ ns for all thin and opaque dielectric test-cases listed in Table 6.1. Table 6.3 shows that at $t = 7$ ns, total amounts of positive and negative surface charges are much higher (in absolute value) for the transparent than for the opaque dielectric located at the same axial position.

As a conclusion, the results obtained in this section show clearly that the radiation emitted by the first discharge may have a significant influence on the reignition below the dielectric obstacle and the dynamics of charging of the dielectric layer.

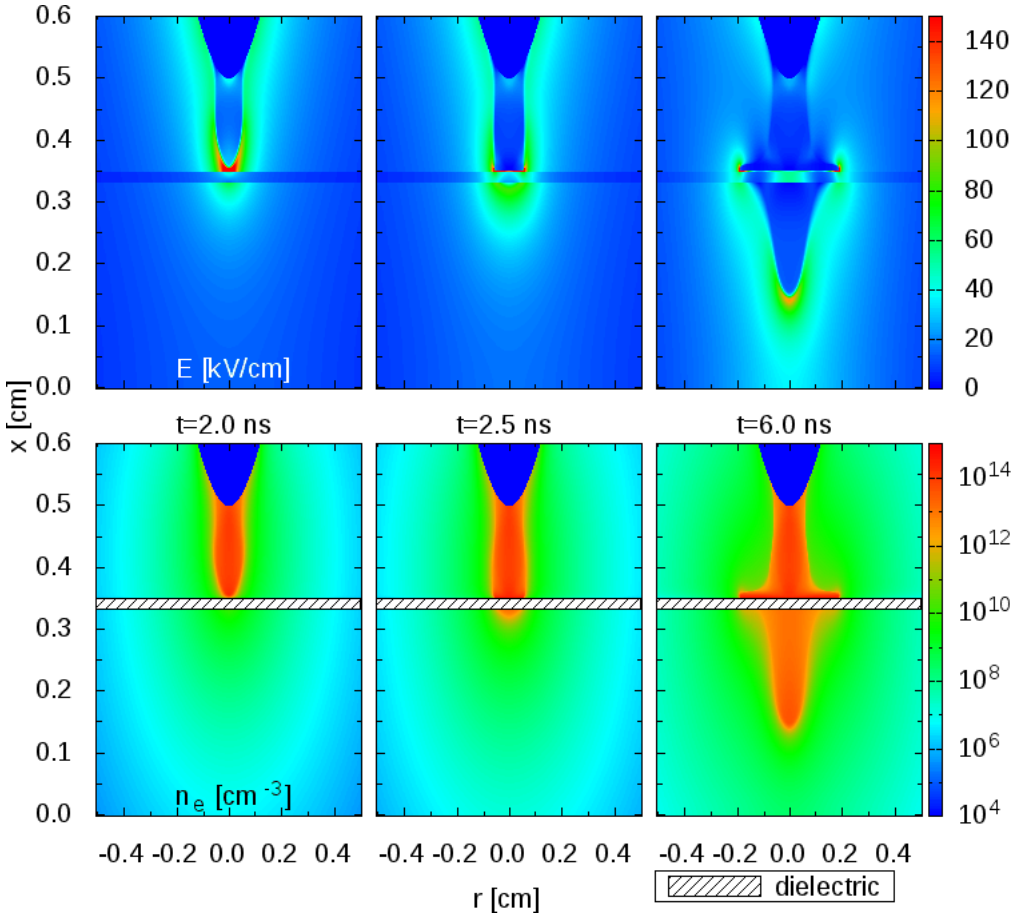

Figure 6.10: *Dynamics of the discharge in the point-to-plane geometry with a thin and transparent dielectric layer located at* $x_{\mathrm{diel}} = 0.35$ *cm for an applied voltage of* $\mathrm{U_a}$*=+13 kV. The thickness of the dielectric is* $\Delta = 176\,\mu\mathrm{m}$ *and its permittivity is* $\varepsilon_{\mathrm{r}} = 5$*. Cross-sectional views of the absolute value of the electric field and electron density at* $t = 2$*,* 2.5 *and* 6.0 *ns. Peak values of the scales of electric field and electron density are of 150 kV* cm^{-1} *and* 10^{15} cm^{-3}*, respectively. Peak values of electric field after the discharge impact on the dielectric are higher and given in the text.*

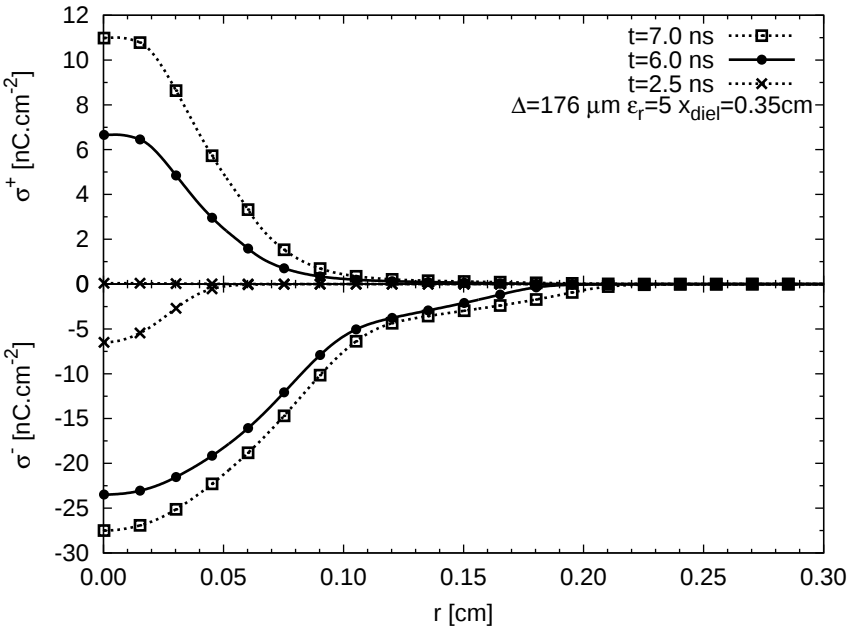

Figure 6.11: *Radial profiles of surface charges on both faces of the dielectric layer at* $t = 2.5$*, 6 and* 7.0 *ns for the same condition as Figure 6.10.*

6.4 Study of the reignition of a discharge below two parallel dielectric layers

In this section we study the influence of placing two thin and opaque dielectric layers with $\varepsilon_r = 5$ at $x_{diel,1} = 0.24$ cm and $x_{diel,2} = 0.15$ cm on the discharge path. Figure 6.12 shows the distributions of the electron density and the absolute value of the electric field at $t = 5.6$ and 8.9 ns. The first streamer discharge ignited at the point impacts the first layer located at $x_{diel,1} = 0.24$ cm at $t = 3.2$ ns, that is to say, 0.1 ns earlier than for the case with one opaque layer at this position. Indeed the presence of the second thin layer increases slightly the capacitance of the whole interelectrode gap and then the first streamer discharge impacts slightly earlier the first layer when two layers are present. After the impact, the first discharge starts to spread on the upper surface of the first dielectric and at $t = 5$ ns a second discharge starts to propagate axially in the second air gap from the bottom of the first dielectric layer towards the upper surface of the second dielectric. This second discharge is a streamer discharge with, on the axis, a peak electric field of 96 kV cm^{-1} and an electron density of 1.46×10^{13} cm^{-3}, when the discharge front crosses the middle of the second air gap. This second streamer discharge impacts the second layer at $t = 6.2$ ns and starts to spread on the upper

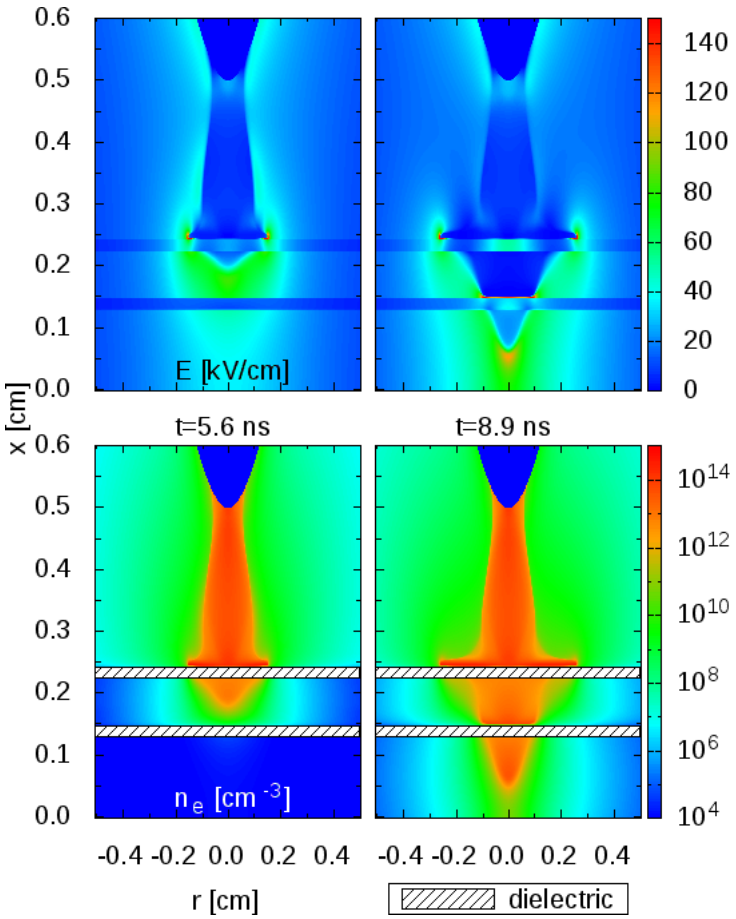

Figure 6.12: *Dynamics of the discharge in the point-to-plane geometry with two thin and opaque dielectric layers located at* $x_{\mathrm{diel}} = 0.24$ *cm and* $x_{\mathrm{diel}} = 0.15$ *cm for an applied voltage of* $\mathrm{U_a}$*=+13 kV. The thickness of both dielectric layers is* $\Delta = 176\,\mu\mathrm{m}$ *and their permittivity is* $\varepsilon_{\mathrm{r}} = 5$*. Cross-sectional views of the absolute value of the electric field and electron density at* $t = 5.6$ *and* 8.9 *ns. Peak values of the scales of electric field and electron density are of 150 kV* cm^{-1} *and* 10^{15} cm^{-3}*, respectively. Peak values of electric field after the first discharge impact on the first dielectric layer are higher and given in the text.*

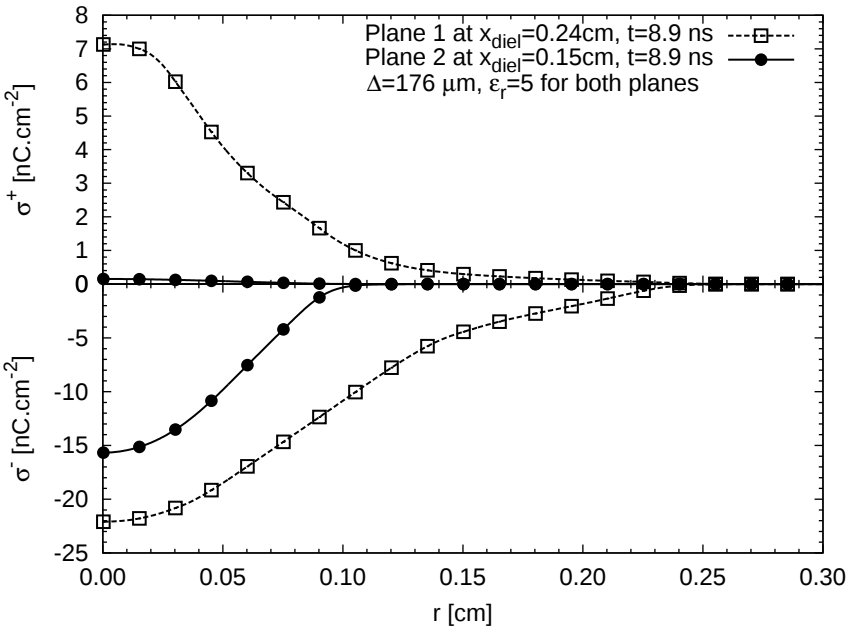

Figure 6.13: *Radial profiles of surface charges on both faces of the two dielectric layers at* $t = 8.9$ *ns for the same condition as Figure 6.12.*

surface of the second dielectric. At $t = 8$ ns, a third discharge starts to propagate axially in the third air gap below the second dielectric towards the plane cathode. As the discharge front crosses the middle of the third air gap, the peak electric field on the axis is of 106 kV cm^{-1} and the electron density is of 2.97×10^{13} cm^{-3}. Then this third discharge is also a streamer discharge. Figure 6.12 shows that for both discharges reignited below the two closely spaced dielectric layers, the radial expansion of these discharges close to the bottom surfaces of the dielectric layers is related to the radial expansion of the surface discharge on the upper surface of the corresponding layer. Finally, we have observed that the third streamer discharge impacts the cathode plane at $t = 9.1$ ns. It is interesting to compare this connection time with the one obtained for one layer. As shown in Table 6.1, for one layer located at $x_{\text{diel}} = 0.24$ cm, the connection time is 12.8 ns and then a second layer located at $x_{\text{diel}} = 0.15$ cm, allows to speed up the propagation of the discharge in the whole interelectrode gap of 3.7 ns. Conversely, for one layer located at $x_{\text{diel}} = 0.15$ cm, the connection time is only of 7.3 ns and then placing a second layer at $x_{\text{diel}} = 0.24$ cm slows down the propagation of the discharge in the whole interelectrode gap of 1.8 ns. It is also interesting to compare the discharge dynamics with two closely spaced thin dielectric layers and with a thick dielectric. Indeed, for the case studied in this section, the upper surface of

the first layer is located at $x_{\text{diel}} = 0.24$ cm and the distance between this surface and the bottom of the second dielectric layer is 1.076 mm. Then this test-case can be easily compared with the case of a thick dielectric with $\Delta = 1$ mm, $\varepsilon_{\text{r}} = 5$ at $x_{\text{diel}} = 0.24$ cm. It is interesting to note that the connection time in the thick case is 10.5 ns, which is 1.4 ns longer than for the case of two layers. Figure 6.13 shows the amount of surface charges on both faces of the two dielectric layers at $t = 8.9$ ns, during the propagation of the third discharge in the interelectrode gap. We note that, as expected, the radial spreading of positive and negative surface charges on the first dielectric layer located at $x_{diel,1} = 0.24$ cm is larger than on the second layer located at $x_{diel,2} = 0.15$ cm. We have calculated the corresponding total charges on both layers at $t = 8.9$ ns, which are of +0.14 nC and -0.99 nC on the first layer and $+1.73\times10^{-3}$ nC and -0.19 nC on the second layer. Then, we note that the amount of positive and negative charges (in absolute value) is the highest for the dielectric layer which is the closest to the point electrode. Similar results have been obtained for the surface charges on several particles placed on the streamer path by (Babaeva et al. 2006). It is interesting to note that for one layer located at $x_{\text{diel}} = 0.24$ cm, as shown in Table 6.5, the amount of positive charges at 9 ns is much less than those obtained for the two layer configuration at $t = 8.9$ ns. Then the presence of a second layer below the first one allows to charge more efficiently the first layer. Conversely, for the case of one layer located at $x_{\text{diel}} = 0.15$ cm, Table 6.3 shows that at $t = 7$ ns, the amount of positive and negative surface charges (in absolute value) is already higher than the amount of surface charges at $t = 8.9$ ns for the two layer configuration. Then, as expected, the presence of a second layer, above the considered layer, decreases the amount of surface charges on the considered layer during the discharge dynamics.

6.5 Conclusion

The main results obtained in this chapter on the study of the dynamics of a positive air discharge at atmospheric pressure behind a dielectric plane obstacle can be summarized as follows:

- In a point-to-plane geometry with a dielectric layer in the interelectrode gap, the first air discharge ignited at the point is stopped in its axial propagation towards the cathode by the dielectric obstacle and spreads along the upper dielectric surface. Depending on the location of the dielectric layer, its permittivity, its thickness and its opacity to radiation, we have shown that a second discharge

may reignite or not below the dielectric. In particular, when the dielectric layer is close to the cathode plane, or when the dielectric layer is thin and transparent to radiation, the second discharge is a positive streamer propagating from the bottom surface of the dielectric layer towards the cathode. Otherwise, in all other cases with reignition shown in this chapter, the second discharge is a weaker ionization front. Surface charges are deposited on both faces of the dielectric layer during the discharge dynamics in the interelectrode gap. Positive charges are deposited on the upper surface of the dielectric layer and negative charges on the bottom surface. The amount of deposited charges depends on the location of the dielectric layer, its permittivity, its thickness and its opacity to radiation. In this chapter, we have shown that the discharge reignition below the dielectric is mostly due to the potential redistribution in the interelectrode gap after the first positive streamer propagation in the first air gap. We have checked that surface charge deposition on the two faces of the dielectric layer has a small influence on reignition.

- Finally, with two closely spaced thin dielectric layers in the discharge path, we have observed a series of discharge spreading/reignition for each dielectric layer. Both faces of the dielectric layers are charged during the discharge dynamics in the interelectrode gap, with the highest amount of positive and negative charges (in absolute value) for the dielectric layer which is the closest to the point electrode.

Chapter 7

Influence of the polarity and amplitude of the applied voltage on the reignition dynamics

7.1 Introduction

In chapter 6, we have studied the reignition dynamics for a constant positive applied voltage at the beginning of the discharge simulation. In this chapter, we consider the same point-to-plane geometry with a fixed position of the dielectric layer between electrodes, and we study the influence of the polarity and amplitude of the applied voltage on the conditions of the reignition below the dielectric layer obstacle. It is interesting to note that these last years, studies on plasma jets have addressed also the question of discharge reignition. Indeed, experimental and numerical results show that after an ionization wave exit from a source tube, it impacts the outer surface of a spatially separate and electrode-less second tube and produces a new ionization wave inside the second tube (Xiong et al. 2013; Lu et al. 2009; Wu et al. 2011; Johnson et al. 2011). In (Xiong et al. 2013), this reignition process was called plasma transfer. In (Xiong et al. 2013), it was shown with 2D numerical simulations that whatever the polarity of the primary ionization wave ignited in the source tube, the secondary ionization wave ignited in the transfer tube is positive. It is interesting to note that a good qualitative agreement with experiments was obtained on the dynamics of the discharge reignition in the transfer tube in (Xiong et al. 2013) for both polarities of the primary discharge. So in this work, we will compare results for different polarities on the reignition dynamics of a discharge at atmospheric pressure with the results of (Xiong et al. 2013).

In Section 7.2, we present the studied discharge set-up and the discharge model. In Section 7.3, for a positive polarity at the point electrode, we study the influence of the applied voltage on the simulation of the dynamics of reignition behind a dielectric obstacle. Then in Section 7.4, we go into the results obtained for the simulation of the dynamics of reignition for a negative polarity at the point electrode.

7.2 Studied configuration and model

The discharge set-up is similar to the one used in chapter 6 and shown in Figure 6.1. In chapter 6, we have studied the discharge dynamics for a positive constant voltage of U_a = +13 kV applied at the point electrode at the beginning of the simulation. In this chapter, we study the influence of the value of the applied voltage and its polarity on the discharge dynamics. We consider variations of U_a in the range 13 to 18 kV for positive polarity and from −9 to −15 kV for negative polarity. For all simulations presented in this chapter, we have considered as a reference a simulation time of $t_{sim}^{lim} = 16$ ns. If a discharge reignites in the second air gap before t_{sim}^{lim}, simulations are stopped after the propagation of the reignited discharge in the second air gap. If there is no reignition in the second air gap before t_{sim}^{lim}, the calculation is stopped at t_{sim}^{lim}.
In chapter 6, we have varied the value of the thickness Δ of the dielectric layer, the axial location of its upper surface x_{diel} and its permittivity ε_r. In this chapter we consider fixed values of $\Delta = 176\mu$m, x_{diel} =0.35 cm and $\varepsilon_r = 5$. For the simulations presented in this chapter, as mentioned in chapter 4, we have used the explicit parallel OPENMP discharge code with the PaStiX solver. All the details of the model are given in chapter 1. The mesh is the same as in chapter 5.
For a negative applied voltage at the point electrode, as already mentioned in the negative CDBD configuration in Section 5.4 and as will be detailed in Section 7.4, we have observed that in some conditions, the negative surface charge on one side of the dielectric layer is high enough (in absolute value) to reverse the electric field close to the dielectric surface. In this case, we have studied the influence of allowing or not electrons deposited on the dielectric surface to be released into the gas phase depending on the drift velocity calculated at the air/dielectric interface. The influence of boundary conditions at the dielectric/air interface on the results will be discussed in Section 7.4.
As in chapter 6, we have assumed, as initial condition, a low uniform

density of 10^4 cm^{-3} electrons and positive ions in air below and above the dielectric layer.

7.3 Influence of the amplitude of a positive voltage applied at the point electrode on the discharge reignition below the dielectric layer

U_a kV	τ_{igni} (ns)	τ_{impact} (ns)	t_I (ns)	K_I^{max}	$E_{moy}(t_I)$ (kV.cm^{-1})	τ_{rei} (ns)	τ_{connec}^{plane} (ns)
+13	0.8	2.0	2.6	17.72	32	-	-
+14	0.7	1.7	2.4	21.5	35.2	-	-
+15	0.6	1.4	2.0	26.65	38	4.5	11.9
+16	0.5	1.2	1.7	32.35	40.9	3.4	7.5
+18	0.4	0.9	1.3	45.5	46.6	2.1	4.5

Table 7.1: *Influence of the amplitude of the positive applied voltage U_a on τ_{igni}, the time of ignition of the first discharge at the point electrode, τ_{impact}, the time of impact of the first positive discharge on the upper surface of the dielectric layer, t_I the time at which the maximum of the ionization integral K_I^{max} is reached, $E_{moy}(t_I)$ the average electric field in the second gap at $t = t_I$, τ_{rei} the time of reignition of a second discharge below the dielectric layer, and τ_{connec}^{plane}, its time of impact at the grounded plane.*

In chapter 6, for a dielectric layer located at x_{diel} =0.35 cm and an applied voltage of U_a = +13 kV, no reignition was observed during the 16 ns simulated. In this section, we study for this position of the dielectric layer, the influence of the applied voltage U_a in the range 13 kV to 18 kV on the reignition of the discharge. For U_a = 18 kV, Figure 7.1 shows the distributions of the electron density and absolute values of the electric field at t = 0.9, 2.1 and 4.5 ns and Table 7.1 gives some characteristics of the discharge dynamics. First we observe the ignition of a positive streamer discharge at the point electrode at τ_{igni} = 0.4 ns. This first discharge propagates in the gap and impacts the dielectric layer at τ_{impact} = 0.9 ns. Then the discharge starts to spread on the upper surface of the dielectric layer. As expected, we note in Table 7.1 that τ_{igni} and τ_{impact} decrease as the applied voltage increases.
As the first discharge approaches the dielectric surface, Figure 7.1 shows

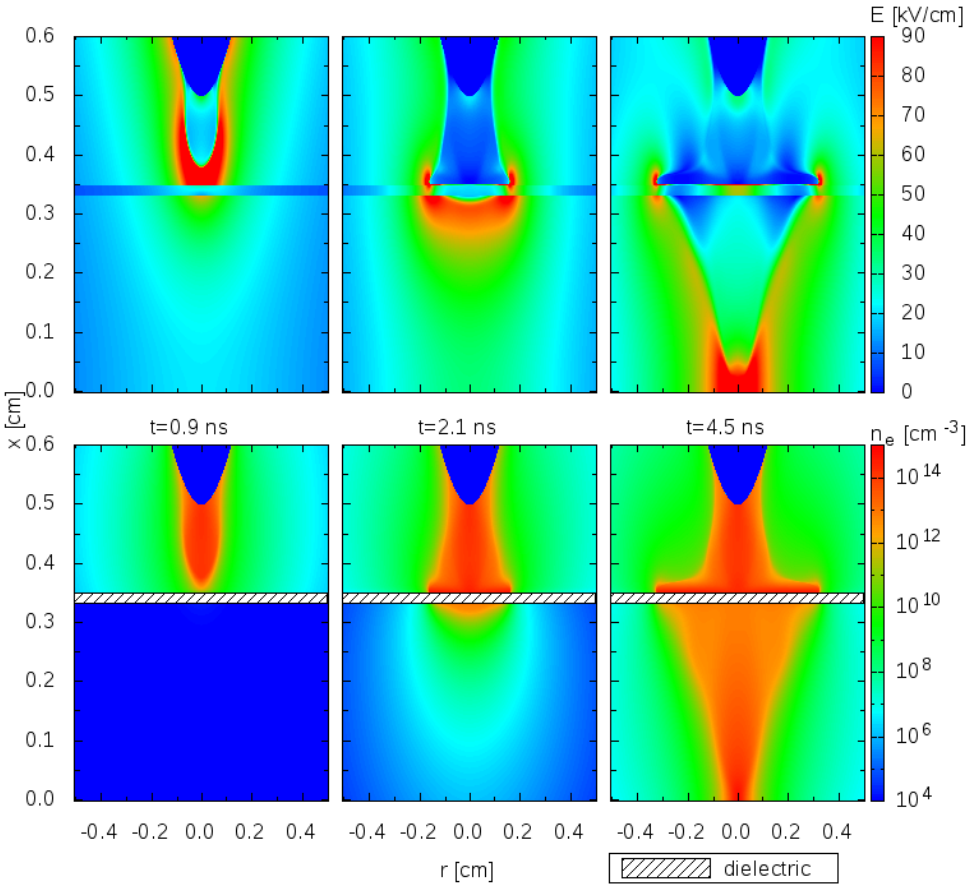

Figure 7.1: *Discharge dynamics with a dielectric layer ($\Delta = 176\,\mu$m and $\varepsilon_r = 5$) located at $x_{diel} = 0.35$ cm. A positive voltage $U_a = 18$ kV is applied at the point electrode. Cross-sectional views of the absolute value of the electric field and electron density at $t = 0.9$, 2.1 and 4.5 ns.*

that the electric field close to the discharge axis in the dielectric layer and in the air gap below the layer increases. Then avalanches originating from seed electrons appear in the second air gap, close to the discharge axis. Figure 7.1 shows that for $U_a = 18$ kV, a second discharge reignites just below the dielectric layer at $\tau_{rei} = 2.1$ ns. This second discharge has a positive discharge front and propagates from the bottom dielectric surface towards the grounded plane. When the discharge front crosses the middle of the second air gap at $t = 3.8$ ns, the values of the peak electric field and the electron density on the axis are 97 kV cm^{-1} and 2×10^{13} cm^{-3}, respectively. Behind the discharge front as it propagates, the electric field is significantly reduced in the ionized channel and we consider that the second discharge ignited below the dielectric layer is a positive streamer discharge. Figure 7.1 shows that this second positive streamer discharge connects at the grounded plane at $\tau_{connec}^{plane} = 4.5$ ns. This dynamics of reignition is in good agreement with the dynamics of plasma transfer observed for a positive polarity in (Xiong et al. 2013) and called top-down process.

Figures 7.2 (a) and (b) show the time evolutions of the radial profiles of surface charges in absolute value on both faces of the dielectric layer for the same condition as Figure 7.1. For $t \geq \tau_{impact} = 0.9$ ns, the first positive discharge spreads along the upper dielectric surface and charges it. As expected, Figure 7.2 (a) shows that the surface charge on the upper dielectric surface is positive and is due to positive ions deposited on the dielectric surface. We note that the positive surface charge increases slowly in time and has only a peak value of 0.1 nC cm^{-2} at $t = \tau_{rei}$. In the second gap, as avalanches originating from seed electrons occur, electrons which are much more mobile than ions, drift towards the point anode and are stopped by the dielectric obstacle and then charge its bottom surface negatively. Then, Figure 7.2 (b) shows that for $t \geq \tau_{impact}$, a negative surface charge is deposited on the bottom dielectric surface and increases (in absolute value) rapidly to reach a peak absolute value of 6.5 nC cm^{-2} at $t = \tau_{rei}$. Figures 7.2 (a) and (b) show that for $t \geq \tau_{impact} = 0.9$ ns, positive and negative surface charges increase (in absolute value) and expand radially, due to the surface streamer propagation on the upper dielectric surface.

To check the influence of surface charges on the reignition below the dielectric layer, Figure 7.3 compares the Laplacian potential calculated on the discharge axis at $t = 0$ s, with the potential calculated in taking into account only surface charges deposited at $t = \tau_{\mathrm{rei}}$, and the total potential calculated at $t = \tau_{\mathrm{rei}}$. We note that the small amount of deposited surface charges on both faces of the dielectric layer at the reignition time induces a

small peak of negative potential of −1.76 kV at the surface of the dielectric on the grounded plane side and then slightly decreases the electric field in the second air gap. However, in comparison with the value of the total potential (16.2 kV) at the same axial position, we note that the decrease in potential due to surface charges is almost negligible and then one can assume that surface charges deposited on both faces of the dielectric layer have a negligible influence on the reignition of the discharge in the second air gap. We have checked that this conclusion is valid for all cases with a second discharge reignition (i.e. for $U_a \geq 15$ kV) in Table 7.1. For $U_a = 18$ kV, Figure 7.3 shows that after the first streamer impact on the dielectric surface, due to the space charges in the streamer channel, the voltage drop in the first air gap is significantly decreased in comparison with the initial Laplacian voltage drop. Then at the time of reignition, Figure 7.3 shows that the most significant voltage drop in the whole interelectrode gap is applied on the second air gap. Then, for an applied voltage of $U_a = 18$ kV, Figure 7.1 shows that at $t = \tau_{rei} = 2.1$ ns, that is to say 1.2 ns after the first streamer impact on the upper dielectric surface, a second positive streamer discharge reignites below the dielectric layer and impacts the grounded plane at $t = \tau_{connec}^{plane} = 4.5$ ns. Table 7.1 shows that for $U_a \geq 15$ kV, as expected, the reignition time of the second discharge and its connection time at the cathode decrease as the applied voltage increases.

To study more precisely the influence of the applied voltage on the reignition in the second gap for a dielectric layer located at x_{diel} =0.35 cm, we have calculated the ionization integral K_I on the length of the second air gap (i.e. $l = x_{diel} - \Delta$) on the symmetry axis. In an attaching gas as air, the ionization integral is given by (Raizer 1991):

$$K_I = \int_0^l \left[\alpha \left(\frac{E}{N}(x) \right) - \eta \left(\frac{E}{N}(x) \right) \right] \mathrm{d}x \tag{7.1}$$

where α is the impact ionization coefficient and η is the attachment coefficient. Both coefficients are dependent on the local reduced electric field $E/N\,(x)$. According to the Meek's criterion, if $K_I = K_{Meek} \simeq 18$ to 21, the exponential avalanche multiplication is such that the electric field of its space charge reaches a value of the order of the external field. However, it is important to note that this criterion has been derived initially for an homogeneous external field with no dielectric boundaries. As shown on Figure 7.1, the electric field in the second air gap is highly non homogeneous. Then, we have also calculated the average absolute value

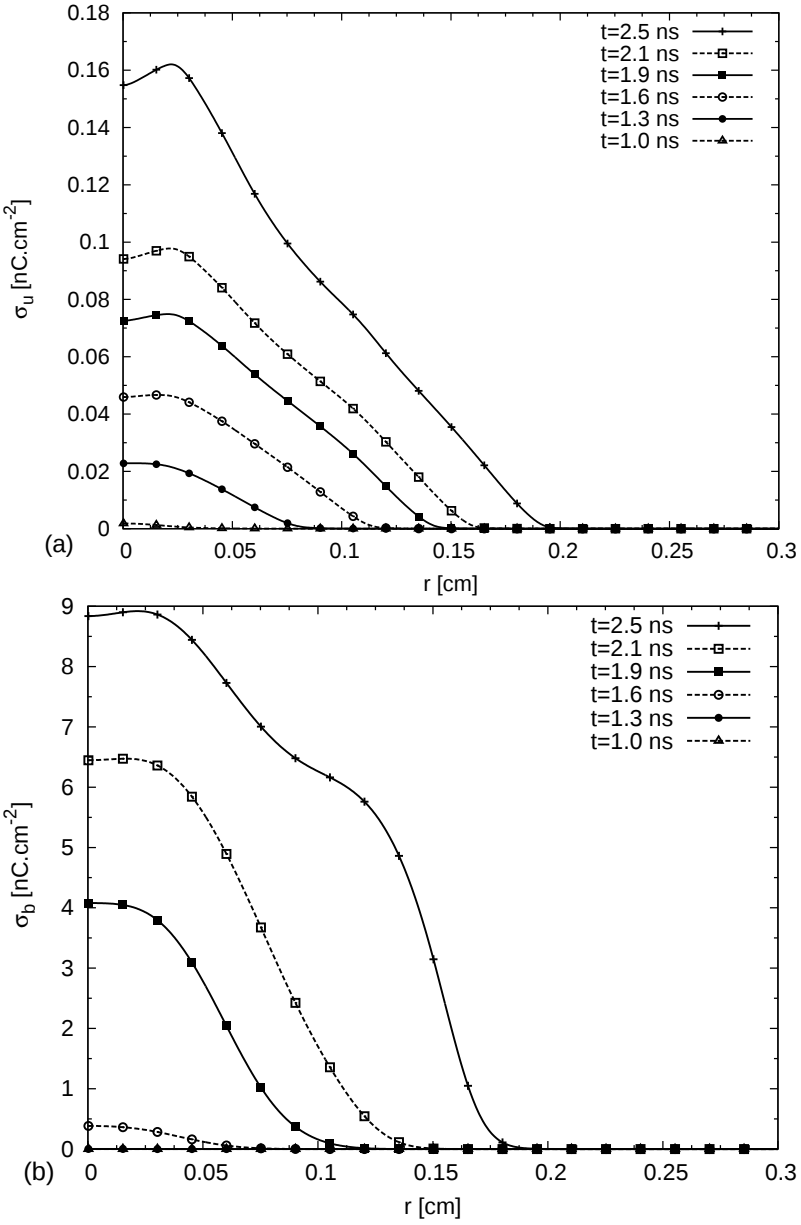

Figure 7.2: *Time evolutions of the radial profiles of positive surface charges σ_u deposited on the upper dielectric surface and absolute value of negative surface charges σ_b deposited on the bottom surface of the dielectric layer for the same condition as Figure 7.1.*

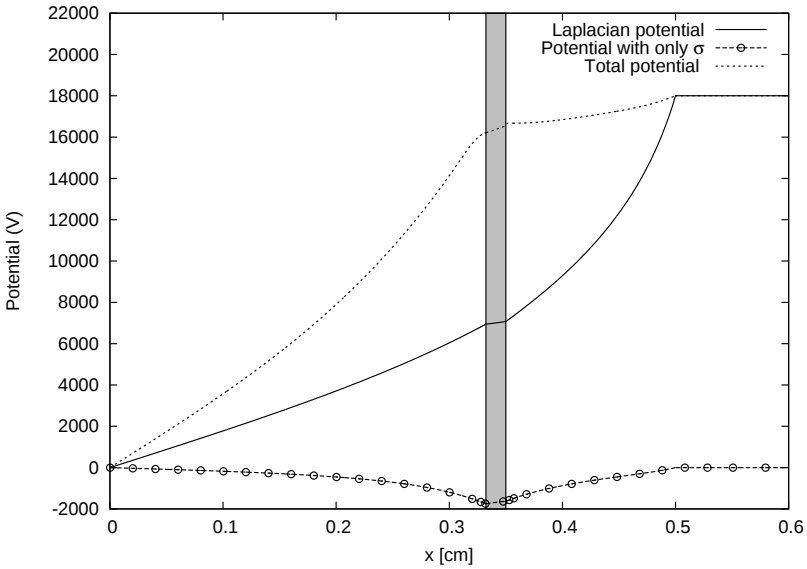

Figure 7.3: *Absolute value of the potential on the symmetry axis for the same condition as Figure 7.1. Laplacian potential at $t = 0$ ns, total potential at $t = \tau_{\text{rei}} = 2.1$ ns and potential calculated in taking into account only surface charges deposited on both faces of the dielectric layer at $t = \tau_{\text{rei}}$.*

of the axial electric field E_{moy} in the second air gap:

$$E_{moy} = \frac{\left| \int_0^l E_x\,(x)\ \mathrm{d}x \right|}{l} \tag{7.2}$$

For all conditions studied in this chapter, we have noted that during the first streamer propagation, the value of K_I increases and reaches a peak value at time $t = t_I$. Then, the coefficient K_I decreases, all the more rapidly that a second discharge reignites below the dielectric layer. Table 7.1 shows that, as the applied voltage increases, the value of t_I decreases and the value of K_I^{max} increases. We also note that the value of the average electric field $E_{moy}(t_I)$ increases as the applied voltage increases. For all studied voltages in the range 13 to 18 kV, we note that $E_{moy}(t_I)$ is higher than 30 kV cm^{-1}, the breakdown electric field in air. However, Table 7.1 shows that no reignition is observed in the second gap for $U_a < 15$ kV. For all studied voltages, we note that the peak value of K_I^{max} is reached between 0.4 and 0.7 ns after the first discharge impact on the upper dielectric surface. Table 7.1 shows that $K_I^{max} > K_{Meek}$ for $U_a >$ 13 kV, but to observe a reignition in the second gap, the applied voltage has to be increased to values higher than 15 kV. So for the conditions studied, a minimum value of $K_I^{max} = K_I^{lim,+} \simeq 26$ has to be reached to observe the breakdown of the point-to-plane interelectrode gap.

7.4 Influence of a negative voltage applied on the point electrode on the discharge reignition below the dielectric layer

In this section, we study the reignition dynamics for a negative applied voltage at the point electrode for an applied voltage U_a in the range -15 to -9 kV. Figure 7.4 shows the distributions of the electron density and

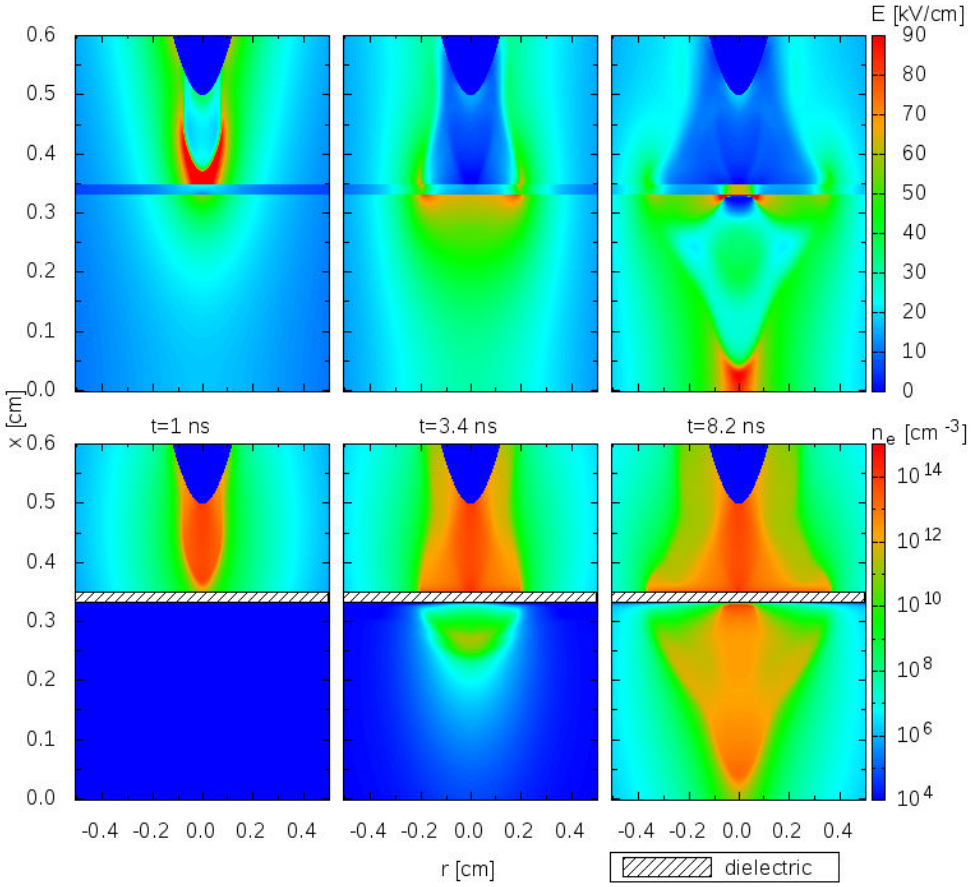

Figure 7.4: *Discharge dynamics with a dielectric layer ($\Delta = 176\,\mu$m and $\varepsilon_r = 5$) located at $x_{diel} = 0.35$ cm. A negative voltage $U_a = -15$ kV is applied at the point electrode. Cross-sectional views of the absolute value of the electric field and electron density at $t = 1.0$, 3.4 and 8.2 ns.*

the absolute value of the electric field at $t = 1,\ 3.4$ and 8.2 ns for an applied voltage of $U_a = -15$ kV and Table 7.2 gives some characteristics of the discharge dynamics. First, we observe the ignition of a negative streamer discharge at the point electrode at τ_{igni}= 0.3 ns. This first negative discharge propagates in the gap and impacts the dielectric layer at $\tau_{impact} = 1$ ns. Then the negative discharge starts to spread on the upper surface of the dielectric layer following the same dynamics as in the negative CDBD configuration studied in Section 5.4. Table 7.2 shows that as $|U_a|$ decreases, as expected, τ_{igni} and τ_{impact} increase. If we compare both polarities for $|U_a| = 13$ to 15 kV, in Tables 7.1 and 7.2, we note that the times of ignition and impact are shorter for a negative polarity.
Figures 7.5 (a) and (b) show the axial profiles of charged species densities and the axial electric field close to the upper dielectric surface at $t = \tau_{impact} =$ 1 ns and $t = 2$ ns for the same conditions as Figure 7.4. At $\tau_{impact} =$ 1 ns, the first negative discharge impacts the dielectric layer and close to the upper dielectric surface, low densities of charged species are obtained whereas a quite high positive value of the axial electric field (about 150 kVcm^{-1}) is reached. Then, a sheath forms and at $t = 2$ ns, as shown on Figure 7.5 (b), a low (even slightly negative i.e. directed towards the grounded plane over about 10 μm above the dielectric surface) axial electric field and high densities of electrons and positive ions are obtained close to the upper dielectric surface. The dynamics of the sheath formation is interesting to point out. First at $\tau_{impact} =$ 1 ns, the electric field is directed towards the point electrode as shown on Figure 7.5(a), and then negative charges (mostly electrons which are much more mobile than negative ions) rapidly accumulate on the upper surface of the dielectric layer. On the axis of symmetry, due to the large amount of negative surface charges deposited on the upper dielectric surface, we have observed a reversal of electric field close to this dielectric surface. Due to this field reversal at the air/dielectric interface, in this chapter, we have tested different boundary conditions for electrons as in the negative CDBD configuration (Section 5.4). First, we have considered that electrons deposited on the dielectric surface are not allowed to be released from the surface based on the sign of their drift velocity at the interface. In this case, we observe that after the impact of the first negative streamer on the upper dielectric surface, due to the high amount of negative charges rapidly deposited on the dielectric surface, the axial electric field rapidly changes of sign and becomes negative (and then is directed towards the grounded plane) on a thickness of 10-15 μm above the dielectric surface. The reversed axial electric field reaches an absolute value of about 150 kV cm^{-1}. Due to this high value, positive charges

drift to the upper dielectric surface to reduce the value of the deposited negative surface charge and then the electric field decreases to very low values. In this case, it is interesting to note that it takes about 1 ns to obtain the sheath formation on the axis of symmetry. Second, we have allowed electrons deposited on the dielectric surface to be released into the gas phase due to the field reversal, based on the sign of their drift velocity at the interface. As a consequence, we have observed that in less than 0.5 ns, close to the axis of symmetry, the negative surface charge on the upper dielectric surface decreases and the electric field close to the upper dielectric surface decreases rapidly to very low values. Then it is interesting to note that with both boundary conditions, at $t = 2$ ns, we have the same profiles of charged species densities and axial electric field on the symmetry axis as shown on Figure 7.5 (b). It is important to point out that, the choice of one of these two boundary conditions has a negligible influence on the reignition dynamics below the dielectric layer. As the first discharge approaches the dielectric surface, Figure 7.4 shows that the electric field close to the discharge axis in the dielectric layer and in the air gap below the layer increases. Then avalanches originating from seed electrons appear in the second air gap. It is interesting to note that the reignition dynamics is different from the one obtained for a positive applied voltage. Indeed, for a negative applied voltage at the point electrode, electrons in the second gap drift towards the grounded plane and then Figure 7.4 shows that at $t = \tau_{rei} = 3.4$ ns a discharge reignites in the second air gap, at a small distance below the dielectric layer. Figures 7.6 (a) and (b) show the time evolutions of the axial electric field and of the electron density on the symmetry axis in the second air gap from $t = 2$ to 8 ns. For $t < \tau_{rei} = 3.4$ ns, we observe that the electron density increases in the second air gap, with a maximum which moves from the vicinity of the dielectric layer toward the grounded plane, in a slowly varying electric field. At $t = 3.4$ ns, the maximum electron density is located at $x = 0.27$ cm and is of 2.1×10^{11} cm^{-3}. For $t \geq 3.4$ ns, on Figures 7.4 and 7.6, we observe the ignition and the propagation of a double headed discharge, with positive and negative discharge fronts. The positive discharge front propagates towards the bottom surface of the dielectric layer. This discharge has only a small distance to develop and impacts the dielectric surface at $\tau_{connec}^{diel} = 6.4$ ns. We observe that the positive discharge front is rather smooth as it starts propagating and becomes sharper as it comes closer to the dielectric surface with at $t = 6$ ns a peak electric field of about 88 kV cm^{-1} and a maximum electron density of the order of 4×10^{12} cm^{-3} behind the discharge front. The negative discharge front propagates towards the grounded plane and impacts it at $\tau_{connec}^{plane} = 8.2$ ns.

We observe that the peak electric field in the negative discharge front and the maximum electron density behind the discharge front increase as the negative discharge propagates toward the grounded electrode. At $t = 8$ ns, just before the connection at the grounded plane, the peak electric field in the negative discharge front is of about 79 kV cm^{-1} with a maximum electron density of the order of 9.6×10^{12} cm^{-3} behind the discharge front. Table 7.2 shows that for $|U_a| \geq 13$ kV, the connection times of the positive and negative fronts on the dielectric surface and grounded plane respectively, decrease as the absolute value of the applied voltage increases. In (Xiong et al. 2013), for plasma transfer with a negative polarity of the first ionization wave, the reignition process is described as a bottom-up process. In their conditions, the second gas gap is between two dielectric layers. They observe that avalanches in the transfer channel start from the bottom dielectric surface and a positive ionization wave propagates to the top wall dielectric surface of the transfer tube. In our conditions, the second air gap is between a dielectric layer and a grounded plane. In this case, we observe a slightly different dynamics with a double headed discharge with one positive discharge front propagating towards the dielectric surface and a negative discharge front propagating towards the grounded plane. However, in this study, as in (Xiong et al. 2013), we note that the reignition dynamics is different depending on the polarity of the first ionization wave.

U_a kV	τ_{igni} (ns)	τ_{impact} (ns)	t_I (ns)	K_I^{max}	$E_{moy}(t_I)$ (kV.cm^{-1})	τ_{rei} (ns)	τ_{connec}^{diel} (ns)	τ_{connec}^{plane} (ns)
-9	0.9	3.7	10.8	1.9	23.2	-	-	-
-11	0.6	2.1	3.7	6.7	27.3	-	-	-
-13	0.4	1.4	2.2	14.25	32.5	12	21.8	18.8
-14	0.4	1.2	1.8	18.9	35.1	4.5	10	11.8
-15	0.3	1.0	1.5	24.1	37.7	3.4	6.4	8.2

Table 7.2: *Influence of the amplitude of the negative applied voltage U_a on τ_{igni}, the time of ignition of the first discharge at the point electrode, τ_{impact}, the time of impact of the first positive discharge on the upper surface of the dielectric layer, t_I the time at which the maximum of the ionization integral K_I^{max} is reached, $E_{moy}(t_I)$ the average electric field in the second gap at $t = t_I$, τ_{rei} the time of reignition of a second discharge below the dielectric layer, τ_{connec}^{diel}, the time of impact on the bottom surface of the dielectric and τ_{connec}^{plane} the time of impact on the grounded plane.*

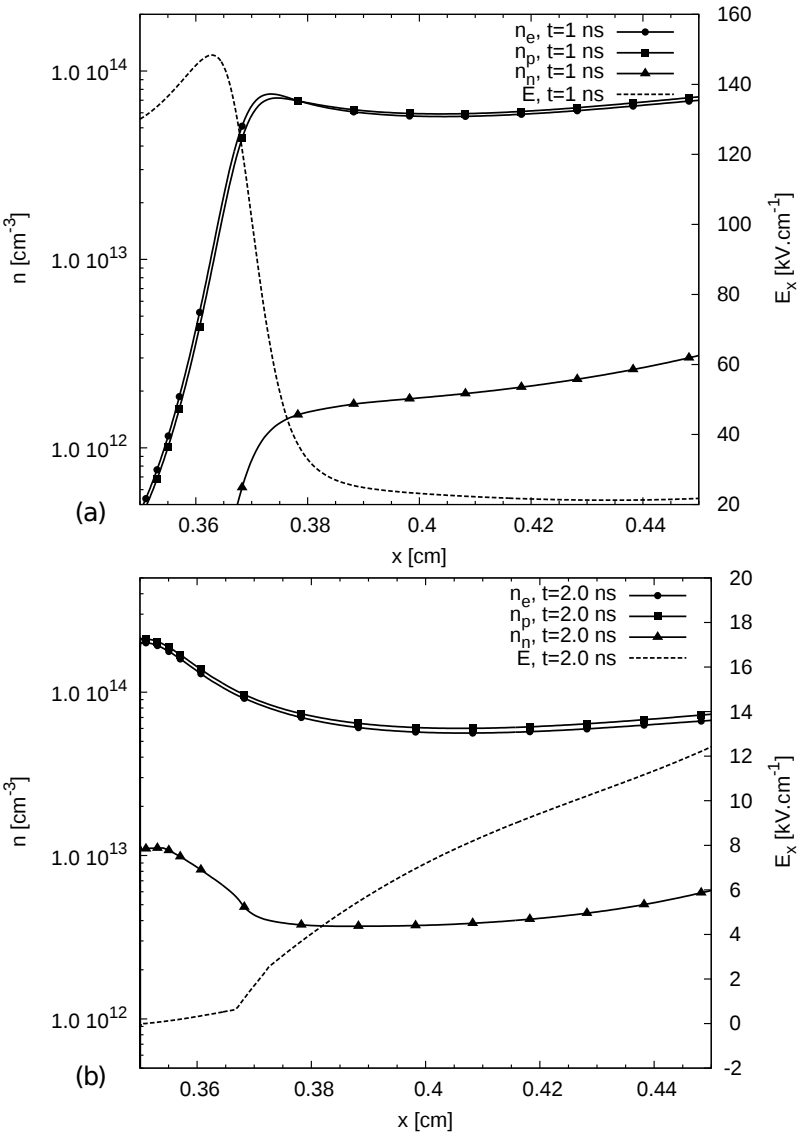

Figure 7.5: *Axial profiles of charged species densities and of the axial electric field close to the upper dielectric surface at* $t = \tau_{impact} = 1$ *ns and* $t = 2$ *ns for the same conditions as Figure 7.4.*

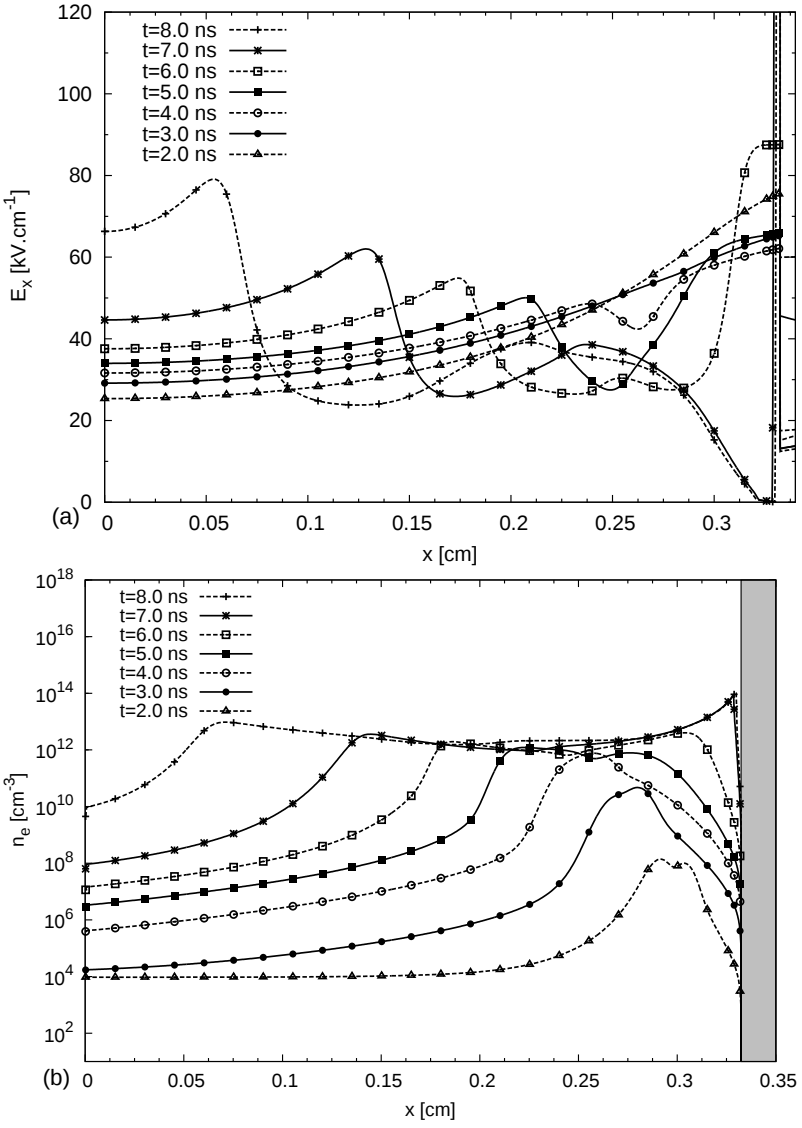

Figure 7.6: *Time evolutions of the axial profiles of electron density on the symmetry axis and of the axial electric field in the second air gap for the same conditions as Figure 7.4.*

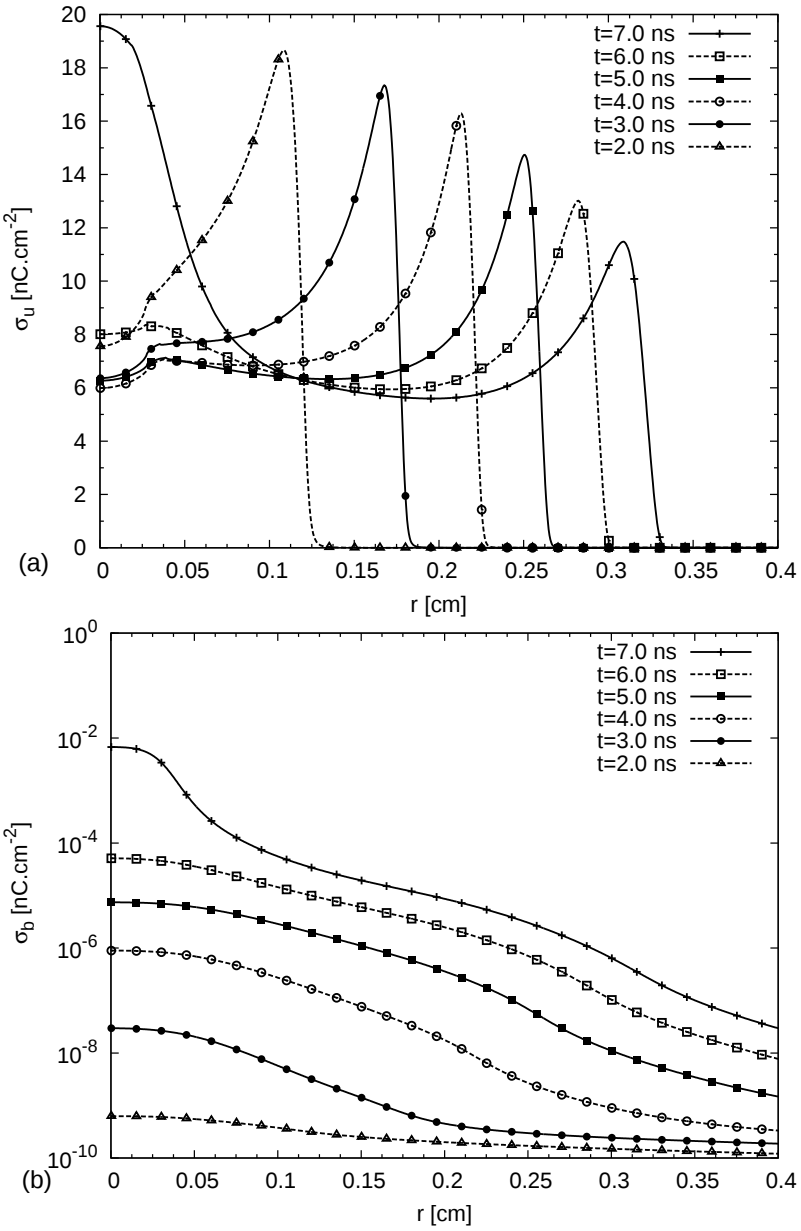

Figure 7.7: *Time evolutions of the radial profiles of the absolute value of negative surface charges σ_u deposited on the upper dielectric surface and positive surface charges σ_b deposited on the bottom surface of the dielectric layer for the same conditions as Figure 7.4.*

Figures 7.7 (a) and (b) show the time evolutions of the radial profiles of surface charges on both faces of the dielectric layer for the same condition as Figure 7.4 for $t = 2$ to 7 ns. For $t \geq \tau_{impact} = 1$ ns, the first negative discharge spreads along the upper dielectric surface and starts to charge it. As expected, Figure 7.7 (a) shows that the surface charge on the upper dielectric surface is negative and is due to electrons, depositing on the dielectric surface. For $t \geq 2$ ns, the maximum of the absolute value of the negative surface charge is out of axis and moves radially following the spreading of the negative surface discharge on the dielectric layer. As for the negative CDBD configuration (Section 5.4 on Figures 5.4 to 5.5 (bottom Figures)), the front of the negative discharge is located on the dielectric surface as it moves radially. At $t = 3$ ns, shortly before $\tau_{rei} = 3.4$ ns, the amount of negative surface charges on the upper dielectric surface has a peak absolute value of 17.3 nC cm^{-2}. We observe that the value of this peak decreases as the negative surface discharge expands radially on the dielectric surface. On the axis of symmetry, on Figure 7.7 (a), we note that for $t = 2$ ns to 4 ns, the absolute value of the surface charge decreases and then for $t > 4$ ns, it increases, slowly at first and then more rapidly as the positive discharge front of the second discharge reaches the bottom surface of the dielectric layer. It is interesting to note that the time evolution of radial profiles of negative surface charges on the upper dielectric surface is quite different from the one obtained in the negative CDBD configuration on Figure 5.9. In the negative CDBD configuration, the maximum of amount of surface charges is always on the axis of symmetry. On Figure 7.7 (b), on the bottom dielectric surface, we note that, during the ignition and propagation of the second discharge, a small, almost negligible, positive surface charge deposits and accumulates in time due to positive ions drifting towards the point electrode and stopped by the dielectric obstacle.

To check the influence of surface charges on the reignition below the dielectric layer, Figure 7.8 compares the Laplacian potential calculated on the discharge axis at $t = 0$ ns, the total potential at $t = \tau_{\mathrm{rei}} = 3.4$ ns and the potential calculated in taking into account only surface charges deposited on both faces of the dielectric layer at $t = \tau_{\mathrm{rei}}$. We note that the large amount of negative charges deposited on the upper surface of the dielectric induces a peak of negative potential of -6 kV at the surface of the dielectric on the grounded plane side. On figure 7.8, at the same axial location, the total potential has a value of -13.7 kV. Then, Figure 7.8 shows that in this simulation, the negative charges deposited on the upper surface of the dielectric accounts for 47.7% of the total potential close to the bottom dielectric surface at the time of reignition. Com-

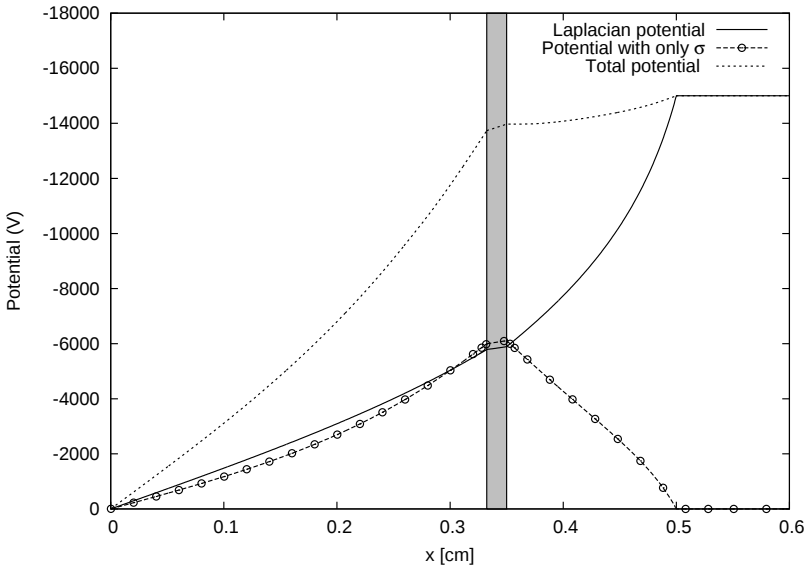

Figure 7.8: *Absolute value of the potential on the symmetry axis for the same condition as Figure 7.4. Laplacian potential at* $t = 0$ *ns, total potential at* $t = \tau_{\text{rei}} = 3.4$ *ns and potential calculated in taking into account only surface charges deposited on both faces of the dielectric layer at* $t = \tau_{\text{rei}}$.

pared to results shown in Section 7.3 for a positive polarity of the first discharge, in the case of a negative discharge impacting the upper surface of the dielectric plane, negative surface charges deposited on the upper dielectric surface of the dielectric layer, have a non negligible influence on the reignition dynamics in the second air gap.

To study more precisely the influence of the negative applied voltage on the reignition in the second gap for a dielectric layer located at x_{diel} =0.35 cm, we have calculated as in Section 7.3 the ionization integral K_I and E_{moy} on the length of the second air gap on the symmetry axis. For all conditions studied in this chapter, we have noted that during the first streamer propagation, the value of K_I increases and reaches a peak value at $t = t_I$. Then, the coefficient K_I decreases, all the more rapidly that a second discharge reignites below the dielectric layer. Table 7.2 shows that, as $|U_a|$ increases, the value of t_I decreases and the value of K_I^{max} increases. For all studied voltages, we note that the time difference between the first discharge impact on the upper dielectric surface at $t = \tau_{impact}$ and the time moment t_I when the coefficient K_I reaches its maximum, decreases as the applied voltage increases. For $U_a = -13$ to -15 kV, it is interesting to point out that this time difference is of about 0.5 to 0.8 ns, close to values obtained for $U_a = 13$ to 15 kV in Table 7.1. Table 7.2 shows that the value of the average electric field $E_{moy}(t_I)$ increases as the applied

voltage increases. It is interesting to point out that a reignition in the second gap is observed for $|U_a| \geq 13$ kV, which corresponds to conditions in which $E_{moy}(t_I)$ is higher than 30 kV cm^{-1}, the breakdown electric field in air. Table 7.2 shows that to obtain a reignition in the second gap and then, the breakdown of the whole interelectrode gap, a minimum value of the ionization integral $K_I^{lim,-} \simeq 14$ has to be obtained. As shown on Figure 7.4 for $U_a = -15$ kV, the reignited double headed discharge is weaker than a double headed streamer discharge in air at atmospheric pressure (Bourdon et al. 2007). Then, as expected, the minimal value of the ionization integral to have a reignition in the second gap $K_I^{lim,-}$ is less than K_{Meek}.
Finally, it is interesting to compare the influence of the polarity on the breakdown of the whole point-to-plane interelectrode gap. We note that the breakdown voltage, for the studied geometry is about $|U_a| = 13$ kV in negative polarity and is higher and about $U_a = 15$ kV for a positive polarity. This breakdown voltage difference between positive and negative polarities is in agreement with experimental results in high voltage applications [(Lebedev et al. 2005) and references therein]. Interestingly, we note that the value of the average electric field in the second air gap is a good criterion for the reignition for a negative polarity. If the average electric field in the second gap reaches the breakdown electric field in air, reignition is observed. Conversely for a positive polarity, the results of Table 7.1 show that even if the average electric field in the second gap is higher than the breakdown electric field in air, no reignition may be observed. Based on the different voltages, it was shown that the minimum ionization integral to have reignition in the second air gap (or breakdown of the whole point-to-plane interelectrode gap) for the studied geometry is $K_I^{lim,-} \simeq 14$ for a negative polarity and is higher and equal to $K_I^{lim,+} \simeq 26$ for a positive polarity.

7.5 Conclusion

The main results of this chapter on the influence of the polarity and amplitude of the applied voltage on the reignition dynamics can be summarized as follows:

- For a positive or a negative voltage applied at the point electrode, first, a streamer discharge ignites at the point and propagates towards the dielectric layer. The polarity of the first streamer discharge is the same as the applied voltage. After the impact on the

dielectric surface, the streamer discharge spreads along the upper dielectric surface and charges positively or negatively depending on its polarity. On the bottom surface of the dielectric layer, a surface charge with an opposite polarity is deposited. When we compare results for a positive applied voltage at the point electrode, where the reignition below the dielectric is mostly due to the potential redistribution in the interelectrode gap after the first streamer propagation in the first air gap and that surface charges deposited on both faces of the dielectric layer have a small influence on reignition, conversely, for a negative applied voltage, negative surface charges deposited on the upper surface of the dielectric layer have a significant contribution on the discharge reignition.

- We have shown that the dynamics of reignition of air discharges below a dielectric layer depends on the polarity of the voltage applied at the point electrode. For a positive applied voltage, if a discharge reignites below the dielectric layer, it is a positive ionization wave propagating from the bottom dielectric surface towards the grounded plane. For a negative applied voltage, if a discharge reignites below the dielectric layer, it is a double headed discharge with positive and negative discharge fronts. The positive discharge front propagates towards the bottom dielectric surface and the negative discharge front towards the grounded plane.

- Finally, we have compared the conditions to obtain a discharge reignition in the second gap, that is to say to have breakdown in the whole interelectrode gap, as a function of the polarity of the applied voltage at the point electrode. It is shown that the minimum applied voltage to have a discharge reignition is lower in absolute value for a negative applied voltage than for a positive one. For the geometry studied in this chapter, we have shown that the minimum ionization integral to have reignition in the second air gap is about 14 for a negative applied voltage and of about 26 for a positive applied voltage.

Chapter 8

Comparisons of experimental and simulation results on the reignition dynamics

8.1 Introduction

In the framework of the ALVEOPLAS project, in this chapter, we present the comparison of experimental results obtained at LPGP with numerical results on the reignition dynamics behind a dielectric plane obstacle of an air discharge at atmospheric pressure.
First in Section 8.2, we present the experimental set up and the numerical model. In Section 8.3, we compare experimental and numerical results in the experimental point-to-plane geometry without the dielectric plane obstacle. Then in Section 8.4, we compare experimental and numerical results with the dielectric plane obstacle placed in the inter-electrode gap. In Section 8.5, we discuss the experimental and numerical results to identify physico-chemical processes that could improve the experimental/modelling comparison. Finally in Section 8.6 we present a numerical study on the influence of emission processes at the cathode surface on the reignition dynamics.

8.2 Experimental set up and numerical model description

Figure 8.1 shows the experimental point-to-plane geometry used in the experiments at LPGP. The point electrode is a sharp anode with a radius of curvature of 50 μm. A segmented cathode is set at 1 cm from the

tip of the anode. A positive square voltage pulse is applied to the point electrode. The maximum applied voltage U_a ranges from 16 kV to 30 kV. The applied voltage has a rise time of t_{rise} = 2 ns and the duration of the pulse is equal to t_{pulse} = 20 ns.

In the experiments, a dielectric layer of thickness Δ is placed in the

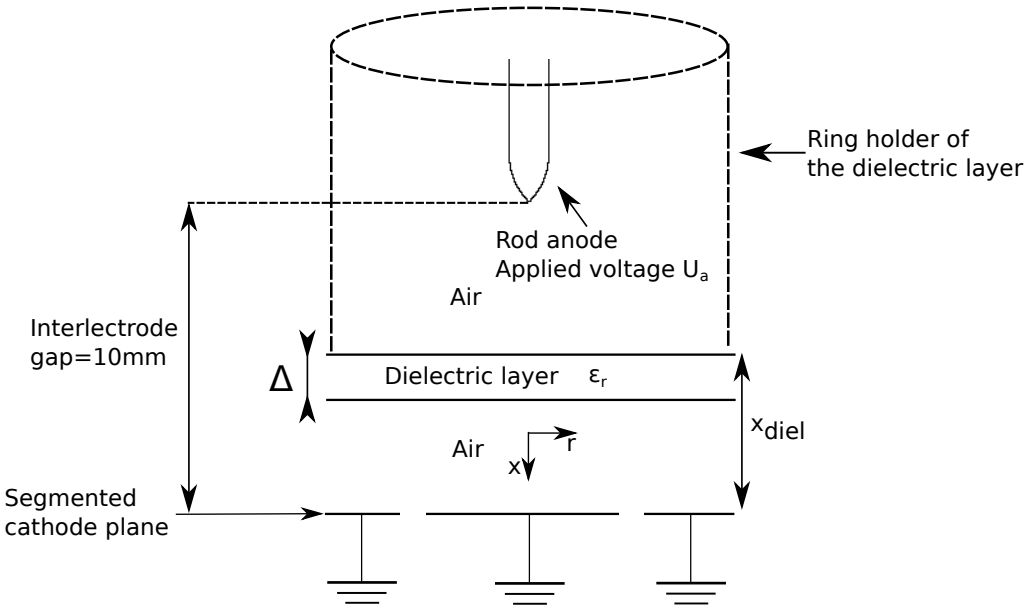

Figure 8.1: *Experimental point-to-plane geometry at LPGP.*

inter-electrode at a distance x_{diel} from the cathode. Different dielectric layers have been used (Glass, Alumina, TOPAS ...) and the influence on the reignition dynamics of their location in the inter-electrode x_{diel} and their thickness Δ was investigated.

It is important to mention that the experimental geometry is presented on Figure 8.1 with the point anode on the top and the segmented cathode on the bottom whereas in the experiments the point electrode is on the bottom and the segmented cathode on the top. Around the point electrode, a dielectric ring is used to hold the dielectric layer in the inter-electrode gap.

It is important to point out that for reignition studies, the experiments are single shot. As diagnostics, current measurements with the segmented cathode are coupled to optical emission measurements with an ICCD camera.

The simulated experimental point-to-plane geometry is shown on Figure

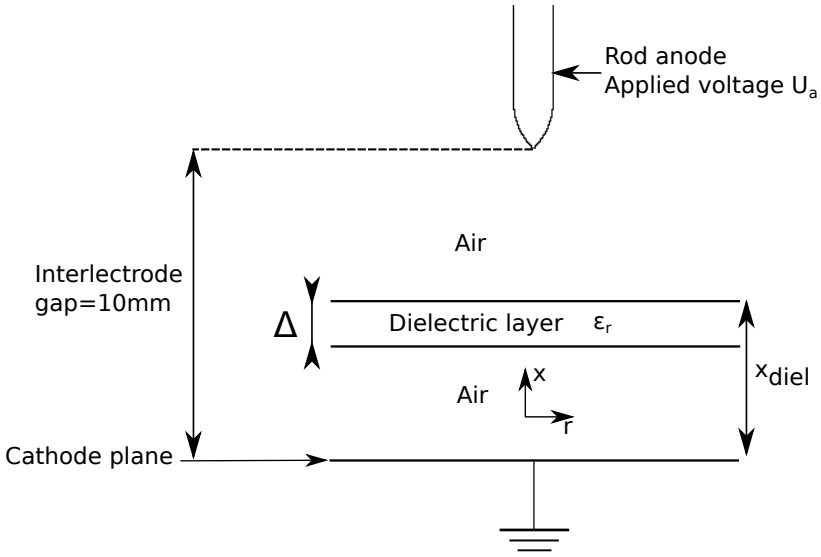

Figure 8.2: *Simulated point-to-plane geometry*

8.2 and is close to the geometry used in experiments. The anode is a 500 μm rod ended by a semi-sphere with a radius of curvature of 50 μm. The cathode plane is located 1 cm from the tip of the anode. In the air gap, when a dielectric plane is considered, its location x_{diel}, its thickness Δ and its relative permittivity ε_r will be given. In the simulations, we have considered that the cathode plane is continuous and not segmented. We have also neglected the dielectric ring holder in the simulations. The computational domain is 2 cm×7 cm. For $0 \leq x \leq 1$ cm, an axial mesh size of 10 μm is used and is refined to 1 μm close to the anode tip and close to the air/dielectric interfaces. Then for $1 \leq x \leq 2$ cm, the mesh size is increased from 1 μm to 30 μm. Radially, a mesh size of 5 μm is used and is refined to 1 μm close to the axis of symmetry and for $0.5 \leq r \leq 2$ cm, the radial mesh size is increased from 5 μm to 30 μm. This level of refinement required a grid size of $n_x \times n_r = 3062 \times 2400$.
Other conditions of the simulations (boundary conditions, time-step calculation) have been presented in detail in chapter 1. As mentioned at the end of chapter 4, the MPI-OPENMP discharge code using domain decomposition has been used for all simulations presented in this chapter.

8.3 Ignition and propagation of a discharge without a dielectric plane obstacle: comparison with experiments

8.3.1 Experimental results without a dielectric plane

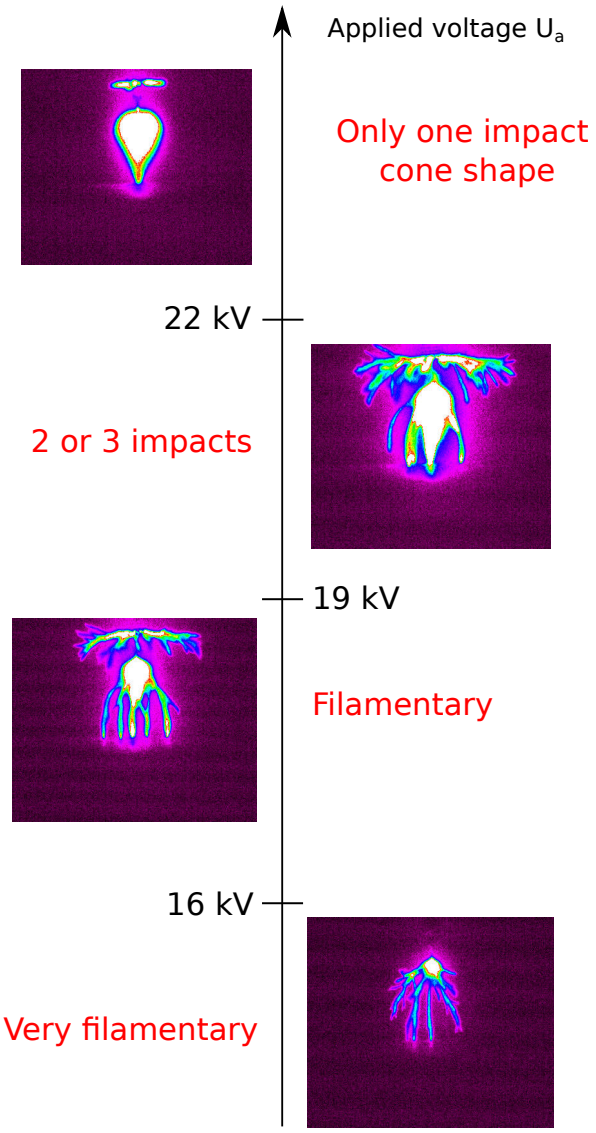

Figure 8.3: *Experimental pictures showing the influence of the maximum applied voltage on the discharge structure ignited at the point anode without a dielectric plane. Credits LPGP*

As a first step in the experiments, the influence of the maximum applied voltage on the discharge structure ignited at the anode was studied. Figure 8.3 shows that by increasing the maximum applied voltage U_a at the point anode, the number of filaments ignited at the point anode decreases. If $U_a > 22$ kV, experimental results show that a single conical discharge is ignited at the point anode.
For U_a= 28 kV, Figure 8.4 shows on optical emission measurements that the maximum diameter of the discharge is $D_{max}^{exp} \sim 8$ mm. By current measurements, the discharge propagation velocity in the air gap was estimated to be in the range of $v_{exp} = 2.6 - 3.2\ 10^8$ cm.s^{-1}.
In order to compare experimental and numerical results using a 2D axisymmetric code, in this work we have carried out simulations only for $U_a > 22$kV, the conditions in which a conical discharge is observed.

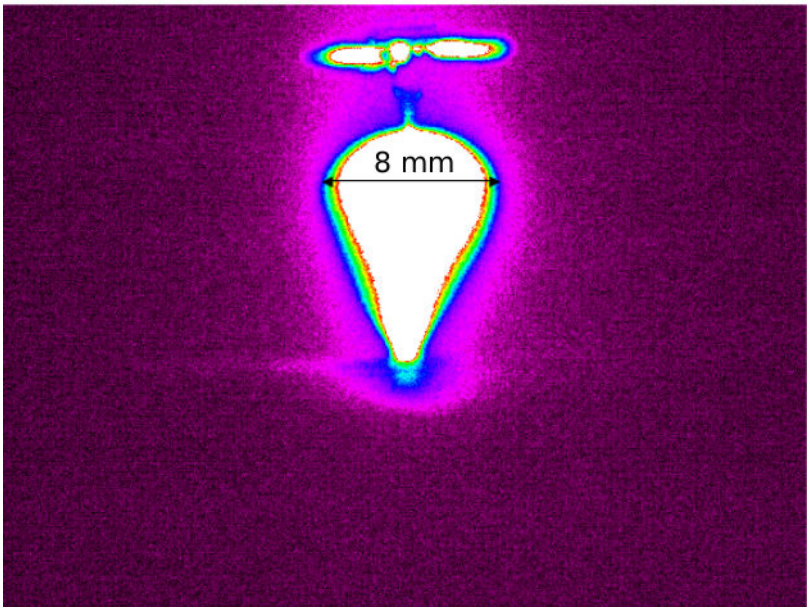

Figure 8.4: *Experimental pictures showing the impact of a single conical discharge with a maximal diameter of* $\sim$ *8 mm for* U_a= *28 kV. Credits LPGP*

8.3.2 Numerical results without a dielectric plane

First, Figure 8.5 shows the applied voltage used in the simulations. As in experiments, a rise time of 2 ns is used. In this section, results are presented for a maximum applied voltage U_a= 30 kV. In the simulations, the applied voltage is assumed to be constant for t>3 ns. As initial con-

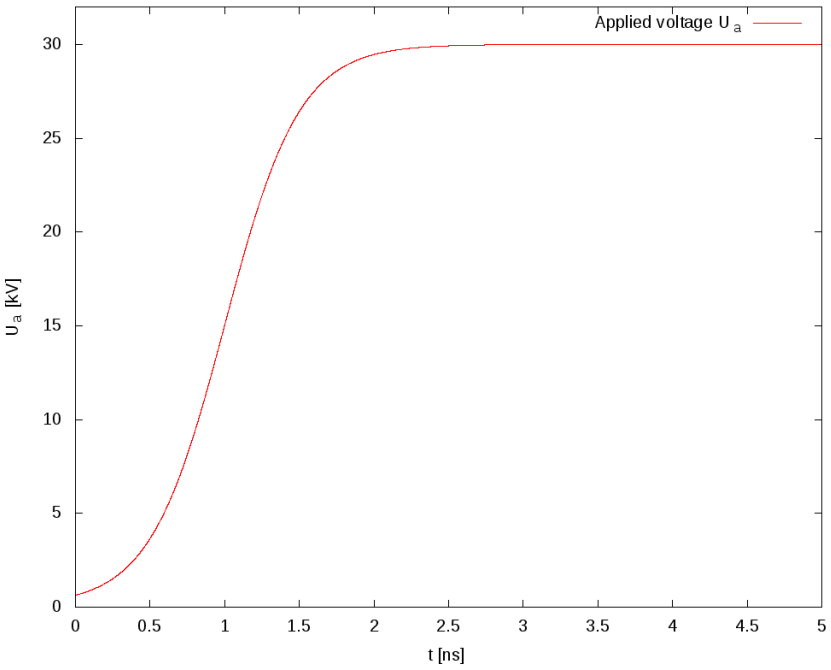

Figure 8.5: *Applied voltage at the anode point in the simulations.*

dition, we have assumed a uniform preionization of electrons and positive ions in the air gap with a density of $10^4 cm^{-3}$.

Figure 8.6 shows the distributions of the electron density and absolute values of the electric field at t=1.7, 3.1 and 4.7 ns. It is interesting to note that the time of ignition of the discharge τ_{igni} is equal to 0.9 ns which corresponds to an applied voltage of $U_a = 12\,kV$. It means that the discharge is already ignited 1.1 ns before the applied voltage at the anode reaches its maximum value of $U_a = 30\,kV$. On Figure 8.6 at t= 1.7 ns, we see the development of a spherical discharge that starts to propagate towards the plane cathode. At t= 3.1 ns, the discharge front is located in the middle of the gap. It is interesting to note that at t= 3.1 ns, the discharge reaches its maximal diameter of $D^{sim}_{max} = 8$ mm. Due to the small radius of curvature of the point and the high applied voltage, this large diameter of the discharge is required to shield the high laplacian electric field at the anode tip ($E_{anode} = 2.2$ MV.cm^{-1} when the applied voltage is equal to $U_a = 30\,kV$).

For t> 3.1 ns, the discharge propagates on the axis of symmetry towards the cathode and the axial electric field in the head of the discharge increases from 90 kV.cm^{-1} at t= 3.1 ns to 144 kV.cm^{-1} at t=$\tau^{plane}_{connec} = 4.7$ ns when the conical discharge impacts the cathode.

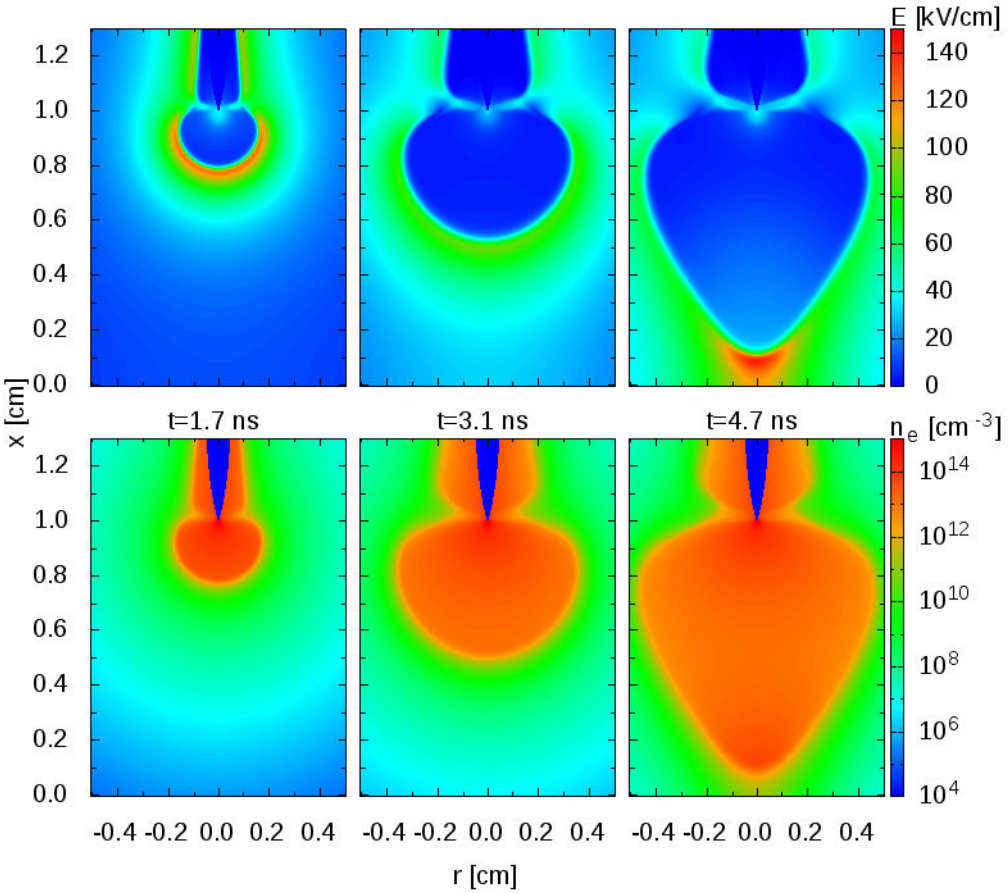

Figure 8.6: *Discharge dynamics without a dielectric plane obstacle for the applied voltage shown on Figure 8.5. Cross-sectional views of the absolute value the electric field and electron density at t=1.7, 3.1, 4.7 ns*

If we now calculate the propagation velocity of the discharge in the simulations v_{num}, we obtain:

$$v_{num} = \frac{d}{\tau_{connec}^{plane} - \tau_{igni}} = 2.6 \times 10^8 \text{ cm.s}^{-1}, \text{ where d=1 cm }, \quad (8.1)$$

which is in good agreement with experiments.

Current calculation without a dielectric plane

Starting from the charge conservation, the current flowing through an enclosed volume (delimited by the surface **S**) in the air gap is conserved following the equation (more details are given in Appendix A):

$$\iint_S \mathbf{J} \cdot \mathrm{d}\mathbf{S} = 0 \ , \tag{8.2}$$

where the total current density **J** is defined as:

$$\mathbf{J} = \mathbf{j_c} + \epsilon_0 \frac{\partial \mathbf{E}}{\partial t} \ , \ \text{where} \quad \mathbf{j_c} = q_e \mathbf{j} \tag{8.3}$$

where $\mathbf{j_c}$ is the current density, $\mathbf{j}$ is the flux of charged species and q_e is the absolute value of electron charge.
By integrating **J** over a surface perpendicular to the x-axis of symmetry, we obtain the net current I shown on Figure 8.7.

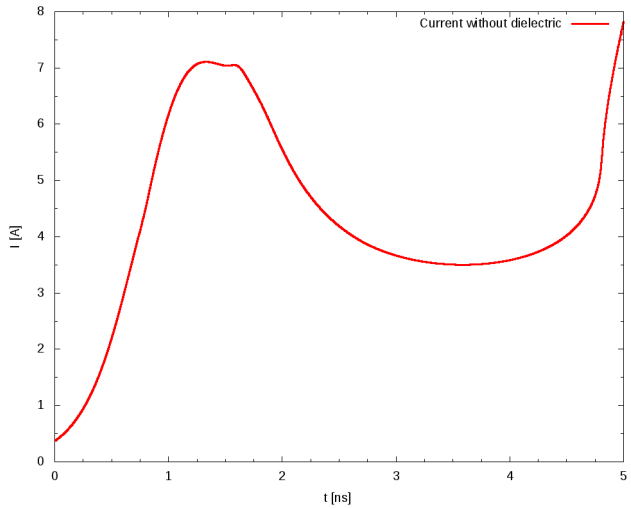

Figure 8.7: *Discharge current for the simulation with the point-to-plane geometry without a dielectric plane obstacle.*

On Figure 8.7, we see an increase of the current from I=0.4 A to I=7 A at t=1.3 ns. This increase is due to the capacitive current induced by the fast increasing voltage applied at the anode point. It is interesting to note that on current calculation, there is no peak of current at the ignition time of the discharge τ_{igni}=0.9 ns. The current is almost constant from t=1.3 ns to t=1.6 ns with a small increase at t=1.6 ns. We recall here that the voltage is still increasing between t=1.3 ns and 1.6 ns. This

means that the space charge created by the ignited discharge is sufficiently strong to shield the laplacian electric field at the point anode. Then for t>1.6 ns, the current decreases until t=3.5 ns to a value of I=3.7 A. This corresponds to the time at which the discharge has finished its radial expansion and starts to propagate towards the cathode. For t>3.5 ns, the current starts to slowly increase to a value of I=4.8 A until t=$\tau_{\text{connec}}^{\text{plane}}$ = 4.7 ns when the conical discharge impacts the cathode. This increase is due to the slow increase of the electric field in the head of the discharge from 90 kV.cm^{-1} at t= 3.1 ns to 146 kV.cm^{-1} at $\tau_{\text{connec}}^{\text{plane}}$ = 4.7 ns. After the impact, Figure 8.7 shows a fast increase of the current due to the conductive channel established between the anode point and the cathode plane. In this work, the simulation is stopped shortly after the connection to avoid the transition to the spark regime.

Optical emission of the discharge without a dielectric plane

To compare with experiments it is interesting to compute the optical emission of the discharge. In air at atmospheric pressure, the emission spectrum of a streamer discharge is usually considered to be dominated by the emission from the second positive band of nitrogen:

$$N_2(C^3\Pi_u) \rightarrow N_2(B^3\Sigma_g^+) + h\nu \ , \tag{8.4}$$

In this work, as in (Bourdon et al. 2010), we have calculated the time evolution of the concentration $[N_2(C^3\Pi_u)]$ using a fourth order Runge-Kutta time integration scheme. It is interesting to point out that the time evolution of the excited state $N_2(C^3\Pi_u)$ is solved simultaneously with streamer equations. In the experiments, to record the optical emission shown on Figure 8.4, the ICCD camera is opened for 10 ns and so to compare with experiments, the simulated emission is time integrated on the whole discharge propagation dynamics (from t=0 ns to t=4.8 ns). After computing the axially symmetric intensity, a direct Abel transformation is performed. More details on the optical emission model are given in Appendix B. Figure 8.8 shows the spatial distribution of the (Abel transformed time integrated over 4.8 ns) 2P emission intensity. Comparing Figure 8.8 and Figure 8.4, we note that we obtain qualitatively the same conical shape with the same maximal diameter of 8 mm.

In conclusion of this section, for the point-to-plane geometry used in the experiments with a sharp point (50 μm of radius of curvature) and an applied voltage higher than 22 kV, in experiments and simulations a conical discharge structure is observed. A good agreement between experiments and simulations is obtained on the maximal discharge diameter and the discharge propagation velocity.

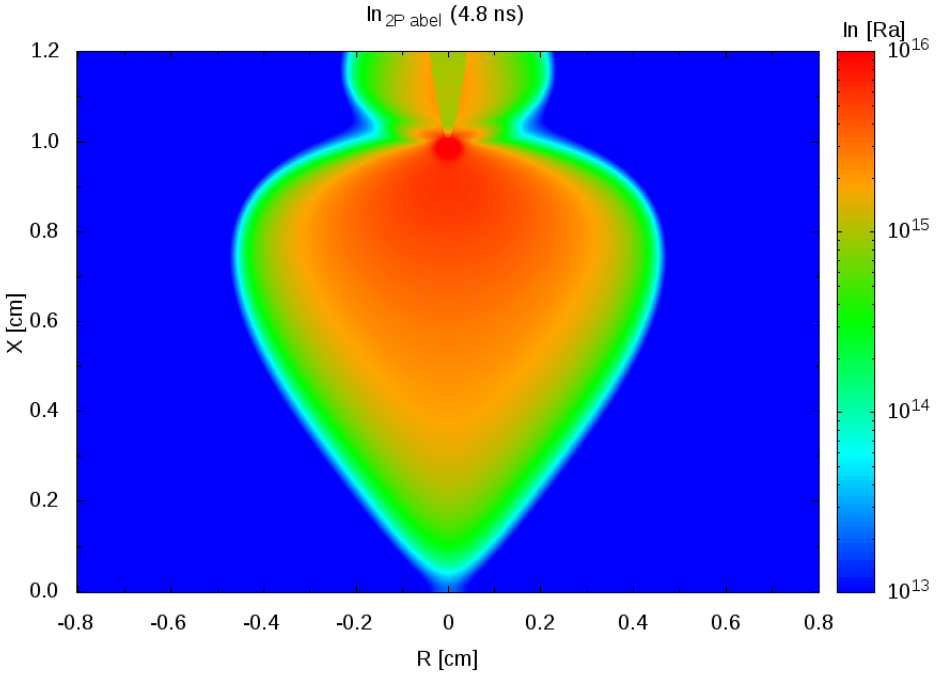

Figure 8.8: *Spatial distribution of the numerically time-integrated-over-4.8-ns Abel-integrated 2P emission intensity with the experimental geometry without a dielectric plane obstacle in the inter-electrode gap.*

8.4 Ignition and propagation of a discharge with a dielectric plane obstacle: comparison with experiments

8.4.1 Experimental results with a dielectric plane obstacle

In the experiments, to determine the occurrence of the reignition process behind a dielectric plane obstacle, current measurements with the segmented cathode are coupled to optical emission measurements.
In current measurements, several peaks (usually 4) of current are recorded. The first peak of current is taken as the reference time t_1. This first current peak corresponds to the capacitive current due to the increasing

voltage and the ignition of the discharge at the point anode. The second peak of current occurs at Δt_{1-2} ~6 ns from the first peak. It is interesting to note that this second peak of current is almost of the same amplitude as the first one. With a high speed camera, no optical emission in the second air gap between the dielectric plane and the cathode surface is observed for this second peak. Then, a third current peak is measured at Δt_{1-3} ~13 ns from the first peak of current. The amplitude of the third current peak is almost the same as the first one and again at that time, no optical emission is observed in the second air gap. At the fourth peak of current at Δt_{1-4} ~18 ns, the current peak amplitude is higher than the previous ones. Figure 8.9 shows that for this fourth current peak, the optical emission of a reignited discharge starting close to the bottom surface of the dielectric and impacting the cathode surface is recorded. It is important to point out that the optical emission in the first air gap between the point anode and the upper surface of the dielectric is not recorded by the camera due to the obstruction by the opaque ring holder (Figure 8.1).

Experimental results show that when the dielectric layer is thick, the

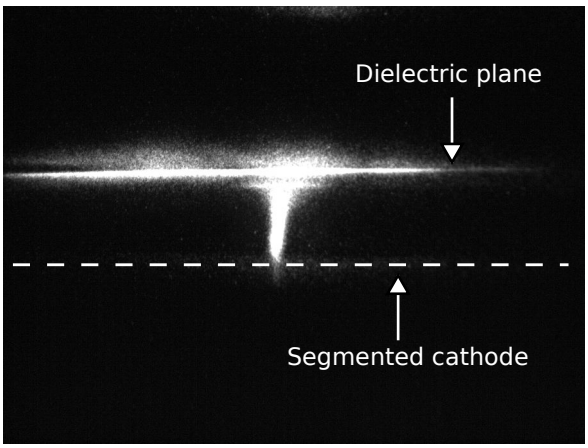

Figure 8.9: *Optical emission measurement with a ICCD camera at* Δt_{1-4} *~18 ns showing the reignition of a discharge ignited close to the bottom surface of the dielectric and impacting the cathode surface. Credits LPGP*

reignited discharge is centered on the axis of symmetry. Out of all the materials tested in the experiments, the thickest dielectric layer studied is of TOPAS polymer (Δ=1 mm) with a relative permittivity $\varepsilon_r = 2.2$. Then to compare with experimental results, in the following section we simulate a dielectric layer of thickness Δ=1 mm with a relative permittivity $\varepsilon_r = 2.2$. In the experiments, the dielectric layer is placed at 0.5 cm from the cathode plane (i.e. x_{diel}= 0.5 cm in Figures 8.1 and 8.2).

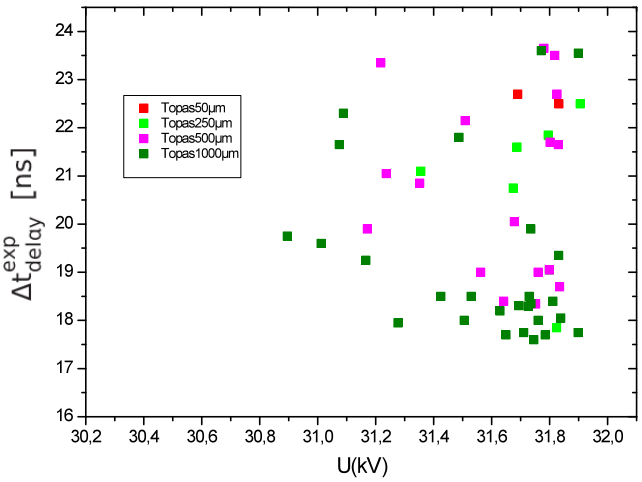

Figure 8.10: *Experimental delays* Δt^{exp}_{delay} *between the ignition at the point of the discharge and the impact on the cathode of the reignited discharge following the experimental methodology for the TOPAS polymer dielectric of various thickness* $\Delta \in [50\ \mu m : 1000\ \mu m]$ *located at* x_{diel}*= 0.5 cm. Credits LPGP*

Following the experimental methodology which coupled current and emission measurements, the reignited discharge is considered to correspond to the fourth current peak. The delay between the ignition of the first discharge at the point anode and the impact of the reignited discharge on the cathode surface Δt_{1-4} is called the experimental reignition delay Δt^{exp}_{delay} in the following. Figure 8.10 presents reignition delays as a function of the applied voltage $U_a = \in [30.8\ kV : 32\ kV]$ for TOPAS dielectric layers of different thicknesses. For Δ=1 mm, the experimental reignition delay is $\Delta t^{exp}_{delay} = \Delta t_{1-4} \in [18\ ns : 24\ ns]$.

8.4.2 Numerical results with a dielectric plane obstacle

We present here simulation results in the point-to-plane experimental geometry with a dielectric plane obstacle. As discussed in the previous section, the dielectric layer of thickness Δ=1 mm and relative permittivity $\varepsilon_r = 2.2$ is located at x_{diel}= 0.5 cm. As initial condition, we have assumed a uniform preionization of electrons and positive ions in both air gaps (above and below the dielectric layer) with a density of $10^4 cm^{-3}$. For a maximum applied voltage $U_a = 30\,kV$ with a rise time of t_{rise}=2

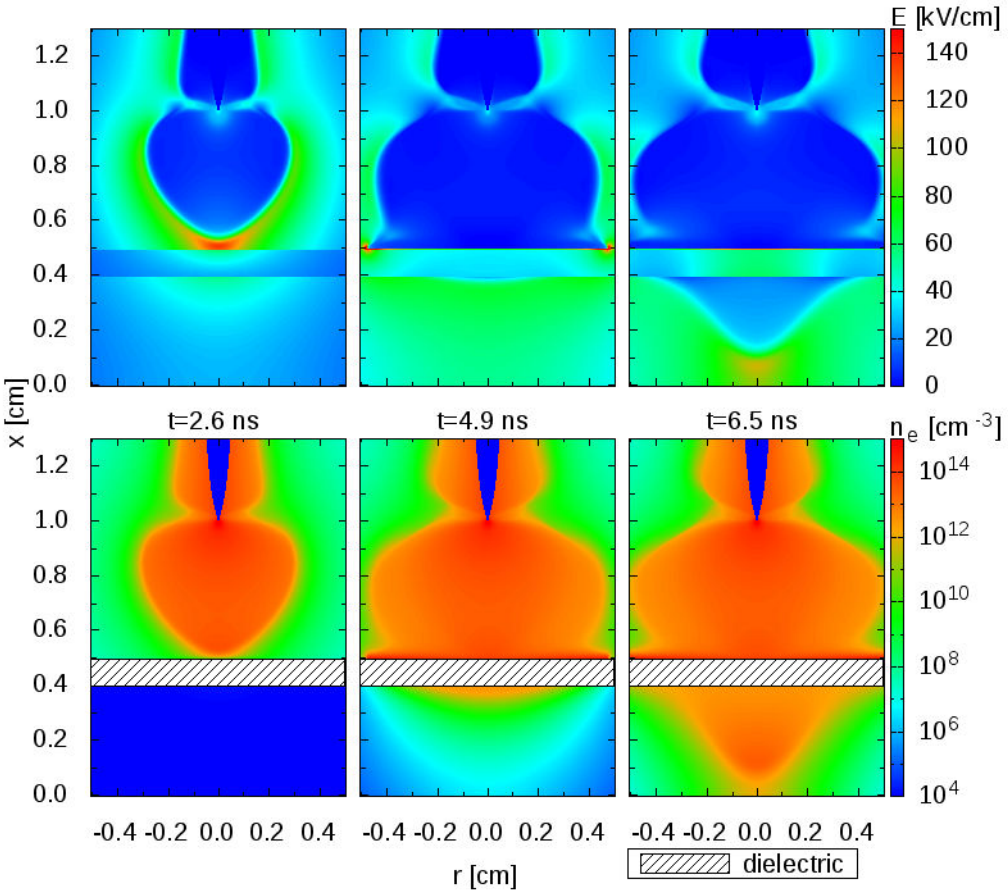

Figure 8.11: *Discharge dynamics with a dielectric plane obstacle for the applied voltage shown on Figure 8.5. Cross-sectional views of the absolute value the electric field and electron density at t=2.6, 4.9, 6.5 ns*

ns applied at the point anode (Figure 8.5), Figure 8.11 shows the distributions of the electron density and absolute values of the electric field at t=2.6, 4.9, 6.5 ns.

It is interesting to note that the discharge dynamics is similar to the positive discharge reignition dynamics described in chapters 6 and 7. For the conditions of Figure 8.11, we observe the ignition of a positive streamer discharge at the point electrode at $\tau_{igni} = 0.9$ ns. This first discharge propagates in the gap and impacts the dielectric layer at $\tau_{impact} = 2.6$ ns. Then the discharge starts to spread on the upper surface of the dielectric

layer. At the same time we observe that the amplitude of the electric field in the second air gap below the dielectric plane increases. At τ_{rei}=4.9 ns, a second positive discharge is ignited close to the bottom surface of the dielectric plane. It is interesting to note that on this experimental geometry the time delay between the time of impact and the time of reignition is small: $\tau_{rei} - \tau_{impact}$=2.3 ns and comparable to delays found in Table 6.1 (in chapter 6, Section 6.3.2). Figures 8.12 (a) and (b) show the time

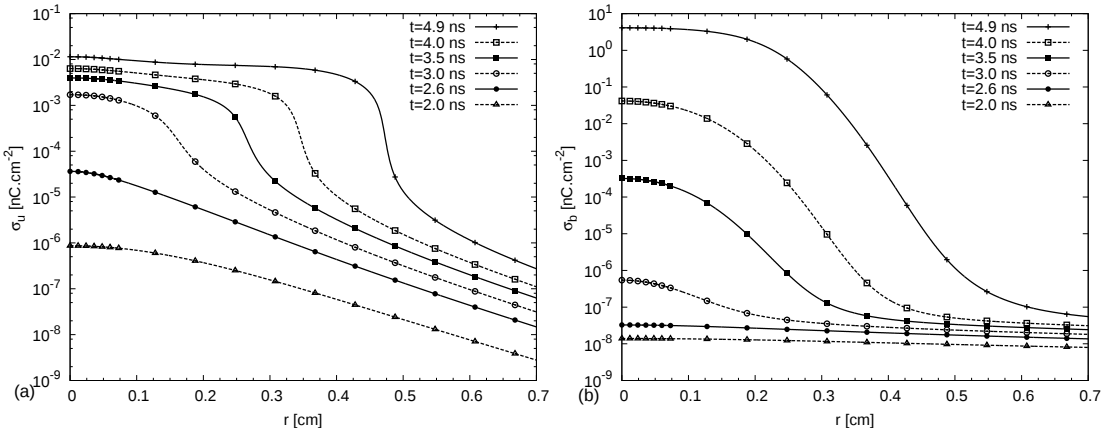

Figure 8.12: *Time evolutions of the radial profiles of positive surface charges σ_u deposited on the upper dielectric surface and absolute value of negative surface charges σ_b deposited on the bottom surface of the dielectric layer for the same condition as Figure 8.11.*

evolutions of the radial profiles of surface charges on both faces of the dielectric layer for the same condition as Figure 8.11. As the first positive discharge spreads on the upper surface of the dielectric plane, the upper surface is charged positively by positive ions and its bottom surface is charged negatively mostly by electrons and negative ions. As in chapters 6 and 7, we have checked that the amount of surface charges is too low at τ_{rei}=4.9 ns to have an influence on the reignition process. Then, the increase of the electric field in the second air gap is mostly due to the potential redistribution in the interelectrode gap after the first positive streamer propagation in the first air gap. It is interesting to note that in the second air gap, for t>2.6 ns, we observe an almost homogeneous electric field which is $\geq$ 50 kV.cm^{-1}, higher than the breakdown field. As a consequence, the charged species density increases rapidly due to ionization processes in the second air gap. Then at t=4.9 ns, a second positive discharge ignites close to the bottom surface of the dielectric and impacts the cathode at $\tau^{plane}_{connec} = 6.5$ ns.

The numerical results show that in the experimental geometry, the dynamics of the reignited discharge is fast (only $\tau^{\text{plane}}_{\text{connec}} - \tau_{\text{rei}}$=1.6 ns). If now we compute the numerical delay between the impact on the cathode of the reignited discharge and the time of ignition of the first discharge at the point anode, we obtain:

$$\Delta t^{\text{num}}_{\text{delay}} = \tau^{\text{plane}}_{\text{connec}} - \tau_{\text{igni}} = 5.6 \text{ ns} \ . \tag{8.5}$$

Compared to the experimental delays $\Delta t^{\text{exp}}_{\text{delay}} = \Delta t_{1-4} \in [18 \text{ ns} : 24 \text{ ns}]$, the numerical delay $\Delta t^{\text{num}}_{\text{delay}}$= 5.6 ns is much shorter.

Current calculation with a dielectric plane

Figure 8.13 shows the calculated current in the experimental point-to-plane geometry with the dielectric plane obstacle. As in the simulation

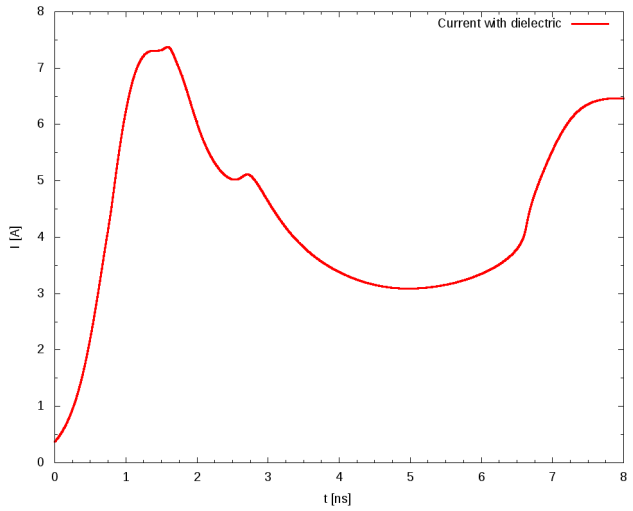

Figure 8.13: *Discharge current for the simulation with the point-to-plane geometry with the dielectric plane obstacle*

without the dielectric plane, the first peak of current is due to the capacitive current induced by the increasing voltage at the point anode. Then a second peak of current representing the impact of the first discharge on the upper surface of the dielectric at τ_{impact} = 2.6 ns is observed. It is due to the change of direction of propagation of the first discharge that is stopped in its axial propagation by the dielectric plane and starts to spread radially on its surface. It is interesting to note that no current peak is observed at the time of reignition τ_{rei}=4.9 ns. After the impact

on the cathode at $\tau_{connec}^{plane} = 6.5$ ns, Figure 8.13 shows that the current increases and reaches a maximum value of 6.45 A at t=7.8 ns. Indeed due to the presence of the dielectric plane in the inter-electrode gap, there is no conductive channel between the point anode and the cathode and thus the dielectric plane limits the current increase at the cathode. It is important to note that we have stopped the simulation at t=8 ns, rapidly after the connection of the reignited discharge at the cathode.

Optical emission with a dielectric plane

Figure 8.14 shows the spatial distribution of the simulated 2P emission intensity. This intensity is Abel-integrated and time integrated over the duration of the discharge propagation between the point electrode and the cathode plane (i.e. over 6.6 ns in this case).

We note that the optical emission intensity coming from the first dis-

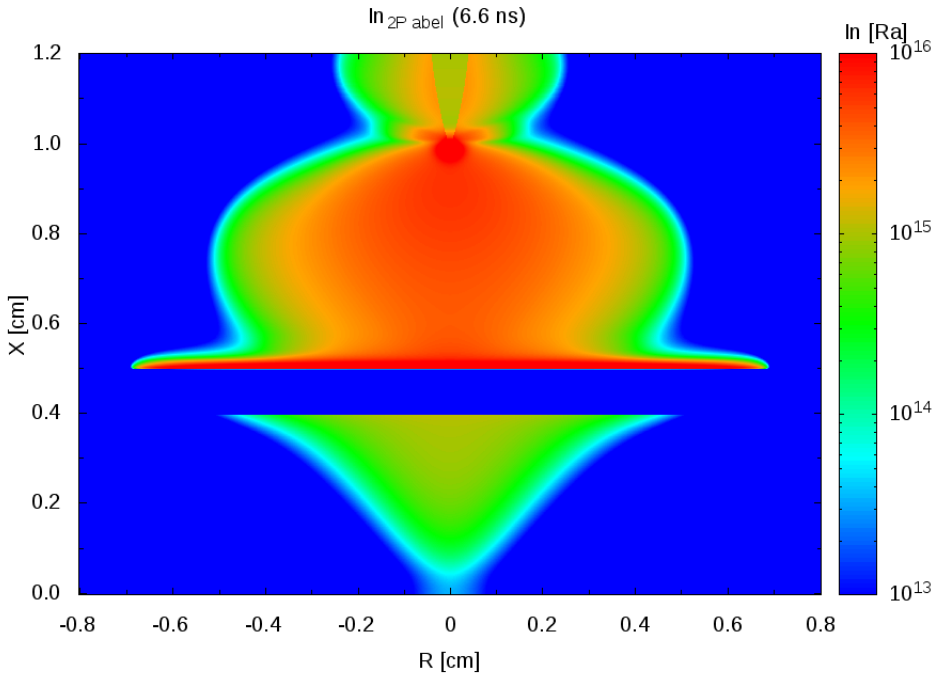

Figure 8.14: *Spatial distribution of the simulated 2P emission intensity (time-integrated-over-6.6-ns Abel-integrated).*

charge spreading on the upper dielectric surface is high (10^{15-16} Rayleigh). It is also interesting to point out that the maxima of intensity are mainly located close to the upper surface of the dielectric and close to the point anode. On the other hand we note that the optical emission intensity in the second air gap is at least one order of magnitude less (10^{14} Rayleigh) than the emission intensity in the first air gap. The simulated optical emission from the first air gap is shown here to compare the emission intensity coming from the first and the second air gaps, even though in the experiments the optical emission intensity from the first air gap is obstructed by the dielectric ring holder.

8.5 Discussion on the comparison of experiments and simulations

In the previous sections, we have shown that for the same voltage conditions with a 1 mm thick TOPAS layer located at x_{diel}= 0.5 cm, the experimental delay $\Delta t_{\text{delay}}^{\text{exp}} = \in [18\text{ ns} : 24\text{ ns}]$ is much longer than the simulated one $\Delta t_{\text{delay}}^{\text{num}}$=5.6 ns. To improve the experiment/modelling agreement, in this section we propose first to analyze in more detail the different current peaks measured and, second to discuss which physico-chemical processes could be missing in the simulations.

a) Analysis of the current peaks measured:
It is worth mentioning that in the experiments, a second peak of current is measured at Δt_{1-2} ∼6 ns, close to the peak of current obtained in the simulation at $\Delta t_{\text{delay}}^{\text{num}}$=5.6 ns. In the experiments, no emission is recorded at Δt_{1-2} ∼6 ns. However Figure 8.14 shows that the simulated emission intensity of the reignited discharge is quite low. This low emission intensity could maybe explain why in the experiments, the camera is not able to record the emission intensity of a reignited discharge at Δt_{1-2} ∼6 ns. This could mean that the second peak of current measured in the experiments could correspond to the impact of a first reignited discharge on the cathode surface.
It is important to note that after the impact of the first discharge on the upper surface of the dielectric layer, the discharge spreads on the dielectric surface and expands radially towards the radial surfaces (metallic and dielectric) of the plasma reactor. Then, due to charge accumulation on the different dielectric surfaces of the reactor, we suggest that the second, third and fourth current peaks could correspond to different

consecutive discharge reignitions. After each reignition event, the dielectric plane obstacle is charged more and more negatively on its bottom surface. Maybe for the fourth peak of current which occurs at the end of the voltage pulse, the sudden release of surface charges accumulated after two previous reignition events could be high enough to explain the reignited discharge emission recorded in the experiments.

b) Additional processes to be considered in the simulations:
In the simulations presented in previous sections, it is assumed that the initial level of seed charges in air is 10^4 cm^{-3}. For the air gap above the dielectric layer, due to the high electric field induced by the sharp point, we have considered that a low value of 10^4 cm^{-3} allows to accurately simulate the discharge ignition at the point. For the discharge propagation towards the upper dielectric surface, the photoionization is the key source term and the low level of seed charges of 10^4 cm^{-3} has a negligible influence on the discharge dynamics.
As shown on Figure 8.11, after the first discharge impact on the upper dielectric surface, the electric field is uniform and higher than the breakdown field in the second air gap. Then, even with a low preionization density of 10^4 cm^{-3} in the second gap, a fast reignition process is observed. So first, we have questioned the value of 10^4 cm^{-3} for seed charges below the dielectric plane for our conditions.
As the experiments are single shot, there are at least few minutes between each applied voltage pulse. In (Pancheshnyi 2005), it is pointed out that different key physical and chemical processes occur in the post-discharge after the end of a voltage pulse:

- First at 300 K, electrons quickly attach to O_2:

$$e + O_2 + O_2 \rightarrow O_2^- + O_2, \text{ with } \Delta t_1 = 20 \text{ ns} . \tag{8.6}$$

- Then, the ion-ion dissociative recombination of O_2^- and O_4^+ occurs:

$$\begin{cases} O_2^- + O_4^+ \rightarrow O_2 + O_2 + O_2 , \\ O_2^- + O_4^+ + M \rightarrow O_2 + O_2 + O_2 + M , \text{ with M= } N_2, O_2 , \\ \Delta t_2 = 10 - 100 \text{ ns} . \end{cases} \tag{8.7}$$

- Then ion diffusion losses at the reactor surfaces and the cathode have to be considered: $\Delta t_3 = 80$ ms.

According to (Pancheshnyi 2005), after a few seconds, the level of seed charges is $\sim n_{n,p} = 10^4$ cm^{-3}. For a longer time between two consecutive applied voltage pulses, the diffusion of ions to the reactor surfaces decreases the level of seed charges to lower values.
First, it is interesting to point out that in previous sections, we have used $n_{e,p} = 10^4$ cm^{-3}, that is to say we have assumed an instantaneous detachment of electrons from negative ions as soon as an electric field is applied. For an initial density of seed charges of $n_{n,p} = 10^4$ cm^{-3}, as the electric field becomes rapidly higher than $E \geq 50$ kV.cm^{-1} in the second gap, we have estimated using the same finite detachment rate as in (Tholin and Bourdon 2013), that the delay induced in the discharge dynamics by detachment is at maximum of a few nanoseconds for the conditions studied in this work. So we conclude that this effect is too small to explain the difference between experimental and numerical reignition delays.
Second, if we consider that there are several minutes between consecutive voltage pulses, according to (Pancheshnyi 2005), the level of seed charges is $n_{n,p} < 10^4$ cm^{-3} in the second air gap. As a first approximation, in this work, we have considered the limit case with no seed charges in the second air gap. As the electric field in the second air gap is directed towards the cathode plane, we have assumed that the only source of electrons in the second air gap is the metallic cathode surface. To test the reignition dynamics with this hypothesis we present simulation results with at t=0 ns no initial seed charges in the second air gap and with an electron emitted from the cathode (averaged density over a cylinder of 100×100 μm) at t=τ_e=16.5 ns, close to the time at which a discharge reignition is observed in experiments.

Figure 8.15, shows the distributions of the electron density and absolute values of the electric field at t=18, 19.4, 22.8 ns. As in previous sections, we note that after the impact of the first discharge on the upper surface of the dielectric plane, the electric field in the second air gap is almost homogeneous and higher ($E \geq 50$ kV.cm^{-1}) than the breakdown field. Then after the electron emission at the cathode at t=τ_e=16.5 ns, we observe at t=18 ns, an increase of the electron density in the second air gap as electrons drift towards the dielectric plane. At t=19.4 ns, a double headed discharge ignites in the second air gap with a positive head propagating towards the cathode surface and a negative head propagating towards the bottom surface of the dielectric plane. At t=τ_{connec}^{plane}=22.8 ns, the positive head impacts the cathode and 0.1 ns later the negative head impacts the bottom surface of the dielectric plane. It is important to note that for $16.5 \leq t \leq 22.8$ ns, the amount of surface charges is very low and has no influence on the reignited discharge dynamics.

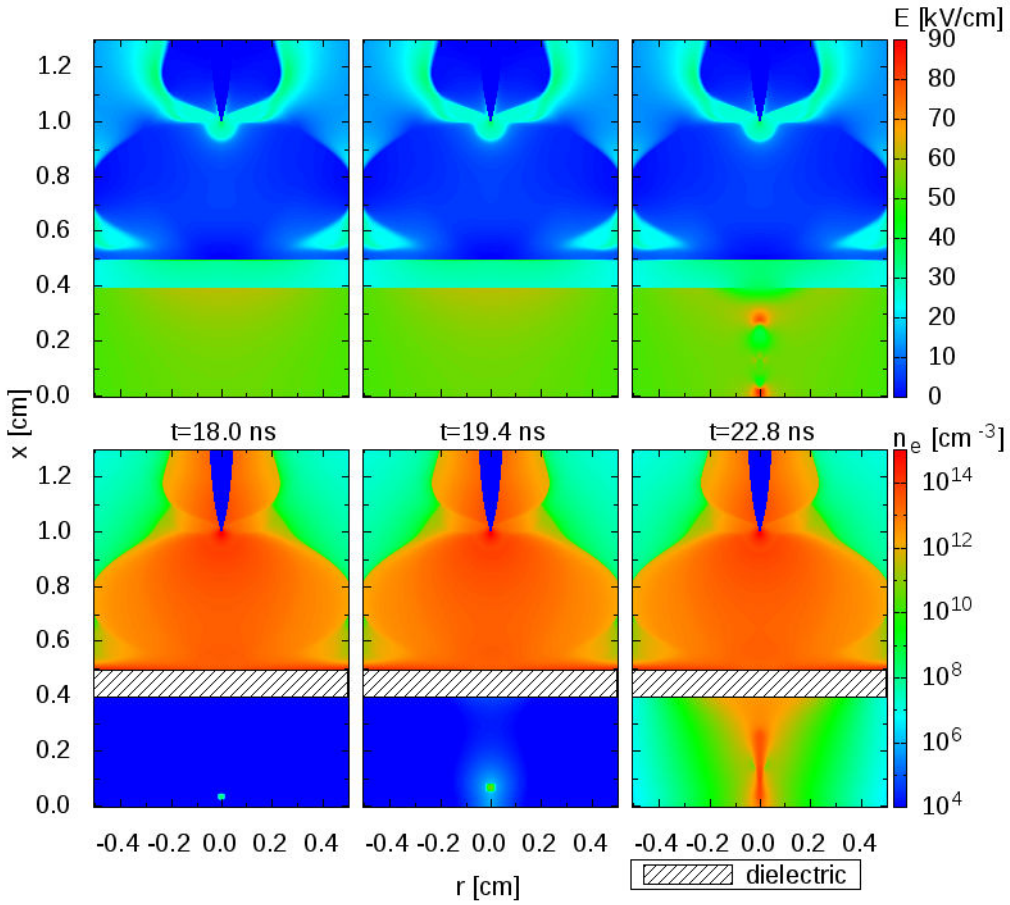

Figure 8.15: *Discharge dynamics with a dielectric plane obstacle. At t=16.5 ns an electron is emitted from the cathode (averaged density over a cylinder of 100×100 μm). Cross-sectional views of the absolute value the electric field and electron density at t=18, 19.4, 22.8 ns*

In this simulation, the numerical reignition delay is equal to Δt_{delay}^{num}=21.9 ns that is to say in the range of the experimental delays $\Delta t_{delay}^{exp} \in [18\text{ ns} : 24\text{ ns}]$. It is interesting to note that with the emission of an electron at t= τ_e=16.5 ns and the time of impact on the cathode surface τ_{connec}^{plane}=22.8 ns, the duration of the formation and propagation of the reignited discharge in the second air gap is $\Delta_{ele} = 6.3$ ns.
As this simplified test case has given promising first results, in the following section we propose to carry out a detailed analysis of the processes that could explain an electron emission from the cathode surface.

8.6 Influence of emission processes at the cathode surface on the reignition dynamics

In this section, we investigate the physical processes that could allow an electron emission from the cathode surface. In the literature, two emission processes are put forward:

a) The thermionic emission process.
The current density J_{R-S} [A.cm^{-2}] at the cathode surface is calculated with the Richardson-Schottky equation (Murphy and Good Jr 1956):

$$J_{R-S} \;=\; A_1 \exp\left(-\frac{\phi - F^{1/2}}{kT}\right) \text{ with F} \propto \beta E_{cath}\ , \tag{8.8}$$

where ϕ is the work function in eV representing the energy required for an electron at the energy Fermi level to be released outside of the metallic cathode and β is the amplification factor of the electric field at the cathode surface E_{cath} (that represents microscopic roughness at the cathode surface). The thermionic effect represents the emission of electrons from a metallic cathode surface induced by the temperature of the cathode surface (here T=300 K). The presence of an exterior electric field at the cathode surface lowers the surface barrier and increases the emission current.

b) The field emission process.
The current density J_{F-N} [A.cm^{-2}] at the cathode surface is calculated with the Fowler-Nordheim equation (Murphy and Good Jr 1956):

$$J_{F-N} \;=\; A_2 \exp\left(-\frac{B_2 \phi^{3/2}}{F}\right) \text{ with F} \propto \beta E_{cath}\ , \tag{8.9}$$

For field emission, the electrons tunnel easily through the field deformed surface barrier.
It is interesting to note that the field emission process coupled with the positive-ion bombardment at the cathode was used in negative streamer simulations to demonstrate the role of the field-effect emission in both the ignition and development of negative coronas (Reess and Paillol 1997; Paillol et al. 2002).

In this work, as the experimental reignition delay 18 ns $\leq \Delta t_{delay}^{exp} \leq$ 24 ns, we have carried out simulations during a total simulation time of t_{simu}=24 ns. At t=0 ns, we have considered no seed charges in the second air gap. In order to calculate the time required to emit one electron from the cathode surface, we have integrated in time the flux of electrons emitted at the cathode surface induced by the thermionic and field emission processes.

β	ϕ			
	3 [eV]	3.5 [eV]	3.8 [eV]	4 [eV]
220	3.1 ns	3.9 ns	4.8 ns	6.2 ns
200	3.3 ns	4.5 ns	6.9 ns	> 24 ns
180	3.7 ns	6.0 ns	> 24 ns	> 24 ns
160	4.3 ns	> 24 ns	> 24 ns	> 24 ns
140	6.4 ns	> 24 ns	> 24 ns	> 24 ns
120	> 24 ns	> 24 ns	> 24 ns	> 24 ns
100	> 24 ns	> 24 ns	> 24 ns	> 24 ns

Table 8.1: *Influence of the value of the work function ϕ and the amplification factor β on the time τ_e required for an electron to be emitted at the cathode surface by thermionic and field emission processes. The notation > 24 ns stands for cases for which τ_e is longer than the simulation time of t_{simu}=24 ns.*

We have varied the value of the work function $\phi \in [3\ eV : 4\ eV]$ which corresponds to usual values for metallic electrodes. In (Reess and Paillol 1997), a value of β=120 for the amplification factor was used, albeit it was for a point metallic cathode. Nevertheless in (Little and Whitney 1963), it was found that even on a polished flat metallic cathode, small point like structures of 2 μm in height were experimentally found and a value of β=100 was defined as an acceptable amplification factor. As in the experiments, a segmented cathode is used, and so it is quite difficult to estimate the value of β. Therefore, in this work, we have varied the amplification factor $\beta \in [100 : 220]$. In the simulations, we have assumed that the chosen values of ϕ and β are constant on the entire cathode

surface.
In Table 8.1, the time to emit an electron from the cathode surface is given for different values of $\phi \in [3\ eV : 4\ eV]$ and $\beta \in [100 : 220]$. For a fixed value of the work function ϕ=3 eV, we note that when the value of β decreases from 220 to 140, the time required to emit an electron increases from τ_e=3.1 ns to 6.4 ns. When the value of β becomes less than 120, the time required to emit an electron increases significantly and becomes larger than $\tau_e > 24$ ns. We note that the transition between $\tau_e < 7$ ns and $\tau_e > 24$ ns occurs for higher values of β as ϕ increases from 3 to 4 eV. For a fixed value of β=220, we see that when the value of the work function increases from 3 eV to 4 eV, τ_e increases from 3.1 ns to 6.2 ns. As β decreases and is between 200 and 140, we observe a transition between conditions with $\tau_e < 7$ ns and with $\tau_e > 24$ ns. We note that the transition occurs at lower values of ϕ as β decreases. For $\beta \leq 120$, we have $\tau_e > 24$ ns for all values of $\phi \in [3\ eV : 4\ eV]$.

β	ϕ			
	3 [eV]	3.5 [eV]	3.8 [eV]	4 [eV]
220	N_e>1	N_e>1	N_e>1	N_e>1
200	N_e>1	N_e>1	N_e>1	$N_e = 2.1\ 10^{-1}$
180	N_e>1	N_e>1	$N_e = 5.1\ 10^{-2}$	$N_e = 6.8\ 10^{-4}$
160	N_e>1	$N_e = 8.6\ 10^{-2}$	$N_e = 7.3\ 10^{-5}$	$N_e = 6.0\ 10^{-7}$
140	N_e>1	$N_e = 5.2\ 10^{-5}$	$N_e = 1.8\ 10^{-8}$	$N_e = 7.7\ 10^{-11}$
120	$N_e = 7.6\ 10^{-3}$	$N_e = 3.4\ 10^{-9}$	$N_e = 3.4\ 10^{-13}$	$N_e = 6.5\ 10^{-16}$
100	$N_e = 2.4\ 10^{-7}$	$N_e = 1.4\ 10^{-14}$	$N_e = 2.5\ 10^{-18}$	$N_e = 4.9\ 10^{-21}$

Table 8.2: *Influence of the value of the work function ϕ and the amplification factor β on the time required for an electron to be emitted at the cathode surface by thermionic and field emission processes. The notation N_e>1 stands for a case when an electron is emitted at the cathode for t<t_{simu}=24 ns.*

In Table 8.2, the number of electrons accumulated at the cathode surface at t_{simu}=24 ns is given for the same conditions as in Table 8.1. For a fixed value of the work function ϕ=4 eV, we see that when the amplification factor decreases from β=200 to 100, the number of electrons accumulated at the cathode surface decreases from $N_e = 2.1\ 10^{-1}$ to $N_e = 4.9\ 10^{-21}$. For ϕ=4 eV, by just increasing the value of β from 200 to 220, an electron is emitted at τ_e=6.2 ns. Finally, the results presented in Tables 8.1 and 8.2 show that the time τ_e to emit an electron at the cathode surface is strongly dependent on the values of β and ϕ.
To be close to the value of the experimental reignition delay $\Delta t_{delay}^{exp} \in$

[18 ns : 24 ns], the emission of an electron has to occur at $\tau_e < t_{simu} = 24$ ns. In Table 8.1, the only conditions to emit an electron from the cathode surface with $\tau_e < 24$ ns, give an emission time $\tau_e \in [3.1\ ns : 6.9\ ns]$. As after the electron emission from the cathode, the dynamics of the discharge is close to the one observed in Figure 8.15, the duration of the formation and propagation of the reignited discharge in the second air gap is of about $\Delta_{ele} = 6.3$ ns. Then we can estimate that the maximal simulated reignition delay is of about $\Delta_{ele}+\tau_e^{max}$=6.3+6.9 ns =13.2 ns. This reignition delay is longer than the one obtained in assuming an uniform preionization of 10^4cm^{-3} in the second air gap ($\Delta t_{\text{delay}}^{\text{num}}$= 5.6 ns), but is still slightly shorter than the experimental reignition delay $\Delta t_{\text{delay}}^{\text{exp}} \in$ [18 ns : 24 ns].

During the preliminary tests carried out in this work, to better understand the influence of the emission processes at the cathode on the discharge reignition, we have carried out a simulation with no initial charges in the second air gap and the instantaneous electron fluxes at the cathode surface due to thermionic and field emission processes for ϕ=4 eV and β=100. Results presented in Table 8.2 shows that for ϕ=4 eV and β=100, the amount of electron accumulated at t_{simu}=24 ns is equal to $N_e = 4.9\ 10^{-21}$, that is to say much less than one electron. As in this work we use a fluid model for the discharge simulation, this test-case is therefore rather non physical. Nevertheless, we propose to present here briefly the reignition dynamics obtained in this case as it is slightly different from the reignition dynamics obtained in previous sections. Figure 8.16 shows the distributions of the electron density and absolute values of the electric field at t=19, 20, 21.7 ns for ϕ=4 eV and β=100. Due to the high electric field (higher than the breakdown field) in the second air gap for t> 2.6 ns (as shown on Figure 8.11), small amount of electrons emitted at the cathode surface produce avalanches and drift towards the bottom dielectric surface. Therefore at t=19 ns, Figure 8.16 shows an increase of electron density close to the bottom surface of the dielectric plane. At t=20 ns, we observe the ignition of weak ionization wave close to the bottom surface of the dielectric plane where the electric field in the head of the discharge is increasing from 60 to 90 kV.cm^{-1}. The reignited discharge propagates towards the cathode and impacts its surface at t=$\tau_{\text{connec}}^{\text{plane}}$ =21.7 ns,
Those results clearly show that even in this extreme case with very low fluxes of electrons at the cathode, as in the second air gap the electric field ($E \geq 50$ kV.cm^{-1}) is higher than the breakdown field, the electron density increases rapidly up 10^{13} cm^{-3}, and the reignition of a weak discharge is observed.

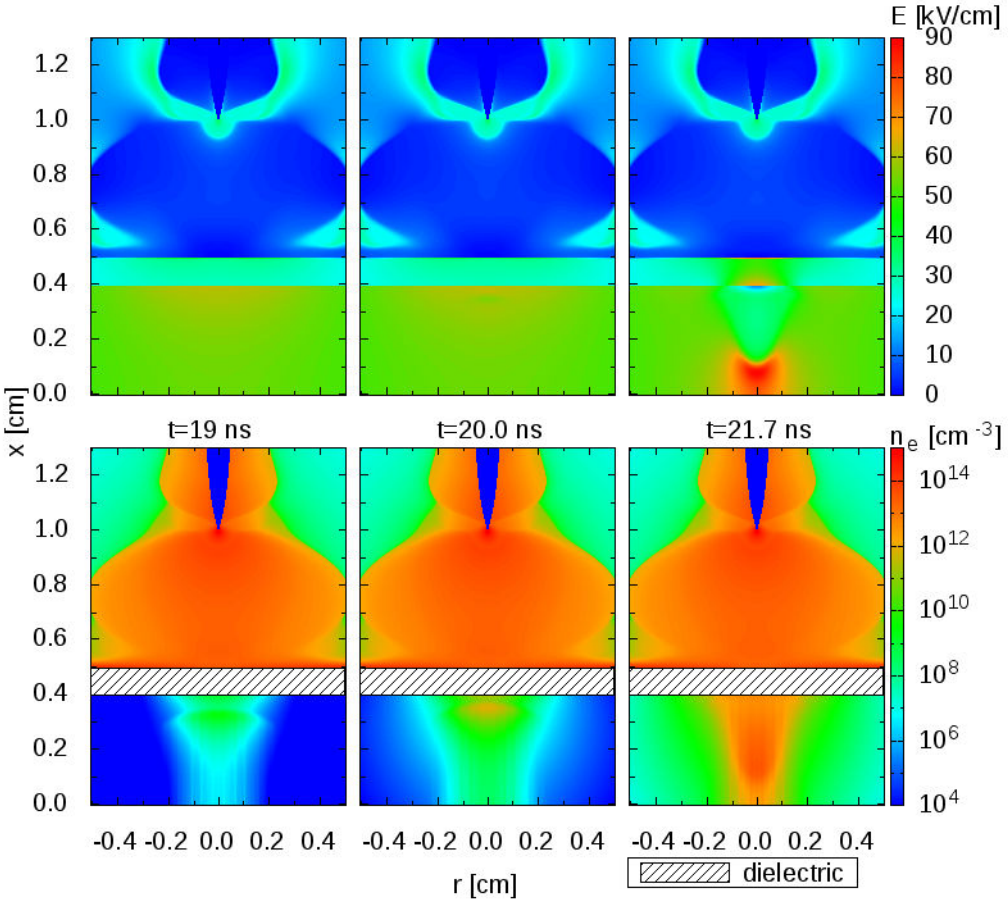

Figure 8.16: *Discharge dynamics with a dielectric plane obstacle. The emission of electrons from the cathode surface is due to the thermionic and field emission processes where ϕ=4 eV and β=100. Cross-sectional views of the absolute value the electric field and electron density at t=19, 20, 21.7 ns*

8.7 Conclusion on the experiment/modelling comparison

In the framework of the ALVEOPLAS project, in this chapter, we have studied the reignition process and compared experimental and numerical results for the experimental geometry and we have shown that:

- Without a dielectric plane obstacle in the inter-electrode gap, experimental and numerical results show that for a maximum voltage of about 30 kV applied at the point anode, a single conical discharge is ignited. We have compared the propagation velocity of the discharge to cross the inter-electrode gap and found a quite good agreement between experimental and numerical results. A good agreement on the maximum diameter of the discharge on experimental and simulated optical emission measurements has also been obtained.

- With a dielectric plane obstacle in the inter-electrode gap, in the experiments, the reignition process is characterized by the occurrence of a current peak (usually the fourth one) at the segmented cathode coupled with optical emission recorded with a fast camera. Using this methodology, experimental results show that the time delay between the ignition at the point anode and the impact on the cathode of the reignited discharge is in the range of $\Delta t_{delay}^{exp} \in [18\ ns : 24\ ns]$. Conversely, the numerical results show that the reignition process is faster with a numerical delay of Δt_{delay}^{num}=5.6 ns.

To improve the agreement between experimental and numerical results on the reignition behind a dielectric obstacle, we have proposed first a new insight in the interpretation of experimental results and second we have studied which physico-chemical processes could be missing in the simulations. The two main results of this analysis are:

- We have shown that maybe the second peak of current measured in the experiments at Δt=6 ns, could correspond to the impact of a first reignited discharge on the cathode. Indeed, this reignition delay is close to the numerical delay of Δt_{delay}^{num}=5.6 ns. In the simulations the optical intensity of the reignited discharge below the dielectric plane is weak. It may explain the difficulty for a high speed camera to detect it. We suggest that successive current peaks obtained

in the experiments could correspond to successive reignition events during the voltage pulse due to surface charges deposition on the different dielectric surfaces of the reactor.

- We have also shown that no matter the level of seed charges in the second air gap, the reignition process occurs due to the high value of the electric field in the second air gap. Therefore we have investigated the influence of electron emission processes from the cathode in the extreme case with no initial seed charges in the second air gap. We have taken into account the thermionic and field emission processes at the cathode surface. We have found that the time to release an electron from the cathode surface is greatly influenced by the work function of the metallic cathode ϕ and the amplification factor β. For the set of values for ϕ and β studied in this work, we have shown that the time to release an electron from the cathode surface is at maximum of 6.9 ns and then the delay for the reignition process is at maximum of Δt_{delay}^{num}=13.2 ns, slightly shorter than the experimental reignition delay $\Delta t_{delay}^{exp} \in [18\ ns : 24\ ns]$.

Chapter 9

Simulation of the ignition and propagation of a helium and air discharge at atmospheric pressure in a dielectric tube

9.1 Introduction

From chapters 6 to 8, we have studied the dynamics of an atmospheric pressure air discharge with a dielectric plane obstacle placed on the path of the discharge. In this case, it can be considered that the dielectric obstacle is an axial constraint on the discharge dynamics. These last few years, with many experimental and numerical studies on plasma jets, a lot of attention has been focused on the ignition and propagation of discharges in rare gases (mostly helium) at atmospheric pressure in dielectric tubes and then in ambient air. In this case, the dielectric tube can be considered as a radial constraint on the discharge dynamics.
In order to simulate the ignition and propagation of a helium discharge in a dielectric tube and then in ambient air for plasma jets, it has been shown that a simple chemical model can be used with only one type of positive helium ions and electrons (Naidis 2010a; Jánský and Bourdon 2011a; Boeuf et al. 2013). Nevertheless, in order to go further and carry out quantitative comparisons with experiments, a more complex chemistry needs to be implemented including several helium ions, excited He atoms and nitrogen ions and excited states in presence of impurities. So far, there is no reference kinetic scheme for a $He - N_2$ mixture for plasma jet studies and different chemical models are used (Naidis 2011a; Breden et al. 2012; Yousfi et al. 2012). It is interesting to note that

previous works on high pressure gas lasers (Pouvesle et al. 1982) on $He-N_2$ mixtures have put forward that three body Penning ionization and charge exchange reactions have to be considered at atmospheric pressure. These reactions are absent of the kinetic schemes used so far for $He-N_2$ discharge simulations in tubes and plasma jets. Then, in this work, we propose to study the influence of these three-body reactions on the dynamics of propagation in a dielectric tube of discharges in a $He-N_2$ mixture at atmospheric pressure. This work is a first step towards the derivation of a reference kinetic scheme for $He-N_2$ discharge simulations at atmospheric pressure for plasma jet applications. In Section 9.2 we present the discharge model used for a $He-N_2$ mixture. Then in Section 9.3, the results of the discharge dynamics in a dielectric tube with and without the three body Penning ionization and charge exchange reactions are discussed.
To better understand the role of the radial constraint induced by the dielectric tube on the discharge structure and dynamics, in Section 9.4, we propose to compare the discharge dynamics for a dielectric tube filled either with a $He-N_2$ mixture or with air at atmospheric pressure. The influence of the tube radius on the air discharge structure is discussed.

9.2 Discharge model for a discharge in a $He-N_2$ mixture at atmospheric pressure

In this work, we consider that the studied gas is composed of helium with nitrogen admixture. The amount of admixture is equal to $\chi_{imp} = N_{N_2}/N_0 = 10^{-3}$ where $N_0 = 2.45\times10^{19}\ cm^{-3}$ is the neutral helium density. In this work, we have taken into account 3 positive ions (He^+, He_2^+ and N_2^+), 1 excited specie (He^*) and electrons. For the discharge simulation, drift-diffusion equations of charged species are coupled to Poisson's equation. The kinetic scheme used in this work is shown on Table 9.1 and was used in (Zhang and Kortshagen 2006) for a study on a atmospheric pressure glow discharge in helium with some nitrogen impurities. In this kinetic scheme, rate coefficients for three body charge transfer and Penning reactions are taken from (Pouvesle et al. 1982). In this work, the helium ionization coefficient is taken from (Marić et al. 2005). The nitrogen ionization coefficient and the electron impact excitation coefficient of helium and electron transport coefficients are calculated with BOLSIG+ (Hagelaar and Pitchford 2005) with cross sections from (Morgan 2011) for He and N_2. For the electron impact excitation coefficient of helium, the total excitation cross section is used. Positive ion mobilities μ_{He^+}=10.0,

$\mu_{He_2^+}$=17.5 and $\mu_{N_2^+}$=20 $cm^2V^{-1}s^{-1}$ are taken from (Ellis et al. 1976). The diffusion coefficient for ions is evaluated using Einstein relation with temperature T=300 K.

Process	Reactions	Rate coefficient
Direct ionization	$He + e^- \rightarrow He^+ + 2e^-$	f(E/N)
	$N_2 + e^- \rightarrow N_2^+ + e^-$	f(E/N)
Excitation	$He + e^- \rightarrow He^* + e^-$	f(E/N)
He^+ conversion	$He^+ + 2He \rightarrow He_2^+ + He$	$1.5 \times 10^{-31}[cm^6s^{-1}]$
Stepwise ionization	$He^* + He^* \rightarrow He^+ + He + e^-$	$8.7 \times 10^{-10}[cm^3s^{-1}]$
	$He^* + He^* \rightarrow He_2^+ + e^-$	$2.03 \times 10^{-9}[cm^3s^{-1}]$
De-excitation	$He^* + e^- \rightarrow He + e^-$	$2.9 \times 10^{-9}[cm^3s^{-1}]$
Penning ionization	$He^* + N_2 \rightarrow He + N_2^+ + e^-$	$7.6 \times 10^{-11}[cm^3s^{-1}]$
	$He^* + N_2 + He \rightarrow 2He + N_2^+ + e^-$	$3.3 \times 10^{-30}[cm^6s^{-1}]$
Charge transfer	$He_2^+ + N_2 \rightarrow N_2^+ + 2He$	$1.1 \times 10^{-9}[cm^3s^{-1}]$
	$He_2^+ + N_2 + He \rightarrow N_2^+ + 3He$	$1.36 \times 10^{-29}[cm^6s^{-1}]$
Recombination	$He^+ + e^- + e^- \rightarrow He + e^-$	$8.0 \times 10^{-20}(\frac{T_g}{T_e})^4[cm^6s^{-1}]$
	$He_2^+ + e^- \rightarrow He + He$	$9.0 \times 10^{-9}[cm^3s^{-1}]$
	$N_2^+ + e^- \rightarrow N + N$	$2.0 \times 10^{-7}[cm^3s^{-1}]$

Table 9.1: *Kinetic scheme for a helium discharge with nitrogen impurities taken from (Zhang and Kortshagen 2006). The rates of the three first reactions are given in the text. T_e is derived from the Einstein relation for electrons.*

For the photo-ionization model we have used the model developed in (Jánský et al. 2012) based on the work of (Naidis 2010a). It is assumed that the ionizing radiation emitted by excited helium species is absorbed by nitrogen molecules of the admixture and ionize them. Here the ionizing radiation is assumed to be proportional to the excitation rate of helium atoms by electron impact with a factor of 0.01. It is assumed that the absorption length of radiation depends on the level of nitrogen admixture as $1/\lambda_{phion} = N_0 \chi_{imp} \sigma_{phion}$, where for the photo-ionization cross section, a typical value of $\sigma_{phion} = 3 \times 10^{-17}$ cm^2 is used. The photo-ionization source term is derived from the numerical solution of the SP3 approximation presented in Chapter 1, assuming only one absorption length (instead of 3 for air). The code used in this chapter is presented in Chapter 4 in Section 4.3.

9.3 Dynamics of a $He - N_2$ discharge at atmospheric pressure in a dielectric tube

The discharge set-up is shown on Figure 9.1. This geometry is very close to the experimental set-up used in (Algwari and O'Connell 2011). In (Jánský et al. 2012), the dynamics of this discharge was simulated with a more simple kinetic scheme than in Table 9.1. In this section, we propose to carry out simulations with the kinetic scheme of Table 9.1 and in particular to study the influence of three body charge exchange and Penning reactions on the discharge dynamics.
On Figure 9.1, the dielectric tube ($\varepsilon_r = 4$) filled with the $He - N_2$ mixture, has an inner radius of 0.2 cm, a thickness of 0.1 cm and is placed from x=0 cm to 3.5 cm. For x<0 cm and x>3.5 cm, the helium channel is surrounded by air ($\varepsilon_r = 1$). In this work, we have assumed that the helium-air mixing outside the tube has a small influence on the discharge dynamics inside the tube and close to the tube exit. A high voltage ring electrode is placed from x=3.0 to 3.2 cm and a grounded ring electrode is placed from x=0.3 cm to 0.5 cm. To ensure as in (Jánský et al. 2012) that the potential decreases down to zero far from the set-up, grounded planes are placed at 5 and 7.5 cm from the left and right edges of the tube respectively. As in (Jánský et al. 2012), the single voltage pulse

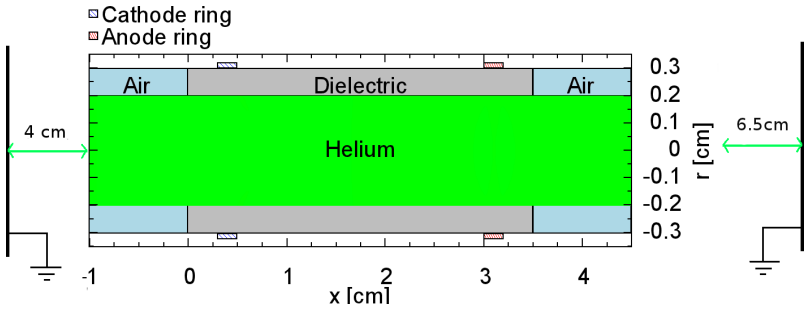

Figure 9.1: *Schematics of the discharge set-up for the helium discharge with nitrogen impurities at atmospheric pressure.*

used in the experiments (Algwari and O'Connell 2011) is approximated by a sinusoidal voltage pulse with a maximum voltage of $U_{max} = 6$ kV and a half period of 3.5 μs.
The grid used in this study is identical to the one used in (Jánský et al. 2012) with a mesh size of 20 and 10 μm in the axial and radial directions, respectively, in the region of discharge propagation (from x=0 to 6 cm and from r=0 to 0.0205 cm). Outside of this domain, the mesh size is expanded using a geometric progression until reaching the boundaries of

the computational domain (from x=-5 to 11 cm and from r=0 to 10 cm). As a result, a grid with $n_x \times n_r$=3114×276 cells is used.
A Neumann boundary condition for the potential is used at the radial open boundary of the computational domain. At each gas-dielectric interface, surface charges obtained by time integrating charged particle fluxes to the dielectric tube surface are taken into account and we have also considered secondary emission of electrons at the dielectric tube surface by ion bombardment (with a secondary emission coefficient of $\gamma = 0.1$). As in (Jánský et al. 2012) a uniform initial density of electrons and positive ions He^+ of n_{init}=10^9 cm^{-3} is taken into account, assuming that several discharges have occurred before the simulated one.

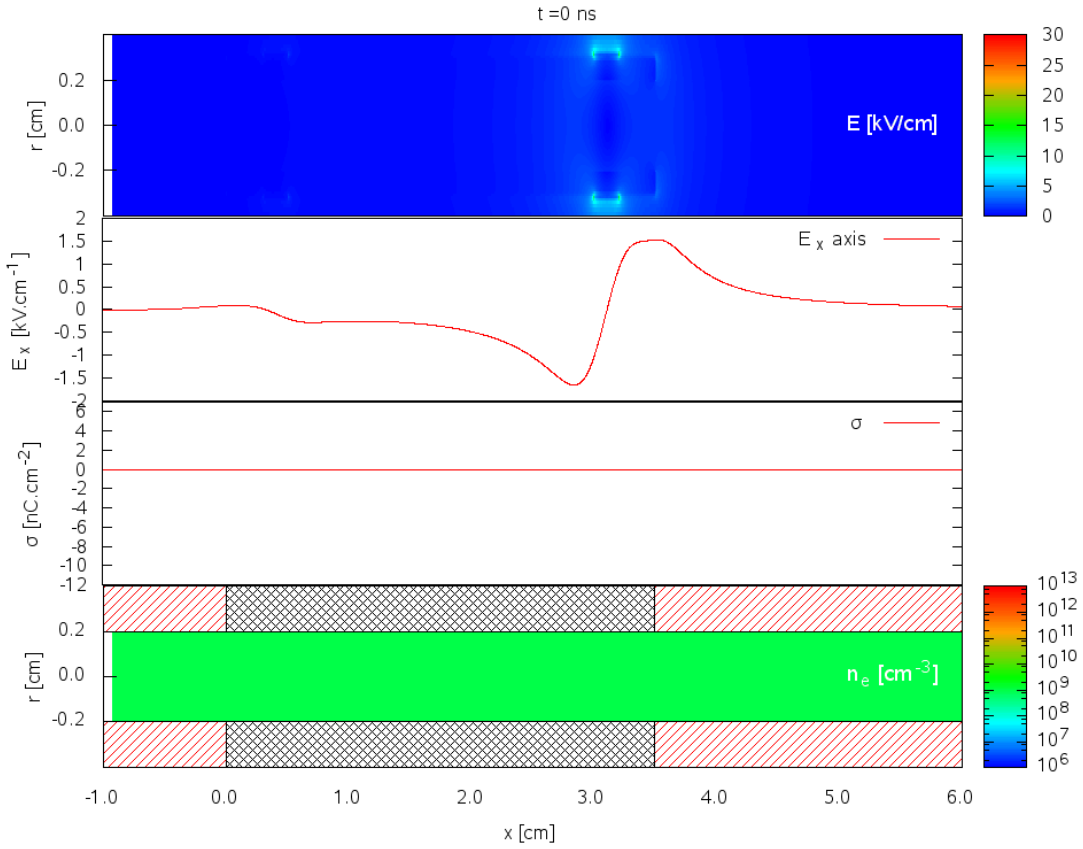

Figure 9.2: *Simulation results of the* $He - N_2$ *discharge for* U_{max} = 6 kV. *Cross-sectional view of absolute values of the electric field, profile of axial electric field on the axis of symmetry, profile of surface charges on the inner surface of the dielectric tube and the distributions of the electron density at t=0 ns.*

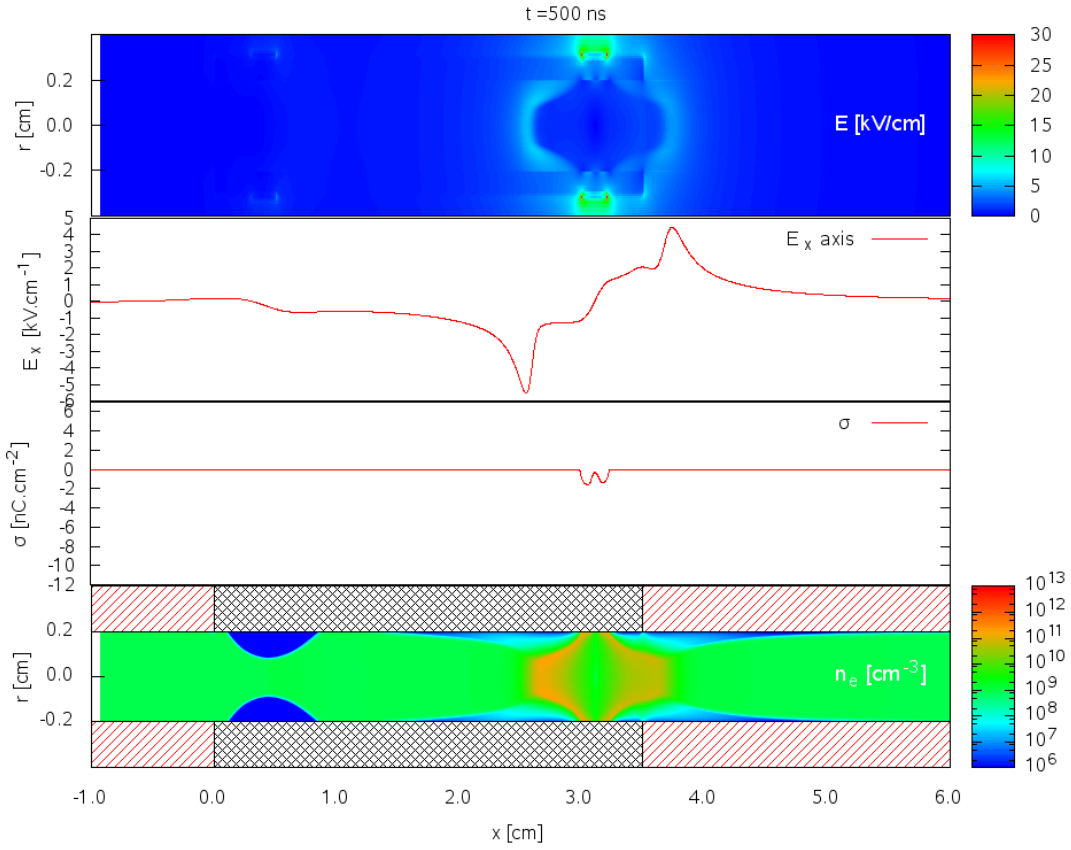

Figure 9.3: *Results at t=500 ns for the same conditions as in Figure 9.2.*

Figures 9.2 to 9.7 show for t=0, 500, 750, 1000, 1050 and 1300 ns the absolute values of the electric field, the profile of axial electric field on the axis of symmetry, the profile of surface charges on the inner surface of the dielectric tube and the distribution of the electron density for U_{max} = 6 kV. At t=0 ns on Figure 9.2, we observe on the profile of axial electric field on the axis of symmetry that there is a minimum of -1.5 kV cm^{-1} and a maximum of 1.5 kV cm^{-1} on the left and right edges of the powered ring electrode respectively. Then on Figure 9.3 at t=500 ns, we observe that at the axial locations of these peaks of electric field, 4 ionization fronts are ignited inside the dielectric tube. Two positive streamer discharges are ignited: one propagating to the left toward the cathode ring and the other one propagating to the right toward the cathode plane on the right side. We also observe two weak negative fronts ignited below the powered ring that propagate toward each other. Below the powered ring, on Figure 9.3, we observe a high deposition of negative

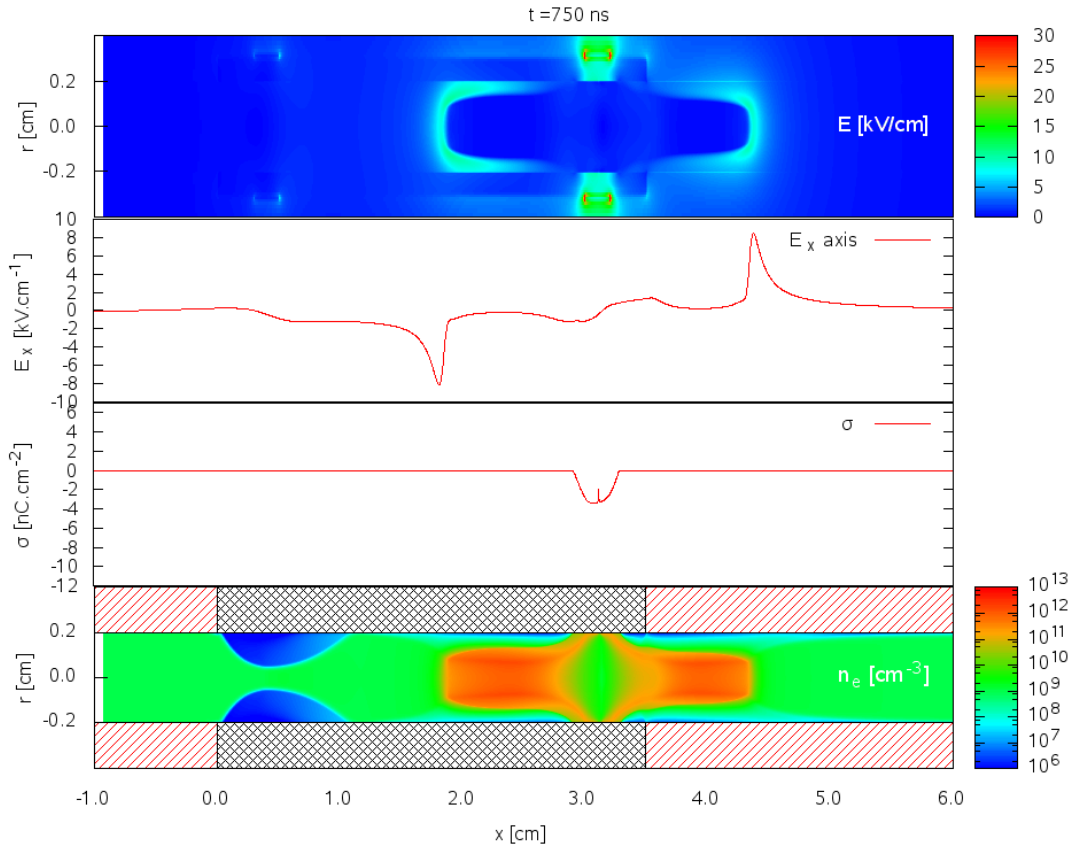

Figure 9.4: *Results at t=750 ns for the same conditions as in Figure 9.2.*

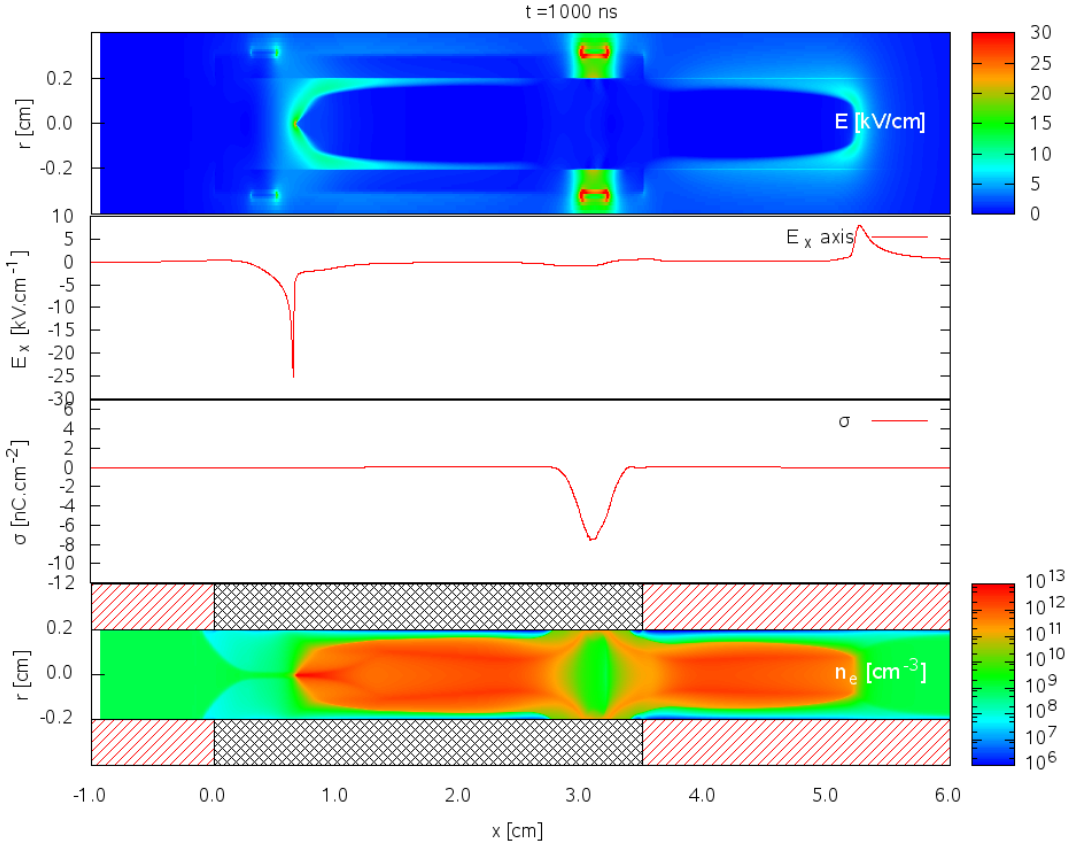

Figure 9.5: *Results at t=1000 ns for the same conditions as in Figure 9.2.*

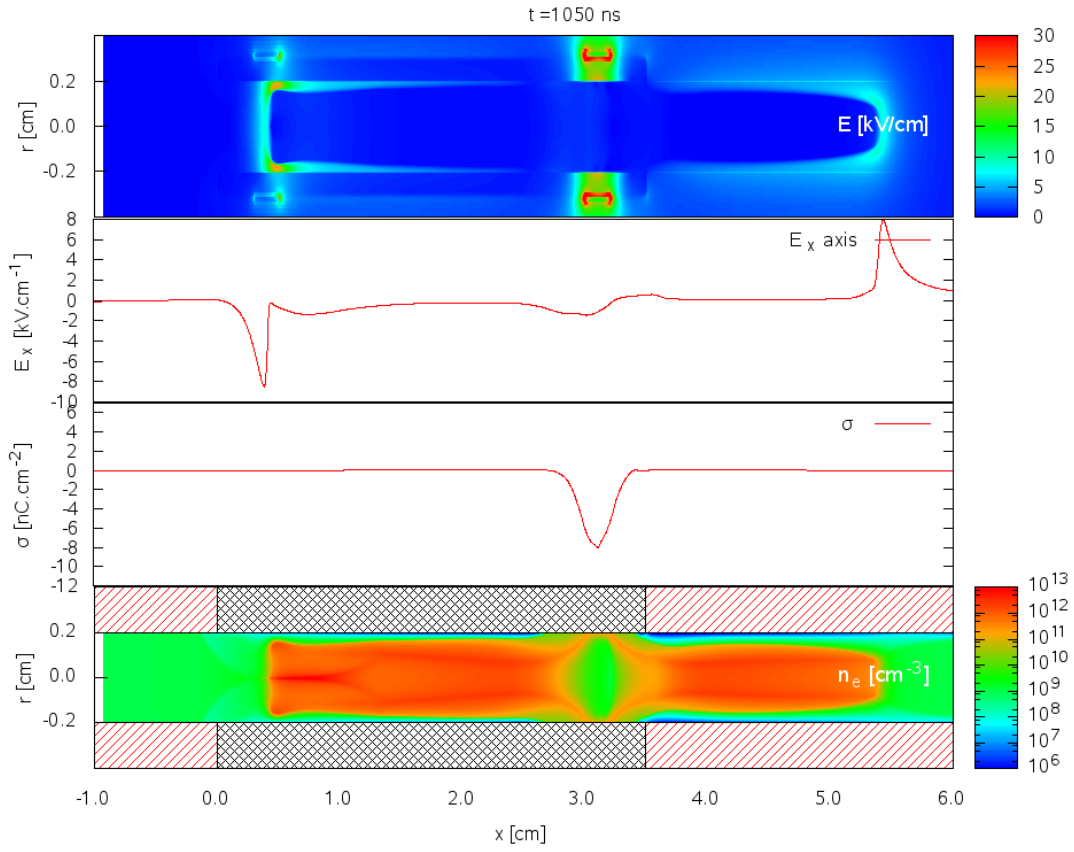

Figure 9.6: *Results at t=1050 ns for the same conditions as in Figure 9.2.*

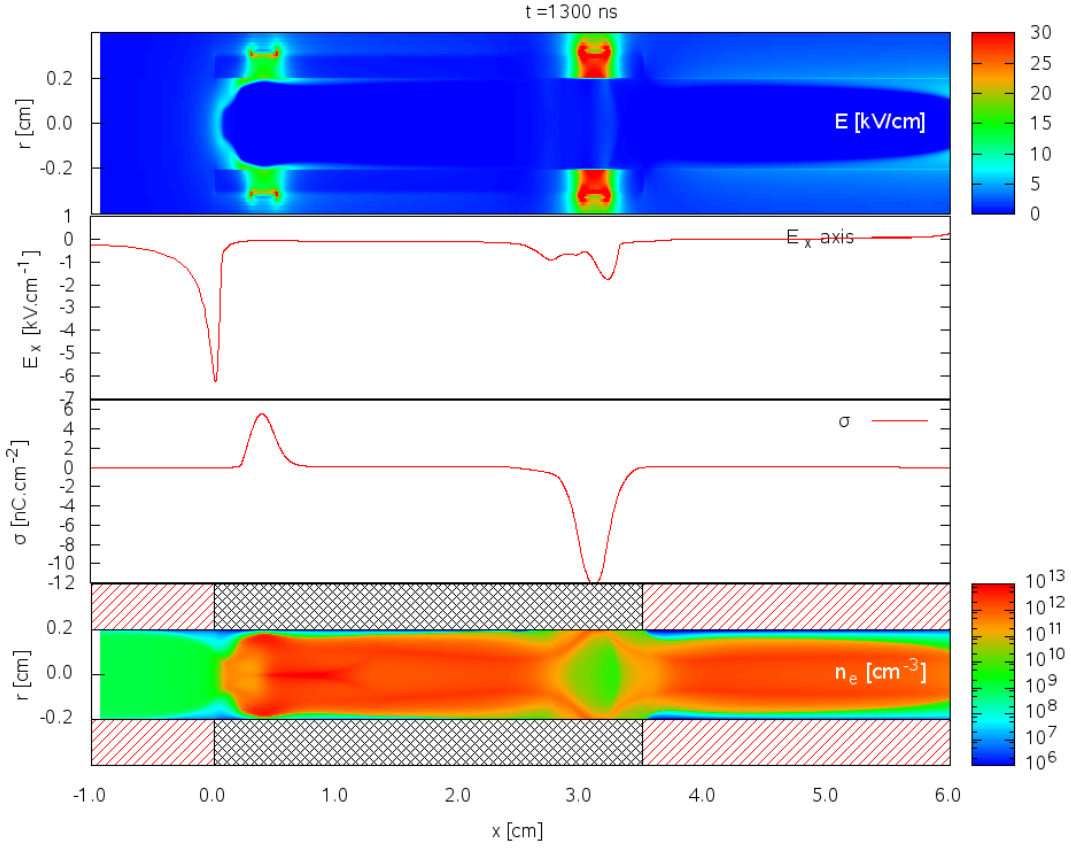

Figure 9.7: *Results at t=1300 ns for the same conditions as in Figure 9.2.*

surface charges on the inner dielectric tube surface with a peak value of -2 nC cm^{-2}. At the same time as in (Jánský et al. 2012), a depletion zone of electrons is formed below the grounded ring and the volume of this zone increases in time. Figure 9.4 at t=750 ns shows the propagation of the two positive discharge fronts on both sides of the powered ring. Both discharge fronts have a rather homogeneous radial structure with a peak value of the magnitude of the electric field equal to E=10 kV cm^{-1} and a electron density equal to $n_e = 10^{12}$ cm^{-3}. As in (Jánský et al. 2012), the amount of negative surface charges deposited on the dielectric surface below the powered ring increases (in absolute value) and as a result during the propagation most of the applied voltage is distributed in the material of the dielectric tube.

On Figure 9.5 at t=1000 ns, we clearly observe the increase of negative surface charges (in absolute value) deposited on the dielectric surface below the powered ring to a value of 8 nC cm^{-2} (in absolute value). Between t=750 ns and t=1000 ns, we note that the discharge propagating towards the cathode ring arrives close to the cathode in the region with volumes depleted of electrons. Due to the photoionization source term, some electrons are created in these depleted volumes as the discharge propagates, but we note nevertheless that the discharge structure slightly changes from t=750 to 1000 ns. At t=1000 ns, the discharge front is located on the axis of symmetry, where the electron density ahead of the discharge is the highest.

At t=1050 ns on Figure 9.6, the positive front of the discharge is below the grounded ring. We note that the radius of the discharge increases and the discharge front impacts the dielectric surface below the grounded ring (due to the electrostatic effect between the positive head of the discharge and the grounded ring). Below the grounded ring, the positive discharge becomes tubular while the second positive discharge front propagating to the right outside the dielectric tube has still a rather homogeneous radial structure. On Figure 9.7 at t=1300 ns, we observe an increase of positive surface charges on the dielectric surface below the grounded ring and at the same time an increase of the negative surface charges (in absolute value) on the dielectric surface below the powered ring. At t=1300 ns, we observe that after impacting the dielectric surface below the grounded ring, the front of the discharge is re-centered around the axis of symmetry. For t>1300 ns this discharge propagates toward the grounded plane on the left i.e. after the grounded ring. Figures 9.8 to Figure 9.10 show cross-sectional views of He^+, He_2^+, N_2^+ and He^* density at t=750, 1050 and 1300 ns. At t=750 ns, Figure 9.8 shows that He^+ ions are produced in the fronts of the two positive discharges and are quickly converted to

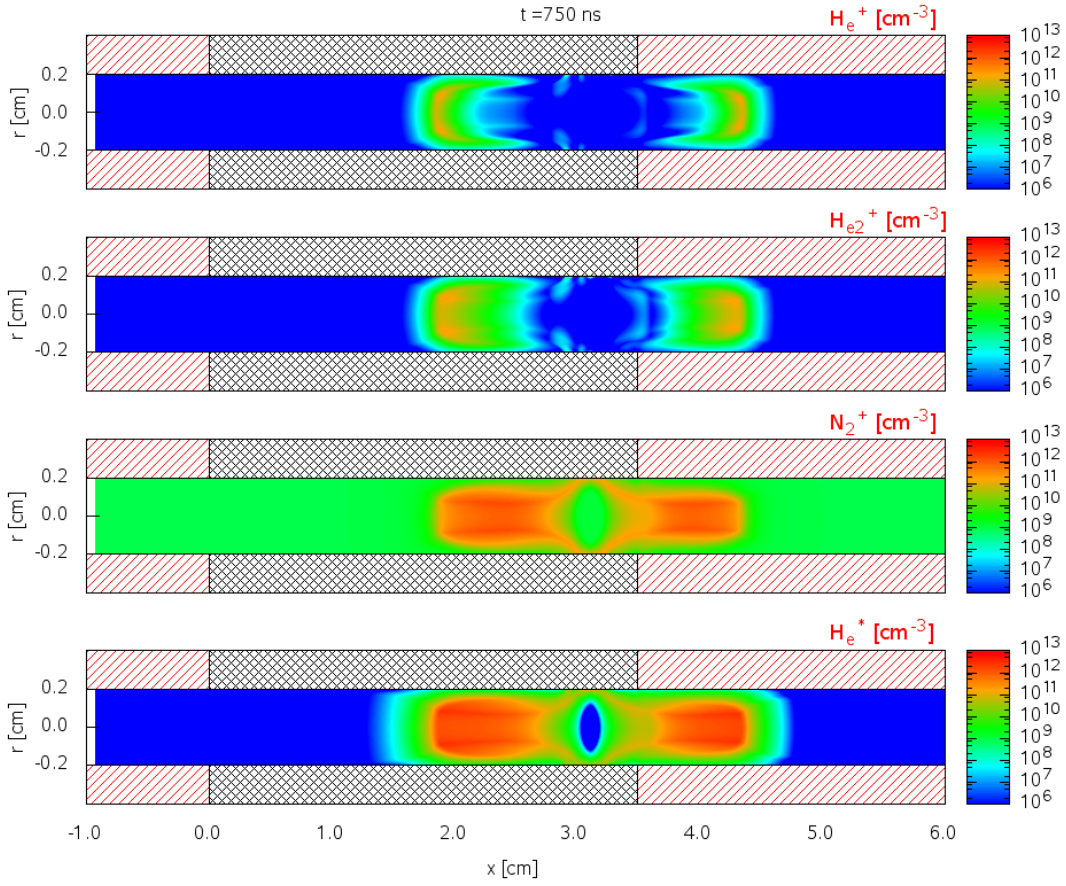

Figure 9.8: *Cross-sectional views of* He^+, He_2^+, N_2^+ *and* He^* *densities at t=750 ns for the same conditions as in Figure 9.2.*

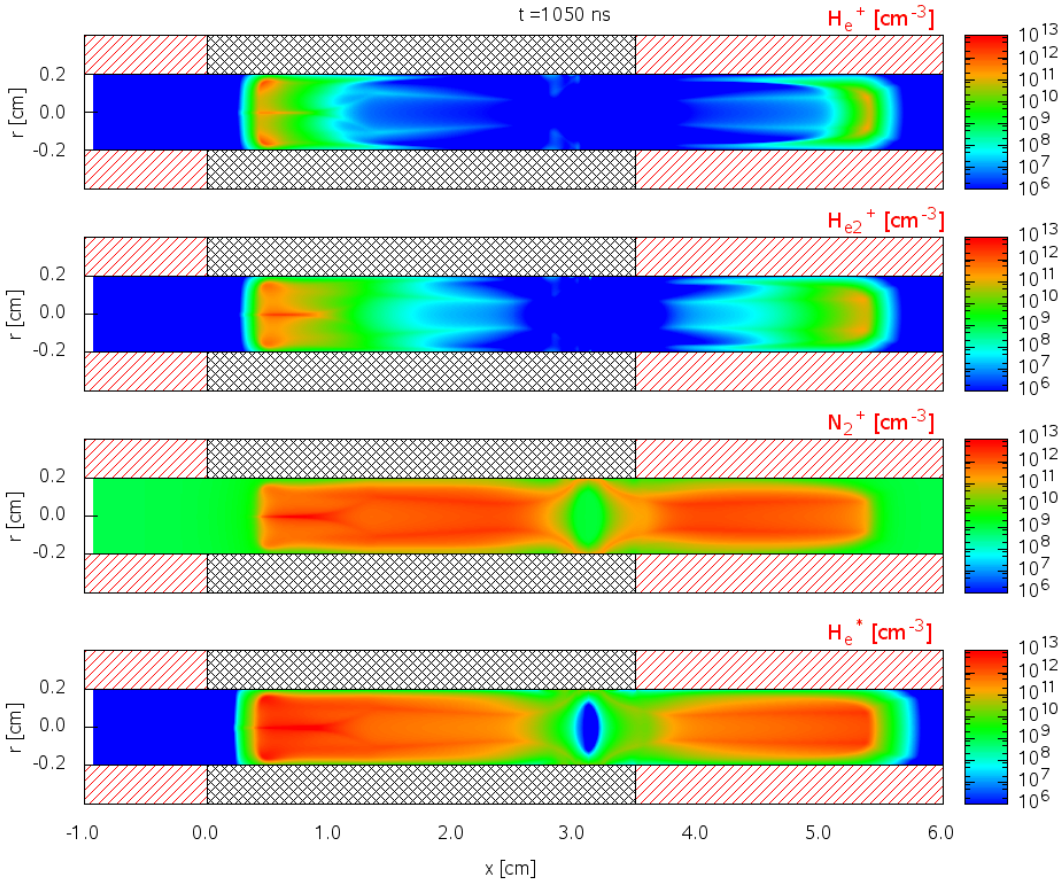

Figure 9.9: *Cross-sectional views of* He^+, He_2^+, N_2^+ *and* He^* *densities at t=1050 ns for the same conditions as in Figure 9.2.*

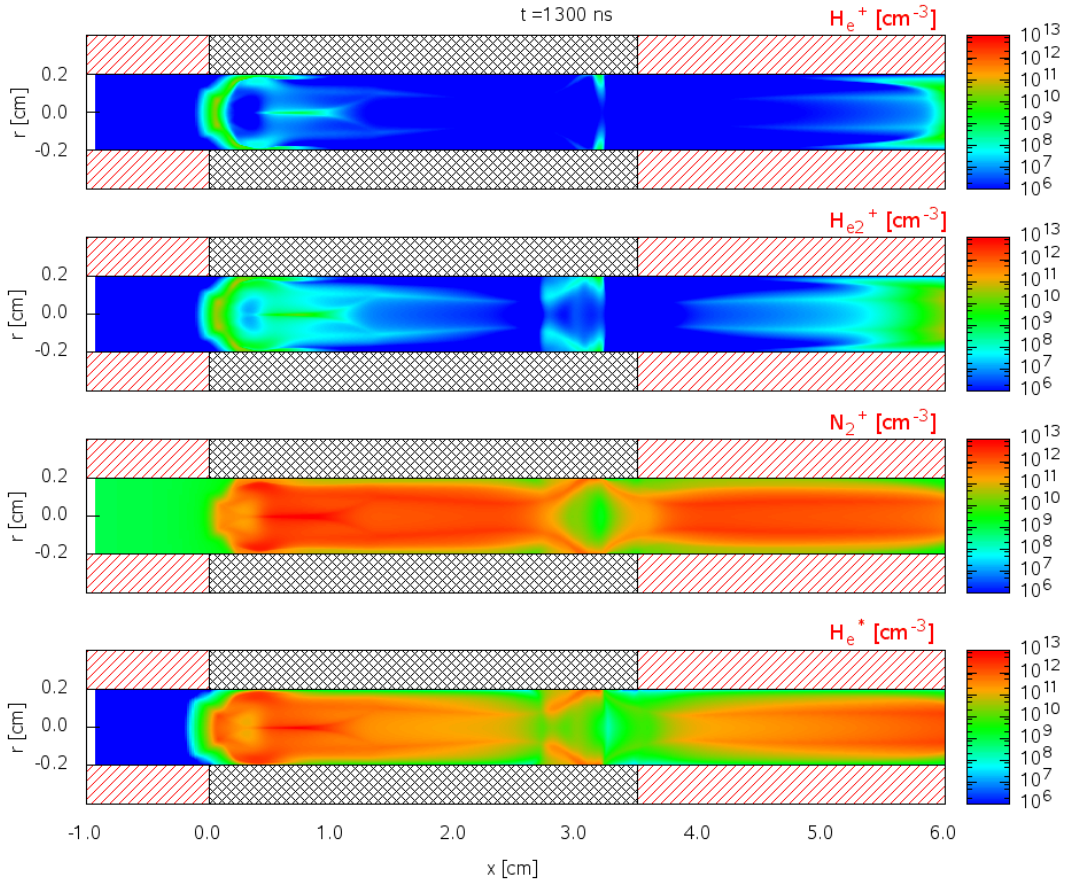

Figure 9.10: *Cross-sectional views of* He^+, He_2^+, N_2^+ *and* He^* *densities at t=1300 ns for the same conditions as in Figure 9.2.*

He_2^+. We also observe that He^* is produced mainly in the discharge front where the electric field is high and the He^* density decreases slowly behind the discharge front. At t=1050 ns, Figure 9.9 shows that the main formation area of N_2^+ ions is in the discharge channel. The formation of N_2^+ ions is mainly due to the Penning ionization process. At t=1300 ns, Figure 9.10 shows an increase of He^* density close to the tube surface below the grounded cathode ring. This increase of the direct excitation process is due to the increase of the electric field in the head of the impacting discharge below the cathode ring shown in Figure 9.7.
In a second step to study the influence of the three body reactions:

- Penning ionization: $He^* + N_2 + He \rightarrow 2He + N_2^+ + e^-$,
- Charge transfer: $He_2^+ + N_2 + He \rightarrow N_2^+ + 3He$,

we have simulated the discharge without these two reactions. Figure 9.11 shows in this case cross-sectional views of He^+, He_2^+, N_2^+ and He^* densities at t=1050 ns. It is important to note that removing three body Penning and charge transfer reactions has no major influence on the discharge structure and dynamics inside the tube. If we compare results at t=1050 ns on Figures 9.9 and 9.11, we observe that without these three body reactions, the discharge propagation is slightly slower. These results clearly show the need to take into account three body charge exchange and Penning reactions to go towards quantitative comparisons with experiments. Currently different research groups are measuring He^* densities in jets and close to the tube exit. In a future work, it would be interesting to investigate in current kinetic schemes used in plasma jet simulations the influence of reactions involving different excited states of He and also He_2^*.

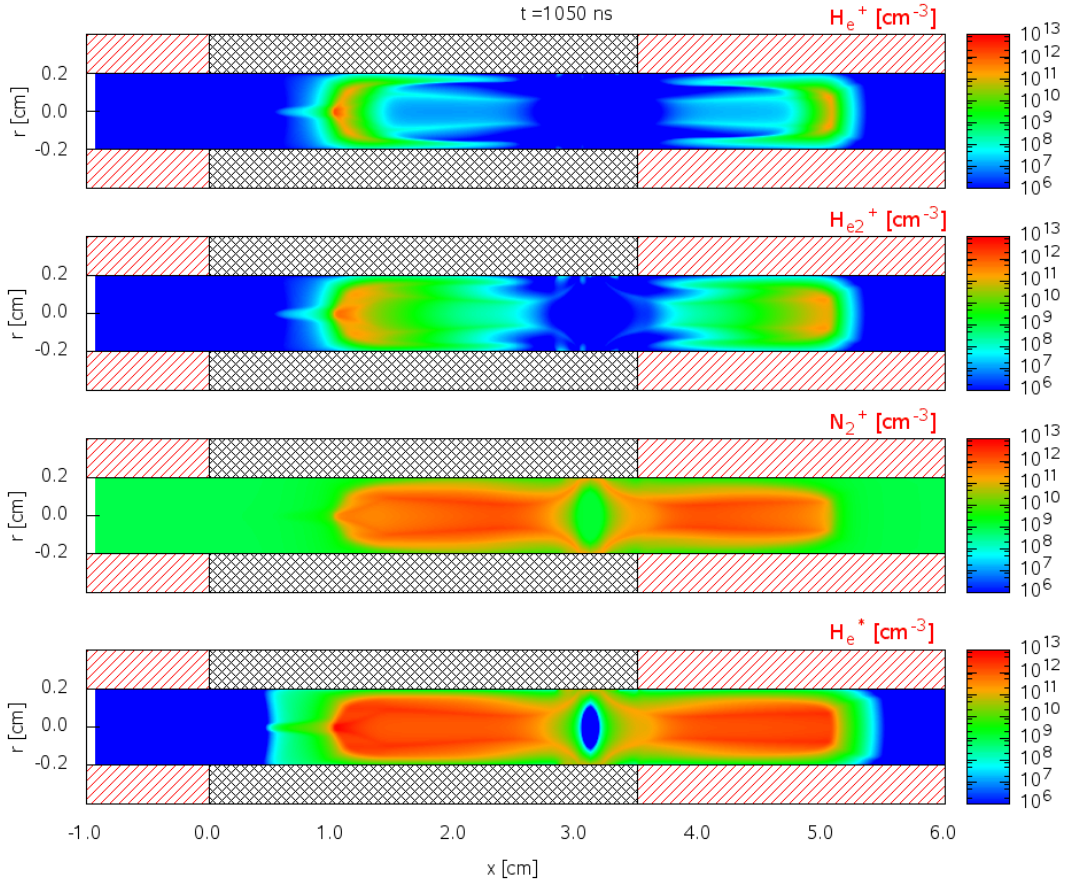

Figure 9.11: *Cross-sectional views of* He^+, He_2^+, N_2^+ *and* He^* *density at t=1050 ns for the same conditions as in Figure 9.2 but without taking into account three body Penning and charge exchange reactions.*

9.4 Influence of the tube radius on the structure of air discharges at atmospheric pressure

In Section 9.3, we have observed the propagation of a rather homogeneous $He - N_2$ discharge inside a dielectric tube with an inner radius of 2 mm. To study the influence of the radial constraint of the dielectric tube on the discharge structure, we propose to compare the discharge dynamics of a discharge in air and in $He - N_2$ at atmospheric pressure for the same inner tube radius. Therefore, in this section, we present air discharge simulations for the same geometry as in Section 9.3, except that a longer

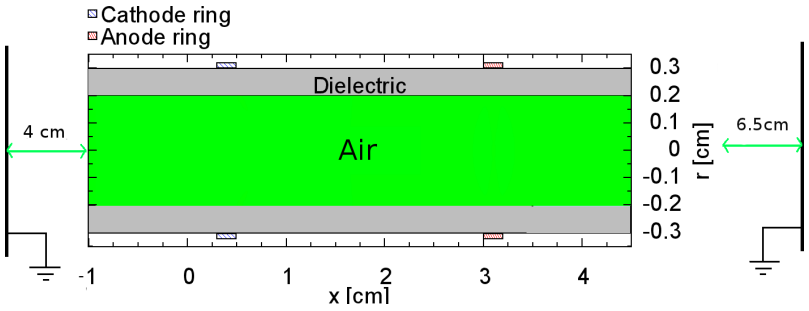

Figure 9.12: *Schematics of the set-up with a long dielectric tube.*

tube is considered. For clarity, the discharge set-up used in this section is shown on Figure 9.12. A mesh size of 10 and 5 μm in the axial and radial directions, respectively is used, in the region of discharge propagation (from x=0 to 6 cm and from r=0 to 0.0205 cm). Outside of this domain, the mesh size is expanded using a geometric progression until reaching the boundaries of the computational domain (from x=-5 to 11 cm and from r=0 to 10 cm). As a result, a grid with $n_x \times n_r$=6114×481 cells is used. The code used is the same as in Section 9.3. For air, the source terms and transport parameters are given in chapter 1.

In order to ignite an air discharge inside the dielectric tube, in comparison to helium in section 9.3, we have increased the voltage to $U_a = 40$ kV to have an electric field on the axis of symmetry higher than 30 kV cm^{-1} ($|E_{axis}|$ =36 kV cm^{-1} at t=0 ns for U_a = 40 kV). For air simulations, we have considered a constant applied voltage. Figures 9.13 to 9.17 show for t=0, 10, 20, 50 and 100 ns the distribution of absolute values of the electric field, the profile of axial electric field on the axis of symmetry, the profile of surface charges on the inner surface of the dielectric tube and the distribution of the electron density. At t=10 ns, Figure 9.14 shows that two positive surface discharges are ignited on both edges of the anode ring close to the inner surface of the dielectric tube. At the same time, we observe a high deposition of negative surface charges on the dielectric surface below the powered ring ($|\sigma^-_{max}|$=13.2 nC cm^{-2}). At t=50 ns on Figure 9.16, the electric field in the head of the positive surface air discharge between the ring electrodes is equal to 297 kV cm^{-1} and the electron density is equal to 3.37 10^{14} cm^{-3}. It is interesting to note that in time for t=10 to 100 ns, from Figure 9.14 to Figure 9.17, negative surface charges on the dielectric surface below the powered ring increases (in absolute value) to reach $|\sigma^-_{max}|$>40 nC cm^{-2} at t=100 ns and as soon as the left hand side positive surface discharge reaches the grounded ring, a high amount of positive charges are deposited ($|\sigma^+_{max}|$>40 nC cm^{-2} at

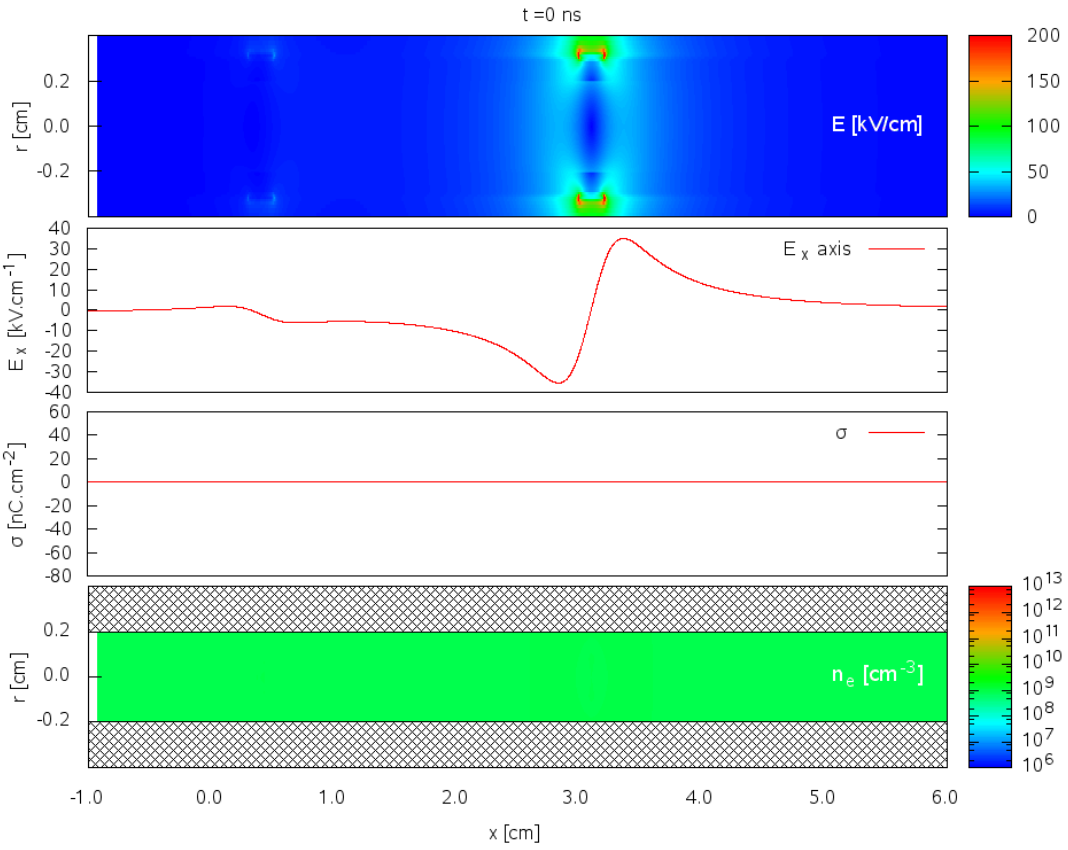

Figure 9.13: *For an air discharge in a tube with a inner radius of 0.2 cm and for a constant applied voltage* $U_a = 40$ kV*, cross-sectional view of absolute values of the electric field, profile of axial electric field on the axis of symmetry, profile of surface charges on the inner surface of the dielectric tube and the distributions of the electron density at t=0 ns.*

t=100 ns) on the dielectric tube surface below the cathode ring. It is important to note that during all the propagation dynamics, the positive discharges propagate only on the dielectric surface and so with an inner tube radius of 0.2 cm and for a constant applied voltage of $U_a = 40$ kV, the ignited positive air discharges have a tubular structure. In Section 9.3, for a $He - N_2$ mixture, for a lower applied voltage, the discharge is shown to fill more homogeneously the tube. It is also interesting to note that to cross the 2.5 cm ring-ring interelecrode gap, it takes ony $\sim$ 100 ns for a discharge in air whereas in a $He - N_2$ mixture it requires ~ 1 μs.

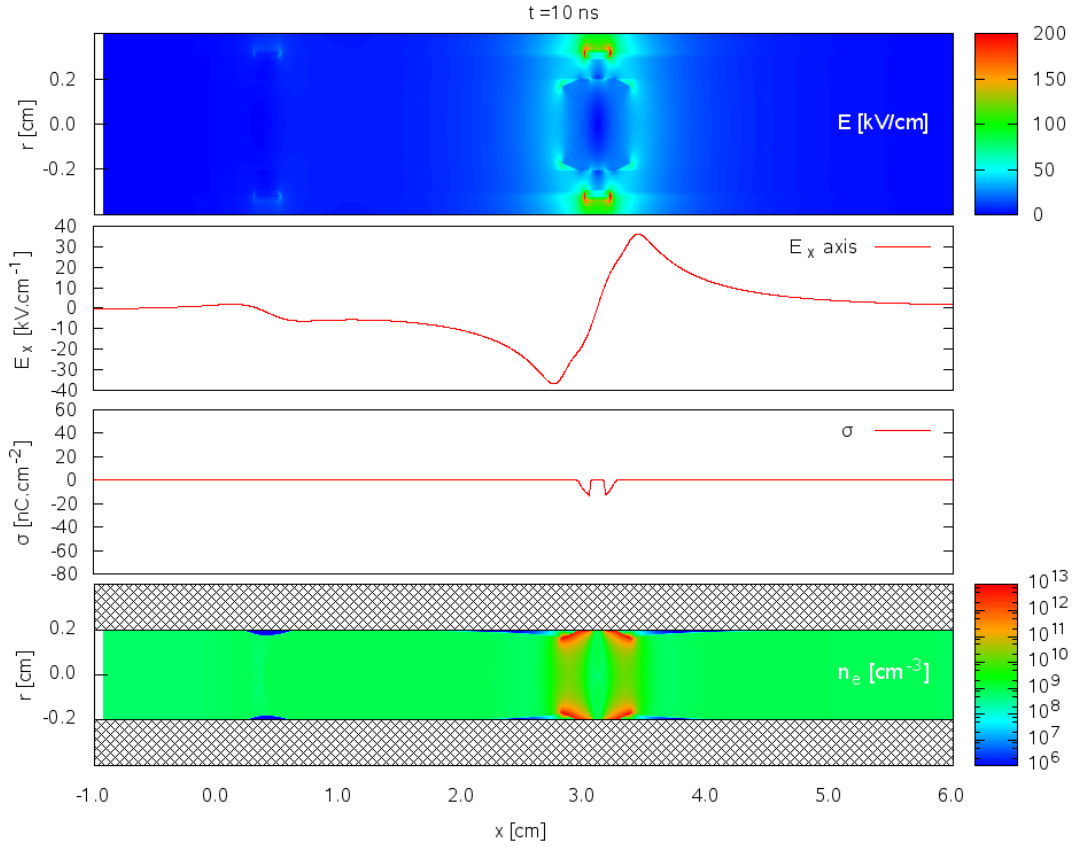

Figure 9.14: *Results at t=10 ns for the same conditions as in Figure 9.13.*

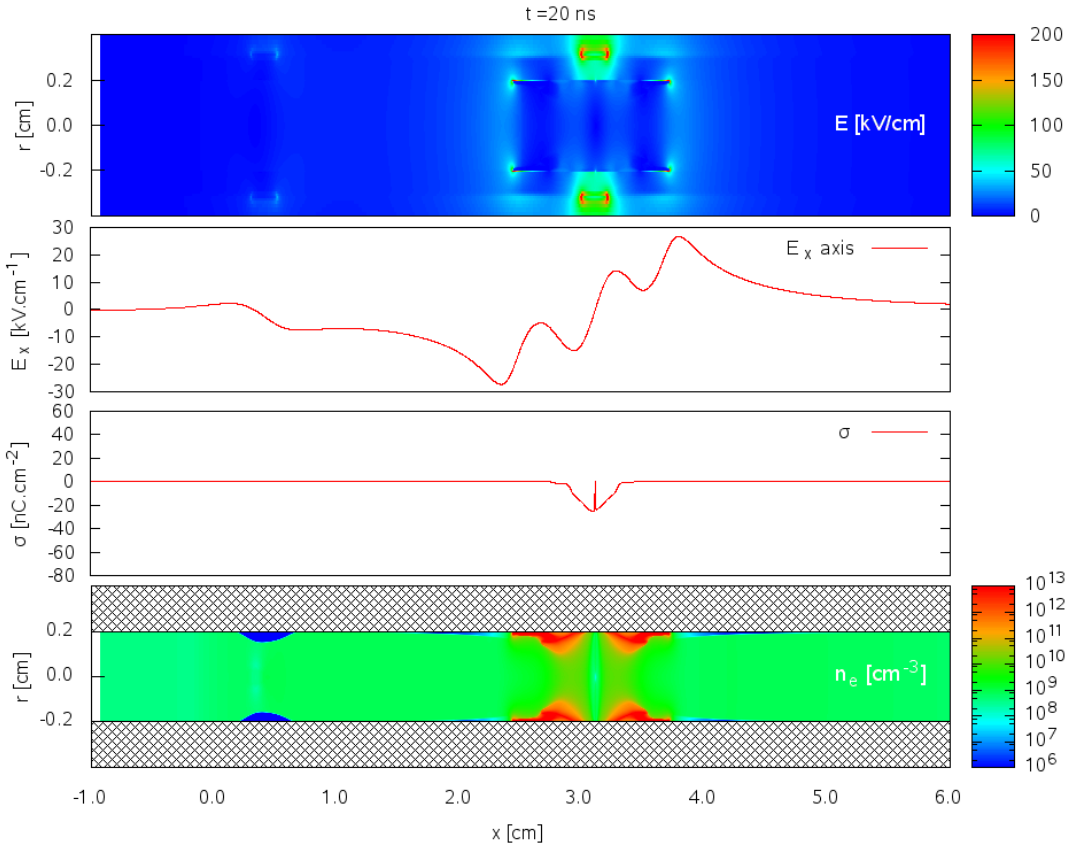

Figure 9.15: *Results at t=20 ns for the same conditions as in Figure 9.13.*

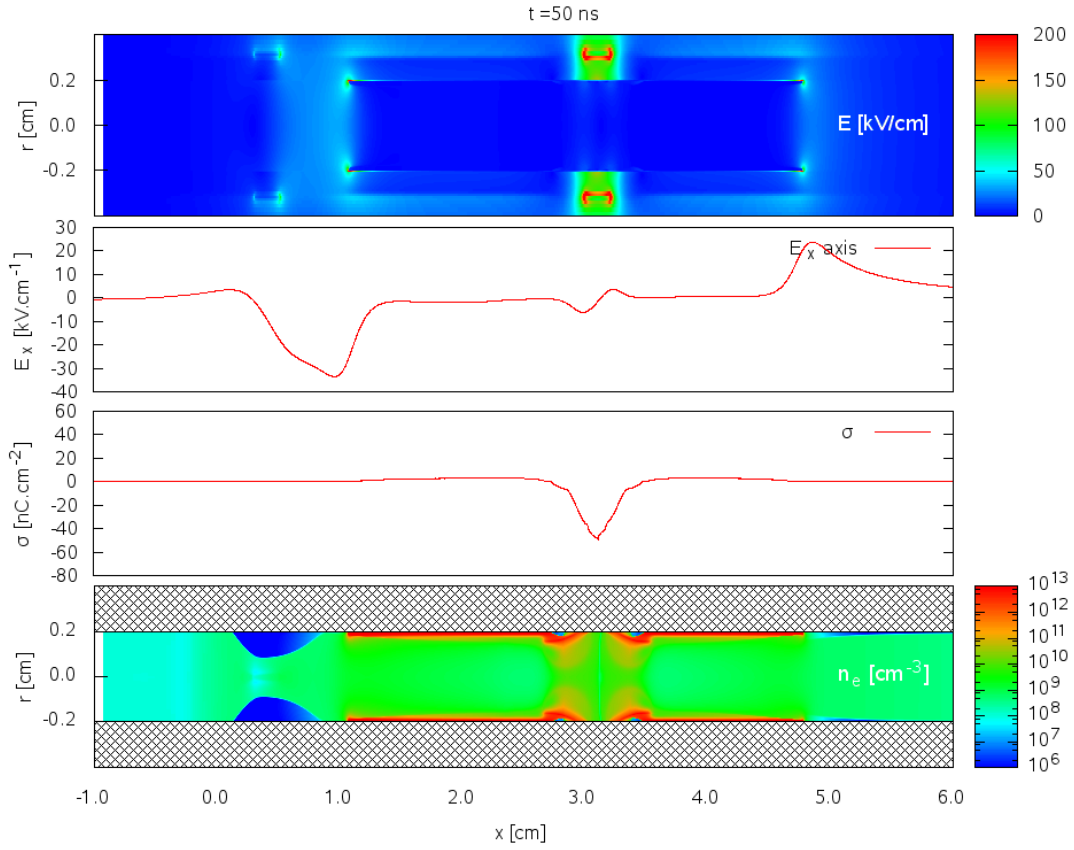

Figure 9.16: *Results at t=50 ns for the same conditions as in Figure 9.13.*

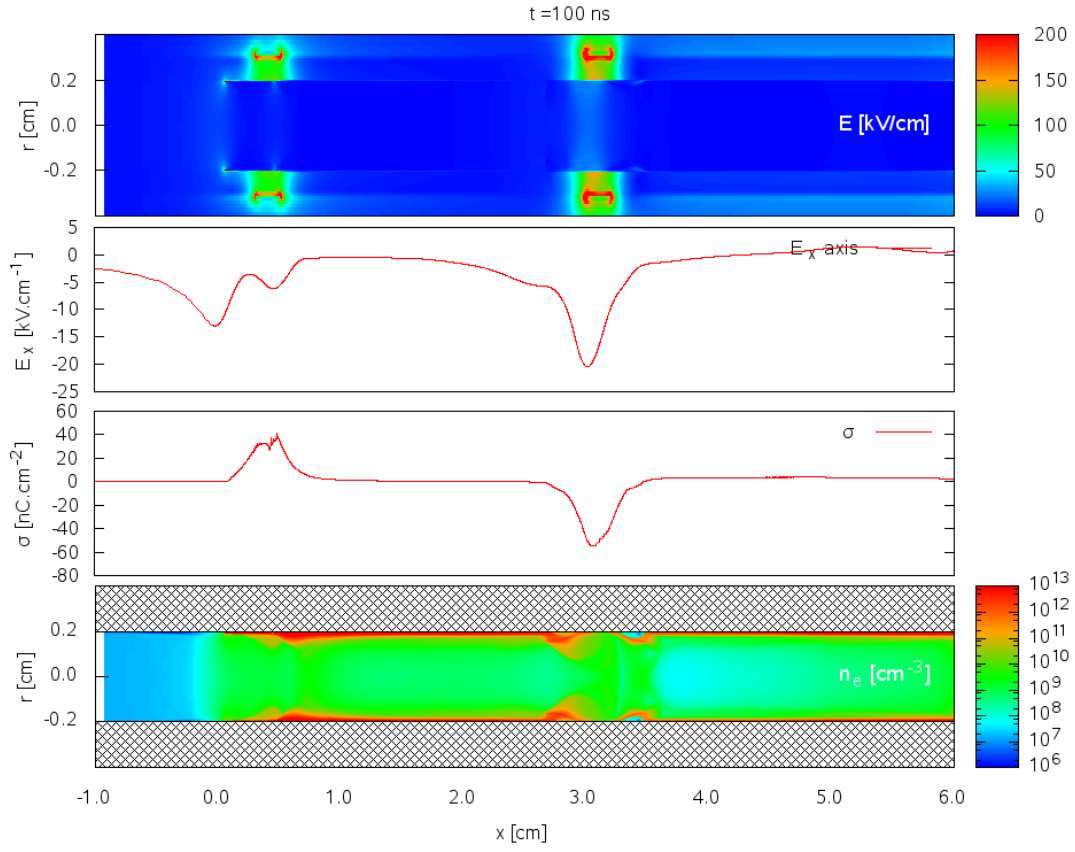

Figure 9.17: *Results at t=100 ns for the same conditions as in Figure 9.13.*

In (Jánský et al. 2010) in a point-to-plane geometry with the point electrode set inside a dielectric tube, it was shown that by decreasing the inner radius of the dielectric tube from 300 μm to 100 μm, the structure of an air discharge at atmospheric pressure propagating in the dielectric tube changed from tubular to homogeneous structure. Then, we have investigated if similar changes could be obtained inside a dielectric tube for a ring-ring electrode geometry when the tube radius is decreased.
Figures 9.18 and 9.19, show at t=0 and 10 ns, first simulation results of the discharge in air for a constant applied voltage U_a = 60 kV for an inner tube radius of 200 μm. The applied voltage has been increased from U_a = 40 kV to 60 kV, in order to have an electric field on the axis of symmetry higher than 30 kV cm^{-1} (for U_a = 60 kV, at t=0ns, $|E_{axis}|$ =47 kV cm^{-1}). At t=10 ns, Figure 9.19 shows that by decreasing the inner tube radius, two more homogeneous positive air discharges are ignited in the tube at the edges of the powered ring and propagate

away from the powered ring. At t= 10 ns, The maximum electric field in the head of the discharge is equal to 620 kV cm^{-1} and the maximum electron density is equal to 1.93 10^{15} cm^{-3} close to the dielectric surface. These first results seem to show that if the tube radius is adapted to the studied gas, homogeneous discharge in tubes could be obtained for other gases than rare gases used so far in plasma jets. These first results on the influence of the tube radius on the discharge structure could be also of interest to optimize the structure and the production of active species in current plasma jets using rare gases.

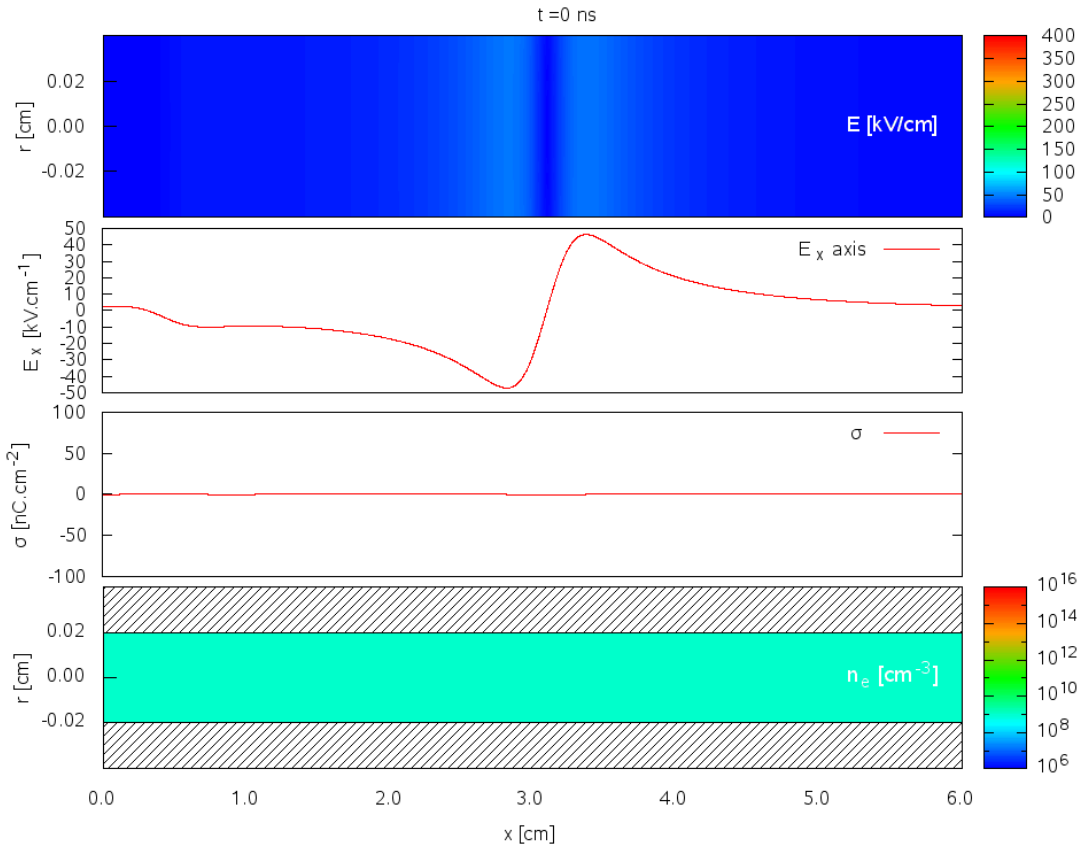

Figure 9.18: *For an air discharge in a tube with a inner radius of 200 µm and for a constant applied voltage* $U_a = 60$ kV*, cross-sectional view of absolute values of the electric field, profile of axial electric field on the axis of symmetry, profile of surface charges on the inner surface of the dielectric tube and the distributions of the electron density at t=0 ns.*

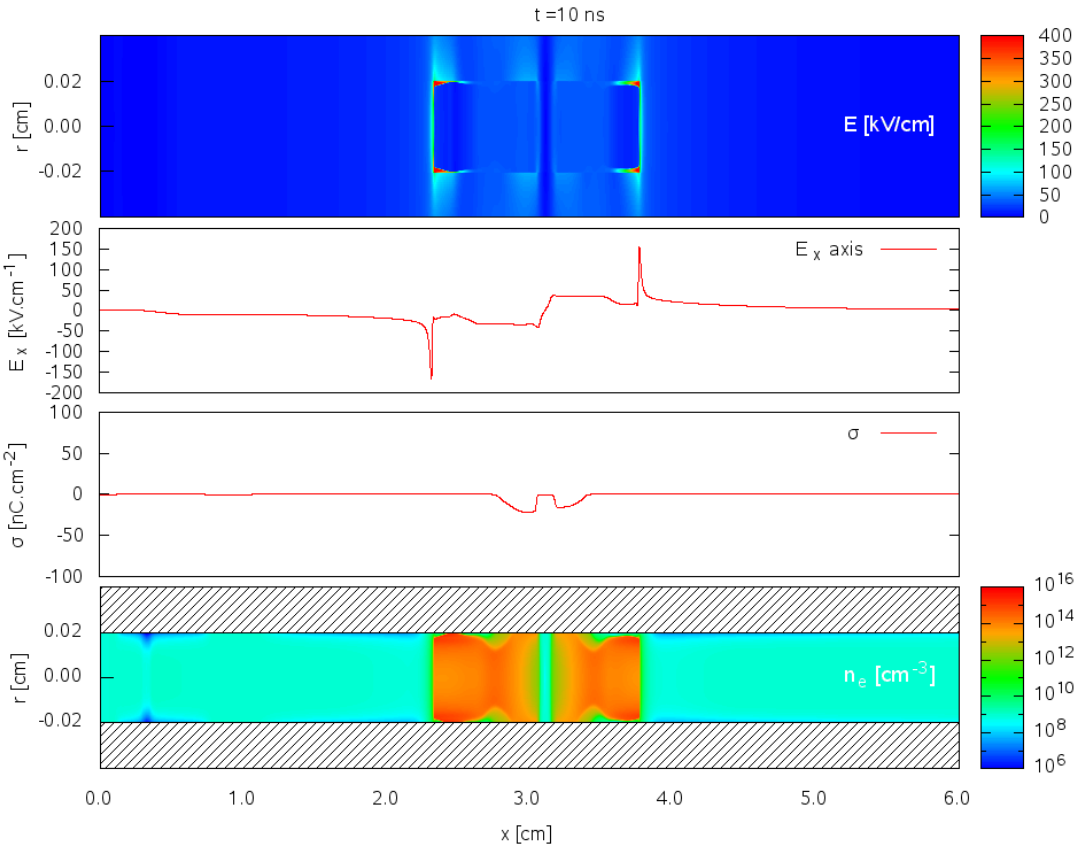

Figure 9.19: *Results at t=10 ns for the same conditions as in Figure 9.18.*

9.5 Conclusion

The main results of this chapter on the simulation of the ignition and propagation of $He - N_2$ and air discharges at atmospheric pressure in a dielectric tube with a ring-ring electrode geometry can be summarized as follows:

- In a $He-N_2$ mixture, in tubes with a inner radius of 2 mm, two positive discharges ignite at the edges of the powered ring and propagate away from it. We have shown that when three body Penning and charge exchange reactions are taken into account, the propagation of the discharge is slightly faster. It would be of great interest to investigate further the chemistry of $He-N_2$ mixtures to go towards quantitative comparison with experiments in tubes and plasma jets.

- We have shown that to have a discharge with a rather homogeneous radial structure, a inner tube radius of 0.2 cm is well adapted for a $He-N_2$ mixture. In air, a much smaller discharge radius of 200 μm is required. As expected to ignite a discharge in air in the same geometry as for a $He - N_2$ mixture, a much higher voltage needs to be applied at the powered ring. Finally, we have shown that the propagation dynamics in air is faster ($\sim$ 100 ns) than the one in a $He-N_2$ mixture (~ 1 μs) to cross the 2.5 cm ring-ring interelectrode gap considered in this work.

Conclusion

Contributions of this thesis

In this Ph.D. thesis, we have carried out numerical simulations to study the influence of dielectric surfaces on the propagation dynamics of discharges at atmospheric pressure.
2D simulations of streamer discharges at atmospheric pressure are known to be computationally expensive. If not optimized, the simulation capabilities of a discharge code are rapidly limited in terms of the size of the simulation domain and the number of species considered. Then, in this work we have implemented modern parallelization techniques into the existing sequential discharge code to increase its computational efficiency. In a streamer discharge code, based on a fluid model, drift-diffusion equations for each charged species are coupled with Poisson's equation. Poisson's equation is solved at each time-step and is the most expensive equation to solve from a computational point of view. As a first step, we have introduced OPENMP protocols in the discharge code and implemented a parallel OPENMP direct solver PaStiX for the resolution of the Poisson's equation. By doing so, we significantly decreased the computational time of the discharge code for small simulation domains where the amount of memory required by the direct solver remains moderate. However, the memory required by the direct solver increases very rapidly with the size of the simulation domain and rapidly exceeds the memory available on a regular node on the "igloo" cluster used to carry out the calculations presented in this thesis. To avoid this limitation, we have used the parallel MPI-OPENMP iterative solver SMG from the HYPRE library. Finally, we have developed a new hybrid MPI-OPENMP discharge code using domain decomposition which considerably decreases the computational time on large simulation domains. In a second step, we have implemented a simple "semi-implicit" scheme to remove the constraint of the dielectric relaxation time-step. This has allowed to decrease the computational time by at least one order of magnitude. We have also improved the numerical

scheme used for the transport of charged species to increase the robustness of the discharge code. Indeed in the head of a streamer discharge, a transport scheme needs to handle density gradients of several orders of magnitude. And so we have tested and implemented a simple non oscillatory, positivity preserving third order convection scheme called UNO3 (Li 2008). We have demonstrated that the UNO3 scheme increases the general robustness and accuracy of the discharge code compared to the Improved Scharfettel-Gummel (ISG) scheme used in the initial code.
Recently, in (Duarte et al. 2012), advanced numerical techniques with adaptive time-splitting schemes coupled with adaptive mesh resolution (AMR) techniques have been developed. These methods allow a significant reduction of the computational cost. In further studies, it would be interesting to implement these advanced techniques to simulate larger simulation domains and even carry out 3D discharge calculations as in (Montijn et al. 2006; Pancheshnyi et al. 2008; Kolobov and Arslanbekov 2012).

In the second part of this thesis, first, we have investigated the dynamics of impact and spreading of an air discharge at atmospheric pressure on a dielectric layer in a point-to-plane geometry where the dielectric is placed on the cathode plane (CDBD configuration). For a positive (or negative) applied voltage at the point electrode, a positive (or negative) discharge ignites at the point electrode and propagates in the gap. After the impact on the dielectric, the positive (or negative) surface discharge starts spreading on the dielectric surface and charging it with positive (or negative) surface charges. By comparing the dynamics of spreading on the dielectric surface of a positive and negative discharge, we have shown that the structure of a negative discharge is different from the one of a positive surface discharge. For a negative surface discharge, the discharge head is on the dielectric surface and the sheath is formed directly behind the front whereas in the positive discharge case, the radial front is located at a small distance from the dielectric surface and the formation of the sheath is much slower.

Then, we have studied the influence of placing a dielectric plane obstacle in the inter-electrode gap on the propagation dynamics of an air discharge at atmospheric pressure. The objective of this study was to find conditions in which a second discharge may reignite behind the dielectric obstacle. In the same point-to-plane geometry as in the CDBD configuration with a dielectric layer placed in the inter-electrode gap and with a positive applied voltage at the point electrode, the first positive air dis-

charge ignited at the point is stopped in its axial propagation towards the cathode by the dielectric obstacle and spreads along the upper dielectric surface. Depending on the location of the dielectric layer, its permittivity, its thickness and its opacity to radiation, we have shown that a second positive discharge may reignite or not below the dielectric. We have shown that for the case of a positive discharge spreading on the upper dielectric surface, the amount of surface charges deposited on the dielectric layer is too low to have an influence on the reignition process and in fact the discharge reignition below the dielectric is mostly due to the potential redistribution in the inter-electrode gap after the first positive streamer propagation in the first air gap.
Conversely, in the case of a negative discharge ignited at the point, we have shown that the negative surface charges deposited on the upper surface of the dielectric layer have a significant contribution on the discharge reignition process. We have also pointed out that the dynamics of reignition of air discharges below a dielectric layer depends on the polarity of the voltage applied at the point electrode. For a positive applied voltage, if a discharge reignites below the dielectric layer, it is a positive ionization wave propagating from the bottom dielectric surface towards the grounded plane. For a negative applied voltage, if a discharge reignites below the dielectric layer, it is a double headed discharge with positive and negative discharge fronts. We have then demonstrated that the minimum applied voltage to have a discharge reignition is lower in absolute value for a negative applied voltage than for a positive one.

In the framework of the ALVEOPLAS project, we have compared our numerical results with experimental results obtained at LPGP laboratory. First we have compared results in the point-to-plane geometry without dielectric. In experiments and in simulations, for a maximum voltage of about 30 kV applied at the point anode, a single conical discharge structure is observed. A good agreement on the maximum diameter of the discharge and its propagation velocity is obtained. In the experiments, with a dielectric plane obstacle in the inter-electrode gap, the reignition process is characterized by the occurrence of a current peak (usually the fourth one) at the segmented cathode coupled with optical emission recorded with a fast camera. Using this methodology, experimental results show that the time delay between the ignition at the point anode and the impact on the cathode of the reignited discharge is in the range of $\Delta t_{delay}^{exp} \in [18\text{ ns} : 24\text{ ns}]$. Conversely, the numerical results show that the reignition process is faster with a numerical delay of Δt_{delay}^{num}=5.6 ns. To improve the agreement between experimental and numerical results

on the reignition behind a dielectric obstacle, we have proposed first a new insight in the interpretation of experimental results and second we have studied which physico-chemical processes could be missing in the simulations:

- First, we have shown that maybe the second peak of current measured in the experiments at Δt=6 ns, could correspond to the impact of a first reignited discharge on the cathode. Indeed, this reignition delay is close to the numerical delay of Δt_{delay}^{num}=5.6 ns. In the simulations the optical intensity of the reignited discharge below the dielectric plane is weak. It may explain the difficulty for a high speed camera to detect it.

- Second, we have investigated the influence of electron emission processes from the cathode in the extreme case with no initial seed charges in the second air gap. We have taken into account the thermionic and field emission processes at the cathode surface. We have found that the time to release an electron from the cathode surface is greatly influenced by the work function of the metallic cathode ϕ and the amplification factor β. For the set of values for ϕ and β studied in this work, we have shown that the time to release an electron from the cathode surface is at maximum of 6.9 ns and then the delay for the reignition process is at maximum of Δt_{delay}^{num}=13.2 ns, slightly shorter than the experimental reignition delay $\Delta t_{delay}^{exp} \in [18\text{ ns} : 24\text{ ns}]$.

To go further in the experiment-modeling comparison, first, it would be of great interest to take into account in the simulations, the exact geometry of the reactor to simulate surface charge deposition on the different dielectric surfaces of the reactor during the voltage pulse. Then, after estimating the time evolution of these surface charges between pulses, we could better study the influence of initial surface charges at the beginning of a voltage pulse on the reignition dynamics behind the dielectric obstacle.
Second, it would be of great interest to carry out additional experimental studies with a non-segmented cathode and with different material for the cathode to study the influence of emission processes from this surface. Additionally, it would be very interesting to develop an hybrid particle-fluid code to investigate in more detail the influence of emission processes at the cathode surface on the ignition of a discharge in the second air gap.

Finally, we have studied the dynamics of discharges propagating in thin dielectric tubes at atmospheric pressure. First, in a $He - N_2$ mixture, in tubes with a inner radius of 2 mm, two positive discharges ignite at the edges of the powered ring and propagate away from it. We have shown that when three body Penning and charge exchange reactions are taken into account, the propagation of the discharge is slightly faster. It would be of great interest to investigate further the chemistry of $He - N_2$ mixtures to go towards quantitative comparison with experiments in tubes and plasma jets. We have shown that to have a discharge with a rather homogeneous radial structure, a inner tube radius of 0.2 cm is well adapted for a $He - N_2$ mixture. In air, a much smaller discharge radius of 200 μm is required. These first results seem to show that if the tube radius is adapted to the studied gas, homogeneous discharge in tubes could be obtained for other gases than rare gases used so far in plasma jets. These first results on the influence of the tube radius on the discharge structure could be also of interest to optimize the structure and the production of active species in current plasma jets using rare gases.

Appendix A

Current calculation

In a streamer discharge code, different methods are used to calculate the current. In this thesis, we present here a quite simple way to calculate the current starting from the charge conservation equation A.1:

$$\frac{\partial \rho}{\partial t} + \nabla \cdot \mathbf{j_c} = 0 \ , \ \text{where} \quad \mathbf{j_c} = q_\text{e}\mathbf{j} \ , \tag{A.1}$$

where ρ is the net space charge density and $\mathbf{j_c}$ is the current density, $\mathbf{j}$ is the flux of charged species and q_e is the absolute value of electron charge. This equation simply states that a change in the value of the net space charge density is only due to a current of charge in and/or out of a point. We recall here the formulation of Poisson's equation:

$$\epsilon_0 \nabla \cdot \mathbf{E} = \rho \ . \tag{A.2}$$

Then equation A.1 becomes:

$$\epsilon_0 \nabla \cdot \frac{\partial \mathbf{E}}{\partial t} + \nabla \cdot \mathbf{j_c} = 0 \ . \tag{A.3}$$

If we integrate equation A.3 on an enclosed volume we have then:

$$\iiint_V \left(\epsilon_0 \nabla \cdot \frac{\partial \mathbf{E}}{\partial t} + \nabla \cdot \mathbf{j_c} \right) \, \mathrm{d}V = 0 \ . \tag{A.4}$$

From the divergence theorem equation A.4 becomes:

$$\iint_S \left(\epsilon_0 \frac{\partial \mathbf{E}}{\partial t} + \mathbf{j_c} \right) \cdot \, \mathrm{d}\mathbf{S} = 0 \ , \tag{A.5}$$

where d$\mathbf{S}$ represents the outward pointing normal vector of the surface that bounds the enclosed volume V. Equation A.5 can be rewritten as:

$$\iint_S \mathbf{J} \cdot \mathrm{d}\mathbf{S} = 0 \ , \tag{A.6}$$

where the total current density $\mathbf{J}$ is defined as:

$$\mathbf{J} = \mathbf{j_c} + \epsilon_0 \frac{\partial \mathbf{E}}{\partial t} \ . \tag{A.7}$$

In equation A.7, $\mathbf{j_c}$ represents the conductive current part and $\epsilon_0 \frac{\partial \mathbf{E}}{\partial t}$ represents the capacitive current part.
If the volume chosen is a square box with two sides starting from the x-axis of symmetry and end at the radial boundary of the simulation domain, then equation A.7 means that all the current going through the defined square box is conserved. Then by integrating the total current density $\mathbf{J}$ (equation A.7) on a surface S perpendicular to the x-axis of symmetry, we can obtain the net current I.

Appendix B

Optical emission calculation

Usually in the simulation of discharges at atmospheric pressure, we solve 2D axi-symmetric continuity equations for charged species coupled with Poisson's equation and we present results as 2D evolutions of the electron density and of the absolute value of the electric field. However, to compare with experiments, it is interesting to compute the optical emission of the discharge.
The emission of a streamer discharge in air at atmospheric pressure in the visible spectrum is usually considered to be dominated by the emission from the second positive band of nitrogen:

$$N_2(C^3\Pi_u) \rightarrow N_2(B^3\Pi_g) + h\nu \tag{B.1}$$

Two other bands can also be considered, the first positive band of nitrogen and the first negative band of the nitrogen ion N_2^+:

$$N_2(B^3\Pi_g) \rightarrow N_2(A^3\Sigma_u^+) + h\nu \tag{B.2}$$
$$N_2^+(B^2\Sigma_u^+) \rightarrow N_2^+(X^2\Sigma_g^+) + h\nu \tag{B.3}$$

The evolution of the concentrations $[N_2(B^3\Pi_g)]$, $[N_2(C^3\Pi_u)]$ and $[N_2^+(B^2\Sigma_u^+)]$ is given by a system of three ODEs. We have included these ODE in the discharge code and these equations are solved explicitly with a fourth order Runge-Kutta time integration scheme. It is important to note these ODEs for excited states is solved simultaneously with the streamer equations. This gives a full time-dependent solution of optical emissions in the modelling of the streamer processes. All coefficients for the three band systems are taken from (Liu and Pasko 2004) and (Bonaventura et al. 2011).
The experimentally detected intensities of light for the three bands are directly proportional to the radiative deexcitation rates of the excited

states (Kozlov et al. 2001):

$$I_k = T_k A_k n_k, \tag{B.4}$$

where k is one of the three excited species $N_2^*(k)$, $A_{N_2^*(k)}$ is the Einstein coefficient of the excited specie $N_2^*(k)$ and T_k is a transmission coefficient, which depends on the characteristics of the optical system and the sensitivity of the detector. In this work, we assume that the transmission coefficients T_k for the three studied bands are equal to 1. The number of photons emitted per second from a volume element $\delta V^i = 2\pi r^i \delta z^i \delta r^i$, where r^i is radial distance and δz^i and δr^i are the axial and radial sizes of cell i, is

$$N^i_{ph,k} = A_k n_k \delta V^i. \tag{B.5}$$

If the discharge is observed along a line of sight, the measured optical emission intensity of each band at a given time is given by:

$$\Psi_k = 10^{-6} \int_{\mathcal{L}} I_k \, dl, \tag{B.6}$$

where I_k is in $\mathrm{cm}^{-3}\mathrm{s}^{-1}$, l is in cm and the intensity Ψ_k is in Rayleighs, and the integration is performed along the optical path $\mathcal{L}$. In this work, as in (Pasko et al. 1997) and (Liu and Pasko 2004), the effects of radiative transfer between the source of the emission and the observer are not taken into account. In Equation (B.6), the intensity, I_k, is an axially symmetric function of cylindrical radius $f(r)$. Then to calculate the intensity Ψ_k for a horizontal line of sight (namely a line perpendicular to the discharge axis), it is necessary to perform the integration in Equation (B.6) taking into account the radial profile of I_k; this is the classical direct Abel's transformation. Then, the emission of each band is time integrated on the duration of the camera gates used in experiments (typically a few nanoseconds).

Appendix C

Discretization of Poisson's equation for a dielectric barrier discharge

In the case of a dielectric barrier discharge, a dielectric material is present in the interelectrode gas gap. In this case, one has to take into account that there are two regions in the interelectrode gap with two different electric permittivities (the gas volume and the dielectric material). Furthermore, during the discharge propagation some charges may be deposited on the dielectric material interface with the gas. For all the different versions of the simulation code developed in this thesis, we used the same approach as in (Jánský et al. 2010; Jánský et al. 2011; Jánský et al. 2012; Célestin et al. 2008; Célestin 2008). We started from the formulation of the electric displacement field $\mathbf{D}$:

$$\nabla \cdot \mathbf{D} = \rho \ , \tag{C.1}$$

where $\mathbf{D} = \varepsilon_0 \mathbf{E} + \mathbf{P}$ and $\mathbf{P}$ is the polarization density of the material. For linear, homogeneous and isotropic dielectric media, $\mathbf{D} = \epsilon \mathbf{E} \equiv \varepsilon_0 \varepsilon_r \mathbf{E}$ where ε_r is the relative permittivity of the dielectric material which then leads to solve:

$$\boldsymbol{\nabla} \cdot (\epsilon(-\boldsymbol{\nabla} \mathrm{V})) = \rho \ , \tag{C.2}$$

Then, we integrate equation C.2 over the volume element $\Omega_{i,j}$ of the cell (i, j):

$$\int_{\Omega} \boldsymbol{\nabla} \cdot (\epsilon(-\boldsymbol{\nabla} \mathrm{V})) \mathrm{d}\Omega = \int_{\Omega} \rho \mathrm{d}\Omega \ . \tag{C.3}$$

Using the Gauss-Ostrogradsky theorem one obtains:

$$\oint_{\Sigma} (\epsilon(-\boldsymbol{\nabla} \mathrm{V})) \cdot \boldsymbol{n} \mathrm{d}\Sigma = \Omega_{i,j} \rho \ , \tag{C.4}$$

where $\mathrm{d}\Sigma$ measures the infinitesimal surface of the cell boundaries and $\boldsymbol{n}$ is the outward unit normal vector. Lets now consider the case of a di-

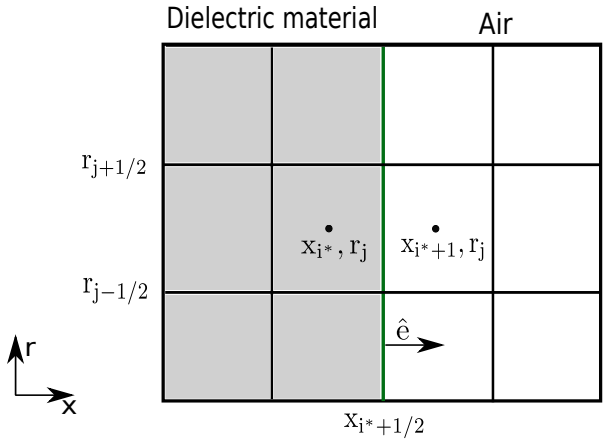

Figure C.1: *Numerical grid in presence of a plane dielectric. The shaded domain represents the dielectric material region. The gas/dielectric interface lies at $x_{i^*+1/2}$ and $\hat{\boldsymbol{e}}$ is the unit vector directed towards increasing x.*

electric plane with a dielectric surface located at $x_{i+1/2}$ as in Figure C.1, although the electrostatic potential is continuous, the axial electric field in this case is not.
It means that to compute the flux of electric field going from the cell i, j to $i+1, j$ through the surface $\Sigma_{i+1/2,j}$, we need to take into account the jump of permittivity and the presence of surface charges located on the surface of the dielectric. Then the flux of electric field flowing through the east interface of the cell i, j is equal to:

$$f_{i+1/2,j}(E) = \epsilon_1 E_{i+1/2,j} \Sigma_{i+1/2,j}$$

$$\text{where} \quad E_{i+1/2,j} = \frac{V_{i,j} - V_{i+1/2,j}}{x_{i+1/2,j} - x_{i,j}} \ , \tag{C.5}$$

To compute the flux of electric field in equation C.5, we need to compute the value of the continuous potential $\mathrm{V_{i+1/2,j}}$ located at $i+1/2, j$. To calculate it, we need to consider that from a general point of view, the jump condition for normal electric field E on the interface of two dielectrics of

permittivity ϵ_1 (defined in cell i,j) and ϵ_2 (defined in cell $i+1,j$) first without surface charges σ located at the interface between the two dielectrics is:

$$-\epsilon_1 \mathbf{E_1} + \epsilon_2 \mathbf{E_2} = 0 \ , \tag{C.6}$$

where $\mathbf{E_1}$= -$E_1\hat{\mathbf{e}}$, $\mathbf{E_2}$= +$E_2\hat{\mathbf{e}}$ and $\hat{\mathbf{e}}$ is the unit vector directed towards increasing x on the example shown on Figure C.1.
Discrete form of this equation using forward and backward differences is:

$$-\epsilon_1 \left(\frac{V_i - V_{i+1/2}}{x_{i+1/2} - x_i} \right) + \epsilon_2 \left(\frac{V_{i+1/2} - V_{i+1}}{x_{i+1} - x_{i+1/2}} \right) = 0 \ . \tag{C.7}$$

Solving this equation for the potential $V_{i+1/2}$ on the interface, we obtain:

$$V_{i+1/2} = \left[\frac{\epsilon_1 V_i (x_{i+1} - x_{i+1/2}) + \epsilon_2 V_{i+1} (x_{i+1/2} - x_i)}{\epsilon_1 (x_{i+1} - x_{i+1/2}) + \epsilon_2 (x_{i+1/2} - x_i)} \right] \ . \tag{C.8}$$

By combining equation C.8 and C.5, we can compute the flux of electric field:

$$f_{i+1/2,j}(E) = \Sigma_{i+1/2,j} \frac{\epsilon_2 \epsilon_1 (V_i - V_{i+1})}{\epsilon_2 (x_{i+1/2} - x_i) + \epsilon_1 (x_{i+1} - x_{i+1/2})} \ , \tag{C.9}$$

$$\text{where } \Sigma_{i+1/2,j} = \pi \Delta r^2_{j-1/2} = \pi (r^2_{j+1/2} - r^2_{j-1/2})$$

If we reformulate it:

$$f_{i+1/2,j}(E) = V^E_{i,j} (V_{i+1} - V_i) \ , \tag{C.10}$$

$$\text{where } V^E_{i,j} = -\pi \Delta r^2_{j-1/2} \frac{\epsilon_{i+1,j} \epsilon_{i,j}}{\epsilon_{i+1,j} (x_{i+1/2} - x_i) + \epsilon_{i,j} (x_{i+1} - x_{i+1/2})}$$

If now we compute all fluxes of equation C.4 and considering that there is a jump of permittivity at each cell interface, we can have a generalized expression:

$$V^E_{i,j} V_{i+1,j} + V^W_{i,j} V_{i-1,j} + V^S_{i,j} V_{i,j-1} + V^N_{i,j} V_{i,j+1} + V^C_{i,j} V_{i,j} = \pi \rho_{i,j} \Delta x_{i+1/2} \Delta r^2_{j-1/2} \ ,$$

with:

$$\begin{cases} V_{i,j}^{E} &= -\pi \Delta r_{j-1/2}^2 \dfrac{\epsilon_{i+1,j}\epsilon_{i,j}}{\epsilon_{i+1,j}(x_{i+1/2}-x_i)+\epsilon_{i,j}(x_{i+1}-x_{i+1/2})} \ , \\ V_{i,j}^{W} &= V_{i-1,j}^{E} \ , \\ V_{i,j}^{N} &= -2\pi r_{j+1/2} \Delta x_{i-1/2} \dfrac{\epsilon_{i,j+1}\epsilon_{i,j}}{\epsilon_{i,j+1}(r_{j+1/2}-r_j)+\epsilon_{i,j}(r_{j+1}-r_{j+1/2})} \ , \\ V_{i,j}^{S} &= V_{i,j-1}^{N} \ , \\ V_{i,j}^{c} &= -(V_{i,j}^{W}+V_{i,j}^{E}+V_{i,j}^{S}+V_{i,j}^{N}) \ , \end{cases} \tag{C.11}$$

where $\Delta x_{i+/2} = x_{i+1/2} - x_{i-1/2}$ and $\Delta r_{j-1/2}^2 = r_{j+1/2}^2 - r_{j-1/2}^2$.

Dielectric surface with surface charges

If there is a deposition of surface charges on a dielectric surface we also need to take it into account. The jump condition for normal electric field E on the interface of two dielectrics of permittivity ϵ_1 (defined in cell i,j) and ϵ_2 (defined in cell $i+1,j$) with surface charges σ in C.cm^{-2} located at the interface between the two dielectrics is:

$$-\epsilon_1 \mathbf{E_1} + \epsilon_2 \mathbf{E_2} = \sigma \ , \tag{C.12}$$

where $\mathbf{E_1}$= -$E_1\hat{\mathbf{e}}$, $\mathbf{E_2}$= +$E_2\hat{\mathbf{e}}$ and $\hat{\mathbf{e}}$ is the unit vector directed towards increasing x on the example shown on Figure C.1.
Discrete form of this equation using forward and backward differences is:

$$-\epsilon_1 \left(\frac{V_i - V_{i+1/2}}{x_{i+1/2}-x_i} \right) + \epsilon_2 \left(\frac{V_{i+1/2}-V_{i+1}}{x_{i+1}-x_{i+1/2}} \right) = \sigma \ . \tag{C.13}$$

Solving this equation for the potential $V_{i+1/2}$ on the interface, we obtain:

$$\begin{aligned} V_{i+1/2} = &\left[\frac{\epsilon_1 V_i (x_{i+1}-x_{i+1/2}) + \epsilon_2 V_{i+1}(x_{i+1/2}-x_i)}{\epsilon_1(x_{i+1}-x_{i+1/2})+\epsilon_2(x_{i+1/2}-x_i)} \right] \ . \\ &+ \left[\frac{\sigma (x_{i+1}-x_{i+1/2})(x_{i+1/2}-x_i)}{\epsilon_1(x_{i+1}-x_{i+1/2})+\epsilon_2(x_{i+1/2}-x_i)} \right] \end{aligned} \tag{C.14}$$

If now we compute the flux of electric field:

$$f_{i+1/2,j}(E) = \Sigma_{i+1/2,j} \frac{\epsilon_2 \epsilon_1 (V_i - V_{i+1})}{\epsilon_2(x_{i+1/2}-x_i)+\epsilon_1(x_{i+1}-x_{i+1/2})} \ , \tag{C.15}$$

$$- \left[\frac{\sigma (x_{i+1}-x_{i+1/2})(x_{i+1/2}-x_i)}{\epsilon_1(x_{i+1}-x_{i+1/2})+\epsilon_2(x_{i+1/2}-x_i)} \right] \Sigma_{i+1/2,j} \tag{C.16}$$

Including the surface charges will not change the coefficient on the left hand side of C.11 but it will add an additional source on the right hand side taking into account the surface charges σ only at the point $(i = i, j)$ and $(i = i + 1, j)$, such that:

$$\begin{cases} \rho^{'}_{i^*+1,j} &= \rho^{'}_{i^*+1,j} + \dfrac{\epsilon_{i+1,j}\sigma_j(x_{i+1/2} - x_{i+1})(\pi\Delta r^2_{j-1/2})}{\epsilon_{i,j}(x_{i+1} - x_{i+1/2}) + \epsilon_{i+1,j}(x_{i+1/2} - x_i)} \ , \\ \rho^{'}_{i^*,j} &= \rho^{'}_{i^*,j} + \dfrac{\epsilon_{i,j}\sigma_j(x_{i+1} - x_{i+1/2})(\pi\Delta r^2_{j-1/2})}{\epsilon_{i,j}(x_{i+1} - x_{i+1/2}) + \epsilon_{i+1,j}(x_{i+1/2} - x_i)} \ . \end{cases} \tag{C.17}$$

Where $\rho^{'}_{i,j} = \rho_{i,j}\pi\Delta x_{i+1/2}\Delta r^2_{j-1/2}$.

Calculation of the electric field in the presence of surface charges at the dielectric interface

As we consider only the electric field directed outward the dielectric interface so on Figure C.1, the electric field computed is E_2:

$$E_2 = \left(\frac{V_{i+1/2} - V_{i+1}}{x_{i+1} - x_{i+1/2}}\right) \ , \tag{C.18}$$

Then we use the definition of $V_{i+1/2}$ from equation C.14 in equation C.18:

$$E_2 = \left(\frac{1}{x_{i+1} - x_{i+1/2}}\right)\left[\frac{\sigma(x_{i+1} - x_{i+1/2})(x_{i+1/2} - x_i)}{\epsilon_1(x_{i+1} - x_{i+1/2}) + \epsilon_2(x_{i+1/2} - x_i)}\right] + \left(\frac{1}{x_{i+1} - x_{i+1/2}}\right)\left[\frac{\epsilon_1 V_i(x_{i+1} - x_{i+1/2}) + \epsilon_2 V_{i+1}(x_{i+1/2} - x_i)}{\epsilon_1(x_{i+1} - x_{i+1/2}) + \epsilon_2(x_{i+1/2} - x_i)} - V_{i+1}\right] \tag{C.19}$$

which gives the following expression for E_2:

$$E_2 = \left[\frac{\sigma(x_{i+1/2} - x_i) + \epsilon_1 V_i - \epsilon_1 V_{i+1}}{\epsilon_1(x_{i+1} - x_{i+1/2}) + \epsilon_2(x_{i+1/2} - x_i)}\right] \ . \tag{C.20}$$

Following the same development, if E_1 is the electric field directed outward the dielectric surface its expression is:

$$E_1 = \left[\frac{-\sigma(x_{i+1} - x_{i+1/2}) + \epsilon_2 V_i - \epsilon_2 V_{i+1}}{\epsilon_1(x_{i+1} - x_{i+1/2}) + \epsilon_2(x_{i+1/2} - x_i)}\right] \ . \tag{C.21}$$

We have carried out different verification test-cases to validate the calculation of surface charges in our code. We present here the results of two

academic test-cases:

In the first test case, Figure C.2 presents the calculation of the axial electric field in a gap where a dielectric plane of ε_r=5 and the two surface of the dielectric are uniformly charged on the left with σ= 8 nC.cm^{-2} at x= 0.4 cm and on the right with σ= -8 nC.cm^{-2} at x= 0.6 cm. The analytical solution gives and electric field equals to $E_x = +\sigma/\varepsilon_0\varepsilon_r =$ 18070.545 $V.cm^{-1}$ in the dielectric plane and 0 elsewhere. As can be seen on Figure C.2, the electrostatic solution calculated with our discharge code gives an exact solution compared to the analytical solution.

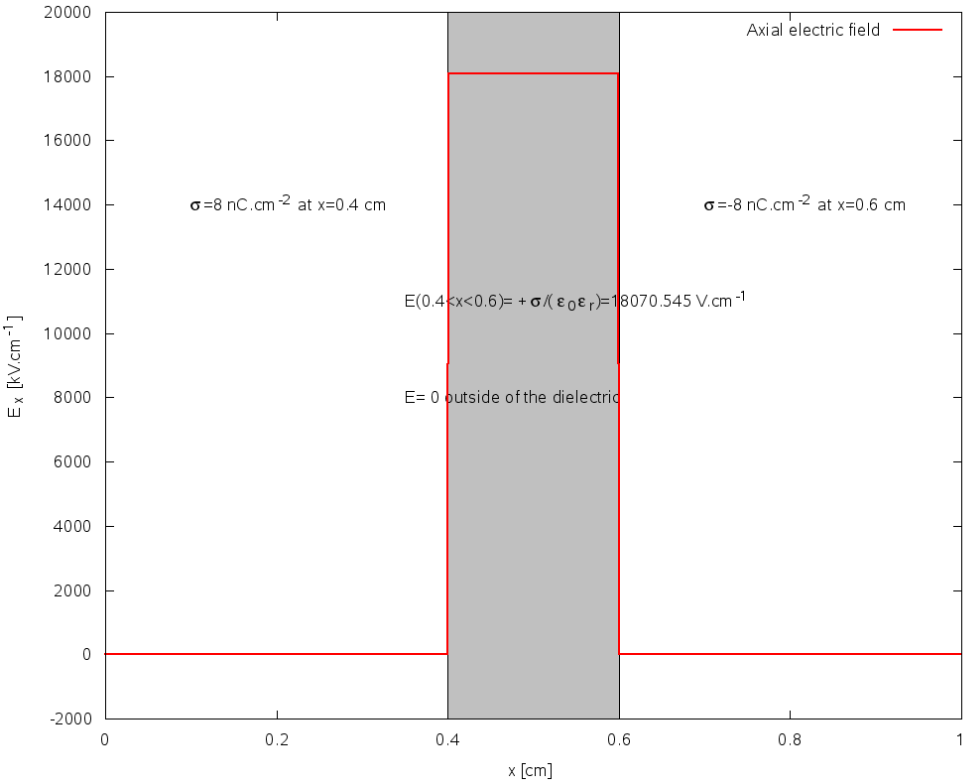

Figure C.2: *Test case 1. Calculation of the electric field in a gap where a dielectric plane of ε_r=5 and the two surface of the dielectric are uniformly charged on the left with σ= 8 nC.cm^{-2} and on the right with σ= -8 nC.cm^{-2} .*

Figure C.3, shows another academic test case where the axial electric field is computed with a dielectric plane of ε_r=1 and its right surface of the dielectric is uniformly charged with σ= 8 nC.cm^{-2} at x= 0.5 cm. As in the first test case, the electrostatic calculation of our discharge code gives the same solution as the analytical solution where

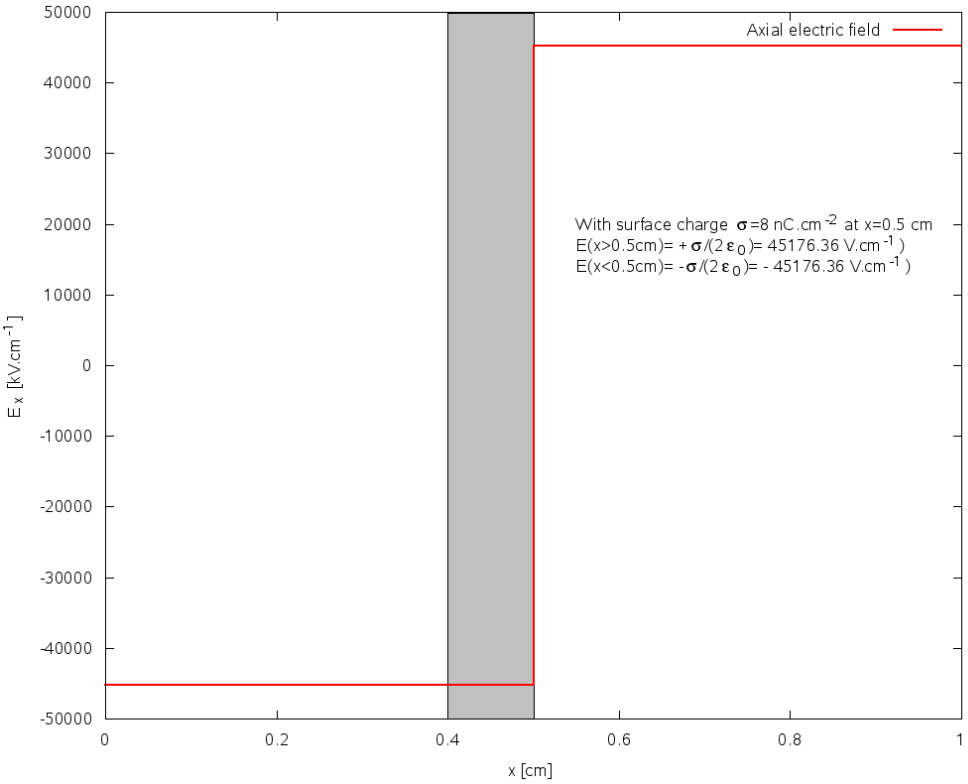

Figure C.3: *Test case 1. Calculation of the axial electric field in a gap where a dielectric plane of ε_r=1 and its right surface of the dielectric is uniformly charged with σ= 8 $nC.cm^{-2}$ at x= 0.5 cm.*

$E_x(x > 0.5\ cm) = +\sigma/(2\varepsilon_0) = \ 45176.36\ V.cm^{-1}$ and $E_x(x < 0.5\ cm) = -\sigma/(2\varepsilon_0) = \ -45176.36\ V.cm^{-1}$.
These two academic test-cases demonstrate the accurate implementation of surface charges in our code.

Appendix D

Validation of the MPI-OPENMP discharge code on Kulikovsky's test-case

In order to validate the use of the MPI-OPENMP discharge code for streamer simulations presented in chapter 4, we compare the results obtained using the results obtained by (Kulikovsky 1998) for the same point-to-plane configuration.

Model description

The parameters of the shape of the hyperboloid anode are

$$\left(\frac{x}{a}\right)^2 - \left(\frac{r}{b}\right)^2 = 1, \tag{D.1}$$

where $a = 1$ cm and $b = 0.18$ cm which corresponds to a radius of curvature of $R_c = b^2/a$ =324 μm. The anode tip is located at 1 cm from a grounded metallic cathode plane ($x = 0$ cm). A constant voltage of U_a =13 kV is applied at the beginning of the discharge simulation at the point anode.
We have used the same transport parameters and reactions rates as in (Kulikovsky 1998). In the work of (Kulikovsky 1998), the photoioniation source term in air is calculated using an optimized integral approach based on the model proposed by (Zhelezniak et al. 1982). In our work we have used the SP3 photoionization model developped in (Bourdon et al. 2007; Célestin 2008). Comparison of the SP3 model and the model used in (Kulikovsky 1998) was carried out in (Bourdon et al. 2007) and results show that both approaches are in very good agreement.

In (Kulikovsky 1998), the computational domain is 6×1.1 cm^2 and is discretized on a grid $n_x \times n_r = 134 \times 640$. The streamer head is covered by a moving window with an uniform fine grid ($\approx$ of 400 cells) with a cell size of 6.3 μm × 8 μm. In this work we have used a fixed grid. Our computational domain was 6×10 cm^2 discretized on a fixed rectilinear grid with $n_x \times n_r = 1328 \times 1267$ cells. The grid is Cartesian, with a fixed cell size of 10 μm in the region where the streamer propagates. Beyond this region (i.e. $x \in$ [1.2,6] cm and $r \in$ [1.1,10] cm), the grid expands according to a geometric progression. As in (Kulikovsky 1998), a neutral plasma spot is placed at the anode tip to initiate streamer formation:

$$n_p(x,r)|_{t=0} = n_e(x,r)|_{t=0} = n_0 \exp\left[-\frac{r^2}{\sigma_r^2} - \frac{(x-x_0)^2}{\sigma_x^2}\right], \qquad \text{(D.2)}$$

where $x_0 = a - \sigma_x$, σ_x= 0.025 cm and σ_r= 0.01 cm. At t=0 there are no negative ions. The initial maximum density is n_0= 10^{14} cm^{-3}.
For this simulation we used 12 MPI processes and the simulation was carried out in less than one hour for a simulation time of 23 ns.

Results

The left panel of Figure D.1 shows the results obtained with our MPI-OPENMP discharge code and the right panel of Figure D.1 shows the results of Figure 2 in (Kulikovsky 1998). Figure D.1 shows the contour lines of the electron density and the magnitude of the electric field. For both panels in Figure D.1, we can see that we have a good agreement with the results of (Kulikovsky 1998). In (Célestin 2008), the same comparison was carried out to validate the legacy discharge code and the comparison is shown on Figure D.2. There are some differences in the results as pointed out in (Célestin 2008) and it can be due to the fact that we use a different model (SP3 model) to calculate the photoionization source term. As introduced in (Célestin 2008) the ghost fluid method is used to accurately describe the real geometry of the anode point for the calculation of electric potential and electric field in this work but not in (Kulikovsky 1998). Finally, the transport scheme used in the MPI-OPENMP discharge code is different where in (Kulikovsky 1998) and (Célestin 2008) the modified Scharfettel-Gummel scheme (Chapter 1) is used whereas in our code we use the explicit third order UNO3 scheme for convection and an explicit second order scheme for diffusion that increased the robustness and accuracy compared to the modified Scharfettel Gummel scheme on coarser mesh (Chapter 2) as used in this example. Nevertheless, we have a good agreement with (Kulikovsky 1998) (Figure D.1) and (Célestin 2008)

(Figure D.2) thus this test-case validate the use of the MPI-OPENMP discharge code.

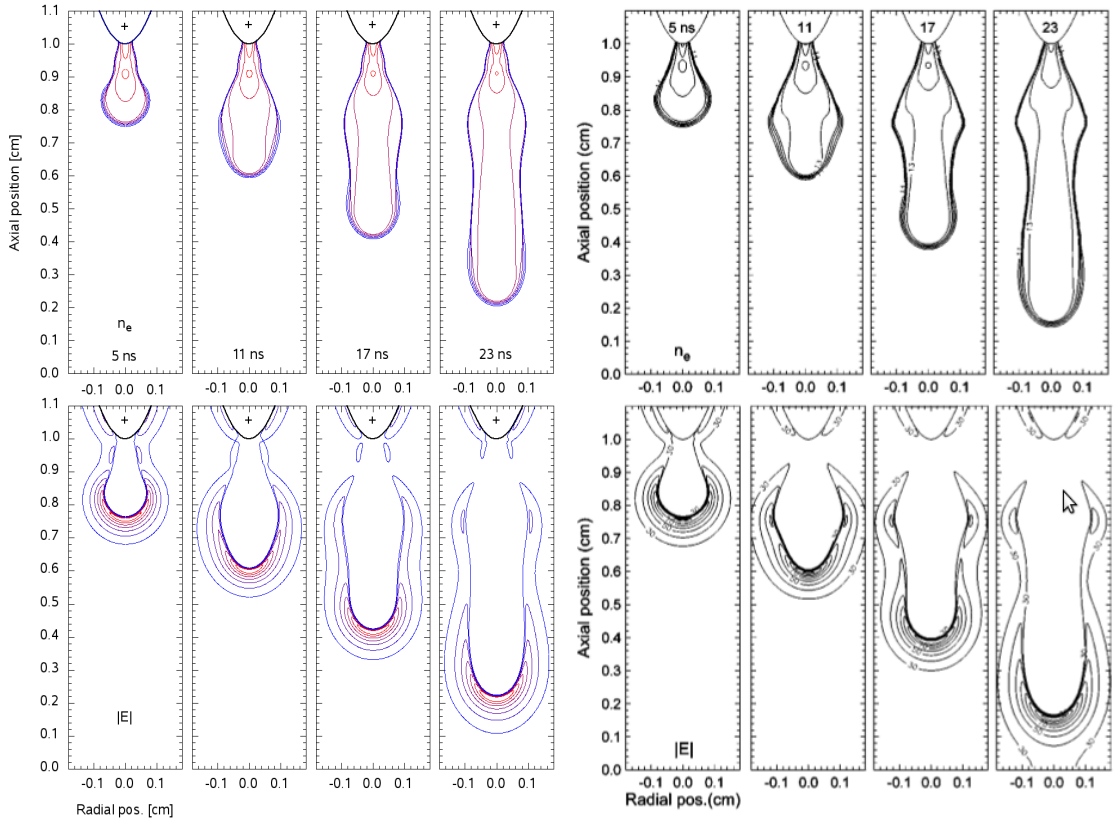

Figure D.1: *Two dimensional isocontours of the electron density and the magnitude of the electric field at t=5, 11, 17 and 23 ns. For the electron density, the isocontours go from* 10^{11} *to* 10^{14} cm^{-3}*, with a multiplier step of* $10^{0.5}$ cm^{-3}*. For the electric field, the isocontours go from 30 to 90* $kV.cm^{-1}$*, with a step of 10* $kV.cm^{-1}$*. The left panel presents results from our MPI-OPENMP discharge code. The right panel is taken from (Kulikovsky 1998)*

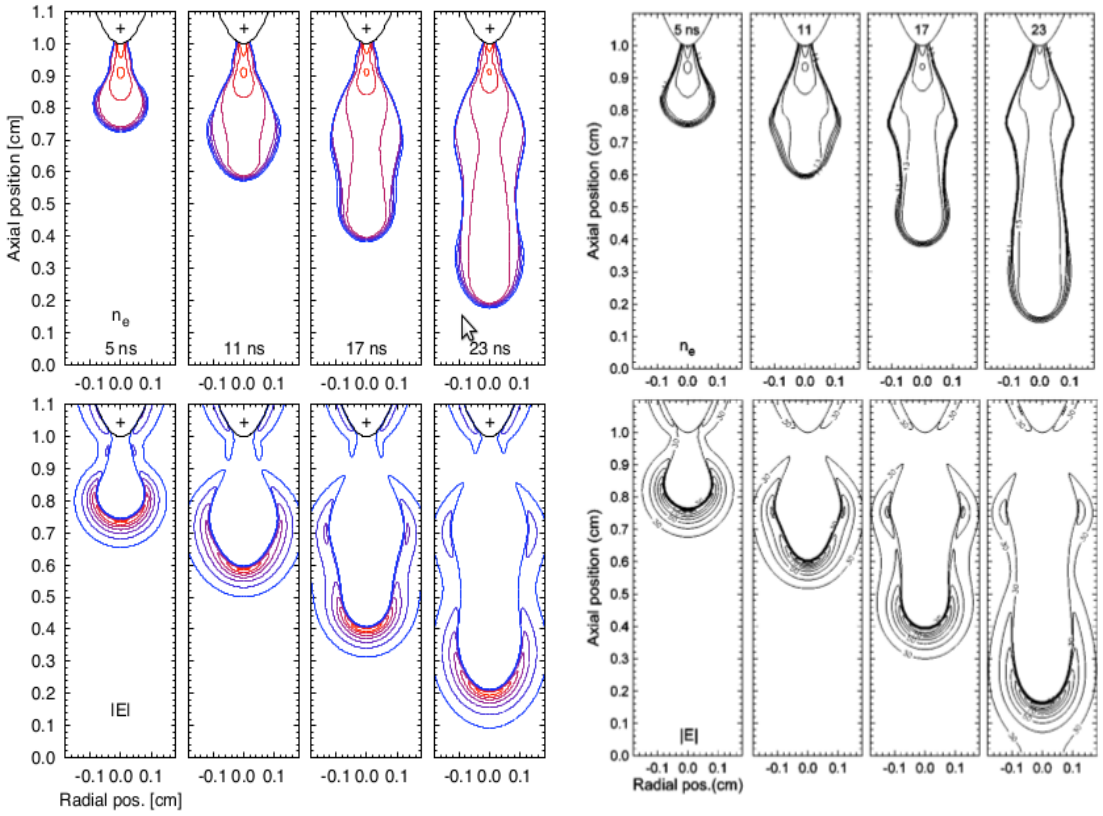

Figure D.2: *Two dimensional isocontours of the electron density and the magnitude of the electric field at t=5, 11, 17 and 23 ns. For the electron density, the isocontours go from* 10^{11} *to* 10^{14} cm^{-3}*, with a multiplier step of* $10^{0.5}$ cm^{-3}*. For the electric field, the isocontours go from 30 to 90* $kV.cm^{-1}$*, with a step of 10* $kV.cm^{-1}$*. The left panel presents results with LDC from (Célestin 2008). The right panel is taken from (Kulikovsky 1998)*

References

Abdel-Salam, M., H. Singer, and A. Ahmed (2001a). Effect of the dielectric barrier on discharges in non-uniform electric fields. *Journal of Physics D: Applied Physics 34*(8), 1219. *(p. 3)*

Abdel-Salam, M., H. Singer, and A. Ahmed (2001b). On the static behaviour of dielectric barrier discharges in uniform electric fields. *Journal of Physics D: Applied Physics 34*(13), 1974. *(p. 3)*

Abdel-Salam, M., A. A. Turky, and A. A. Hashem (1998). The onset voltage of coronas on bare and coated conductors. *Journal of Physics D: Applied Physics 31*(19), 2550. *(p. 3)*

Abdulle, A. (2001). Fourth order chebyshev methods with recurrence relation. *SIAM J. Sci. Comput. 23*(6), 2041 – 2054. *(p. 72)*

Akishev, Y., G. Aponin, A. Balakirev, M. Grushin, V. Karalnik, A. Petryakov, and N. Trushkin (2011). 'memory' and sustention of microdischarges in a steady-state dbd: volume plasma or surface charge? *Plasma Sources Science and Technology 20*(2), 024005. *(p. 85)*

Akishev, Y., G. Aponin, A. Balakirev, M. Grushin, V. Karalnik, A. Petryakov, and N. Trushkin (2013a). Dbd surface streamer expansion described using nonlinear diffusion of the electric potential over the barrier. *Journal of Physics D: Applied Physics 46*(46), 464014. *(p. 88)*

Akishev, Y., G. Aponin, A. Balakirev, M. Grushin, V. Karalnik, A. Petryakov, and N. Trushkin (2013b). Spatial - temporal development of a plasma sheet in a surface dielectric barrier discharge powered by a step voltage of moderate duration. *Plasma Sources Science and Technology 22*(1), 015004. *(p. 93)*

Algwari, Q. T. and D. O'Connell (2011). Electron dynamics and plasma jet formation in a helium atmospheric pressure dielectric barrier discharge jet. *Applied Physics Letters 99*(12), 121501 – 121501. *(p. 4, 180)*

Amestoy, P., I. Duff, J. L´Excellent, and J. Koster (2001). A fully asynchronous multifrontal solver using distributed dynamic scheduling.

SIAM Journal on Matrix Analysis and Applications 23(1), 15–41. *(p. 15, 26, 44)*

Babaeva, N. Y., A. N. Bhoj, and M. J. Kushner (2006). Streamer dynamics in gases containing dust particles. *Plasma Sources Science and Technology 15*(4), 591. *(p. 108, 127)*

Babaeva, N. Y. and M. J. Kushner (2011). Ion energy and angular distributions onto polymer surfaces delivered by dielectric barrier discharge filaments in air: I. flat surfaces. *Plasma Sources Science and Technology 20*(3), 035017. *(p. 79, 81, 85, 87)*

Balay, S., J. Brown, K. Buschelman, W. D. Gropp, D. Kaushik, M. G. Knepley, L. C. McInnes, B. F. Smith, and H. Zhang (2013). Petsc web page. http://www.mcs.anl.gov/petsc. *(p. 33)*

Becker, K. H., K. H. Schoenbach, and J. G. Eden (2006). Microplasmas and applications. *Journal of Physics D: Applied Physics 39*(3), R55. *(p. 1)*

Bessières, D., J. Paillol, A. Bourdon, P. Ségur, and E. Marode (2007). A new one-dimensional moving mesh method applied to the simulation of streamer discharges. *Journal of Physics D: Applied Physics 40*(21). *(p. 53, 55)*

Bhoj, A. N. and M. J. Kushner (2008). Repetitively pulsed atmospheric pressure discharge treatment of rough polymer surfaces: I. humid air discharges. *Plasma Sources Science and Technology 17*(3), 035024. *(p. 1)*

Boeuf, J., L. Yang, and L. Pitchford (2013). Dynamics of a guided streamer plasma bullet in a helium jet in air at atmospheric pressure. *Journal of Physics D: Applied Physics 46*(1), 015201. *(p. 177)*

Bonaventura, Z., A. Bourdon, S. Celestin, and V. P. Pasko (2011). Electric field determination in streamer discharges in air at atmospheric pressure. *Plasma Sources Science and Technology 20*(3), 035012. *(p. 211)*

Bourdon, A., Z. Bonaventura, and S. Celestin (2010). Influence of the pre-ionization background and simulation of the optical emission of a streamer discharge in preheated air at atmospheric pressure between two point electrodes. *Plasma Sources Science and Technology 19*(3), 034012. *(p. 157)*

Bourdon, A., V. P. Pasko, N. Y. Liu, S. Célestin, P. Ségur, and E. Marode (2007). Efficient models for photoionization produced by non-thermal gas discharges in air based on radiative transfer and the helmholtz equations. *Plasma Sources Science and Technology 16*(3), 656. *(p. 10, 11, 146, 221)*

Breden, D., K. Miki, and L. Raja (2012). Self-consistent two-

dimensional modeling of cold atmospheric-pressure plasma jets / bullets. *Plasma Sources Science and Technology 21*(3), 034011. *(p. 177)*

Célestin, S. (2008). *Study of the dynamics of streamers in air at atmospheric pressure*. Ph. D. thesis, Ecole Centrale Paris, ECP, Châtenay Malabry. *(p. 10, 11, 15, 213, 221, 222, 224)*

Célestin, S., Z. Bonaventura, B. Zeghondy, A. Bourdon, and P. Ségur (2009). The use of the ghost fluid method for poisson's equation to simulate streamer propagation in point-to-plane and point-to-point geometries. *Journal of Physics D: Applied Physics 42*(6), 065203. *(p. 14)*

Célestin, S., G. Canes-Boussard, O. Guaitella, A. Bourdon, and A. Rousseau (2008). Influence of the charges deposition on the spatio-temporal self-organization of streamers in a dbd. *Journal of Physics D: Applied Physics 41*(20), 205214. *(p. 5, 79, 81, 85, 213)*

COMSOL (2009). Comsol multiphysics. http://www.comsol.com/. *(p. 33)*

Daru, V. and C. Tenaud (2004). High order one-step monotonicity-preserving schemes for unsteady compressible flow calculations. *Journal of Computational Physics 193*(2), 563 – 594. *(p. 55)*

Douat, C., G. Bauville, M. Fleury, M. Laroussi, and V. Puech (2012). Dynamics of colliding microplasma jets. *Plasma Sources Science and Technology 21*(3), 034010. *(p. 4)*

Du, H. (2000). *Use of three-dimensional hydrodynamic model and accurate advection scheme for modeling flushing dynamics and developing segmentation schemes in indian river lagoon*. Ph. D. thesis, University of Florida Digital Collections. *(p. 53)*

Duarte, M., Z. Bonaventura, M. Massot, A. Bourdon, S. Descombes, and T. Dumont (2012). A new numerical strategy with space-time adaptivity and error control for multi-scale streamer discharge simulations. *Journal of Computational Physics 231*(3), 1002 – 1019. *(p. 204)*

Ducasse, O., L. Papageorghiou, O. Eichwald, N. Spyrou, and M. Yousfi (2007). Critical analysis on two-dimensional point-to-plane streamer simulations using the finite element and finite volume methods. *Plasma Science, IEEE Transactions on 35*(5), 1287 – 1300. *(p. 15)*

Durand, E. (1966). *Electrostatique. Tome II Problèmes généraux conducteurs*. Masson. *(p. 87, 115)*

Ehlbeck, J., U. Schnabel, M. Polak, J. Winter, T. von Woedtke, R. Brandenburg, T. von dem Hagen, and K.-D. Weltmann (2011). Low temperature atmospheric pressure plasma sources for micro-

bial decontamination. *Journal of Physics D: Applied Physics 44*(1), 013002. *(p. 4)*

Ellis, H., R. Pai, E. McDaniel, E. Mason, and L. Viehland (1976). Transport properties of gaseous ions over a wide energy range. *Atomic Data and Nuclear Data Tables 17*(3), 177 – 210. *(p. 179)*

Ferziger, J. and M. Peric (2002). *Computational Methods for Fluid Dynamics*. Springer London, Limited. *(p. 17, 22)*

Fromm, J. E. (1968). A method for reducing dispersion in convective difference schemes. *Journal of Computational Physics 3*(2), 176 – 189. *(p. 52)*

Gibalov, V. and G. Pietsch (2000). The development of dielectric barrier discharges in gas gaps and on surfaces. *Journal of Physics D: Applied Physics 33*(20), 2618. *(p. 93, 95, 97)*

Golubovskii, Y. B., V. A. Maiorov, P. Li, and M. Lindmayer (2006). Effect of the barrier material in a townsend barrier discharge in nitrogen at atmospheric pressure. *Journal of Physics D: Applied Physics 39*(8), 1574. *(p. 89)*

Guaitella, O., E. Foucher, A. Sobota, and A. Rousseau (2013). Spreading of atmospheric pressure plasma jet on a dielectric surface. *Bulletin of the American Physical Society 58. (p. 4)*

Hagelaar, G. and G. Kroesen (2000). Speeding up fluid models for gas discharges by implicit treatment of the electron energy source term. *Journal of Computational Physics 159*(1), 1 – 12. *(p. 43)*

Hagelaar, G. and L. Pitchford (2005). Solving the boltzmann equation to obtain electron transport coefficients and rate coefficients for fluid models. *Plasma Sources Science and Technology 14*(4), 722. *(p. 178)*

Hairer, E. and G. Wanner (1996). *Solving ordinary differential equations II, 2nd Edition,*. Springer-Verlag, Berlin. *(p. 72)*

Hensel, K., Z. Machala, and P. Tardiveau (2009, 8). Capillary microplasmas for ozone generation. *The European Physical Journal - Applied Physics 47. (p. 1)*

Hensel, K., V. Martišovitš, Z. Machala, M. Janda, M. Leštinský, P. Tardiveau, and A. Mizuno (2007). Electrical and optical properties of ac microdischarges in porous ceramics. *Plasma Processes and Polymers 4*(7-8), 682–693. *(p. 1)*

Hensel, K. and P. Tardiveau (2008). Iccd camera imaging of discharges in porous ceramics. *Plasma Science, IEEE Transactions on 36*(4), 980–981. *(p. 1)*

Hundsdorfer, W. and J. G. Verwer (2003). *Numerical solution of time-dependent advection-diffusion-reaction equations*, Volume 33.

Springer. *(p. 17)*

HYPRE (2007). hypre: a library of high performance preconditionners. http://www.llnl.gov/casc/linear solvers/. *(p. 33, 36, 44, 68)*

Ibuka, S., T. Nakamura, T. Murakami, H. Kondo, K. Yasuoka, and S. Ishii (2001). Novel plasma reactor using honeycomb ceramics driven by a fast si-thyristor for environmental applications. In *Pulsed Power Plasma Science, 2001. PPPS-2001. Digest of Technical Papers*, Volume 2, pp. 1118–1121 vol.2. *(p. 1)*

Jánský, J., Q. T. Algwari, D. O'Connell, and A. Bourdon (2012). Experimental - modeling study of an atmospheric-pressure helium discharge propagating in a thin dielectric tube. *(p. 5, 179, 180, 181, 187, 213)*

Jánský, J. and A. Bourdon (2011a). Simulation of helium discharge ignition and dynamics in thin tubes at atmospheric pressure. *Applied Physics Letters 99*(16), 161504 – 161504. *(p. 177)*

Jánský, J. and A. Bourdon (2011b, 7). Surface charge deposition inside a capillary glass tube by an atmospheric pressure discharge in air. *The European Physical Journal - Applied Physics 55*. *(p. 3, 26)*

Jánský, J., P. L. Delliou, F. Tholin, P. Tardiveau, A. Bourdon, and S. Pasquiers (2011). Experimental and numerical study of the propagation of a discharge in a capillary tube in air at atmospheric pressure. *Journal of Physics D: Applied Physics 44*(33), 335201. *(p. 3, 21, 87, 213)*

Jánský, J., F. Tholin, Z. Bonaventura, and A. Bourdon (2010). Simulation of the discharge propagation in a capillary tube in air at atmospheric pressure. *Journal of Physics D: Applied Physics 43*(39), 395201. *(p. 3, 5, 11, 16, 21, 26, 79, 87, 198, 213)*

Johnson, V., W. Zhu, R. Wang, J. Lo Re, S. Sivaram, J. Mahoney, and J. L. Lopez (2011). A cold atmospheric-pressure helium plasma generated in flexible tubing. *IEEE Transactions on Plasma Science 39*(11), 2360 – 2361. *(p. 4, 129)*

Kim, H.-H. (2004). Nonthermal plasma processing for air-pollution control: A historical review, current issues, and future prospects. *Plasma Processes and Polymers 1*(2), 91–110. *(p. 1)*

Kolobov, V. and R. Arslanbekov (2012). Towards adaptive kinetic-fluid simulations of weakly ionized plasmas. *Journal of Computational Physics 231*(3), 839 – 869. *(p. 204)*

Kozlov, K., H. Wagner, R. Brandenburg, and P. Michel (2001). Spatio-temporally resolved spectroscopic diagnostics of the barrier discharge in air at atmospheric pressure. *Journal of Physics D: Applied Physics 34*(21), 3164. *(p. 212)*

Kulikovsky, A. (1995a). A more accurate scharfetter-gummel algorithm of electron transport for semiconductor and gas discharge simulation. *Journal of Computational Physics 11*(1), 149 – 155. *(p. 19, 20, 21)*

Kulikovsky, A. (1995b). Two dimensional simulation of the positive streamer in n_2 between parallel-plate electrodes. *Journal of Physics D: Applied Physics 28*(12), 2483 – 2493. *(p. 21)*

Kulikovsky, A. A. (1997). Positive streamer between parallel plate electrodes in atmospheric pressure air. *Journal of Physics D: Applied Physics 30*(3), 441 – 450. *(p. 21)*

Kulikovsky, A. A. (1998). Positive streamer in a weak field in air: A moving avalanche-to-streamer transition. *Physical Review E 57*(6), 7066. *(p. 70, 221, 222, 223, 224)*

Laroussi, M., M. G. Kong, G. Morfill, and W. Stolz (2012). *Plasma medicine, Applications of low temperature gas plasmas in medicine biology*. Cambridge University Press. *(p. 4)*

Lax, P. and B. Wendroff (1960). Systems of conservation laws. *Communications on Pure and Applied Mathematics 13*(2), 217–237. *(p. 50, 52)*

Lebedev, S., O. Gefle, and Y. Pokholkov (2005). The barrier effect in dielectrics: the role of interfaces in the breakdown of inhomogeneous dielectrics. *IEEE Transactions on Dielectrics and Electrical Insulation 12*(3), 537 – 555. *(p. 3, 117, 146)*

Lee, H. W., G. Y. Park, Y. S. Seo, Y. H. Im, S. B. Shim, and H. J. Lee (2011). Modelling of atmospheric pressure plasmas for biomedical applications. *Journal of Physics D: Applied Physics 44*(5), 053001. *(p. 4)*

Leonard, B. (1991). The ultimate conservative difference scheme applied to unsteady one-dimensional advection. *Computer Methods in Applied Mechanics and Engineering 88*(1), 17 – 74. *(p. 50, 53)*

Leonard, B., A. P. Lock, and M. K. MacVean (1996). Conservative explicit unrestricted-time-step multidimensional constancy-preserving advection schemes. *Monthly Weather Review 124*(11), 2588 – 2606. *(p. 58)*

Li, J. (2008). Upstream nonoscillatory advection schemes. *Monthly Weather Review 136*(12), 4709 – 4729. *(p. 50, 51, 52, 53, 55, 57, 58, 204)*

Lin, K.-M., C.-T. Hung, F.-N. Hwang, M. Smith, Y.-W. Yang, and J.-S. Wu (2012). Development of a parallel semi-implicit two-dimensional plasma fluid modeling code using finite-volume method. *Computer Physics Communications 183*(6), 1225 – 1236. *(p. 43)*

Little, R. and W. Whitney (1963). Electron emission preceding electrical breakdown in vacuum. *Journal of Applied Physics 34*(8), 2430 – 2432. *(p. 170)*

Liu, N., S. Célestin, A. Bourdon, V. P. Pasko, P. Ségur, and E. Marode (2007). Application of photoionization models based on radiative transfer and the helmholtz equations to studies of streamers in weak electric fields. *Applied Physics Letters 91*(21), 211501. *(p. 10)*

Liu, N. and V. P. Pasko (2004). Effects of photoionization on propagation and branching of positive and negative streamers in sprites. *Journal of Geophysical Research: Space Physics 109*. *(p. 21, 211, 212)*

Liu, N. and V. P. Pasko (2006). Effects of photoionization on similarity properties of streamers at various pressures in air. *Journal of Physics D: Applied Physics 39*(2), 327 – 334. *(p. 15, 21)*

Lu, X. and M. Laroussi (2006). Dynamics of an atmospheric pressure plasma plume generated by submicrosecond voltage pulses. *Journal of Applied Physics 100*(6), 063302. *(p. 4)*

Lu, X., M. Laroussi, and V. Puech (2012). On atmospheric-pressure non-equilibrium plasma jets and plasma bullets. *Plasma Sources Science and Technology 21*(3), 034005. *(p. 4)*

Lu, X., Q. Xiong, Z. Xiong, J. Hu, F. Zhou, W. Gong, Y. Xian, C. Zou, Z. Tang, Z. Jiang, and Y. Pan (2009). Propagation of an atmospheric pressure plasma plume. *Journal of Applied Physics 105*(4), 043304. *(p. 4, 129)*

Marić, D., M. Radmilović-Radenović, and Z. L. Petrović (2005). On parametrization and mixture laws for electron ionization coefficients. *The European Physical Journal D-Atomic, Molecular, Optical and Plasma Physics 35*(2), 313 – 321. *(p. 178)*

Mizuno, A., Y. Yamazaki, H. Ito, and H. Yoshida (1992). Ac energized ferroelectric pellet bed gas cleaner. *Industry Applications, IEEE Transactions on 28*(3), 535–540. *(p. 1)*

Montijn, C., W. Hundsdorfer, and U. Ebert (2006). An adaptive grid refinement strategy for the simulation of negative streamers. *Journal of Computational Physics 219*(2), 801 – 835. *(p. 204)*

Morgan, W. (2011). Morgan database. http://www.lxcat.Laplace.univ-tlse.fr/. *(p. 178)*

Morrow, R. and J. J. Lowke (1997). Streamer propagation in air. *Journal of Physics D: Applied Physics 30*(4), 614. *(p. 10, 15)*

Murphy, E. L. and R. Good Jr (1956). Thermionic emission, field emission, and the transition region. *Physical review 102*(6), 1464. *(p. 169)*

Mussard, M. D. V. S., O. Guaitella, and A. Rousseau (2013). Propagation of plasma bullets in helium within a dielectric capillary-influence of the interaction with surfaces. *Journal of Physics D: Applied Physics 46*(30), 302001. *(p. 4)*

Naidis, G. (2010a). Modelling of streamer propagation in atmospheric-pressure helium plasma jets. *Journal of Physics D: Applied Physics 43*(40), 402001. *(p. 177, 179)*

Naidis, G. (2011a). Modelling of plasma bullet propagation along a helium jet in ambient air. *Journal of Physics D: Applied Physics 44*(21), 215203. *(p. 177)*

Naidis, G. and J. Walsh (2013). The effects of an external electric field on the dynamics of cold plasma jets-experimental and computational studies. *Journal of Physics D: Applied Physics 46*(9), 095203. *(p. 4)*

Naidis, G. V. (2010b). Modelling of streamer propagation in atmospheric-pressure helium plasma jets. *Journal of Physics D: Applied Physics 43*(40), 402001. *(p. 4)*

Naidis, G. V. (2011b). Modelling of plasma bullet propagation along a helium jet in ambient air. *Journal of Physics D: Applied Physics 44*(21), 215203. *(p. 4)*

Naidu, M. and V. Kamaraju (2004). *High Voltage Engineering*. published by Tata McGraw-Hill 3rd edition. *(p. 3)*

Ogata, A., K. Yamanouchi, K. Mizuno, S. Kushiyama, and T. Yamamoto (1999). Decomposition of benzene using alumina-hybrid and catalyst-hybrid plasma reactors. *Industry Applications, IEEE Transactions on 35*(6), 1289–1295. *(p. 1)*

Paillol, J., P. Espel, T. Reess, A. Gibert, and P. Domens (2002). Negative corona in air at atmospheric pressure due to a voltage impulse. *Journal of applied physics 91*(9), 5614 – 5621. *(p. 170)*

Pancheshnyi, S. (2005). Role of electronegative gas admixtures in streamer start, propagation and branching phenomena. *Plasma Sources Science and Technology 14*(4), 645. *(p. 166, 167)*

Pancheshnyi, S., P. Ségur, J. Capeillère, and A. Bourdon (2008). Numerical simulation of filamentary discharges with parallel adaptive mesh refinement. *Journal of Computational Physics 227*(13), 6574 – 6590. *(p. 204)*

Papageorghiou, L., E. Panousis, J. F. Loiseau, N. Spyrou, and B. Held (2009). Two-dimensional modelling of a nitrogen dielectric barrier discharge (dbd) at atmospheric pressure: filament dynamics with the dielectric barrier on the cathode. *Journal of Physics D: Applied Physics 42*(10), 105201. *(p. 81, 85)*

Pasko, V., U. Inan, T. Bell, and Y. N. Taranenko (1997). Sprites produced by quasi-electrostatic heating and ionization in the lower ionosphere. *Journal of Geophysical Research: Space Physics (1978–2012) 102*(A3), 4529 – 4561. *(p. 212)*

PaStiX (2012). Pastix (parallel sparse matrix package): a scientific library that provides a high performance parallel solver for very large sparse linear systems based on direct methods. http://pastix.gforge.inria.fr//. *(p. 15, 34)*

Pechereau, F., J. Jánský, and A. Bourdon (2012). Simulation of the reignition of a discharge behind a dielectric layer in air at atmospheric pressure. *Plasma Sources Science and Technology 21*(5), 055011. *(p. 16, 26)*

Pouvesle, J., A. Bouchoule, and J. Stevefelt (1982). Modeling of the charge transfer afterglow excited by intense electrical discharges in high pressure helium nitrogen mixtures. *The Journal of Chemical Physics 77*, 817. *(p. 178)*

Raizer, Y. P. (1991). *Gas Discharge Physics*. Springer, Berlin, Heidelberg. *(p. 90, 134)*

Reess, T. and J. Paillol (1997). The role of the field-effect emission in trichel pulse development in air at atmospheric pressure. *Journal of Physics D: Applied Physics 30*(22), 3115. *(p. 170)*

Reuter, S., J. Winter, A. Schmidt-Bleker, D. Schroeder, H. Lange, N. Knake, V. S. von der Gathen, and K.-D. Weltmann (2012). Atomic oxygen in a cold argon plasma jet: Talif spectroscopy in ambient air with modelling and measurements of ambient species diffusion. *Plasma Sources Science and Technology 21*(2), 024005. *(p. 4)*

Robert, E., V. Sarron, D. Riès, S. Dozias, M. Vandamme, and J. M. Pouvesle (2012). Characterization of pulsed atmospheric-pressure plasma streams (paps) generated by a plasma gun. *Plasma Sources Science and Technology 21*(3), 034017. *(p. 4)*

Roe, P. L. (1985). Some contributions to the modelling of discontinuous flows. *Lectures in Applied Mathematics 22*, 163–193. *(p. 52)*

Sakiyama, Y., D. B. Graves, J. Jarrige, and M. Laroussi (2010). Finite element analysis of ring-shaped emission profile in plasma bullet. *Applied Physics Letters 96*(4), 041501 – 041501. *(p. 4)*

Sands, B. L., B. N. Ganguly, and K. Tachibana (2008). A streamer-like atmospheric pressure plasma jet. *Applied Physics Letters 92*(15), 151503. *(p. 4)*

Scharfetter, D. and H. Gummel (1969). Large-signal analysis of a silicon read diode oscillator. *Electron Devices, IEEE Transactions*

on 16(1), 64–77. *(p. 18)*

Solov'ev, V., A. Konchakov, V. Krivtsov, and N. Aleksandrov (2008). Numerical simulation of a surface barrier discharge in air. *Plasma Physics Reports 34*(7), 594 – 608. *(p. 81, 93, 97)*

Takacs, L. L. (1985). A two-step scheme for the advection equation with minimized dissipation and dispersion errors. *Monthly Weather Review 113*(6), 1050–1065. *(p. 52)*

Tardiveau, P., C. Boyer, F. Jorand, C. Postel, and S. Pasquiers (2005). Optical and electrical characterization of pulsed dielectric barrier discharges in heterogeneous structures. *Plasma Science, IEEE Transactions on 33*(2), 314 – 315. *(p. 1)*

Teschke, M., J. Kedzierski, E. G. Finantu-Dinu, D. Korzec, and J. Engemann (2005). High-speed photographs of a dielectric barrier atmospheric pressure plasma jet. *IEEE Transactions on Plasma Science 33*(2, Part 1), 310 – 311. *(p. 4)*

Tholin, F. and A. Bourdon (2011). Influence of temperature on the glow regime of a discharge in air at atmospheric pressure between two point electrodes. *Journal of Physics D: Applied Physics 44*(38), 385203. *(p. 11, 16, 21)*

Tholin, F. and A. Bourdon (2013). Simulation of the stable quasi-periodic glow regime of a nanosecond repetitively pulsed discharge in air at atmospheric pressure. *Plasma Sources Science and Technology 22*(4), 045014. *(p. 167)*

Ventzek, P. L. G., T. J. Sommerer, R. J. Hoekstra, and M. J. Kushner (1993). Two-dimensional hybrid model of inductively coupled plasma sources for etching. *Applied Physics Letters 63*(5), 605–607. *(p. 43, 44)*

Villa, A., L. Barbieri, M. Gondola, and R. Malgesini (2013). An asymptotic preserving scheme for the streamer simulation. *J. Comput. Phys. 242*, 86–102. *(p. 43, 44)*

Vitello, P. A., B. M. Penetrante, and J. N. Bardsley (1994, Jun). Simulation of negative-streamer dynamics in nitrogen. *Phys. Rev. E 49*, 5574–5598. *(p. 23)*

Wu, S., Z. Wang, Q. Huang, Q. Xiong, and X. Lu (2011). Plasma plume ignited by plasma plume at atmospheric pressure. *IEEE Transactions on Plasma Science 39*(11), 2292–2293. *(p. 4, 129)*

Xiong, Z., E. Robert, V. Sarron, J. Pouvesle, and M. Kushner (2013). Atmospheric-pressure plasma transfer across dielectric channels and tubes. *Journal of Physics D: Applied Physics 46*(15), 155203. *(p. 4, 129, 133, 140)*

Yousfi, M., O. Eichwald, N. Merbahi, and N. Jomaa (2012). Analysis

of ionization wave dynamics in low-temperature plasma jets from fluid modeling supported by experimental investigations. *Plasma Sources Science and Technology 21*(4), 045003. *(p. 177)*

Zhang, P. and U. Kortshagen (2006). Two-dimensional numerical study of atmospheric pressure glows in helium with impurities. *Journal of Physics D: Applied Physics 39*(1), 153. *(p. 178, 179)*

Zhelezniak, M., A. K. Mnatsakanian, and S. Sizykh (1982). Photoionization of nitrogen and oxygen mixtures by radiation from a gas discharge. *High Temperature Science 20*, 357 – 362. *(p. 10, 221)*